Quantum dash based photonic integrated circuits for optical telecommunications

Siddharth Joshi

THÈSE DE DOCTORAT DE
l'UNIVERSITÉ PIERRE ET MARIE CURIE

Spécialité

Télécommunications et Électronique

École doctorale Informatique, Télécommunications et Électronique (Paris)

Présentée par

Siddharth Joshi

Pour obtenir le grade de

DOCTEUR de l'UNIVERSITÉ PIERRE ET MARIE CURIE

Sujet de la thèse :

Circuits intégrés photoniques à base de boîtes quantiques pour télécommunications optiques (Thèse n° 2014TELE0031)

soutenue le 05 novembre 2014

devant le jury composé de :

M. Abderrahim Ramdane	Directeur de thèse
M. François Lelarge	Encadrant de thèse
M. Jeremy Witzens	Rapporteur
M. Beatrice Dagens	Rapporteur
M. Chirstophe Peucheret	Examinateur
M. Aziz BENLARBI-DELAI	Examinateur

Université Pierre et Marie CURIE

ET

Telecom SudParis

Quantum Dash based Photonic Integrated Circuits for Optical Telecommunications

Author :
Siddharth Joshi

Academic Supervisor :
Prof. Abderrahim Ramdane
Industrial Supervisor :
Dr. François Lelarge

A thesis submitted in fulfilment of the requirements
for the degree of
Doctor of Philosophy

in the

L'école doctorale informatique,
télécommunications et électronique

13 novembre 2014

Jury for this Dessertation

Rapporteur **Dr. Beatrice DAGENS**	Directeur de Recherche chez Université Paris-Sud 11 et Institut d'Electronique Fondamentale, Orsay
Rapporteur **Prof. Jeremy WITZENS**	Head, Integrated Photonics Laboratory, Sommerfeldstraße 24 52074 Aachen, Germany
Jury Member **Prof. Aziz BENLARBI-DELAÏ**	Professeur et Directeur du L2E, Université Pierre et Marie CURIE, Paris
Jury Member **Prof. Christophe PEUCHERET**	Professeur, École Nationale Supérieure des Sciences Appliquées et de Technologie (ENSSAT-Lannion), Lannion
Thesis Director **Prof. Abderrahim RAMDANE**	Director, Laboratoires de Photonics et de Nanostructures, Centre Nationale de Research Scientifique , Marcoussis)
Thesis Supervisor **Dr. Francois LELARGE**	Research Engineer, Alcatel Lucent Bell Labs (3-5 Lab), Marcoussis, France

Association and Funding

III-V Lab, a private Research & Development organisation jointly established by Alcatel-Lucent and Thales in 2004 under the French "Group of Economic Interest" (GIE) status, concentrates in a single entity the most advanced industrial research capabilities in the field of III-V semiconductors in Europe.

Dispersion **I**mmune **Q**uantum **DOT** (DIQDOT) based sources for next generation access networks is a project supported by Agence Nationale de la Recherche (The French National Research Agency). The DIQDOT project aimed at developing novel GREEN optical sources for low cost, low consumption, athermal, access network infrastructure that support a number of access network topologies.

Postgraduate **R**esearch on **P**hotonics as an **E**nabling **T**echnology is an Initial Training Network funded by the EU Framework Programme 7 Marie Curie Actions, which aims to train the next generation of photonics researchers in the full range of skills required for a multi-disciplinary, industry-focused career in photonics. This work was funded by the EU FP7 Marie Curie Action FP7-PEOPLE-2010-ITN through the PROPHET project, Grant No. **264687** and is linked with the work packages WP1 and WP3 of the project.

Declaration of Authorship

I, Siddharth Joshi, declare that this thesis titled, 'Quantum Dash based Photonic Integrated Circuits for Optical Telecommunications' and the work presented in it are my own. I confirm that:

- This work was done wholly or mainly while in candidature for a research degree at this University.
- Where any part of this thesis has previously been submitted for a degree or any other qualification at this University or any other institution, this has been clearly stated.
- Where I have consulted the published work of others, this is always clearly attributed.
- Where I have quoted from the work of others, the source is always given. With the exception of such quotations, this thesis is entirely my own work.
- I have acknowledged all main sources of help.
- Where the thesis is based on work done by myself jointly with others, I have made clear exactly what was done by others and what I have contributed myself.

Signed:

Date:

For my parents. . .

Acknowledgements

It would not have been possible to write this doctoral thesis without the help and support of people around me. This thesis owes its existence to help, support and inspiration of several people. I would like to take this opportunity to extend my gratitude to them. First and foremost I would like to thank my supervisor and my mentor Dr. Francois Lelarge. I would like to thank him for encouraging my research and for allowing me to grow as a researcher. His advice on both research as well as on my career have been priceless. I would like to thank him for his enormous support, guidance and trust he put in me to carry out my research at 3-5 Lab. I would also like to thank my academic supervisor, Prof. Ramdane, for his support throughout the course of this work. I would like to thank Dr.Francois Bruilluet and Dr. Jean-Louis Gentener for entrusting me with this position at III-V lab.

I thank the members of the doctoral committee: Dr. B. Dagens, Prof. J. Witzens, Prof. C. Peucheret, Prof. A. Benlarbi-Delai, Prof. J. Witzens, Prof. J. Witzens, for accepting to be the part of the Jury for this work and for having willingly examined and judged this PhD dissertation.

I express my gratitude to Dr. Nicolas Chimot, who helped me at various stages of this dissertation from the conception to the realisation of the final devices to making correction in the dissertation. I would extend my sincere regards to my officemates Dr. Sophie Barbet who trained me in the processing technology and helped me with the development of technology for the integrated DML devices; also Nadine Lagay, Dr. Olivier Drisse and Dr. Romain Brenot for all the candid moments in the office. I extend my thanks to Florent Franchin, Delphine Lenteri, Estelle Doudorin, Florence Martin, Alain Accard, Jean-Guy Provost, Yohann Moustapha-Rabault, Frédéric Pommereau, François Alexandre, Philippe Berdaguer, Valérie Deshayes, Christophe Kazmierski, Jean-François Paret, Muriel Reit, Benjamin Saturnin, Alexandre Garreau for all their support and help on various issues during this work, it is due to their expertise helped this work progressed at a fast pace. I would also like to thank Pascale Téfaine, who helped me with several administrative issues throughout my stay at 3-5 Lab, she was always a life saver when it came to the administration.

I would like to take the opportunity to thank the Marie Curie actions and the Initial Training Network PROPHET (Postgraduate Research on Photonics as an Enabling Technology) for funding my research. The PROPHET consortium provided me with a diversified scientific environment and an opportunity to collaborate with various prestigious research institutions around Europe.

A part of the work was done in collaboration with CNRS - Laboratoire de Photonique et de Nanostructures (LPN), where I worked with two other PROPHET fellows Cosimo Calo and Konstantinos Papatryphonos, I would like to thank them for their support and friendship. At the same time I would extend my thanks to Vivek Venkatesan, Dr. Oriane Mollet, Dr. A. Martinez and Dr. K Merghem for fruitful discussions. During the course of this work, I had the opportunity to be at the beautiful city of Cork (Ireland). At the Tyndall national institute, Cork I had the opportunity to worked with Dr. Guillaume Huyet, Dr. Tomasz Piwonski and, Kasia Komolibus. Ms Komolibus was an excellent host for me at Tyndall and I would like to specially thank her for her support during my short stay at Tyndall. I would like to thank Dr. Luiz A Neto, Dr. M.Gay from ENSSAT, Lannion and Q.Daniel, Dr. P.Chanclou, Dr. B.Charbonnier and Dr. F.Silaou from Orange Labs, Lannion for their help and support on contributing towards the understanding on the bandwidth enhancement with passive filters. I would also like to thank Prof. Yaneck Gottesman for fruitful discussions on the ring resonators and for measurement on the passive optical components.

A special thanks to my family. Words cannot express how grateful I am to my mother for all of the sacrifices that you've made on my behalf. Your prayer for me was what sustained me thus far. I would like to thank Serenika Assas, Maria Anagnosti, Konstantinos Pantzas, Carmen Gomez, Dimitris Kazazis, Phillipe Angilini for the help and support and all of my friends who supported me in writing, and incented me to strive towards my goal.

Contents

List of Figures

List of Tables

Abbreviations

AC	**A**uto**c**orrelation
ASE	**A**mplified **S**pontaneous **E**mission
APD	**A**valanche **P**hotodiode
AWG	**A**rrayed **W**aveguide **G**rating
BA	**B**road **A**rea
BER	**B**it **E**rror **R**atio
BRS	**B**urried **R**idge **S**tripe
CML	**C**hirp **M**anaged **L**aser
DBAR	**D**ash in a **BAR**rier
DBR	**D**istributed **B**ragg **R**eflector
DCA	**D**igital **C**ommunication **A**nalyser
DER	**D**ynamic **E**xtinction **R**atio
DFB	**D**istributed **F**eed**B**ack
DML	**D**irectly **M**odulated **L**aser
DoS	**D**ensity **o**f **S**tates
DWELL	**D**ash in a **WELL**
EML	**E**xternally **M**odulated **L**aser
EaML	**E**lector-**a**bsorption **M**odulation **L**aser
FP	**F**abry **P**érot
FWHM	**F**ull **W**idth at **H**alf **M**aximum
FSR	**F**ree **S**pectral **R**ange
FTTH	**F**ibre **T**o **T**he **H**ome
ITU-T	**I**nternational **T**elecommunication **U**nion-**T**elecommunication(Standardization Sector)
GSMBE	**G**as **S**ource **M**olecular **B**eam **E**pitaxy
LEF	**L**inewidth **E**nhancement **F**actor
LCA	Lightwave Component Analyser
MBE	**M**olecular **B**eam **E**pitaxy
MOVPE	**M**etal **O**rganic **V**apor **P**hase **E**pitaxy
ML	**M**ode **L**ocking
MLL	**M**ode **L**ocked**L**aser
MZ	**M**ach-**Z**ehnder

MZI	**M**ach-**Z**ehnder **I**nterferometer
NGPON	**N**ext **G**eneration **P**assive **O**ptical **N**etworks
NRZ	**N**on-**R**eturn-to-**Z**ero
OFDM	**O**rthogonal **F**requency **D**ivision **M**ultiplexing
OLCR	**O**ptical **L**ow **C**oherence **R**efractometry
PIC	**P**hotonic **I**ntegrated **C**ircuits
PoF	**P**assive **o**ptical **F**ilter
PRBS	**P**seudo-**R**andom **B**it **S**equence
PL	**P**hoto-**L**uminescence
QD	**Q**uantum **Dot**
QDash	**Q**uantum **Dash**
QW	**Q**uantum **W**ell
QWire	**Q**uantum **W**ire
RWG	**R**idge **W**ave-**G**uide
RF	**R**adio **F**requency
RoF	**R**adio **o**ver **F**iber
SEM	**S**canning **E**lectron **M**icroscopy
SOA	**S**emiconductor **O**ptical **A**mplifier
SSMF	**S**tandard **S**ingle **M**ode **F**ibre
TEM	**T**unneling **E**lectron **M**icroscopy
WDM	**W**avelength **D**ivision **M**ultiplexing

UNIVERSITÉ PIERRE ET MARIE CURIE

Abstract

L'école doctorale informatique,
télécommunications et électronique

Doctor of Philosophy

Quantum Dash based Photonic Integrated Circuits for Optical Telecommunications

by Siddharth Joshi

This PhD dissertation presents a study on the properties of novel quantum dash nanostructures and their properties for application in optical telecommunications. Over the last decade, the scientific community has gained considerable interest over these nanostructures and several demonstrations have been made on their interesting optical and electronic properties, notably owing to their strong quantum confinement. This dissertation focuses on conception, fabrication and system demonstration of integrated optical transmitters based on quantum dash material. A first part of this work analyses the properties of qdashes theoretically and experimentally for their use as an active material in directly modulated lasers. The dynamic properties of this material are then evaluated, leading to optical transmission distances in the range of 0-100 km under direct modulation. The transmission is particularly studied with a passive optical filter to enhance the dynamic extinction ratio. The use of such passive filters is studied in detail. An innovative and fully integrated optical transmitter is finally demonstrated by integrating a ring-resonator filter to a distributed feedback laser. The second part of this work focuses on mode locked lasers based on this material and in particular the methods of integration of such devices on InP are explored. Thus an innovative Bragg mirror design is developed, leading to a mode locked laser integrated with a semiconductor optical amplifier.

UNIVERSITÉ PIERRE ET MARIE CURIE

L'école doctorale informatique,
télécommunications et électronique

Résumé

Circuits intégrés photoniques à base de boîtes quantiques pour télécommunications optiques

par Siddharth Joshi

pour obtenir le grade de

DOCTEUR

Ce travail de thèse présente une étude sur les propriétés de nanostructures de type bâtonnets quantiques et de leur application pour les télécommunications optiques. Durant la dernière décennie, ces nanostructures, ont démontré des propriétés optiques et électroniques intéressantes en raison notamment d'un fort confinement quantique dans les trois dimensions d'éspace. Cette thèse porte sur la conception et la fabrication d'émetteurs optiques intégrés à base de ce matériau et de leur implémentation dans des systèmes de communication. La première partie de ce travail analyse les propriétés de ces nanostructures, théorique et expérimentale. Elles sont utilisées comme matériau actif de lasers modulés directement en amplitude. Les propriétés dynamiques de ces lasers sont ensuite évaluées et des transmissions sur fibre optique entre 0 et 100 km sont ensuite démontrées en utilisant un filtre étalon permettant d'augmenter en particulier le taux d'extinction dynamique. En s'appuyant sur cette démonstration basée sur des éléments discrets, une version monolithique intégrant un laser et un résonateur en anneaux a été réalisée. La dernière partie de ce travail porte sur des lasers à blocage de mode à base de ce matériau et en particulier sur les méthodes d'intégration sur substrat InP. En particulier, un design de miroir de Bragg innovant a été développé à cet effet et une démonstration d'un laser a blocage de mode intégré avec un amplificateur optique à semi-conducteur a été réalisée.

Circuits photoniques intégrés à base de bâtonnetes quantiques

Les propriétés électroniques d'un matériau sont très fortement dépendantes de sa taille et de sa forme. Les effets du confinement peuvent être observables dès que le diamètre de l'objet est comparable à la longueur d'onde de la fonction d'onde électronique. En particulier, les essais de croissances de boîtes quantiques auto-assemblées sur substrat (100)-InP ont aboutis à la formation de nanostructures allongées appelées Quantum Dashes (QDashes). Ce sont des hétérostructures de faible dimension, typiquement de 200 et 300nm de long, de 10 et 20nm de large et de 1 à 2nm de haut. La figure. 1, présente une telle structure observée au microscope électronique à transmission.

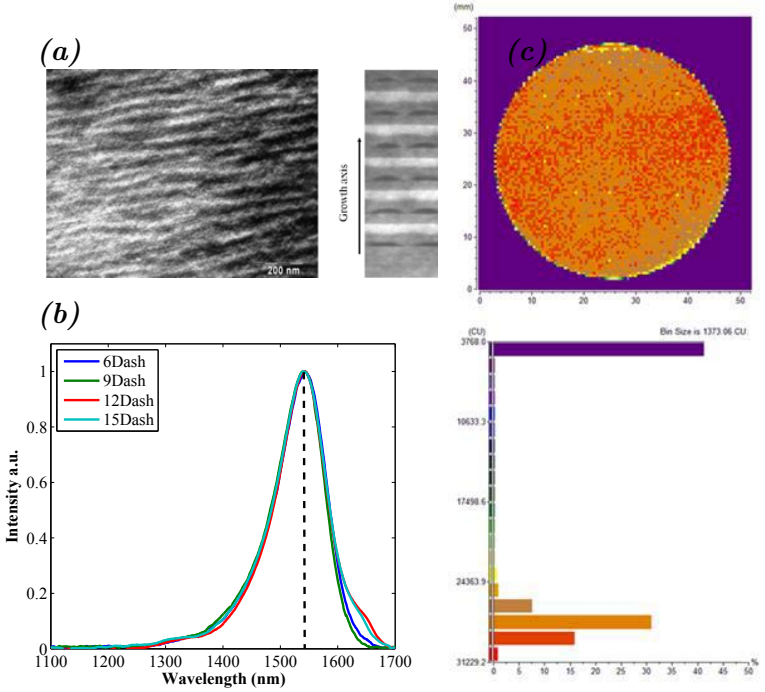

Figure 1: Structure des QDash observée au microscope électronique à transmission

La structure active d'un laser constituée d'une seule couche de QDashes présente un confinement optique trop faible pour obtenir un gain optique suffisant pour compenser les pertes optiques de la cavité. Afin d'augmenter le gain, les QDashes sont épitaxiées en plusieurs couches. Des lasers dits « larges » sont fabriqués pour évaluer la qualité du matériau en termes de performance laser (courant de seuil, gain modal, pertes internes, rendement quantique externe). Au cours de ce travail, nous avons fabriqués des lasers avec différents nombres de couches de QDashes. Les paramètres fondamentaux du matériau sont ensuite évalués à partir des mesures de puissance optique sur des lasers « larges » de différentes longueurs, comme le montre les figures 2

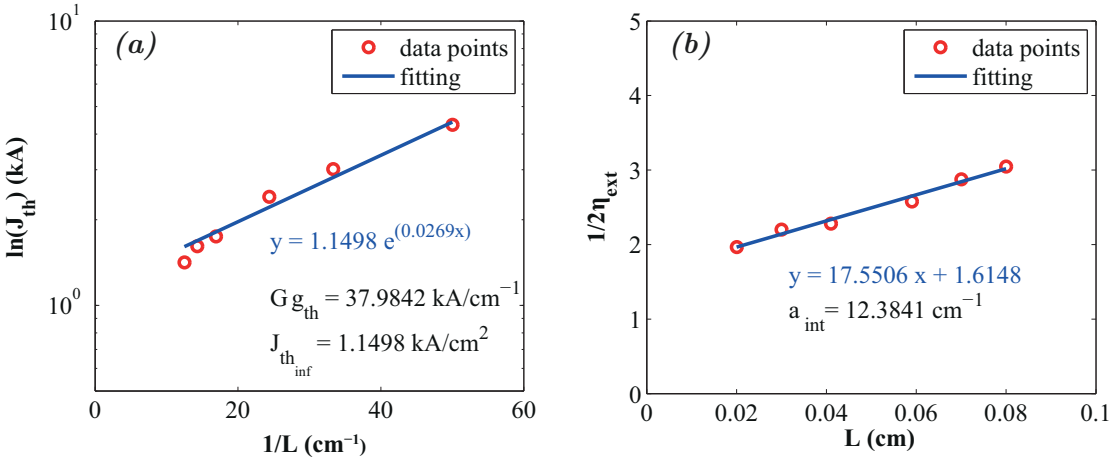

FIGURE 2: (a) Threshold current density J_{th} as a function of inverse cavity length, the intercept on y-axis gives the value of $J_{th_{inf}}$ (b) Inverse of external quantum efficiency as a function of length of the broad area laser

Le tableau suivant présente les paramètres déduits de ces mesures pour différentes structures DWELL (Dash in a Well) et DBAR (Dash in a barrier). Il existe un optimum entre fort gain modal et faibles pertes internes. Nous avons pu montrer que le gain net par QDash diminue fortement au-delà de 9 couches de QDashes. Cette diminution est attribuée à la ré-absorption de la puissance optique par les couches de QDashes.

DBAR Stack	Γ%	$J_{th_{inf}}$ (kA/cm^2)	Γg_{th} (cm^{-1})	α_i (cm^{-1})
6 Layers	0.90	1.15	37.98	12.38
9 Layers	1.35	1.73	64.92	27.15
12 Layers	1.80	1.96	52.24	19.44
15 Layers	2.25	2.06	56.71	18.72

TABLE 2: Threshold current density J_{th}, Modal gain Γg_{th} and internal loss α_i different stack layers in a DBAR structure.

Le dopage du matériau est également un paramètre ayant un impact fort sur les performances d'un laser. Nous avons étudié l'impact du dopage dans des structures lasers à 6 couches de QDashes. La table 4 présente les résultats obtenus pour différents types

DWELL Stack	Γ%	$J_{th_{inf}}$ (kA/cm^2)	Γg_{th} (cm^{-1})	α_i (cm^{-1})
6 Layers	0,94	0,95	38.56	11.63
12 Layers	1.67	1.73	48.86	19.11
15 Layers	2.3	2.31	61.58	25.32

TABLE 3: Threshold current density J_{th}, Modal gain Γg_{th} and internal loss α_i different stack layers in a DWELL structure.

Doping Type	$J_{th_{inf}}$ (kA/cm^2)	Γg_{th} (cm^{-1})	α_i (cm^{-1})
n-doped (Si 1E+18)	0.941	30.45	13.98
no doping	0.95	38.56	11.63
p-doped (Be-1E+18)	2.189	64.17	26.38
p-doped (Be-2E+18)	2.24	60.03	34.80

TABLE 4: Threshold current density J_{th}, Modal gain Γg_{th} and internal loss α_i for different doping-types in DWELL structures.

et niveau de dopage et une comparaison à un matériau non-dopé a été faite. Le dopage n n'apporte pas d'amélioration significative tandis que le dopage p entraîne une augmente du seuil du laser à cause d'une augmentation des pertes d'absorption. Néanmoins, cette augmentation du seuil reste acceptable au niveau composant puisque en contrepartie, à la fois le gain modal et les performances en température du laser sont améliorés.

Des simulations avec le logiciel ALCOR développé par France Télécom/ CNET ont été faites pour identifier la largeur de coupure monomode des lasers à base de QDashes et le confinement du mode optique dans le matériau actif. Le comportement monomode du laser est maintenu jusqu'à une largeur de ruban de 1.7 μm. Le mode transverse en champ proche est représenté sur la figure 3 Il est à noter que le mode est presque gaussien à la différence des structures RIDGE où le mode a une forme de « poire ». La figure 4 montre une image MEB d'une structure laser en technologie BRS.

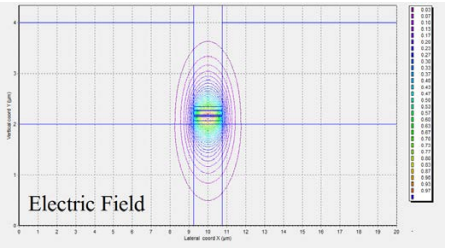

FIGURE 3: Near field calculation of Electric filed and Intensity at the output of the BRS structure.

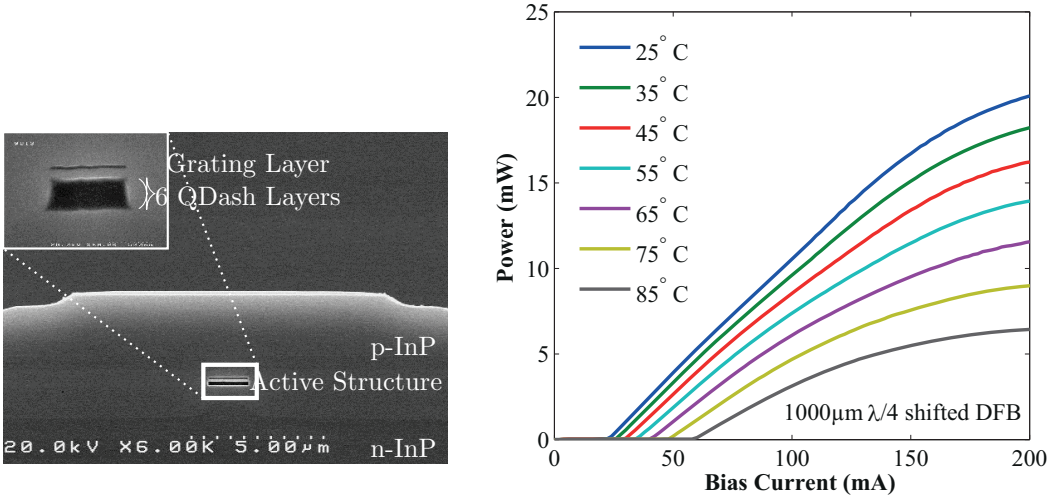

FIGURE 4: Scanning Electron Micrograph of the device fabricated using BRS technology

Nous avons utilisé ce matériau pour concevoir des lasers de type DFB, qui bien que la puissance émise est diminuée de moitié par rapport aux lasers Fabry-Perot (FP) à cause du saut de phase dans son réseau de Bragg, présente des caractéristiques en températures très bonnes et d'excellentes puissances optiques émises (figure 4). Le spectre optique monomode avec un saut de phase $\lambda/4$ est présenté figure 5. Le SMSR est d'environ 45dB. La largeur de raie optique de ces DFB est entre 1 et 5MHz suivant le matériau actif utilisé.

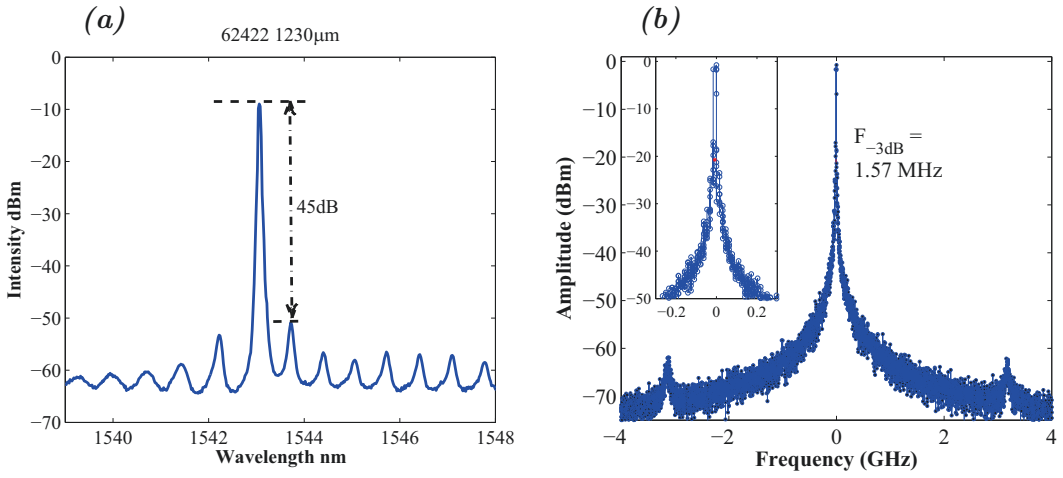

FIGURE 5: (a)Optical Spectrum of a DFB Lasers with a ridge-width of 1.5 μm showing a single longitudinal mode. (b) High resolution optical spectrum showing optical linewidth of the DFB laser.

Les caractéristiques dynamiques de ces lasers ont également été évaluées comme la bande passante, la fréquence de relaxation, le facteur d'amortissement, le paramètre de Henry, le chirp et le gain différentiel. Le design même de la structure active va avoir un impact fort sur ces paramètres à travers la largeur des barrières et des couches de

confinement, ainsi que la géométrie du laser. La figure 6 montre les mesures de bandes passantes électro-optiques pour différentes structures avec un courant injecté de 100mA.

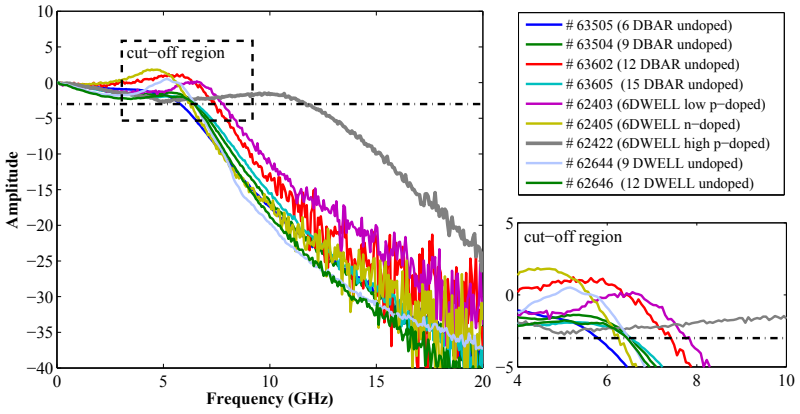

FIGURE 6: Small Signal Modulation response of a QDash Lasers width various epitaxial structures for maximum possible 3dB cut-off.

La fréquence de relaxation et le facteur d'amortissement sont évalués pour des structures non-dopées de type DBAR et DWELL (tables 5, 6 et 7). Nous avons pu constater que les structures DWELL présentaient des facteurs d'amortissement très faibles.

Wafer #	Stack #	$\Gamma_0 = 1/\tau_c$ (GHz)	K (ns)
63505	6	5.64	0.52
63504	9	5.92	0.42
63602	12	6.41	0.34
63605	15	6.73	0.33

TABLE 5: K-factors and damping offset for DBAR structures

Wafer #	Stack #	Γ_0 (GHZ)	K (ns)
62400	4	3.48	0.40
62407	6	3.98	0.27
62644	9	4.78	0.27
62646	12	4.20	0.28

TABLE 6: K-factors and damping offset for DWELL structures

Wafer #	Doping Type	Γ_0 (GHZ)	K (ns)
62405	Si-Doped	3.15	0.37
62407	un-Doped	3.98	0.27
62127	Be 2.5e-17	4.01	0.27
62406	Be 3e-17	4.41	0.26
62426	Be 6e-17	4.41	0.26
62403	Be 1e-18	4.61	0.29
62422	Be 2e-18	5.69	0.22

TABLE 7: K-factors and damping offset for various doping concentrations in DWELL structures with 6 dash layers

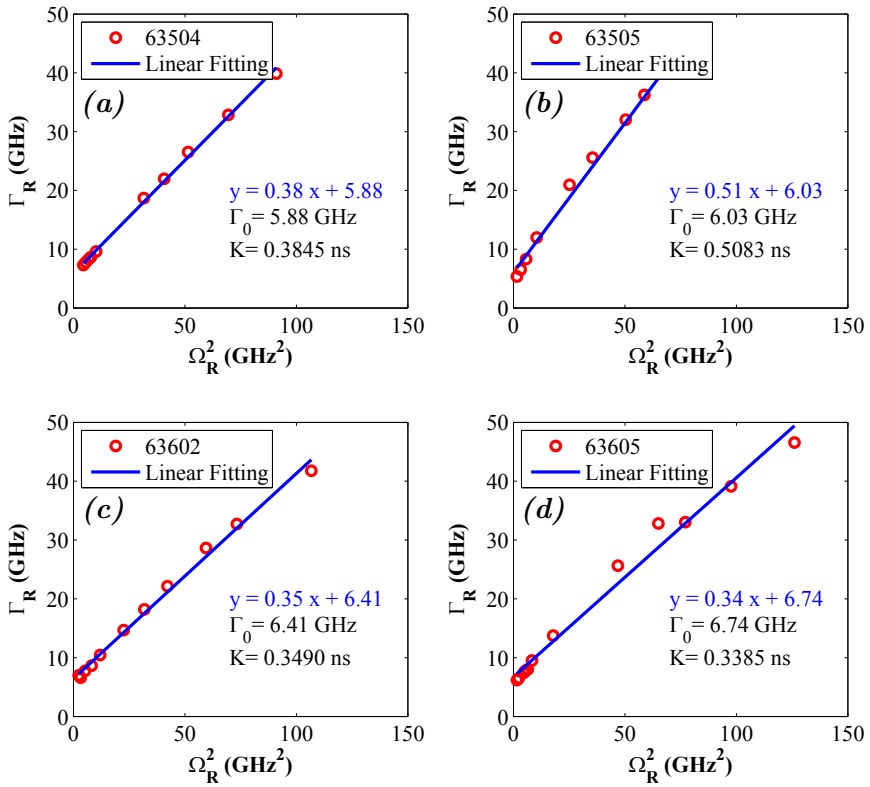

FIGURE 7: Damping rate Γ_R as a function of Square of relaxation oscillation frequency Ω_R with extracted value of Damping offset Γ_0 and Damping factor K for 63505(6-BAR), 63504(9-DBAR), 63602(12-DBAR), 63605(15-DBAR)

Le gain différentiel des lasers est un paramètre très utile pour évaluer le potentiel d'un laser en termes de performances en modulation. Il peut être évalué à partir des mesures de réponses électro-optiques des lasers en petit signal à partir de l'expression 1.

$$\Omega_R^2 = \frac{\Gamma \eta_i v_g}{4\pi^2 eV} \frac{dg}{dn}(I - I_{th}) \tag{1}$$

Une comparaison quantitative du gain différentiel a été faite à partir des pentes des courbes de figure 8, où plus la pente sera élevée pour le même volume actif et le même confinement optique, plus il sera élevé. Nous avons pu démontrer qu'il est nettement amélioré pour les structures avec un dopage de type p, et à l'inverse, sa valeur est nettement diminuée avec un dopage de type n (figure 8).

La bande passante des lasers permet de déterminer jusqu'à quel débit de données optiques il peuvent être utilisés. Néanmoins, les transmissions des données optiques sont rendues également très compliquées à cause du phénomène de chirp en fréquence (« glissement ») notamment à cause de la dispersion chromatique dans une fibre optique. Le paramètre de Henry permet d'évaluer le chirp d'un laser lorsqu'il est modulé. Nous

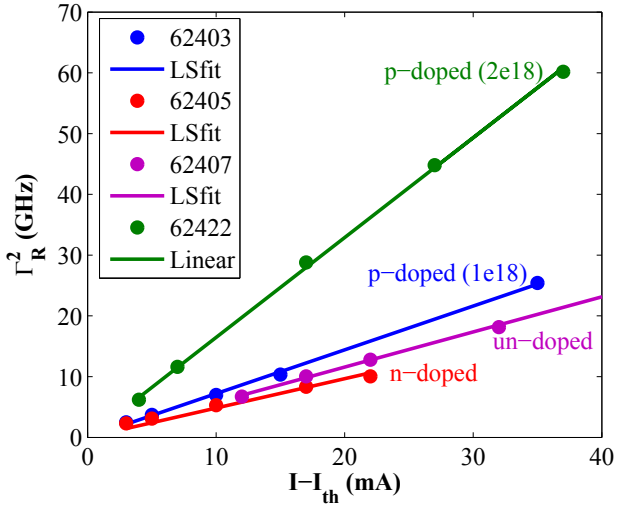

FIGURE 8: Square of resonance frequency Ω_R vs $I - I_{th}$ for different doping in barriers.

avons mesuré ce paramètre pour différentes types de structures avec dopage de type p au-dessus du seuil du laser (donc dans des conditions réelles d'utilisation du laser).

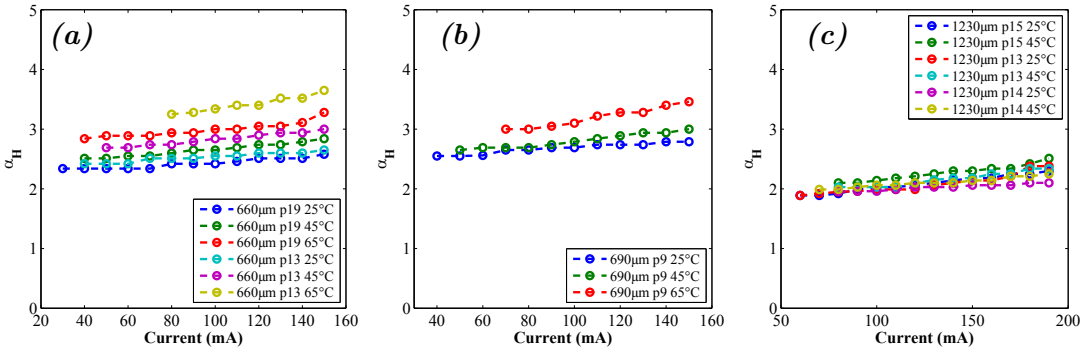

FIGURE 9: α_H-parameter measured at higher temperatures for lasers of similar lengths

Dans les figures 9 nous pouvons constater que le paramètre de Henry reste stable au-dessus du seuil et qu'il ne change pas de valeur également en-dessous. Ce résultat est vraiment relié à la nature même de ce type de matériau et du dopage de type p qui entraînent une réduction de la densité d'états qui implique une réduction importante de la valeur du paramètre de Henry.

Néanmoins, l'évaluation du paramètre de chirp en petit signal reste insuffisante pour appréhender totalement le comportement du laser dans des conditions pratiques et réelles, notamment à cause de la dépendance du laser à l'indice de modulation. Dans des conditions réelles, l'indice de modulation est comparable a la bias actuel de la laser. Il est ainsi primordial d'évaluer le chirp aussi dans des conditions de larges signaux. Nous l'avons évalué en modulant le courant avec des impulsions carrées d'une durée de 1ns d'après la méthode de FM et AM séparation. La figure 11 montre un chirp adiabatique

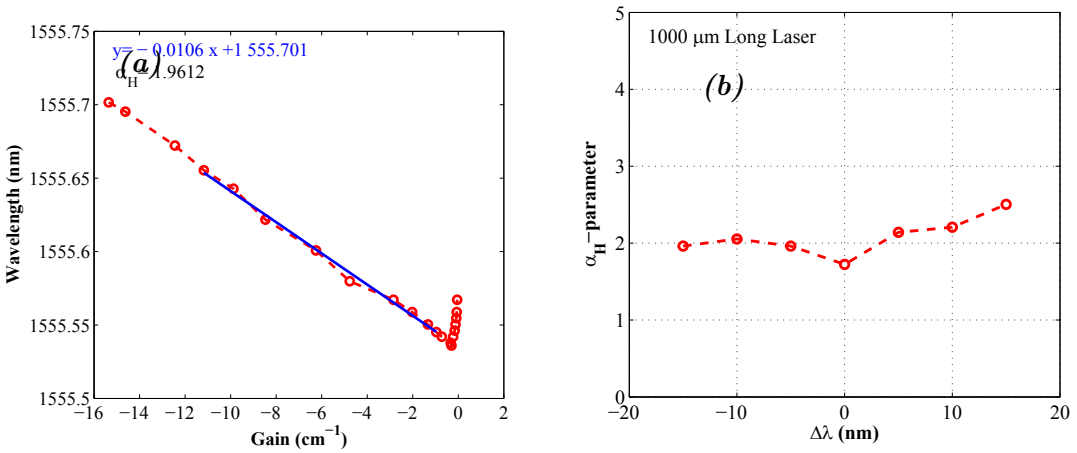

FIGURE 10: (a) α_H-parameter measured using Hakki Pauli Method for a 1000 μm long cavity for a negative detuning of 10 nm from the gain peak using 10% duty cycle pulsed current injection. (b) Gain vs Wavelength and extracted α_H-parameter.

de 2GHz et un chirp transitoire de 1GHz, ce qui démontre que de faibles valeurs peuvent être atteintes avec ce type de matériau, le rendant très prometteur pour effectuer de la transmission de données sur fibre optique.

$$\Delta\nu = \nu - \nu_{th} = \frac{\alpha_H}{4\pi}\left(\underbrace{\frac{1}{P}\frac{dP}{dt}}_{TransientChirp} - \underbrace{\frac{R_{sp}}{P} + \frac{\epsilon_{NL}P}{\tau_P}}_{AdiabaticChirp}\right) \tag{2}$$

La bande passante élevée, le faible facteur de Henry et la faible valeur du chirp dans les lasers à base de QDashes en font d'excellents candidats pour les transmissions sur fibre optique. Nous avons évalués ces performances en modulant les lasers avec un signal NRZ d'une longueur de mots 2e31-1. La puissance optique est limitée à +3dBm dans la fibre optique pour s'affranchir d'éventuels effets non-linéaires. Le courant de polarisation et l'amplitude de modulation sont optimisés pour transmettre sur la plus grande distance possible et ces conditions sont ensuite conservées pour les distances plus courtes. Le taux d'erreur en fonction de la puissance incidente en réception sur une photodiode APD et les diagrammes de modulations optiques sont présentés sur les figures 12 pour des distances entre 0 et 100km. Le taux d'extinction dynamique reste néanmoins faible (¡3dB). La distorsion des yeux optiques est sensible à partir de 25km de fibre optique, où ils commencent à se fermer. Les yeux optiques pour une distance de 100km restent ouverts grâce à un effet de DST.

Le taux d'extinction dynamique peut être augmenté en utilisant un filtre étalon passif. Comme les bits « 0 » sont décalés vers le rouge à cause du chirp adiabatique, leur amplitude peut être sélectivement diminuée par rapport aux bits « 1 » grâce au

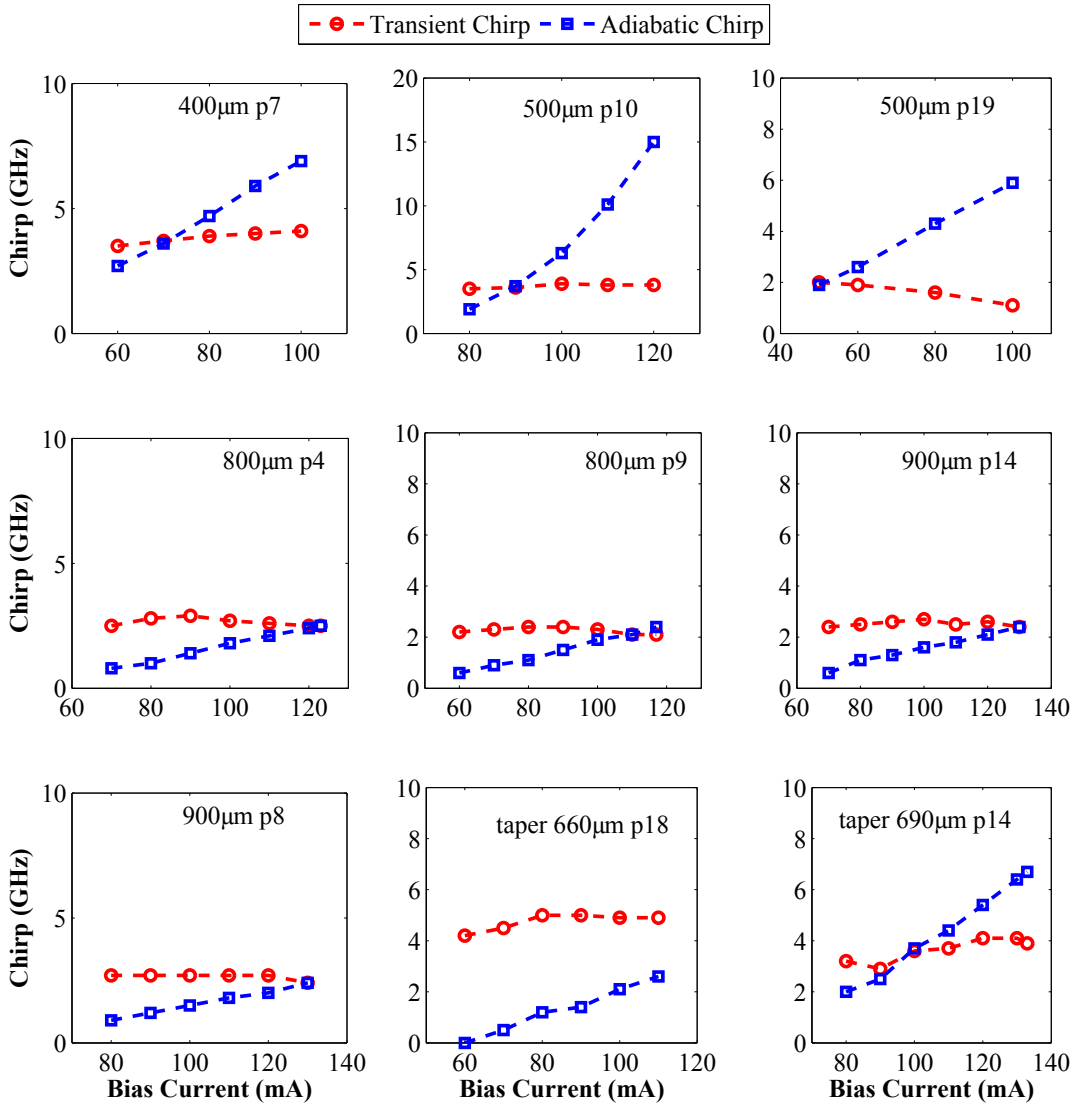

FIGURE 11: Extracted Chirp Values vs Biasing Current for various DFB lasers. The DER is kept constant at 3dB.

filtrage d'un filtre étalon. Les mesures de transmissions sont ainsi répétées en plaçant le filtre étalon directement après le laser modulé directement (figure 13).

Il faut noter que la position de la longueur d'onde du laser par rapport au filtre étalon a un impact très important sur les performances en transmission. Nous avons décalé cette position en modifiant la température du laser dans une gamme de 1°C. Cette faible variation n'a pas d'impact sensible sur le chirp du laser. La figure montre 14 Le taux d'erreur présente des performances optimales dans une gamme de 0.4-0.7° par rapport au maximum de transmission du filtre étalon. Les diagrammes optiques sont présentés figure 14 pour différentes valeurs de décalages. Pour un décalage de 0.6◦C le filtre ouvre l'œil optique et augmente considérablement le taux d'extinction dynamique.

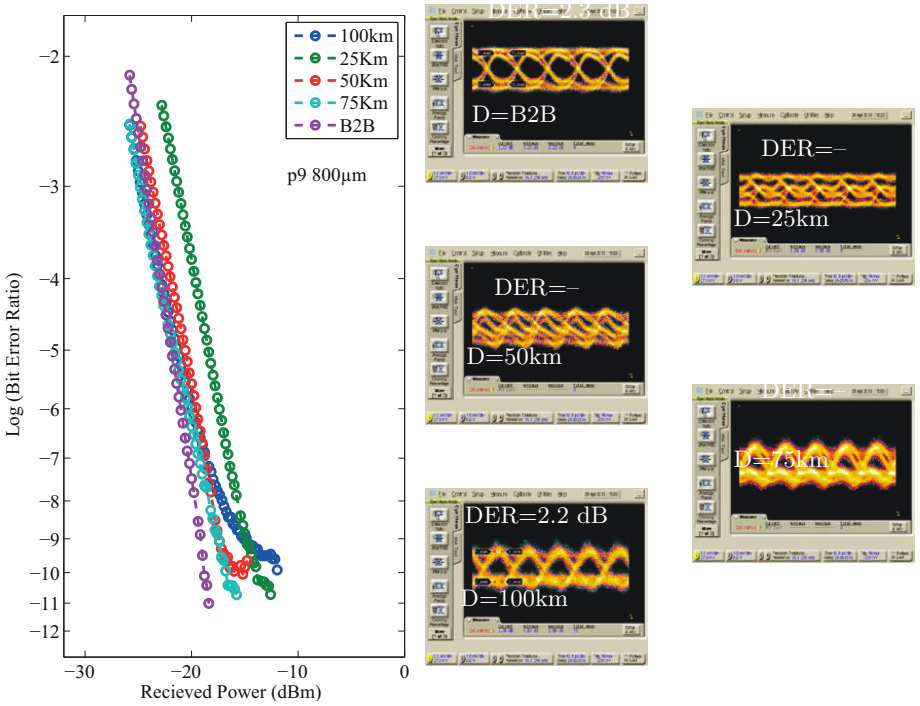

FIGURE 12: A standard 10Gbps transmission using a $\lambda/4$-phase shifted DFB with p-doped QDash as active material showing transmission up to 100 km

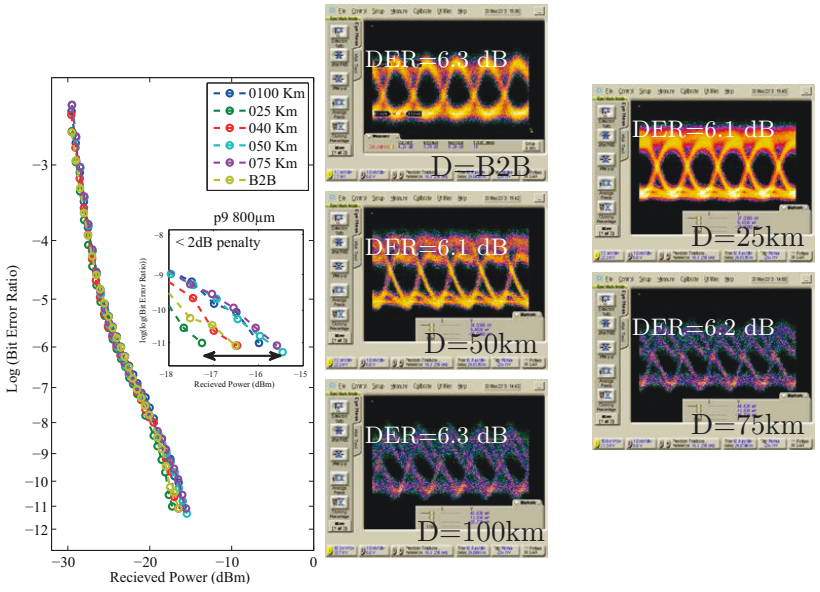

FIGURE 13: A standard 10Gbps transmission using a $\lambda/4$-phase shifted DFB with p-doped QDash as active material showing transmission up to 100 km with 6dB extinction ratio.

Lorsque le décalage dépasse 1◦C, le taux d'extinction ne peut plus être mesuré car la puissance optique devient trop faible.

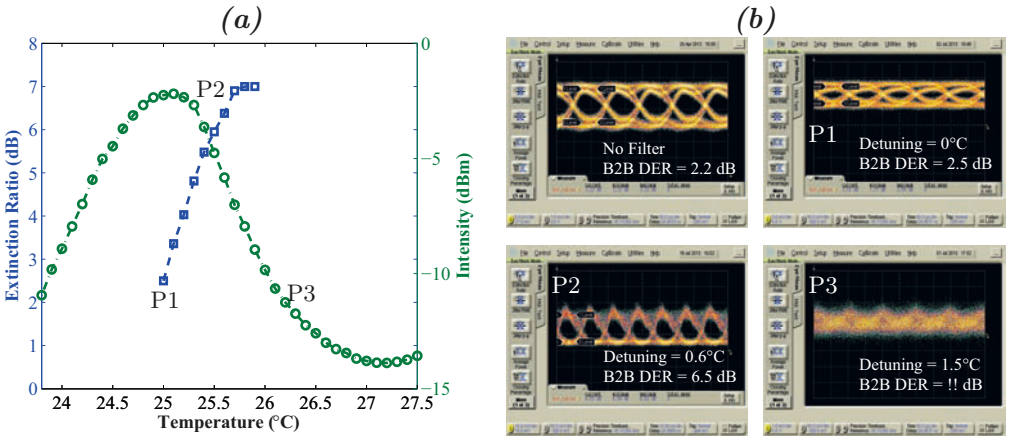

FIGURE 14: (a) Measured Intensity Transfer function of the filter as a function of temperature and the DER at respective points. (b) Eye diagrams at point P1, P2 and P3 on the filter with detuning of 0°C, 0.6°C and 1.5°C respectively

Il y a différentes manières pour réaliser un filtrage optique dans des circuits photoniques comme les films fins, les AWG, les réseaux de Bragg et les interféromètres de type MZ et les résonateur en anneaux. Les paramètres importants sont la pente du filtre (en dB/GHz), l'extinction, les pertes d'insertions et la compacité.

Les résonateurs en anneaux sont d'excellents candidats pour l'intégration en particulier parce qu'il est possible d'avoir un contrôle fin sur les paramètres du filtrage. Dans un premier temps, nous avons étudié en détail l'objet passif pour réussir une intégration avec un laser DFB. Le rapport on/off, la pente, l'intervalle spectrale libre sont définis correctement afin de reproduire les résultats obtenus avec le filtre étalon en espace libre. Les caractéristiques du résonateur en anneaux sont dépendantes en particulier du taux de couplage de la lumière. Il est par exemple nécessaire d'opérer proche du couplage critique pour obtenir une extinction élevée (figure 15). Le couplage peut être obtenu de différentes manières comme avec un contact direct entre le guide d'entrée et l'anneau, un couplage via un interféromètre multi-mode (MMI) ou par couplage évanescent via un coupleur directionnel (figure 17).

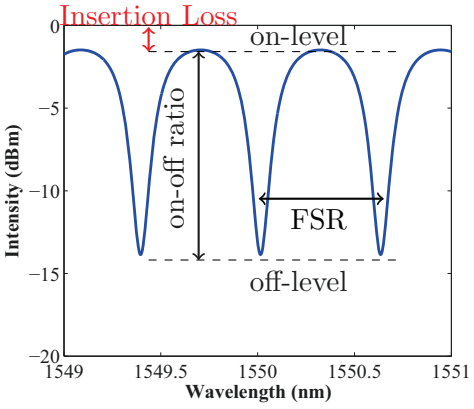

FIGURE 15: Intensity transfer function of a passive optical filter showing on-off ratio, insertion losses and filter slope.

Nous avons opté pour le coupleur directionnel formant une région de couplage dite « racetrack coupler » (figure 17 (a)). Nous avons évalué le couplage à partir de différentes longueurs de coupleurs et avec différents espacements entre le guide d'entrée et l'anneau (figure 17(c)).

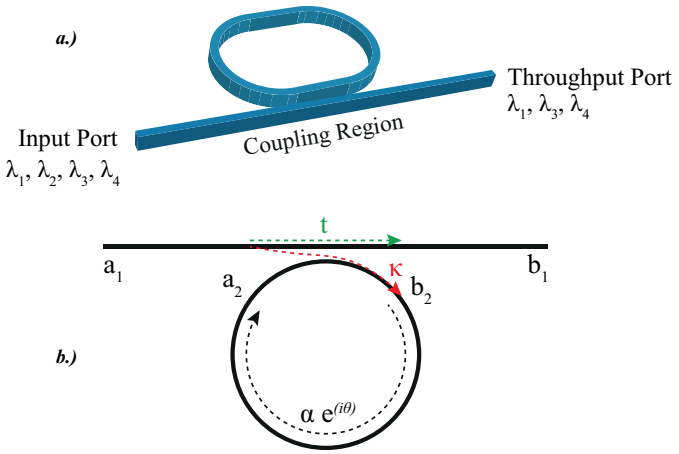

FIGURE 16: a.)Illustration of a single bus single ring resonator showing Input and Throughput ports. b.) Schematics of coupling in a single bus ring resonator for the case of lossless coupling.

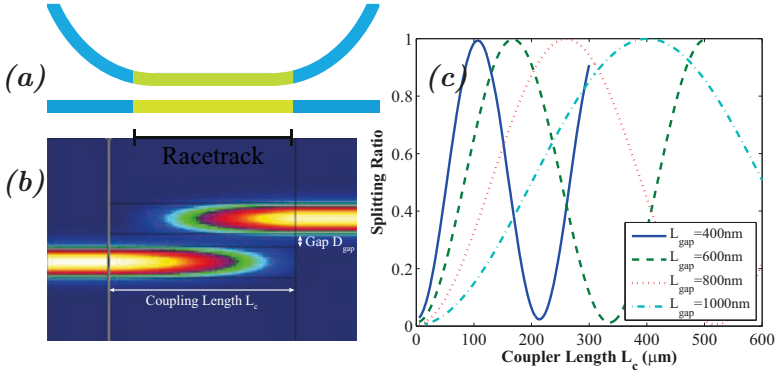

FIGURE 17: (a) Illustration of a ring resonator with a racetrack coupler. (b) Simulation of directional coupler to calculate the ideal coupling distance and length of the coupler. (c) The splitting ratio between the two waveguides as a function of Coupler length L_C for various values of gap between the waveguides.

Il est par ailleurs très important de réduire à la fois les pertes de propagation dans les guides et en particulier les pertes de rayonnement intervenant lors du trajet de la lumière dans l'anneau. Il existe donc un compromis entre ces pertes de rayonnement et la diminution de la taille de l'anneau pour des raisons d'encombrement. Nous avons dans un premier temps évalué les pertes de propagation dans des guides droits par réflectométrie cohérente (figure 18). Les guides sans hydrogénation présentent des pertes de 28dB/cm alors qu'elles sont réduites à 1.6dB/cm avec. Dans un second temps, nous avons évalué les pertes de rayonnement en utilisant des structures semi-circulaires en fonction du rayon de courbure de l'anneau. Elles décroissent très fortement jusqu'à un rayon de 300μm environ. Ce résultat a permis d'évaluer le rayon minimal à utiliser pour nos structures. Nous avons fait le choix de fabriquer des anneaux avec un rayon de 400μm.

Nous avons ensuite fabriqué des anneaux avec des coupleurs directionnels avec un espacement entre le guide d'entrée et l'anneau de 400, 600 et 800nm. Ces valeurs ont

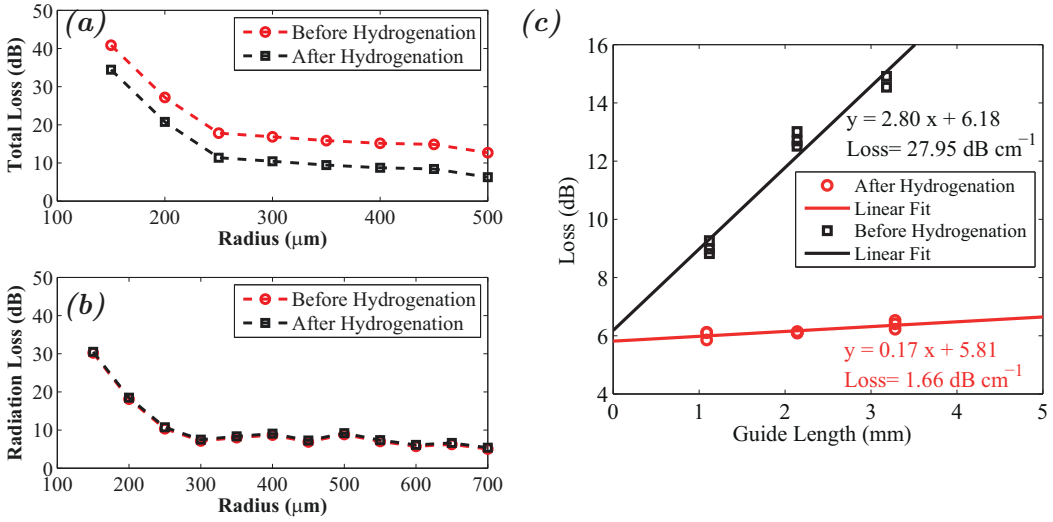

FIGURE 18: (a) Total Losses as a function of Radius of the semi-circular waveguide. (b) Extracted radiation losses from the waveguides. (c) Fabricated semi-circular structures for evaluation of Radiation losses in the ring resonator.

été définies en s'appuyant sur des simulations évaluant la gamme de longueur à viser pour que le couplage varie entre 0 et 100% (figure 17). Nous avons pu démontrer que les anneaux conçus dans cette technologie présentaient une grande gamme de couplage et donc qu'il était possible d'ajuster les caractéristiques fondamentales de l'anneau comme la pente, en vue du remplacement du filtre étalon en espace libre. Les figures 19(a) et (b) présentent la pente en dB/GHz et le rapport on/off en fonction de la longueur du coupleur directionnel.

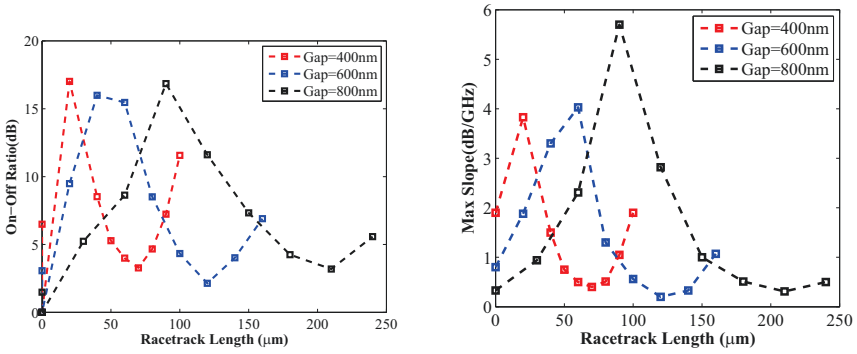

FIGURE 19: On-off ratio for ring resonator as a function of racetrack length

Un rapport on/off jusqu'à 15dB et une variation de la pente entre 1 et 6dB/GHz ont été démontrés expérimentalement pour tous les espacements. Un résultat très important également a été l'évaluation de la tolérance à la position de la longueur d'onde du laser par rapport à une résonance du spectre de l'anneau sur les valeurs du taux d'erreur et du taux d'extinction. Nous avons démontré que la température pouvait être

accordée dans une gamme de $\pm 0.3°C$ pour le filtre étalon en espace libre avec une pente de 1dB/GHz. Ces tolérances sont présentées sur les figures 20 pour 0 et 65km de transmission.

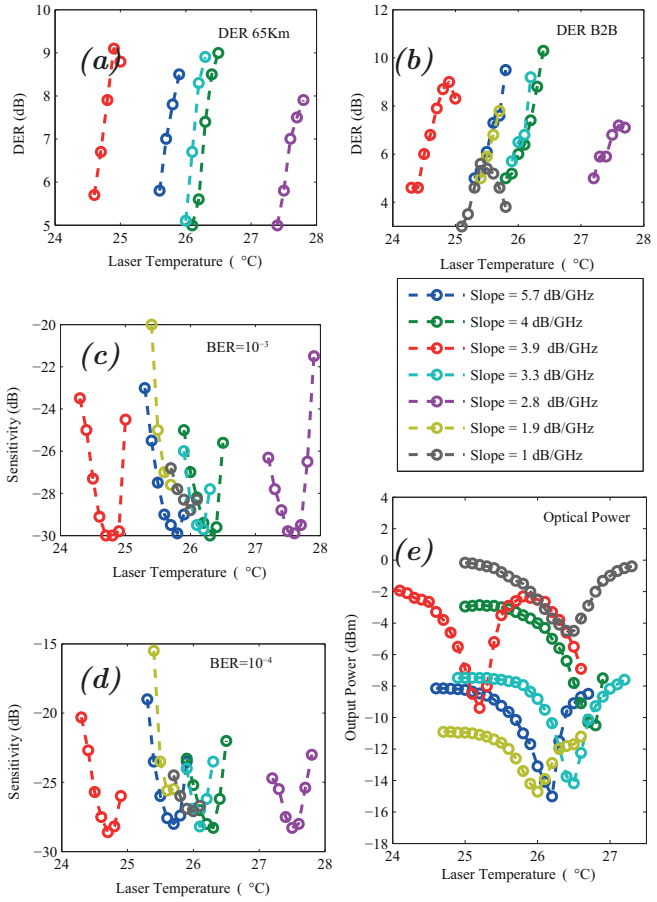

FIGURE 20: (a) DER for various ring resonator slopes after 65km fibre transmission (b) in Back to Back condition. (c) Sensitivity measurement for ring resonator slopes at a BER of 1e-3 in B2B condition (d) at a BER of 1e-4 in B2B condition (c) Intensity transfer functions for ring resonator slopes at B2B condition

L'anneau avec une pente de 1dB/GHz ne permet pas de ré-ouvrir correctement l'oeil optique à 10Gbs (5.5dB). Par contre, les anneaux avec des pentes de 4db/GHz permettent d'atteindre des taux d'extinctions de l'ordre de 10dB. La gamme d'ajustement du positionnement de la longueur d'onde du laser décroit à 0.3°C. (figure). Enfin, les filtres avec la pente la plus élevée présentent les meilleures performances en transmission.

Nous avons évalué performances en transmissions en utilisant un anneau avec une pente de 4dB/GHz (figures 21 et 22). La température du laser est variée par pas de 0.1°C autour de 25°C.

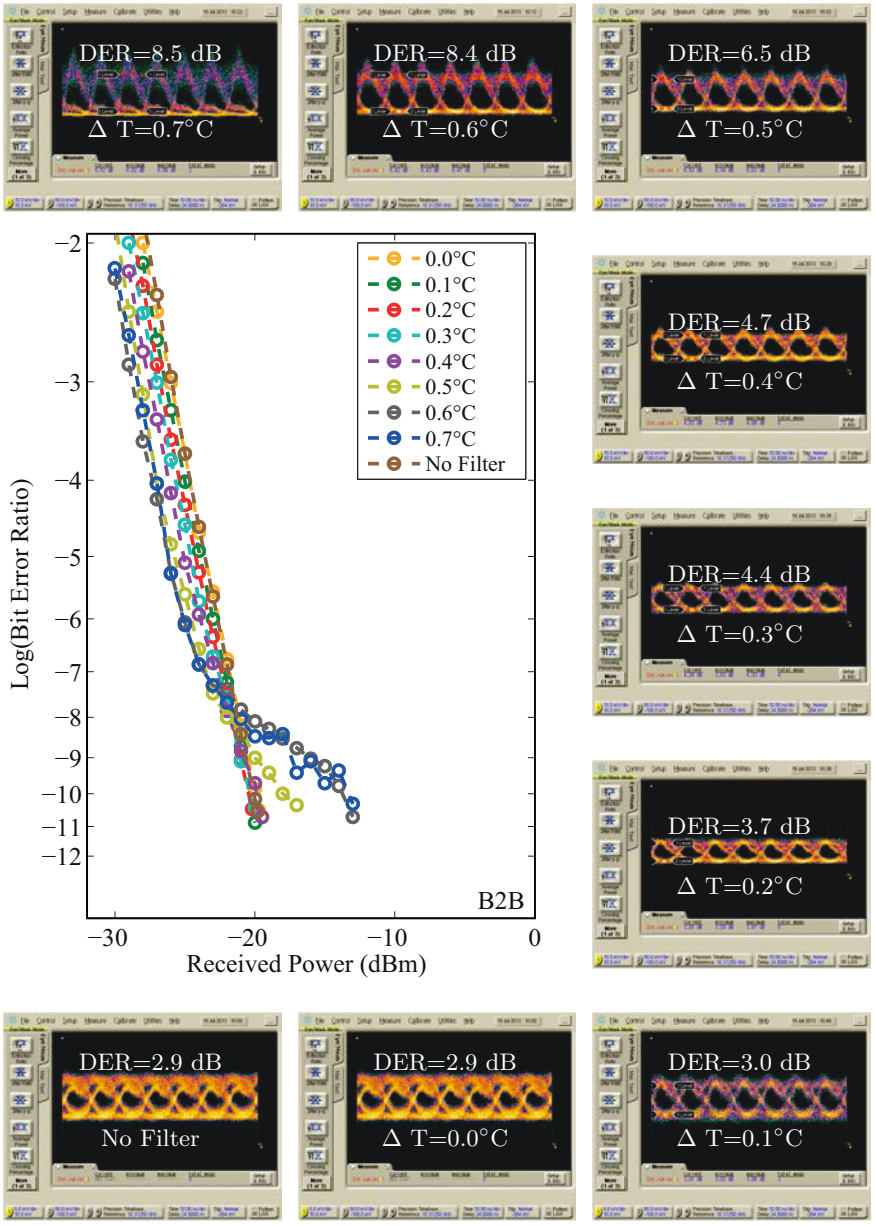

FIGURE 21: Optical transmission using a ring-resonator as a passive optical filter with radius 400 μm, gap between guides (D_{gap})=600nm and a racetrack length (L_{race})=60 μm corresponding to a slope of 4dB/GHz at various detuning in B2B condition

Le taux d'extinction dynamique est désormais supérieur à 8dB pour toutes les distances de transmission, en accord avec le chirp adiabatique de l'ordre de 2GHz et la pente du résonateur de l'ordre de 4dB/GHz permettant une suppression efficace des bits « 0 ».

Ces résultats très prometteurs ont servis de guide pour le design de la version intégrée de l'anneau avec un laser modulé directement, à la fois sur le choix du rayon, de l'espacement entre les guides du coupleur directionnel, de l'efficacité attendues des

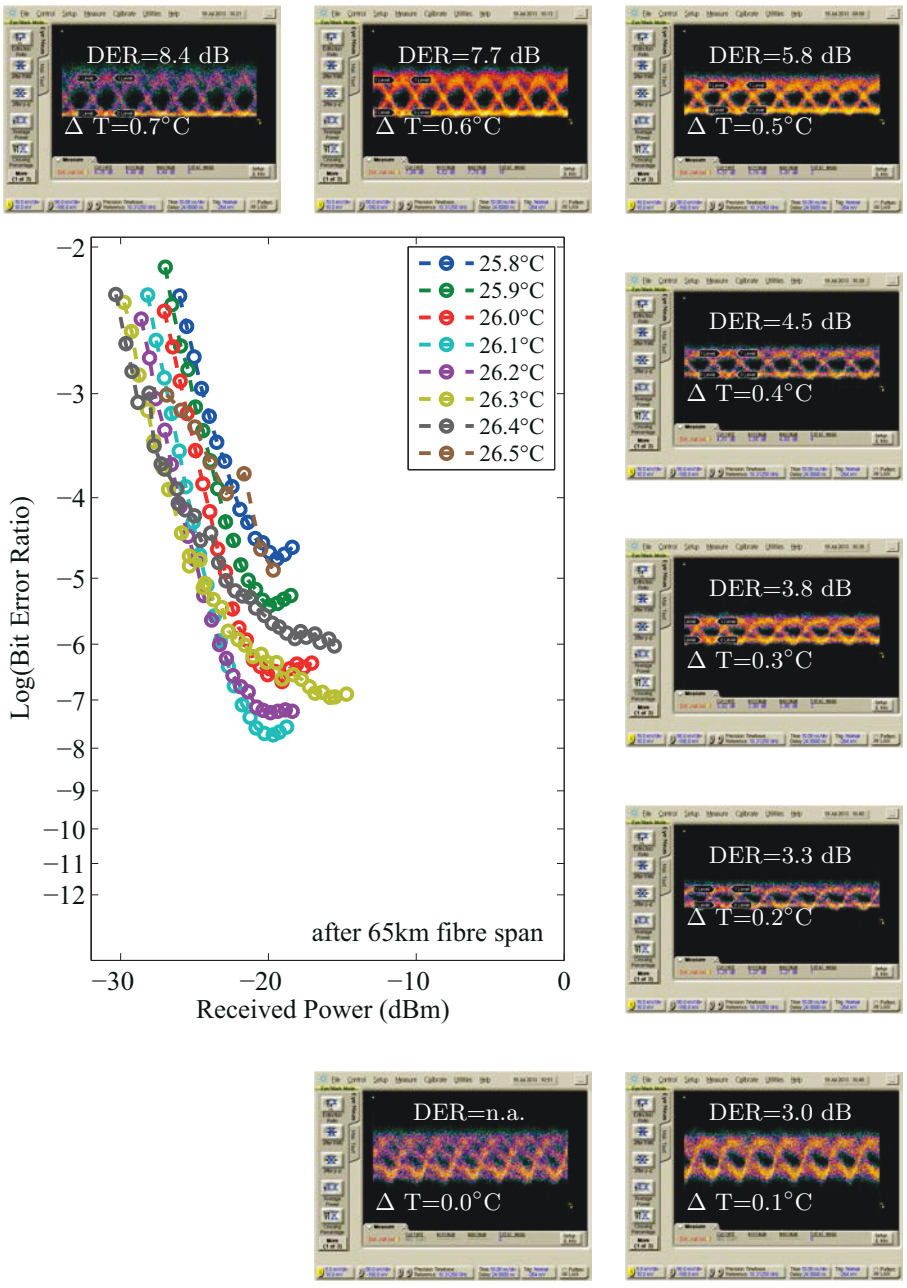

FIGURE 22: Optical transmission using a ring-resonator as a passive optical filter with radius 400 μm, gap between guides (D_{gap})=600nm and a racetrack length (L_{race})=60 μm at at various detuning after a fibre span of 65km

résistances chauffantes à la fois au niveau de l'anneau et/ou du laser, de la puissance optique attendue 6dBm à 25°C.

Lasers a blocage de modes

Une des caractéristiques importantes des lasers à QDashes est leur large spectre de gain entraînant un spectre d'émission FP large. De plus, les lasers FP à base de QDashes démontrent un blocage de mode optique résultant en une self-pulsation optique très efficace. Nous avons étudié des lasers à blocage de mode à une ou deux sections de gain.

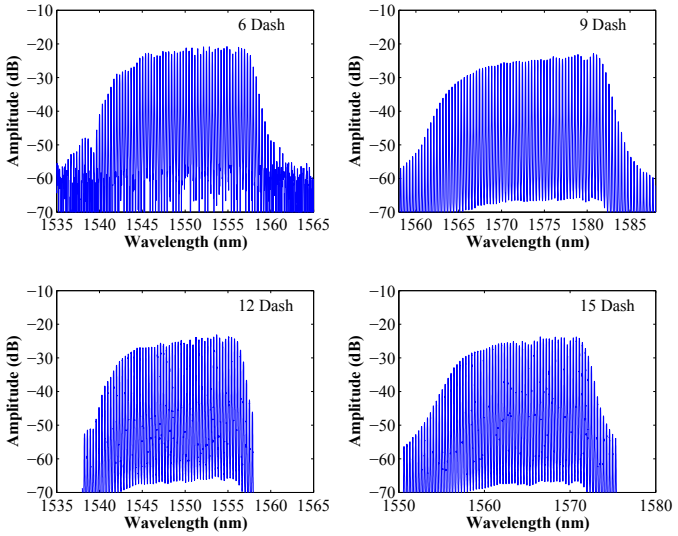

FIGURE 23: Optical Spectres of a 1000 μm long as cleaved FP QDash Laser with a ridge withd of 1.5 μm for various dash layers in a DBAR structure

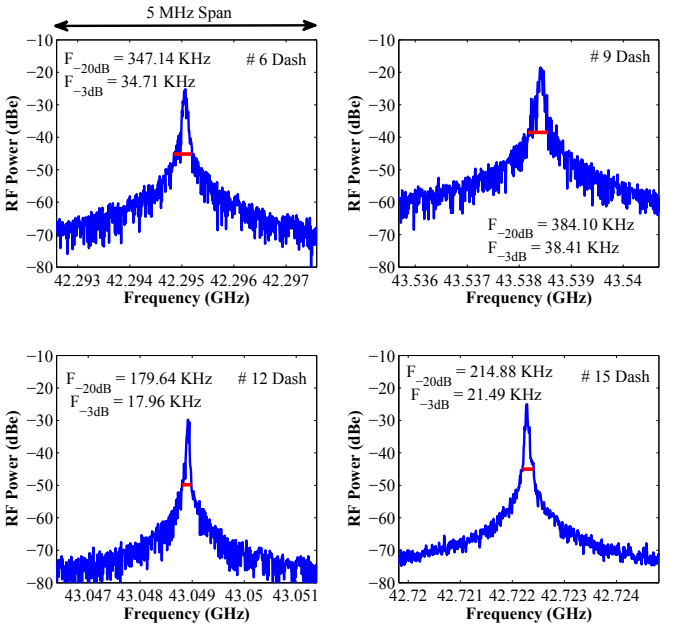

FIGURE 24: Radio-Frequency Linewidths of a 1000 μm long as cleaved FP QDash Laser with a ridge withd of 1.5 μm for various dash layers in a DBAR structure

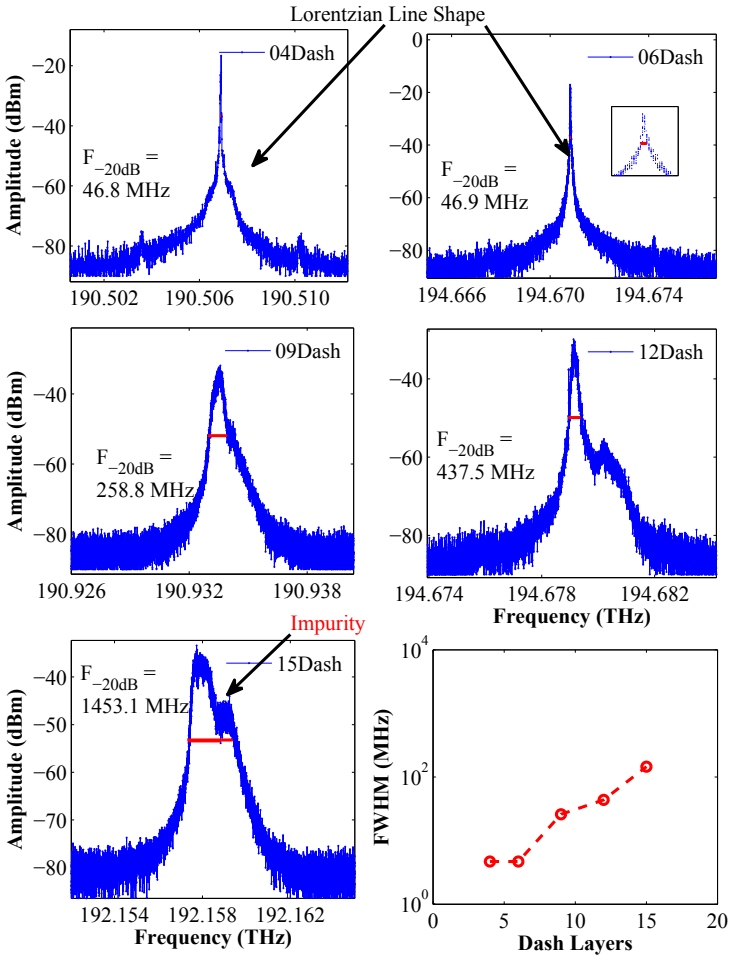

FIGURE 25: Optical Line-widths of a 1000 μm long as cleaved FP QDash Laser with a ridge withd of 1.5 μm for various dash layers in a DBAR structure

La qualité du matériau épitaxié au 3-5lab a permis de réaliser de nombreuses démonstrations de lasers à blocage de mode, notamment en faisant varier le nombre de couches de QDashes (6,9, 12 et 15) et d'évaluer son impact sur les caractéristiques statiques et dynamiques. Les figures 23 présentent les spectres optiques pour des lasers FP de 1000μm de long avec un ruban large de 1.5μm pour les différentes couches de QDashes. La largeur de raie optique a également été évaluée comme le présente la figure 24 Les valeurs sont entre 20 et 80 kHz, respectivement pour les structures à 6, 9 ,12 et 15 QDashes. Ces valeurs démontrent une amélioration nette par rapport aux matériaux conventionnels où les valeurs de largeurs sont de plusieurs centaines de MHz.

L'intervalle spectral libre est défini par la longueur de la cavité optique. Or, il existe une certaine imprécision sur le clivage qui peut être dépassée en fermant la cavité optique par exemple par un réseau de Bragg permettant d'intégrer ces lasers à des circuits phoniques. Le challenge est de définir correctement le réseau de Bragg afin qu'il ne perturbe pas le spectre optique à la fois en amplitude et en phase et qu'il maintienne donc l'enveloppe optique large de 10 à 12nm. Nous avons évalué par des simulations la

longueur et la force du réseau nécessaire au bon fonctionnement du laser à blocage de mode et notamment permettant de se substituer à un clivage facette.

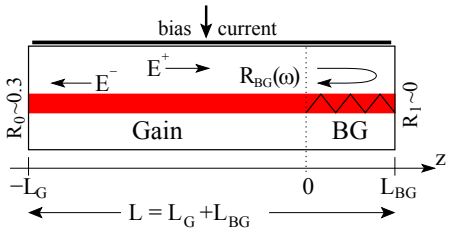

FIGURE 26: Schematic representation of the ML laser with the Bragg grating induced frequency dependent field reflection $R_{BG}(\omega)$.

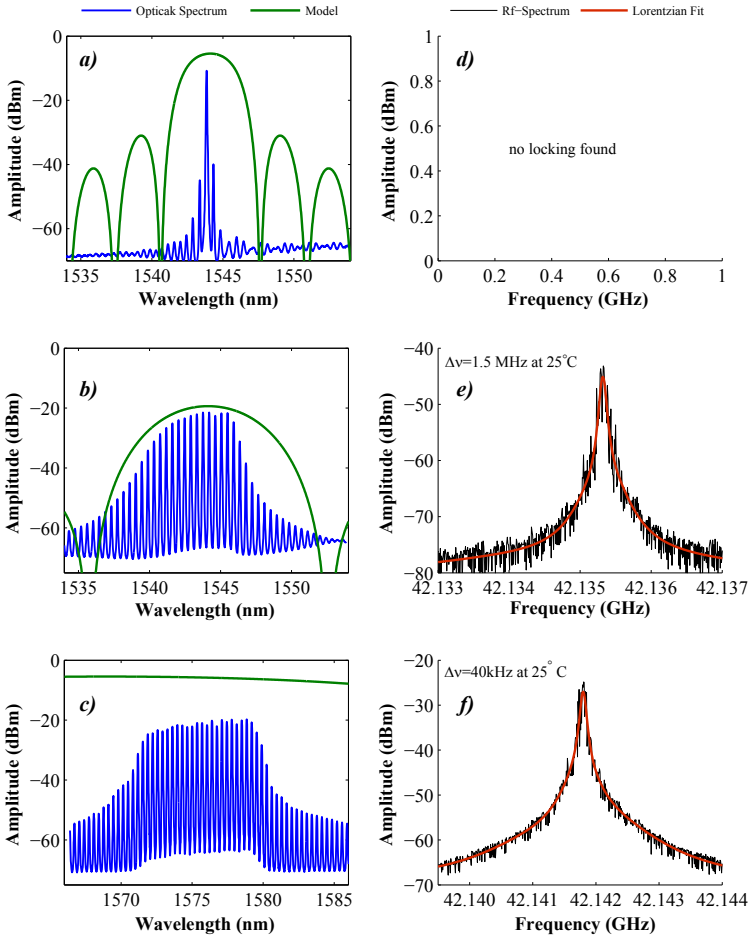

FIGURE 27: Optical Spectres and RF Line-widths of Bragg Lasers with (a,d) $\kappa = 40\,\mathrm{cm}^{-1}$, $L_{BG} = 250\,\mu\mathrm{m}$; (b,e) $\kappa = 200\,\mathrm{cm}^{-1}$, $L_{BG} = 50\,\mu\mathrm{m}$; (c,f) $\kappa = 400\,\mathrm{cm}^{-1}$, $L_{BG} = 25\,\mu\mathrm{m}$

Trois types de réseaux de Bragg ont été fabriqués comme le montre la figure 26 La valeur de la force de couplage visée est obtenu en modifiant la profondeur de gravure des dents du réseau défini sur le ruban. Nous avons observé que l'augmentation de la largeur de la bande passante du réseau entraînait une réduction de la largeur de raie RF

(figure 27). Des largeurs de raie de l'ordre de 40kHz ont été atteintes avec des réseaux de Bragg de réflectivité large de 10nm ce qui est comparable à celles obtenus avec des lasers FP standards.

La figure 28 présente l'évolution de la largeur de raie RF en fonction du courant pour le dispositif avec la plus large réflectivité de Bragg. Les gammes de courant avec un blocage de mode effectif sont indiquées par des flèches sur la figure. Les largeurs de raie sont de l'ordre de 100kHz et moins sur des gammes de courant de l'ordre de 20 à 50mA autour de 300mA.

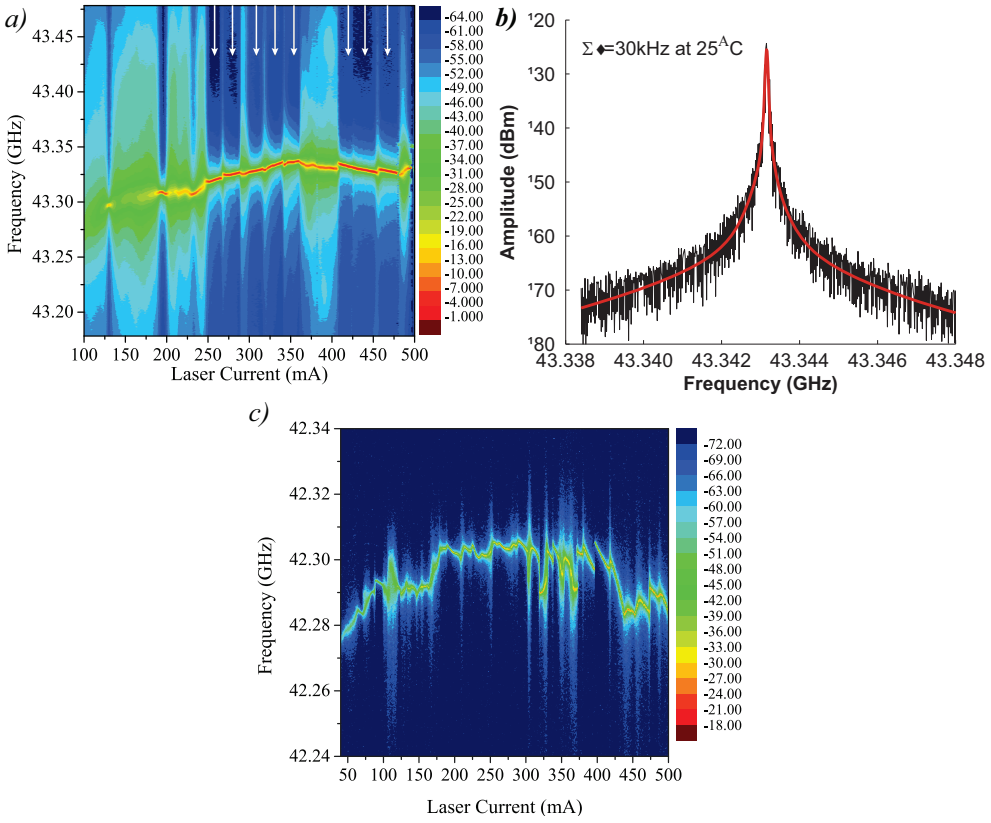

FIGURE 28: (a) RF-spectrum mapping for grating with $\kappa = 400$ cm^{-1}, $L_{BG} = 25\,\mu$m, which shows regions with very narrow line-width (marked with arrows) with some fluctuations. (b) Corresponding RF line-width of 30 kHz obtained at a bias current of 310 mA. (c) RF-spectrum mapping for FP laser with similar fluctuations in RF line-width.

Cette démonstration permet d'envisager la réalisation de lasers à blocages de mode dans des circuits photoniques intégrés pour être utilisés comme peignes de sources modulées à très haut débit.

Chapter 1

Introduction

1.1 Growth of demand for Access Networks

The desire for multi-media content and richly interactive data services is shaping a new era for telecommunications networks. Present networks need to be capable of offering Triple Play services, namely Internet-Protocol-TV, Video-on-Demand, Voice-over-IP and High-Speed Internet Access. The phenomenal growth requires huge increase in the bandwidth provision of access networks [3–5]. The costs of optical network roll-out are extremely high, so it is usually not viable to deploy multiple networks in a given region. A model which is expected to be increasingly common is one in which several operators use the same network infrastructure. An important issue is the high cost of current optical network technologies, which makes them unsuitable for deployment in regions of low population density or poor service take-up [4]. In this context, the physical reach is an important parameter. The new generations of passive optical network system are standardised by IEEE (10G-EPON) and ITU-T NG-PON1 [6, 7]. These standards propose a symmetric solution 10 Gbps for up- and down-stream and an asymmetric solution 10 Gbps downstream and 2.5 G(ITU) or 1.25 G(IEEE) for upstream. The asymmetric solution will be the main options deployed in the optical access network as a first step. Operators believe indeed that in the immediate future, providing 10 Gbps symmetric bit rate options cannot be developed at a reasonable cost for Fiber To The Home (FTTH) until about 2-3 years. As the standardization of NGPON

is still open, it is the right time to develop and propose innovative products that would be subject to mass deployment in the next 5 years. The development of a very simple, compact, Isolator and Peltier-free solution is therefore needed for creating a sustainable Internet through innovation.

1.1.1 State of the Art for transmitters in access networks

There are several ways to increase the transmission bandwidth and hence the data rate using conventional lasers. However, one has to bear in mind factors such as cost of deployment, footprint of the device, power consumption etc. Based on these criterion, several solutions have been proposed to tackle the growing demand of internet bandwidth. These solutions can be categorized as follows

1. ***Transmission using direct modulation***

   Direct modulation of DFB laser.

   Chirp Managed Laser

   Dispersion Supported Transmission

   Single Side Band Modulation

2. ***Transmission with external modulator***

   Lithium Niobate modulator based optical Transmitter.

   Electro-absorption modulator based optical Transmitter

3. ***Transmission using dispersion compensation techniques***

   Electronic dispersion compensation

   Pre-emphasis on electrical input signal

   Optical dispersion compensation

Transmission using direct modulation of light had been investigated since the invention of first semiconductor lasers[8–10]. The optical transmission were however limited due to the limited distance-bandwidth product that could be achieved using direct modulation of semiconductor lasers. The limitation in speed is mainly due to the capacity of these semiconductor lasers to translate the electrical signal into an optical signal, due to the low modulation bandwidth of the lasers. A greater problem is the limitation in the distance of transmission, which comes from the frequency chirping inherent to electrical

modulation of the laser. Several solutions have been proposed to manage the laser chirp. A first solution consists in carrying out a proper management of chirp and spectrum reshaping using the technique of Dispersion Supported Transmission(DST) [1, 11]. The DST is rather well adapted to reach intermediate distances (typically between 100 km and 300 km). The drawback of this technique is that it induces a Dynamic Extinction Ratio (DER) that is very low. A recently proposed solution is the so called Chirp Managed Laser(CML^{TM}) [12] with an optical spectrum re-shaper to increase dispersion tolerance. However, the targeted transmission distance ranges (from 200 km to 600 km) are far beyond the optical access network standards. Beside, this solution makes it necessary to precisely tune the laser wavelength to the optical spectrum re-shaper characteristic, which requires the use of a complex feedback loop that makes it viable for very long distance networks but unsuitable for low cost applications. The modulation of optical signals is also possible using external modulators. There are several solutions using the external modulation which consists of using either an electro-absorption modulator (EaML) or an external modulator (EML). But the external modulation schemes almost always induces a loss of optical power due to the absorption into the modulator. To improve the situation, it is possible to use a passive taper section and to grow different materials for the laser and the modulator. But this increases the technological complexity and leads to a energy hungry 3-sections device. It is thus necessary to discuss these solutions in details to identify the state-of-art for optical access networks.

Directly modulated lasers

Direct modulation of a laser can be done by injecting the electrical data signal directly to the laser in addition to the laser bias current. The data signal changes the carrier density thereby changing the output power of the laser emission. A schematic of a directly modulated laser is presented in Fig. 1.1. Directly modulated lasers (DMLs) are attractive candidates for access networks owing to their high output power, low threshold current, tolerance to optical feedback, and ability to operate in semi-cooled or un-cooled conditions. However, for a conventional Quantum Well (QW) based DML, the transmission distances are limited to the range of about 30 km, because of frequency chirping at 1.550 μm inherent to high bit rate direct modulation. It is also difficult to achieve high DERs. Generally, it is difficult to achieve high modulation bandwidth by using the conventional bulk and quantum well material, however transmissions up to

10 Gbps have been demonstrate using highly optimised quantum well material using an AlInGaAs based active structures. Use of aluminium however is discouraged due to challenges in wafer processing technology. High bit rate modulation had been nevertheless been demonstrated using aluminium free quantum dash [13] and quantum dot [14] active structures. The laser parameters such as modulation bandwidth, differential gain, linewidth enhancement factor, laser chirp, turn-on delay etc., will be discussed in details over the course of this thesis.

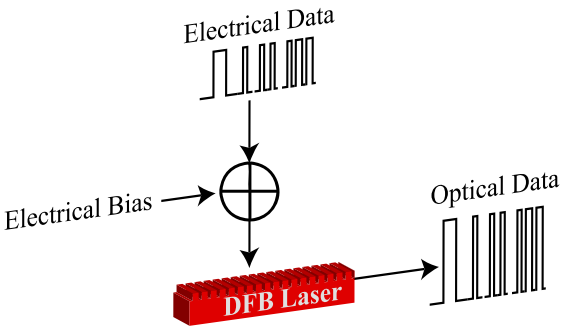

FIGURE 1.1: Illustration of a directly modulated laser, showing electrical data signal as input and optical data signal as output

Chirp managed laser (CML)

Chirp managed lasers (CML) rely on proper management of chirp in the transmission system. The CML actually takes advantage of the chirp of a DML to extend the reach. The continuous phase shift of the optical carrier associated with the adiabatic chirp of the laser upon modulation, together with the action of a passive optical filter for spectral reshaping generates a phase rule, according to which, 1 bits separated by odd number of 0 bits are π out of phase. This increases the dispersion tolerance by the destructive interference of the energy in the bits that are leaving their time slots to spill into adjacent time slots [15]. A CML uses a directly modulated laser in combination with an optical spectrum re-shaper (OSR). The OSR is used to convert the conventional chirp of the laser to a flat top chirp, and also produces an FM to AM conversion. At the same time a CML uses two photo-diodes to keep a strict control on of the laser wavelength and power at all times [12].

This technique for optical transmission is highly efficient. Thanks to the DML, it requires low power consumption. Transmissions in excess of 600 km have been demonstrated and DER >10 dB can be achieved very easily using this technique. However,

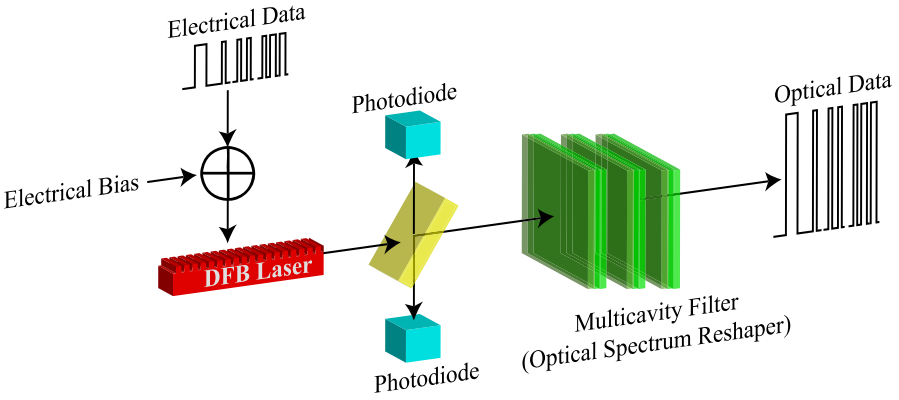

FIGURE 1.2: Illustration of a Chirp Managed Laser (CML^{TM}), showing a DML with optical spectrum re-shaper and control photo-diodes

the compensation of thermal chirp and locking of the laser frequency to the filter becomes a problem, as one has to use complicated feedback loop to readjust the laser bias. Secondly, the module for such device is arranged based on free space optics [12]. Integrated solution based on this approach have also been demonstrated recently using the planar lightwave circuit (PLC) approach [16]. As shown in Fig.1.3 this solution is branded as the CML-PLC. The integration of the filter is possible but it still requires a feedback loop to manage the chirp. In the CML approach a very important constraint is imposed on the laser chirp. The adiabatic laser chirp in case of a CML should be exactly half of the desired modulation speed. Thus it would require a very accurate control on the fabrication of the DFB lasers.

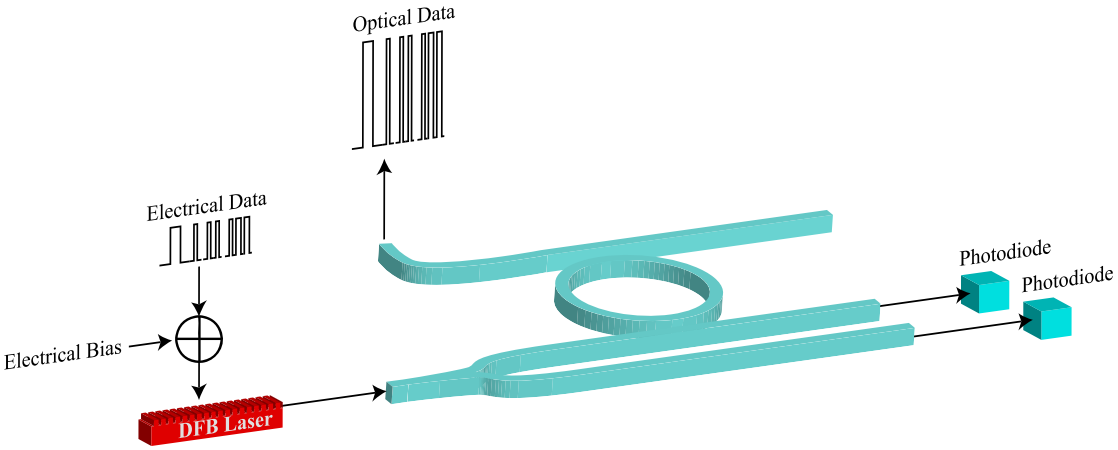

FIGURE 1.3: Illustration of a (CML^{TM})-PLC, showing a DML with optical spectrum re-shaper and control photo-diodes

Dispersion supported transmission (DST)

Dispersion supported transmission was introduced in the early 90's as a novel approach for transmission beyond the dispersion limit [11]. Transmission over fiber spans in excess of 250 km had been demonstrated. The main concept of the dispersion supported transmission is the conversion of the laser induced frequency modulation into an amplitude modulation of the signal by the dispersion of the transmission. DST wisely uses the dispersion with a modified electrical signal, it also a frequency shift keying instead of amplitude shift keying. It is based on the fact that the initial signal (assuming only adiabatic chirp) from the laser after passing through a dispersive fibre can be treated as a differential signal in intensity due the frequency to amplitude conversion. Thus after a direct detection of the signal, a first order low pass filter can be used as an integrator to recover the original data signal. The drawback of this approach is, however, the low extinction ratio and complicated signal post-processing.

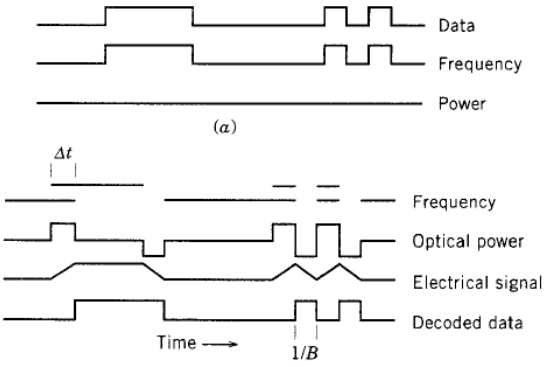

FIGURE 1.4: Dispersion compensation using FSK coding: (a) Optical frequency and power of the transmitted signal. (b) Frequency and power of the received signal and the electrically decoded data (after [1])

Electro-optic modulators, externally modulated laser (EML)

External modulation of an optical field of the laser is possible using an external modulator. This can be achieved by giving a certain fixed bias current to the laser, which emits a constant optical intensity. This optical output from the laser is then passed through an external modulator, usually a Mach-Zehnder (MZ) Modulator, where the optical field is modulated with the data signal. An schematic of an EML is presented in Fig 1.5. It is based on the fact that the refractive index of some materials can be modified

by applying an external electric field and using the *linear electro-optic effect* [17, 18]. The direct dependence of the phase of electric field on the refractive indices, induces a phase shift in the optical field. The induced phase shift in the optical field can then be translated to amplitude using an interferometric arrangement.

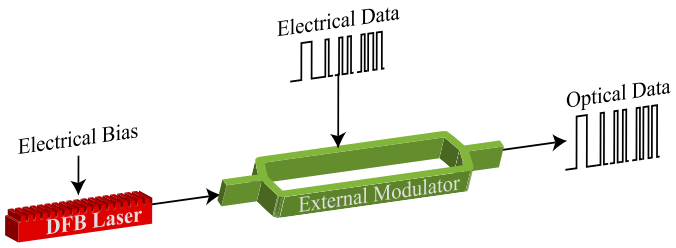

FIGURE 1.5: Schematic of a Mach-Zehnder modulator (Electro-optic modulator) based externally modulated laser. The laser here is applied with a constant bias and thus emits a constant optical intensity, the data signal is applied to the modulator.

A problem in such modulators is frequency chirping, however this can be solved by using a push-pull configuration [19]. This scheme of optical data transmission is very efficient in terms of the quality of optical data signal. Modulators offering an extinction ratio of about 13 dB at 40 Gbps are readily available in the market today. However the size of the device dramatically increases due to the large size of the MZ-modulator (3-5 cm). Integration of MZ-modulators on Photonic Integrated Circuits have also been demonstrated both on InP-platform [20] and on Silicon Photonics platform [21]. But again the complexity in design of such integrated circuits poses to be a huge drawback for such optical transmission devices. Lithium niobate MZ modulators are usually suited for use downstream optical transport application, but would make the module for up-streaming optical network units (ONU) considerably large.

Electro-absorption modulated laser (EaML)

An electro-absorption modulated laser is another integrated solution for high bit rate transmissions. It relies on the fact that the effective band-gap of the semiconductor reduces when a voltage is applied across it. Thus, if the modulator material is chosen so that its band-gap E_g is slightly larger than input photon energy $E = h\nu$, when no voltage is applied across it, the material behaves as transparent to the input light signal. On the other hand, when a voltage is applied across it, the input optical field is absorbed. In case of the EaML, the absorber can be as short as 10% of the total device length and can be integrated to the DFB. This results in highly compact devices. The DER also

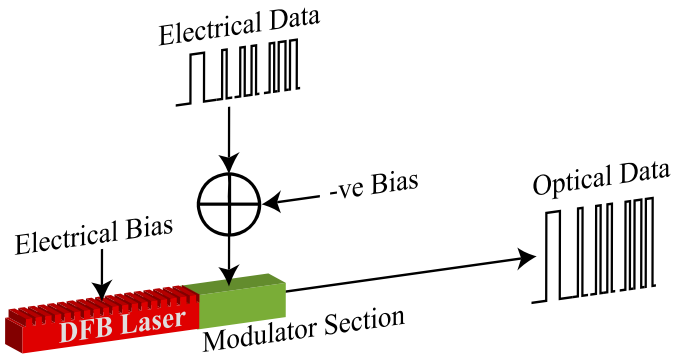

FIGURE 1.6: Schematic of an electro-absorption modulated laser. Note that the constant biased laser and the modulator can be integrated on the same substrate.

remains in the range of 9-12 dB, which guarantees a high quality optical transmission. High speed (25 Gbps) [22], high extinction ratios have readily been demonstrated using such technique. This device class is thus suited for distances covering the range of access and metropolitan networks [23]. One of the major disadvantages, however, of the electro-absorption modulators is the loss of optical power (in the range of 3-5 dB power loss) due to absorption. Also, there is a small chirp [24] involved due to the change in the refractive index of the material induced as a results of the Kramers-Krönig relations. This chirp is however much smaller than the one induced in directly modulated lasers.

Transmission using electronic dispersion compensation (EDC) and electrical pre-emphasis

EDC is another approach to solve the problem of distorted signal at the fibre output caused by fibre dispersion and laser chirp as long as the dispersion is not very large. EDC however relies on tapped delay line equalizers (transversal filters), where parts of the electronic input signal are subject to different time delays and recombined after amplification with suitable levels. EDC can be used to eliminate short amounts of dispersion when direct detection is used and is generally not very useful for large transmission distances. On the other hand, when coherent detection scheme is used, the EDC scheme can used the phase information to completely equalize the chromatic dispersion [25]. The complete retrieval of the phase information is complicated and undesired.

Electrical pre-emphasis can also be used to compensate small amounts of dispersion by pre distorting the optical signal such that it interacts with transient response

of the laser to modify the frequency chirping behaviour of the laser. In addition to the operational complexity pre-emphasis also adds to the cost of the optical transmission system and thus will not be a very attractive candidate for access network systems.

Summary

External modulation usually results in a very good quality of transmission but at the cost of higher power consumption. Also the device footprint is usually very high due to the discrete components used. Thus external modulation is usually avoided as the large device foot-print makes them complicated to be deployed for up-streaming ONU. Electro-absorption technique of external modulation is promising. However, the transmission is dispersion limited. Spectral filtering techniques such as CML^{TM} and CML-PLC also lead to a good quality however the transmission distances covered by these techniques are above 200 km and at the same time they require a complicated feedback loop to manage the laser chirp. They also hold a specific requirement on the laser chirp for phase inversion. These lasers are excellent for long reach transmissions however they do not necessarily provide a flexibility for the access sections of the network. Coherent transmission technologies, are very promising for very high data rate transmission. However, the complexity of the coherent transmission and coherent detection is one of the challenges for the access section. Electronic dispersion compensation and pre-emphasis usually do not provide a very strong improvement in performance. Table 1.1 summarizes optical emitters which can be potentially used for access and metropolitan networks. It compares various technologies, some of which are well developed, while others are still under investigation.

Directly modulated lasers (DMLs) are interesting candidates owing to low power consumption, high output power and device simplicity. However the transmission is limited due to frequency chirping of the laser and high line-width enhancement factors of conventional materials. The use of nano-structure is expected to offer ultra-low chirp lasers, which might improve the transmission performance of DMLs. Thus direct modulation and direct detection with lasers based on semiconductor nano-structures could prove to be one of the best candidates for optical transmission in access section of optical networks. The spectral efficiency of these lasers can be improved using a passive optical filter making them strongly immune to dispersion. QDash material is one of the

Approach	Cost	Footprint	P-Output	Consumption	Complexity	Integrability	Quality	Maturity	Comments
EML	High	High	Low	High	High	No	Excellent	Commercial	Large foot-print and non-integrability make this technology complicated to be used on PICs
EaML	Low	Low	Low	Low	Low	Yes	Very Good	Lab/Mature	Good candidate for access network, however the power output is very low and also chirp limits the transmission.
DFB-DML	Low	Low	High	Low	Low	Yes	Good	Commercial	High chirp makes transmission limited to very short distances
CML^{TM}	Low	Low	High	High	High	No	Excellent	Commercial	complicated as it requires feedback loop, chirp must be half the bit-rate, targets as distances > 200 km, in-addition re-shaper is used in free space for the classic CML
CML-PLC	Low	Low	High	High	High	Yes	Excellent	Mature	Integrated version of CML but feedback loop still needed
DST	-	-	-	-	-	-	Poor	Mature	Low extinction ratio is a big drawback for this transmission scheme, covers only distances beyond 100km
Coherent	High	Low	High	Low	High	-		Laboratory	very hig speeds of transmission but implementation is complicated
EDC / Pre-emphasis			-					Mature	useful for small improvement in performance
DCF		-	-	-	-	-		Mature	Not a cost effective method

TABLE 1.1: Summary of optical emitters and transmission schemes that can be potentially used for Access and Metro networks

very promising nano-structures which can be used to fabricate directly modulated lasers immune to chromatic dispersion. It is expected that the properties of this novel material would allow to fabricate directly modulated optical sources, while still maintaining high modulation speeds of up to 10 Gbps. It is also expected that high temperature tolerance characteristics of QDash material would potentially help operation of these lasers in un-cooled or semi-coooled conditions.

1.2 On the use of semiconductor nano-structures for optical telecommunications

Semiconductor (SC) lasers have been marked with several breakthroughs, throughout their history. The first light emissions from a semiconductor (GaAs) diode laser was demonstrated in 1962 by General Electric [26] and IBM T.J. Watson research centre [27]. These first laser diodes were homo-junction devices operating in pulsed operation at 77 K. The homo-junction devices. These first lasers showed light emission at cryogenic temperatures, due to an absence of a proper wave guiding mechanism. This was however soon over come by the introduction of the heterojunction [28] followed by the invention of the double-heterojunction lasers [29, 30]. The double heterojunction lasers were the first semiconductor lasers to show room temperature operation. It is now widely recognized that the major breakthrough in the field of semiconductor diode lasers occurred when the idea of using a double heterostructure as an active region of an injection laser to achieve efficient electron confinement was implemented [31]. An important theoretical step was also taken in 1966, when the importance of optical confinement (waveguiding) for the realization of laser action in was stressed. However due to the then use of primitive epitaxial technique of Liquid Phase Epitaxy (LPE), it was very tricky and relatively difficult to fabricate such lasers. The advancement of epitaxial techniques such as Molecular Beam Epitaxy (MBE), Metal-oxide Vapour Phaser Epitaxy (MOVPE) and Gas Source Molecular Beam Epitaxy (GSMBE) led to the significant improvements in the fabrication process and operation characteristics to these class of lasers. The new epitaxial techniques also lead to the predicted Quantum wells (QWell) [32] and, the invention of QWell lasers [33] followed in year 1976 from the group of Charles H. Henry at the Bell Laboratories. The QWell and multi-QWell lasers showed significant improvements over the conventional bulk material due to the quantum sized effects. The invention of QWell

lasers triggered a sharp growth towards studies on low-dimensional semiconductor materials. Low dimensional heterostructure lasers had been the subject of attention since their concept was proposed by Arakawa et al [34]. Arakawa et al predicted further improvement in laser performance upon reduction of dimensionality. Room-temperature operation of the Quantum Dot(QD) lasers were soon demonstrated [35, 36]. Over the past few years considerable progress had been made over the development of QD lasers [37, 38]. A comprehensive viewgraph on development of semiconductor laser [2] is presented in Fig. 1.7.

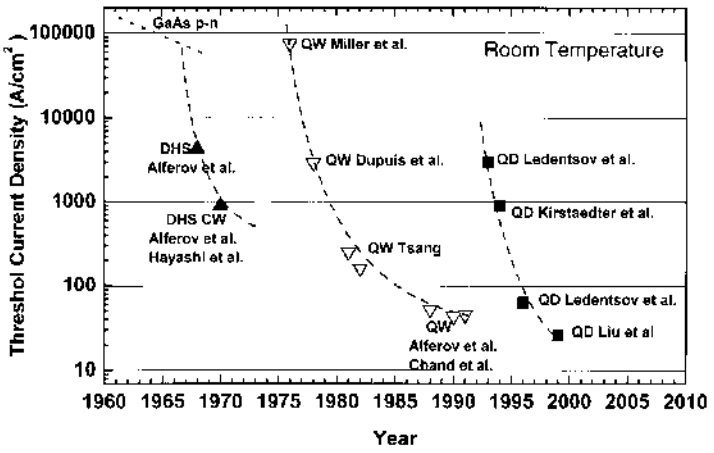

FIGURE 1.7: A brief history of semiconductor lasers (from [2])

The evolution of threshold current density shows a strong improvement upon use of QD structures as shown Fig. 1.7. It is widely believed that the difference between the QDs and conventional QWells is not very large [39]. However the nano-structures out-perform the conventional QWell material, when dynamic properties are compared. Semiconductor lasers and amplifiers with nano-structures as their gain medium hold the promise of improved characteristics for optoelectronic devices, when compared to conventional QWell structures [40–42].

QDashes or elongated QDs are low dimensional materials which show properties between those of a QD and a QWire. Like QDs these nano-structures confine the electrons and holes in all three spatial dimensions. In QDs this confinements results in discrete quantized energy levels and a delta-function density of states. But due to the non-uniformity of the size in QDashes and their wire like behaviour the density of states broaden from delta functions to spikes [43]. The nano-structures are of special interests because they are self-assembled on commercially favoured InP (100) substrates.

The progress in semiconductor nano-technology, through development in growth methods and that of processing techniques of these materials have opened new avenues for the telecommunication industry. QDash material holds special promises for the field of optical telecommunication, with theoretically predicted chirp free, low line-width, low-noise devices. Several demonstrations have been made using QDot lasers emitting in both the 1.3 μm wavelength range (dispersion free communication window) on GaAs substrates and 1.55 μm wavelength range (low-loss communication window) on InP substrates. QDashes have been used to demonstrate lasers showing very low threshold current density, ultra-high characteristic temperatures (T_o), fast-carrier dynamics and near-zero linewidth enhancement factor (α_H parameters). Apart from these static features, very low phase noise frequency combs and ultra-short pulsed laser sources have also be demonstrated using this novel material system. Another important feature of these nano-structures is that their emission wavelength can be tuned by increasing or decreasing their size. This feature has been used within this work to fabricate devices on InP substrates emitting at wavelengths ranging from 1.3 μm up-to 2 μm.

1.3 Scope of this Thesis

This thesis explores the properties of QDash nano-structures and potential application in telecommunication networks. The QD structures have been grown and explored over a vast set of materials. Most of the previous studies have dealt with InAs QD structures grown on GaAs substrates [35, 42, 44–46]. There are ongoing studies on InAs QDs on GaSb substrates, which are still in their infancy [47, 48]. The research work focuses on the use of the novel InAs semiconductor QDash material grown on InP substrates as active medium for the fabrication of lasers for direct modulation and low phase noise optical sources. Directly modulated lasers are potential candidates for optical access networks because of the low power consumption and compact size. The low linewidth enhancement factor and low chirp are some of the interesting properties predicted for QDash based devices, which promise better performance in transmission systems. Large transmission distances with p-doped QDash lasers have recently been demonstrated by our lab [49]; the Dynamic Extinction Ratio in this case was then increased using an etalon filter. The present work aims to exploit this approach by integrating p-doped Q-Dash distributed feedback lasers with a ring resonator, which will act as an optical

filter. The research deals with modelling of the active and passive components such as the ring resonator, Fabry-Perot and the DFB-laser; fabrication of such components in the III-V Lab clean-rooms facility; characterisation of these devices and finally system level demonstrations as a proof of the concept.

Within the purview of this work, effort have been made towards development of Photonic Integrated Circuits (PICs) for the 1.55 μm wavelength range, using the InAs QDash active regions grown on InP substrates. Two distinct properties of this material system have been exploited.

— Firstly, owing to the dynamic properties of QDash, this material system has been explored to fabricate single wavelength optical transmitters for access and metropolitan networks immune to fibre dispersion. ***Ultra-low frequency chirped directly modulated lasers*** showing modulation bandwidths beyond 10 GHz have been demonstrated. These low chirp optical sources have finally been combined with a passive optical filter to demonstrate an innovative optical transmitter for access networks on InP PIC platform, showing a directly modulated transmission in the distance ranges of 0-100 km.

— Another growing area of interest for InAs/InP Qdashes is the investigation of single section mode locked lasers (MLL) and optical frequency comb sources. Due to the large gain-bandwidth of the QDashes, a simple Fabry-Perot laser cavity with Qdashes active region results in a frequency comb source with a typical comb width in the range of 10-12 nm. In addition the FP cavity is capable of emitting ultra-short pulses owing to the phase locking of the FP modes. This unique feature of Qdashes, owing to a non-linear effects such as four-wave-mixing, had been widely studied over the past decade. No efforts however have been made to integrate these lasers with other optical components to enhance their functionality. Within this work an innovative approach was used to demonstrate ***integrated QDash MLLs*** on InP PIC platform without perturbing the laser performance and in particular the phase noise quality of the laser.

Both single wavelength lasers arising from QDash DFBs and multi-wavelength lasers arising from QDash-FP can be efficiently used for high data rate optical communications. Moreover, the lasers based on Qdash materials are expected to have a

performance edge over those using conventional material. One of the areas in telecommunication networks where an improvement is required is the access section. Access network are expected to operate ta a data rate of 10 Gbps in range of 0-65 km for the modern standards. However, the conventional material operating in the 1.3 μm dispersion free window cannot transmit to these distances due to limitation in losses, and the conventional material operating at 1.55 is limited due to dispersion. The dispersion immune QDash lasers can thus be a vital solution for the access networks. Over the course of this work a special attention has been paid towards resolving the problems for access networks. On the other hand, the QDash-MLLs find applications in vast range of areas ranging from applications in bio-medical optics to applications in optical communication such as Radio over Fibre and Ultra-broadband sources for Ultra Dense-WDM. This thesis will review some of the properties of the QD-MLL but mainly focus on integration of mode locked laser devices to increase their functionalities on PICs.

Thesis Organisation

The report is organised as follows Chapter 2 introduces the QDash nano-structure. Starting with the definition of quantum confined structures in Section 2.1, it discusses the density of states and expected properties from QDash materials in Section 2.4. Fabrication technology of lasers from these structures is then discussed in Section 2.5. The central interest of this thesis is the use of QDash material for fabrication dispersion immune DMLs. The properties of QDash lasers are studied in details and discussed in Chapter 3. It firstly discusses the theory of SC lasers in Section 3.1. The static characteristics of fabricated QDash buried ridge lasers are discussed in section 3.3, followed by the dynamic characteristics such as modulation bandwidths, line-width enhancement, and frequency chirp in section 3.4. It is demonstrated that these lasers are capable of repeater less optical communication over distances in excess of 100 km. Further improvements in these transmission quality occurs, upon use of a passive optical filter. Chapter 4 describes the fabrication of ring-resonator based filters on InP substrates. The problems related to the fabrications of such resonators on InP substrates are described. Finally, a highly-efficient, cost-effective and compact optical transmitter assembly, which completely fits the criteria for Next Generation PON2 is discussed in Chapter 4 as described by the ITU-T access network standards. This chapter then develops the technological process for monolithic integration of the ring resonator and a DFB laser device.

The mode-locking performance of Fabry Perot lasers from these nano-structures have been well studied over the last decade. There is however a strong need and interest for these devices to be integrated on InP, to utilize the full potential of these devices. An effective Bragg grating design for integrating these mode-locked lasers is discussed. Other methods to integrate such devices on the InP platform are discussed in Chapter 5.

Chapter 2

Nanostructures based devices: from expectations to true achievements

Semiconductor quantum dot (QD) and dash (QDash) nano-structures have been of strong interest to the scientific community over the last two decades. Owing to their three dimensional quantum confinement, these nano-structures are expected to show a strong improvement in the optical and electronic properties of devices fabricated using them as active material. This chapter presents a review on the properties of QDs and QDashes and compare them with conventional material in Sections 2.1.

The growth methods of QDs and Qdashes are presented in Section 2.2. Various possible epitaxial layer arrangement schemes, used within this work have been described in the following sub-section(2.2.3). Section 2.4 will deal with the properties expected from QDash lasers. This section will discuss the properties of Qdashes such as threshold current density, modal and differential gain and, the line width enhancement factor. Finally this chapter will conclude with the fabrication technologies followed for the realization of active devices from these nano-structures in Section 2.5.

2.1 Quantum Confined Materials

The electronic and optical properties of a material are strongly dependent on the size and shape of the material. The quantum confinement effects can be observed once the dimensions of the material is of the same magnitude as the wavelength of the electron wave function. Based on the confinement of the electrons, materials have been classified as Bulk, Quantum- Wells, Wires and Dots.

Bulk material can be described as unconfined materials, i.e. the charge carriers are not confined in any spatial dimensions. In Quantum wells (QWell) the carriers are confined in one spatial dimension. These are generally implemented by burying the confining material within a barrier material. As shown in Fig 2.1, the carriers in a QWell are confined in y-direction, but are free to move in x and z directions. In quantum wires carriers are confined in two spatial dimensions, x and y-directions and free to move along the length of the wire i.e. in z-direction. In QDs the carriers are confined in all three spatial dimensions.

Theoretical studies indicate that QD and QWire lasers have many potential performance advantages over conventional QWell lasers. First, a QD or QWire laser has a lower filling factor (volume of material to be pumped) and an improved Density of States (DoS) function compared with a QWell laser. The theoretical DoS function become sharper as the carrier dimensionality decreases. Equation 2.1 describes the theoretical DoS function for a bulk material, which has a square root dependence on energy. Figure 2.1 shows the theoretical DoS function for a QWell (one dimension of quantum confinement) which increases in steps at each QWell energy level, the theoretical DoS function for a QWire (two dimensions of quantum confinement) and DoS function for a QD (three dimensions of quantum confinement). The QDs noticeably have a delta-like DoS function (e.g., a finite number of states available only at the QD).

$$\rho(E) \propto \begin{cases} (E - E_c)^{\frac{1}{2}}, & \text{for Bulk Material} \\ \text{Constant}, & \text{for QWells} \\ (E - E_c)^{-\frac{1}{2}}, & \text{for QWires} \\ \delta(E - E_c), & \text{for QDs} \end{cases} \tag{2.1}$$

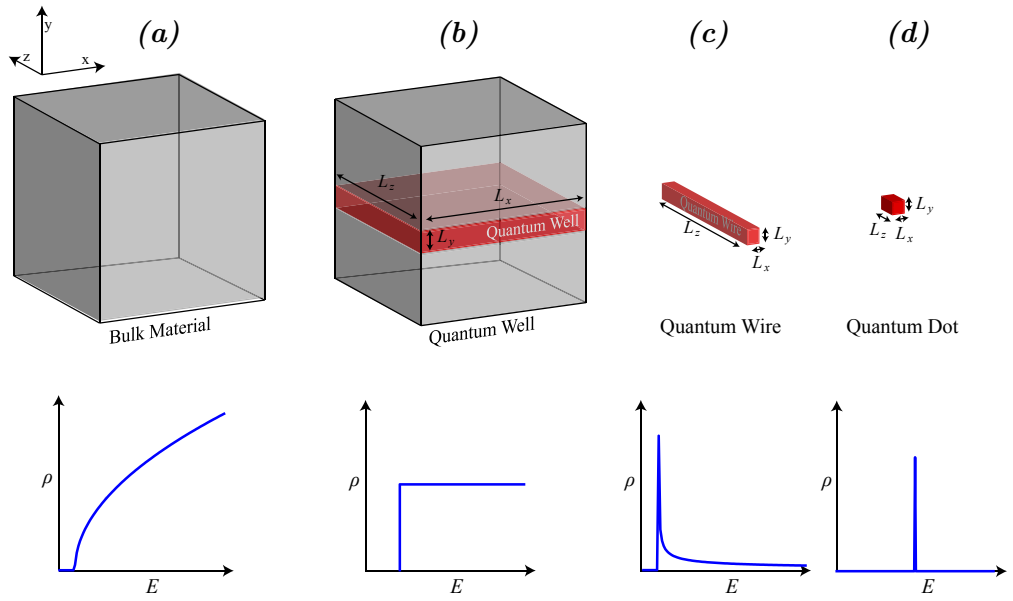

FIGURE 2.1: Bulk, QWell, QWire and QD, the red colour shows the region where the carriers are confined. The corresponding dispersion relations showing density of states (DoS) ρ as a functions of photon energy E.

Theoretical calculations indicate that the threshold current of a semiconductor laser may be improved by using QD active regions. This is due to the smaller volume of active material and reduced number of states. The low active volume is very important as it governs several features in semiconductor laser diode.

2.1.1 Particle in a box

The energy states of a QD can be best described by a particle in a three dimensional potential well. For this it can be assumed that the particle is free to move only within the box, i.e. it is confined within a box. Further, the electron is treated as a free particle in the three dimensions of the box with infinite walls [50]. We assume that the box has dimensions L_xL_y and L_z, and that the electron inside only experience the potential $V(x, y, z)$ associated with impenetrable walls. If $\psi(x, y, z)$ is the wave function of the electron in the material the time independent Schrödinger equation is represented as

$$\hat{\mathcal{H}}\psi(x, y, x) = E\psi(x, y, z) \tag{2.2}$$

where $\hat{\mathcal{H}}$ is the Hamiltonian operator and E is the energy distribution. The Schrödinger equation in Cartesian coordinates can be expanded as

$$-\frac{\hbar^2}{2m}\left(\frac{\partial^2}{\partial x^2}+\frac{\partial^2}{\partial y^2}+\frac{\partial^2}{\partial z^2}\right)\psi(x,y,z)+V(x,y,z)\psi(x,y,z)=E\psi(x,y,z) \tag{2.3}$$

Assuming the particle behaves as a free electron gas, the potential V will be zero within the box and infinity outside and at the boundaries. This can can be expressed as

$$V(x,y,z)=\begin{cases}0, & \text{if } 0<x,y,z<L_x,L_y,L_z\\ \infty, & \text{otherwise}\end{cases} \tag{2.4}$$

The wave function ψ can be further separated in Cartesian coordinates as

$$\psi(x,y,z)=X(x)Y(y)Z(z) \tag{2.5}$$

substituting 2.5 in 2.3

$$-\frac{\hbar^2}{2m}\left(Y(y)Z(z)\frac{\partial^2 X}{\partial x^2}+X(x)Z(z)\frac{\partial^2 Y}{\partial y^2}+X(x)Y(y)\frac{\partial^2 Z}{\partial z^2}\right)=(E_x+E_y+E_z)X(x)Y(y)Z(z) \tag{2.6}$$

The equation can be simplified by substituting the energy E for propagation vector $k_x=\frac{\sqrt{2mE_x}}{\hbar}$, $k_y=\frac{\sqrt{2mE_y}}{\hbar}$, $k_z=\frac{\sqrt{2mE_z}}{\hbar}$

$$\frac{\partial^2 X}{\partial x^2}={k_x}^2X,\qquad \frac{\partial^2 Y}{\partial y^2}={k_y}^2Y,\qquad \frac{\partial^2 Z}{\partial z^2}={k_z}^2Z \tag{2.7}$$

The solutions for these differential equations can be written as

$$\begin{aligned}X(x)&=A_xSin(k_xX)+B_xCos(k_xX)\\ Y(y)&=A_ySin(k_yY)+B_yCos(k_yY)\\ Z(z)&=A_zSin(k_zZ)+B_zCos(k_zZ)\end{aligned} \tag{2.8}$$

Each of the materials (Bulk, QWell, QWire and QD) will have, different boundary conditions influencing the values the propagation vector k. For the bulk material, $L_x, L_y, L_z >>$ de Broglie wavelength of the charge carriers, the carriers are thus free to move without a boundary using the boundary conditions, that the wave-function of the particle vanishes at the boundary of the box i.e. $X(0)=Y(0)=Y(0)=0$ and $X(L_x)=Y(L_y)=Z(l_z)=$

0, the propagation vectors can be written as

$$\begin{aligned} k_x L_x &= \pi n_x, \quad n_x = 1, 2, 3... \\ k_y L_y &= \pi n_y, \quad n_y = 1, 2, 3...and \\ k_z L_z &= \pi n_z, \quad n_y = 1, 2, 3... \end{aligned} \tag{2.9}$$

The normalized wave-function and energy can be expressed as

$$\phi_{n_x,n_y,n_z)} = \sqrt{\frac{8}{L_x L_y L_z}} \sin\left(\frac{\pi n_x}{L_x}\right) \sin\left(\frac{\pi n_y}{L_y}\right) \sin\left(\frac{\pi n_z}{L_z}\right) \tag{2.10}$$

$$E(n_x, n_y, n_z) = \frac{\hbar^2 \pi^2}{2m} \left(\frac{n_x^2}{L_x^2} + \frac{n_y^2}{L_y^2} + \frac{n_y^2}{L_y^2}\right) \tag{2.11}$$

Thus, the energy relation of the QDs are expected to show discrete energy levels, depending on the quantum numbers n_x, n_y, n_z. If the box is symmetrical($L_x = L_y = L_z$), degenerate states are present. If the box is not symmetrical, then degenerates states are absent. Also, the energy of the ground state would depend on the size (L_x, L_y, L_z) of the QD. As a consequence, QDs can be tuned in size to give high or low effective band-gaps, and thus result in a size dependent optical frequency emission. The property of the quantum confined material to be able to tune the emission wavelength as a function of their size can be exploited to cover a set of wavelength ranges. Within the course of this work, efforts were made to cover the wavelengths between 1.3 μm to 2 μm using the quantum dash material.

2.1.2 Quantum dash band structures

QDs/QDashes are nano-structures embedded in a material of relatively higher band-gap energy (usually a Barrier or a QWell). The electronic states in a QD/QDash can be described by a system of Ground State (GS) and an Excited State (ES) embedded between band of pseudo continuous states of the wetting layer and the barrier material (material of higher band-gap) or substrate depending on the band parameters as shown in Fig 2.2(a). In QDs, this type of band structure is expected to give rise to very fast carrier dynamics and thus fast gain recovery times. In QDash however, the band structures sometimes show a saturation behaviour and give rise to transport effects [51].

(a) QD/QDash band structure (b) Spectral features of QD/QDash

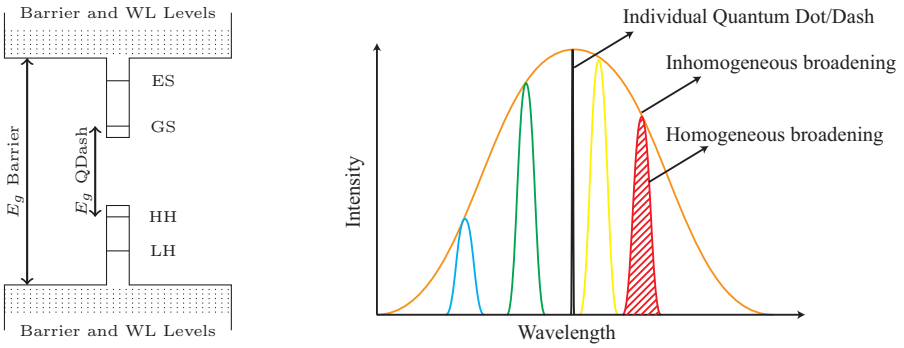

FIGURE 2.2: (a) Typical band structure of a QD/QDash. (b) Spectral features of a QD/QDash, showing homogeneous broadening, inhomogeneous broadening and emission from individual QD/QDash

The non-uniformity in size of both QDs and Quantum dashes gives rise to an in-homogeneously broadened optical gain spectrum as can be seen in Fig 2.2(b). At the same time the homogeneous broadening is observed in laser emission. The overlap of homogeneous and inhomogeneous broadening results in a phase-locked optical spectrum in FP laser cavities of both QD and QDash materials.

2.2 Growth of quantum dots/dashes

Over the last two decades, considerable effort has been devoted to the fabrication of semiconductor heterostructure that provide three-dimensional carrier confinement. QDs and QDashes have been fabricated using various approaches. These can be broadly classified into Top-Down (TD) approach and Bottom-Up (BU) approach. The TD approach, as the name suggests relies on taking a large template and reducing it down to smaller particles. These include techniques like lithographic process, nano-patterning etc. The bottom up approach includes epitaxial growth using molecular beam epitaxy (MBE) or chemical vapour deposition (CVD).

2.2.1 Fabrication using lithographic patterning

Initially, lithographic techniques were considered the most straight-forward way of fabricating semiconductor QDs. Several techniques have been investigated. These include optical lithography and holography [52–54], X-ray lithography, electron-beam

lithography [55], focussed ion beam lithography [56] and contact imprinting [57]. These patterning techniques have many advantages and still attract much attention. These are

— QDs of any shape can be fabricated.

— Compatible with most PIC technologies.

— Developed semiconductor fabrication technologies can be used to fabricate such nano-structures.

However, the feature size for QDs still remain to be limited by the resolution of the particular lithographic technique. Also, such techniques always require a chemical etching step, which involves a risk to introduce contaminations to the fabricated nano-structures. Techniques such as growth on pre-patterned substrates [58], selective intermixing based on ions implantation [59], selective intermixing based on laser annealing [60] and strain induced lateral confinement have also been demonstrated to result in quantum confined nano-structures. The nano-structures produced from these techniques however rarely result in device quality material due to high defect densities [51].

2.2.2 Epitaxial techniques : self-assembled quantum dots and dashes

Self-organised growth of QDs and dashes has been successfully demonstrated using both Molecular Beam Epitaxy (MBE) and Metal-Organic vapour phase epitaxy (MOVPE). The so called Stranski-Krastanov (SK) growth mechanism has been demonstrated to be most suited and successful approach for growth of QDs and Qdashes, producing device quality material. SK growth is an intermediary thin film growth process characterized by both 2D layer and 3D island growth. Transition from the layer-by-layer to island-based growth occurs at a critical layer thickness dependent on the chemical and physical properties of the substrate and thin-film materials. It is based on the fact that, when a material is grown on a lattice miss-matched substrate, the resulting strain produces coherent strain islands on a film of same material once a critical thickness (wetting layer) has been deposited on the substrate as shown in Fig. 2.3. These islands can be subsequently buried to produce a three-dimensional carrier confinement in the islands, resulting in QDs.

The SK growth is called self-organised due to the fact that the islands nucleate spontaneously, leading to a spatial distribution. One of the biggest advantages of self-organised growths is that it requires a single growth step, thus allowing to achieve a low

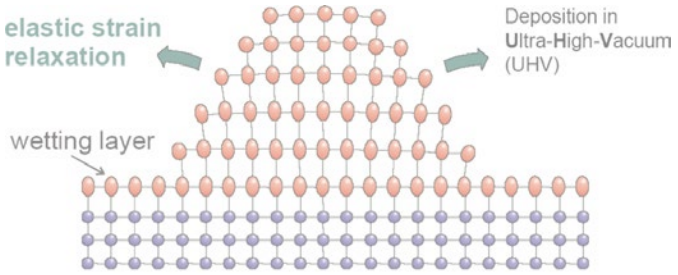

FIGURE 2.3: SK growth showing island formation due to strain relaxation after obtaining a critical thickness.

defect density. Moreover, the self-organised growth results in very high density of island formation.

The lattice mismatch plays a very important role in the formation of such self assembled structures. For example, in the InAs/GaAs material system the lattice mismatch between InAs to the substrate material GaAs is about 7 %, thus small dimension isotropic QDs are easily formed in this material system. On the other hand in InAs/InP, the lattice mismatch between the InAs and substrate InP(100) is about 3.5 %, which is relatively low. This low lattice mismatch makes it difficult for this material system to achieve isotropic island formation. Thus the islands formed on InP(100) substrate appear to be elongated.

2.2.3 Epitaxial structures

Self assembled quantum dots and dashes can be arranged in various epitaxial structures, as presented in Fig. 2.4. The simplest structures are where the dash layers are grown on an InGaAsP barrier material. The first and the most important step of laser fabrication is the design of the epitaxial layer. The design of the epitaxial layer determines the carrier transport to the active region and also the carrier confinements. Thus, it is of prime importance to carefully select the material and the epitaxial layers. In the literature, various designs for epitaxial layers have been investigated over the past years. These include dash-in-a-barrier (DBAR), dash-in-a-well (DWELL) and tunnel injection (TI) as shown in Fig. 2.4

For the present work a DWELL type design is being utilized for directly modulated lasers as it had been observed to give a high modulation bandwidth. In a DWELL epitaxial design, the InAs QDashes are sandwitched between two QWells. This block

can be stacked in layers to desired number of QDash stacks assembly. Finally this layer is sandwitched between the confinement layers to make the active section. Here the QWells act as carrier traps and no recombination takes place through the QWells. The quantum wells also helps in attracting the optical mode towards the dashes thereby increasing the modal gain of the laser. The DBAR structure consists of an InAs dash layer buried with an InGaAsP barrier. This structure had been previously observed to show an excellent mode locking performance [61] and hence had been used as a default epitaxial structure for Mode locked lasers.

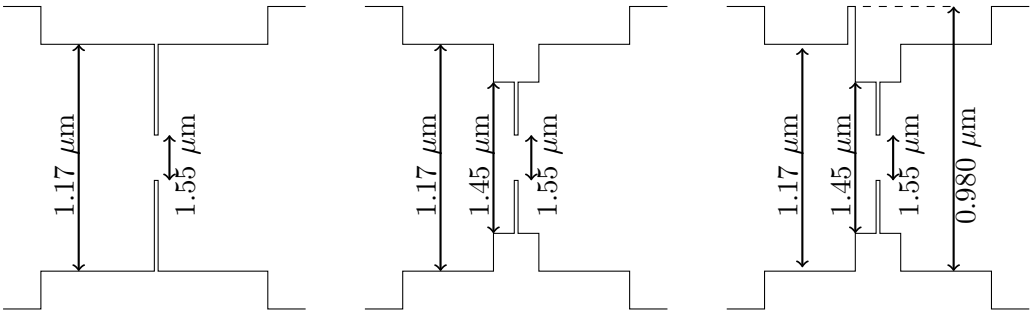

(a) Dash in a Barrier (b) Dash in a Well (c) Tunnel Injection

FIGURE 2.4: Various epitaxial layer structures used for growth of Qdashes
(a) Dash in a barrier (DBAR), where the InAs Qdashes are sandwitched between barriers of a quaternary material.
(b) A Dash in a well (DWELL) structure, where the Qdashes are buried within a QWell which is buried in a quaternary barrier.
(c) The tunnelling injection type design, where the injection of the carriers is controlled by a quantum barrier.

2.3 Quantum dash material

Attempts to grow self assembled QDs on commercially favoured indium phosphide substrate in (100)-facet orientation, resulted in elongated nano structures, which are now called QDashes. QDashes are low dimensional heterostructures, with typical length of 200 to 300 nm, width of 10 to 20 nm and height of 1 to 2 nm. A tunnelling electron microscope (TEM) image of such QDashes is presented in Fig 2.5(a), showing the typical dimensions of such a material. The elongation of the InAs island formed on the InP substrate is due to the low lattice mismatch of 3.5% between InP and InAs as opposed to the InAs island formation on GaAs substrate where the lattice mismatch is about 7%. Nevertheless, owing to their low dimensions, these structures are expected to exhibit several interesting optical and electronic properties.

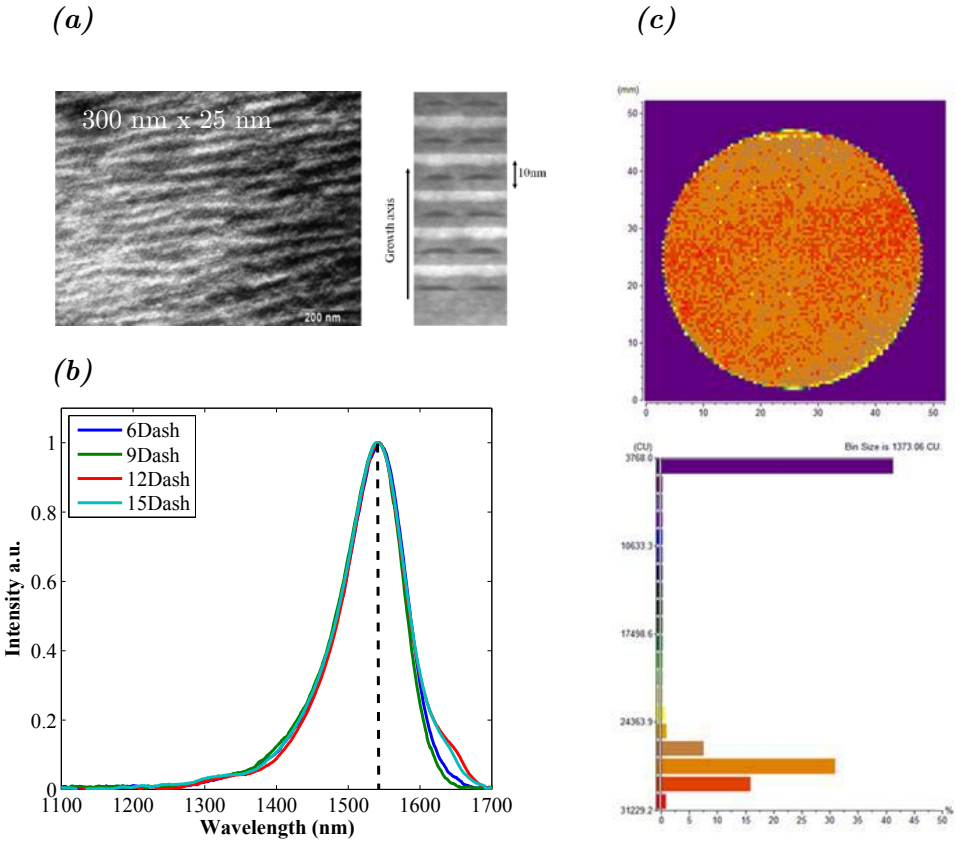

FIGURE 2.5: (a) Plane view electron microscope image of InAs QDashes, dimensions indicated as 25 nm by 300 nm Cross section TEM of the QDash structure showing 6 layers of QDashes stacked over each other, where each layer is measured to be 1 nm in height. (b) Room temperature PL from QDash structures, with different number of stack layers. (c) PL-intensity from the wafer surface, showing uniformity in QDash growth on the wafer.

Due to the low active volume of the QDash structures, the optical confinement within the QDashes would remains small, if only a single layer of QDash is used in the active region. This would result in very low modal gain, which would remain insufficient to overcome cavity losses. One of the ways to deal with this problem is the stacking of QDash layers in the active structure. At epitaxial facilities of III-V Lab, growth conditions were optimized in order to keep a full width at half maximum (FWHM) of the photo-luminescence (PL) spectrum almost constant when the number of stack is increased up to 15 layers, leading to a value of 100 nm at room temperature [62], as shown in Fig. 2.5(b). TEM images of the cross section of the active layer reveal a very ordered growth, where the dashes are seen to be spatially aligned, as presented in Fig 2.5(a). The uniformity of the PL as a function of wafer position is presented in Fig 2.5(c), and the wafers grown using self-assembly show a uniform PL intensity over the wafer. These

results indicate key improvement in reducing the homogeneous broadening arising due to the size fluctuation and composition variation in different stack layers.

2.3.1 Confinement in quantum dashes

The quantum confinement in QDashes had been a subject of debate. Several theoretical and experimental studies have been performed over the last decade to consolidate the concept of carrier confinement in QDashes. Most studies suggest that due to the large length of the QDashes (between 200 nm - 300 nm), QDashes show DoS similar to that of QWire [41, 43, 63]. Wie et al [43] suggest that there is a large variation in the length of QDashes. This fluctuation in the length could be as large as 30% from the average length of a QDash. Due to this size fluctuation, some QDashes acquire a carrier confinement in all three dimensions, while others show a confinement in two dimensions. The behaviour of the ensemble of QDashes is much inclined to that of QWires. Zilkie et al [63] compare the carrier recovery times in semiconductor optical amplifiers, of devices composed of QDash active region with QWell and QDs. Their findings suggest a 1-D QWire type behaviour in QDash opposed to 0-D behaviour of the QDs. At the same time some experimental results suggest the behaviour to be close to that of QDs [38, 62]. It is believed that the resemblance of experimental behaviour to QDs can be attributed to the high degree of confinement in one direction (height of the QDashes $\approx 1\ nm$). The nature of DoS of QDashes is thus not extremely well understood. However, it can be expected that these nano-structures will show behaviour between QDs and QWires.

2.4 Expected properties from quantum dash lasers

The multi-dimensional carrier confinement in QDs and QDashes gives rise to a set of interesting properties compared to their bulk counterparts, as had been theoretically predicted [34] and had been experimentally demonstrated by various research groups [2, 38, 42, 62]. These properties include low threshold current densities, high material gain, fast carrier dynamics, high differential gain, small α-parameter and high tolerance to optical feedback.

Threshold current density

With the decreasing dimensionality of the gain medium in the active region, the DoS and the gain spectrum become narrower. The reduced DoS also decreases the number of states to be filled before the medium becomes transparent to the injection. Thus the transparency current and the injection current is theoretically expected to reduce in QD and QDash lasers [64]. It had been experimentally demonstrated that QD lasers can reach extremely low threshold current densities [65–68] as compared to their bulk [69] and QWell [70] counterparts.

High characteristics temperature

Another consequence of the reduced DoS is the reduction of temperature sensitivity. It had been theoretically shown by Arakawa et al [34] that the threshold current of the QD lasers should be independent of temperature, thus making QD lasers threshold theoretically immune to temperature variation (T_o=∞) as long as the populations in higher sub-bands remains negligibly small. The population of the higher sub-bands in QDashes is often reduced using a p-type doping. In fact, a very high temperature tolerance had been observed for QD lasers experimentally [37, 68]. This tolerance in temperature is not just limited to the threshold density but can also be seen in other laser characteristics such as α-parameter [71].

High material gain

The reduction in density of state also leads to a narrow and sharp gain spectrum with optical gain considerably higher when compared to the conventional QWell or bulk material [40]. It is theoretically predicted that the material gain is maximum when the direction of the electric field is parallel to the longest dimension of the QD. Thus, QDash structures are expected to show an improved material gain characteristics. A more relevant parameter of the laser gain characteristics is the modal gain. It can be simply defined as a product of mode confinement factor with the material gain. The modal gain is however limited in QDs due to the low confinement. This can however be solved by stacking more layers of QD in the active region. Modal gain up-to 60 cm^{-1} have been demonstrated in QDash [72].

Fast carrier dynamics

The carrier dynamics in a QDash device is also expected to be very fast compared to QWell or bulk materials owing to the low gain volume of the QDash material. Gain recovery times as low as 80 ps have been demonstrated for QDs, but they are slightly higher for QDash materials [63]. The fast carrier dynamics in such material not only proves to be very important in applications such as all optical switching but also in direct modulation of QD lasers.

Small linewidth enhancement factor (LEF) (α_H)

Near zero LEF have been predicted for QD lasers [42], owing to their quasi-symmetric gain spectrum. Theoretically QD lasers should lead to lower LEF as compared to QWells (around 2-3 for optimised QWell structures), but the value of the LEF in both QDs and QDashes is limited owing to the higher lying levels (Wetting layers and excited state). Nevertheless extremely low (near-zero) values of LEF have been demonstrated using a TI design [73]. In QDashes, the saturation of the Qdash material results in large LEFs. This effect of state filling can be readily observed in un-doped QDashes, where the LEF increases to large values (30) [63] with the injected current. The concept of LEF is very important for directly modulated lasers and thus ways to reduce the line-width enhancement factor will be discussed later in this thesis (see Section 3.4.3).

High differential gain

Differential gain (σ_g) is defined as the change in gain with the change in number of injected carrier. The differential gain of a laser is directly related to the LEF. Hence, a lower differential gain would result in low LEF, low chirp and high depth of modulation. σ_g as high as 2×10^{-12} cm^2 have been demonstrated for QD lasers as opposed to 9×10^{-16} cm^2 for conventional QWell lasers [42].

Optical feedback sensitivity

A reduction in sensitivity to optical feedback is also expected as a result of low LEF. High tolerance to optical feedback has readily been demonstrated using both QD

and QDash materials [74]. A tolerance to optical feedback of up to -16 dBm had been demonstrated on QDash lasers [75]. The reduced sensitivity to optical feedback and high temperature tolerance are key features that open the way for an isolator-free and cooler-less optical transmission device.

2.5 Fabrication technology

Over the past few decades the fabrication technology on InP-platform has matured to an industrial scale. The fabrication at laboratory scale, however, varies between laboratories. Various technologies can be used on a laboratory scale to fabricate active and passive devices for telecommunication applications. These can be broadly divided into two categories based on the fabrication facility and application.

Ridge Wave-Guide (RWG) Technology: The lasers fabricated using the RGW process are ideal for optical communication, as they do not have a problem related to carrier leakage. RWG devices are index guided devices and thus result in large modulation bandwidths. The RWG technology using QDash material is expected to produce Al-free DMLs which can modulated in excess of 20 GHz. This type of technology is suited to produce only isolated devices as, it cannot facilitate active-passive integration. Most fabrication facilities prefer this type of technology as it does not require an in-process regrowth step [76].

Buried Ridge Structure (BRS) Technology : BRS technology as opposed to RGW requires an in-process regrowth step, which makes it unsuitable for most fabrication facilities. The BRS fabrication has a drawback that it requires an intermediate growth step. Thus it is preferably performed in fabrication facilities with a growth facility. In addition, this type of technology is prone to carrier leakage, resulting in lasers with RC limited modulation bandwidths. There are several methods under investigation to solve the problem of the carrier leakage, nevertheless using standard BRS would lead to a finite carrier leakage. The advantage of the BRS approach is that the devices fabricated using this technology are very robust and show a prolonged lifetime as compared to the RWG lasers. And most importantly, BRS technology also allow active-passive integration using the butt-joint (BJ-BRS) fabrication technique. As III-V Lab is equipped with a re-growth facility, attention will be paid towards the BRS approach of fabrication

as the ultimate goal is the fabrication of active and passive components on the same substrate.

2.5.1 Broad area lasers

Broad area (BA) lasers are fabricated to test the quality of the material in terms of lasing performances. The technological steps to fabricate a broad area laser are fairly simple. The epitaxial structure is first regrown with a top cladding of about 2000 nm of p-doped InP using MOVPE. A photo-lithography is performed with a mask containing broad stripes, with the width in range of 25 μm to 100 μm. The lithography is followed by deposition of p-metal contact, which is lifted off from the Photo-resist using acetone. This results in stripes of metal of varying width as top contact. Metal is deposited for n-contact after the thinning of the substrate to 120 μm. The general technological step for fabrication of a broad area laser are presented in figure 2.6. The steps involved in

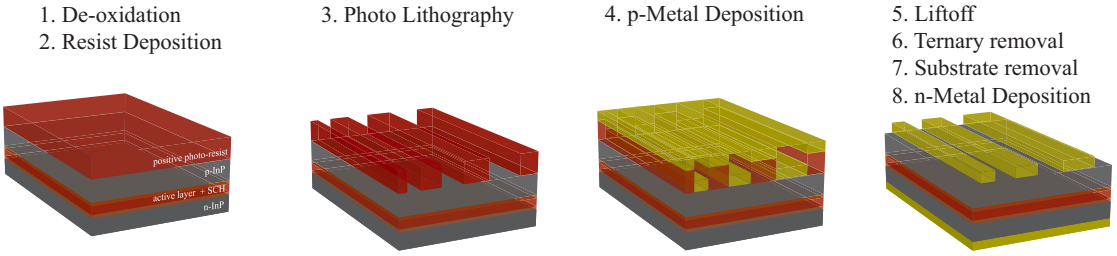

FIGURE 2.6: Illustration of technological steps followed for fabrication of a Broad area laser

fabrication of a BA laser can be summarized as below

1. ***Epi-wafer Regrowth***: The wafer is regrown with a thick epitaxial layer of Indium Phosphide, which serves as an upper cladding layer. Over the InP a thin layer of InGaAs contact layer is grown.

2. ***Photo-lithography***: The regrown-wafer is then prepared for photo-lithography. The wafer is first de-oxidized and a positive resist is deposited over the mask. The wafer is then subjected to a lithographic exposure with a mask having broad stripes ranging between 25 μm and 100 μm in width. The lithography is subsequently developed using a developer solution.

3. ***Top Contact***: The photo-lithography results in a wafer which contains areas blocked by the photo-resist and areas which are open. (Ti/Pt/Au) is deposited over the entire wafer followed by a lift-off using acetone bath. Acetone dissolves

the photo-resist under the metal, and lifts-off the metal from the areas where photo resist was deposited. This results in areas containing broad stripes of metal on top of the wafer.

4. ***Bottom Contact***: To deposit the bottom contact, the substrate of the wafer is thinned down to about 100 μm. The thinned wafer is then subjected to a deposition of (Pt-Au).

BA lasers are subsequently obtained by cleaving the laser bars with different cavity lengths. These lasers are used to evaluate the threshold current density J_{th}, modal gain Γg_m, internal losses α_{int}, external differential quantum efficiency η_{ext} and various important electrical properties. BA lasers are preferred for evaluation of the material for two reasons. Firstly, BA lasers are very easy to fabricate and secondly because the optical modes are completely confined within the active region of the laser. Thus measurements on broad area lasers will give an accurate information on optical and electrical properties of the material.

2.5.1.1 Material characterization

Broad area lasers were fabricated with varying numbers of stack layers. The static characteristics of the material such as modal gain, threshold current density are extracted from the light-current (LI) curves of these lasers using the following relations

$$\ln\left(\frac{J_{th}}{J_o}\right)\Gamma g_{th} = \frac{1}{L}\ln\left(\frac{1}{R_1 R_2}\right) + \alpha_{int} \tag{2.12}$$

$$\frac{1}{\eta_{ext}} = \frac{e}{\eta_i \hbar\omega}\left(1 + \frac{2\alpha_i}{\frac{1}{L}\ln\left(\frac{1}{R_1 R_2}\right)}\right) \tag{2.13}$$

where J_o is the transparency current density, e is electronic charge η_i is the internal quantum efficiency and $\hbar\omega$ is the photon energy. Measurements are made for lasers of different lengths. The threshold current I_{th} and slope efficiency of the lasers are then calculated from the LI characteristics. As the width w of the laser ridge is known, the threshold current density $J_{th} = I_{th}/(L * w)$, $\ln(J_{th})$ is then plotted against the inverse of the length and is presented in Fig. 2.7(a). The threshold current density for an infinite length $\ln J_{th_{inf}}$ and the modal gain Γg_{th} of the material can be extracted from this curve from Eq.2.12.

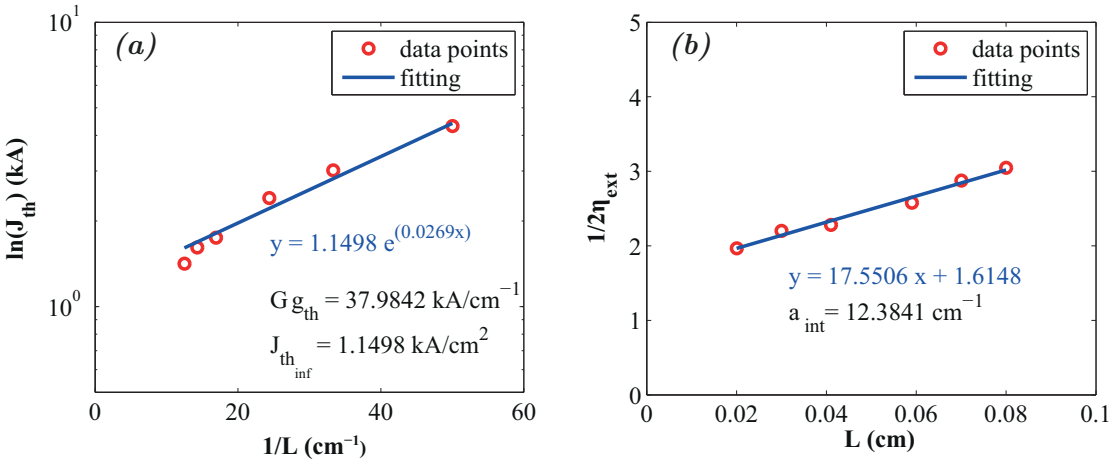

FIGURE 2.7: (a) Threshold current density J_{th} as a function of inverse cavity length, the intercept on y-axis gives the value of $J_{th_{inf}}$ (b) Inverse of external quantum efficiency as a function of length of the broad area laser

The internal losses α_i can be extracted in a similar fashion from equation 2.13. The extraction of internal loss and internal quantum efficiency is presented in Fig. 2.7(b). These extractions were performed for different numbers of stack layers in DBAR structures. A summary of these parameters as a function of number of stacking layers is presented in Table. 2.1. These parameters were also extracted for the DWELL design with varying stack layers, and is presented in Table. 2.2. A significant increase in the threshold current density can be noted when the number of stack layers is increased in the DBAR structures. The optimum stacking number is nevertheless a trade-off between high modal gain and small internal losses. Table. 2.1 and Table. 2.2 show that the net gain per dash layer decreases sharply when the stacking is increased beyond 9-dash layers. This can be attributed to re-absorptions of optical power within the dash layers. Thus, there is no practical interest in increasing the stacking beyond 9 layers for DBAR design and 6-layers for DWELL design.

DBAR Stack	Γ%	$J_{th_{inf}}$ (kA/cm^2)	Γg_{th} (cm^{-1})	α_i (cm^{-1})
6 Layers	0.90	1.15	37.98	12.38
9 Layers	1.35	1.73	64.92	27.15
12 Layers	1.80	1.96	52.24	19.44
15 Layers	2.25	2.06	56.71	18.72

TABLE 2.1: Threshold current density J_{th}, Modal gain Γg_{th} and internal loss α_i for different number of stack layers in a DBAR structure.

A similar study was performed for different doping levels in DWELL structures

DWELL Stack	Γ%	$J_{th_{inf}}$ (kA/cm^2)	Γg_{th} (cm^{-1})	α_i (cm^{-1})
6 Layers	0,94	0,95	38.56	11.63
12 Layers	1.67	1.73	48.86	19.11
15 Layers	2.3	2.31	61.58	25.32

TABLE 2.2: Threshold current density J_{th}, Modal gain Γg_{th} and internal loss α_i for different number of stack layers in a DWELL structure.

with 6-DWELL stacks, where the Barriers were doped with n-type doping with a dopant concentration of 10^18 cm^{-1}, an intermediate p-doping with a dopant concentration of 10^18 cm^{-1} and a standard p-doping with a dopant concentration of 2×10^18 cm^{-1}. These were compared with un-doped material and are presented in Table. 2.3. The n-doped material does not lead to a significant improvement in the static characteristics. The p-doped sample degrades the threshold current density and increases internal losses as expected due to the optical absorptions in p-doped barrier layers. Nevertheless, the threshold current densities can be maintained within acceptable limits for device fabrication. Also, high modal gain can be maintained and at the same times it is expected to improve the temperature characteristics in devices, a phenomena which is well observed [37]. The improvement in modal gain is an important result for the growth of p-doped QDash structures. This work would focus on the studies on devices from such p-doped structures for high-speed directly modulated lasers in Chapter 3 and un-doped DBAR structures for integrated low-phase noise sources further described in Chapter 5.

Doping Type	$J_{th_{inf}}$ (kA/cm^2)	Γg_{th} (cm^{-1})	α_i (cm^{-1})
n-doped (Si 1E+18)	0.941	30.45	13.98
no doping	0.95	38.56	11.63
p-doped (Be-1E+18)	2.189	64.17	26.38
p-doped (Be-2E+18)	2.24	60.03	34.80

TABLE 2.3: Threshold current density J_{th}, Modal gain Γg_{th} and internal loss α_i for different doping-types in DWELL structures.

2.5.2 Buried ridge lasers

When the static characteristics of the material are found to be good, it can be processed for more complicated technologies, to yield single mode lasers. The buried ridge scheme of fabrication for active devices is complicated as compared to broad area or ridge wave-guide scheme of fabrication. However, BRS lasers have the advantage of not

only being mono-modal but being very robust as the wave-guide is burried under a thick layer of InP. At the same time, the BRS technology requires a regrowth of the upper-cladding layer, after certain steps of technology. Most of the processing is performed on the epitaxial layers without regrowth. This type of technology thus requires great care during the fabrication of devices. BRS lasers can be fabricated using both photo-lithography and electron-beam lithography based on the desired feature size. Feature size as low as 1 μm can be fabricated using photo-lithography, however for smaller feature sizes, electron beam lithography is more suited. The major technological steps performed for the BRS defined by photo-lithography are presented in Fig. 2.8

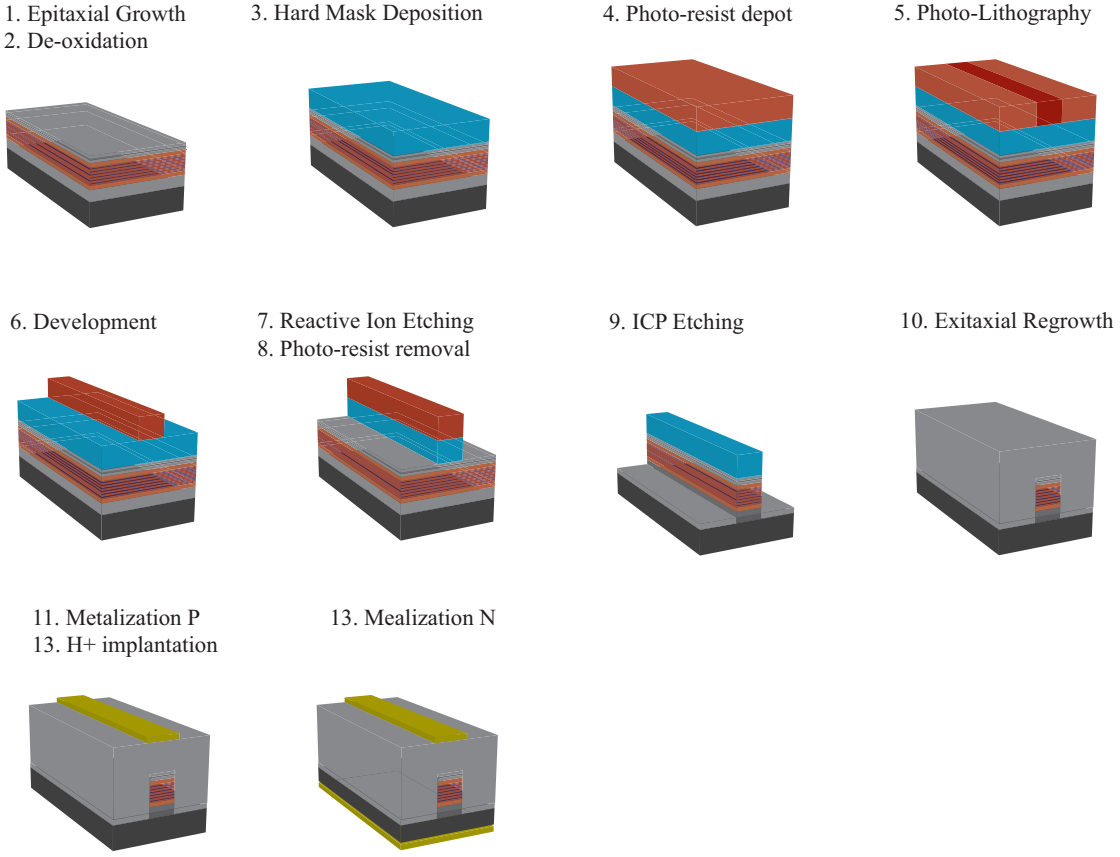

FIGURE 2.8: Illustration of technological steps followed for fabrication of a buried ridge structure laser using Photo-lithography

1. ***De-oxidation and Hard Mask Deposition***: Once the epitaxial structure is grown, it needs to be de-oxidized before any processing can be done on it. De-oxidation is followed by dehydration of the wafer. Thereafter, a slow deposition of SiO_2 or Si_3N_4 is performed which acts as a hard-mark for the photo-lithographic process.

2. ***Photo-lithography***: The wafer is subjected to deposition of a primer solution, which helps the photo-resist to firmly stick on the wafer surface. A negative resist is then deposited followed by an exposure (see. Fig 2.8(4 and 5)). Note that the mask designs and polarities have to be adjusted in advance according to type of structures needed. An exposure is then performed using the physical mask. The photo-lithographic exposure is followed by a post exposure bake needed by most negative photo-resists, and finally the photo-resist is developed. This results in areas protected by the resists and other areas where the deposited oxide is visible, as seen in Fig 2.8 step (6).

3. ***Etching Process***: Both wet and dry etchings can be performed at this stage for transferring the ridge structures to the epitaxial wafer however, dry etching is mostly preferred due to the anisotropy of dry-etching process.

   (a) ***Reactive-ion-etching (RIE)***: The wafer is then subjected to a RIE-process, to transfer the resist mask on to the Oxide/Nitride hard mask. The photo-resist is then removed using acetone. The transferred patterns now contain oxide ridges stripes on top of the active structures as shown in Fig 2.8 step (7-8).

   (b) ***Inductively Coupled Plasma (ICP)***: ICP is the used to etch the active structure at all places but the region covered by the hard mask. The active structure is etched till the buffer or stop-etch layers (see. Fig 2.8(9)). It is however preferred not to etch the structures very deep as this might induce losses in the final devices.

4. ***Regrowth***: The structure is subjected to a metal-oxide vapour phase epitaxy, to regrow the InP on and around the etched structure. Usually a 2 μm thick InP is grown followed by a 300 nm thick InGaAs to facilitate the deposition of p-contact metal. This regrowth buries the ridge within the InP completely, making the wave-guide very robust. This regrowth can also be done using a semi-insulating material (SiBH regrowth), which also reduces the carrier leakage, however this is beyond the scope of this thesis.

5. ***p-Metallisation***: The wafer after regrowth is ready for p-contact deposition. A lithography is performed to deposit the photo-resist and localize the position of the metal contact, followed by a deposition of the p-metal (Ti/Pt/Au). A

lift-off of the photo-resists is performed which leaves regions covered with metal over the buried ridge wave-guide.

6. ***H^+ Implantation***: The deposited metal is usually very wide (100 μm in width). Thus, this metallization would allow a lot of current to leak through the InP making the active devices very inefficient. It is thus important to inhibit the carriers and allow them to pass only through the regions directly above the wave-guide. This carrier restriction can be performed using either a semi-insulating regrowth step or by implantation of H^+-ions to restrict carrier transport from the InP. For this the regions of implantations are first localized near the ridges to about 5 μm using a positive resist and a positive mask. The development of the photo-lithography results in regions over wave-guide covered with photo-resist which protect these regions from implantation. The wafer is then implanted with H^+-ions at different energies.
7. ***n-Contact***: The substrate of the wafer is subsequently thinned to around 120 μm and the n-contact (Pt/Au) is deposited on the back of the wafer.

When the desired feature size is below the resolution of the photo-lithography, fabrication of BRS structures is done using E-Beam Lithography. Most technological steps in this scheme remain the same as that of photo-lithography, however a titanium hard mask is used to define the lithography in addition to the oxide hard mask. The major technological steps are depicted in Fig. 2.9. A Scanning Electron Micrograph of the final devices fabricated using a BRS technology is presented in Fig. 2.10. It should be noted that both active and passive devices can be fabricated using BRS technology. In addition, active and passive devices can be integrated together on the same substrate, using the butt-joint technique, details of active-passive integration technology are discussed in Chapter 4.

2.6 Summary

Numerous demonstrations have been made on the properties of quantum dash nano-structures. These include demonstrations of static characteristics of QDash lasers such as high modal gain and low threshold current density, as well as those on dynamic

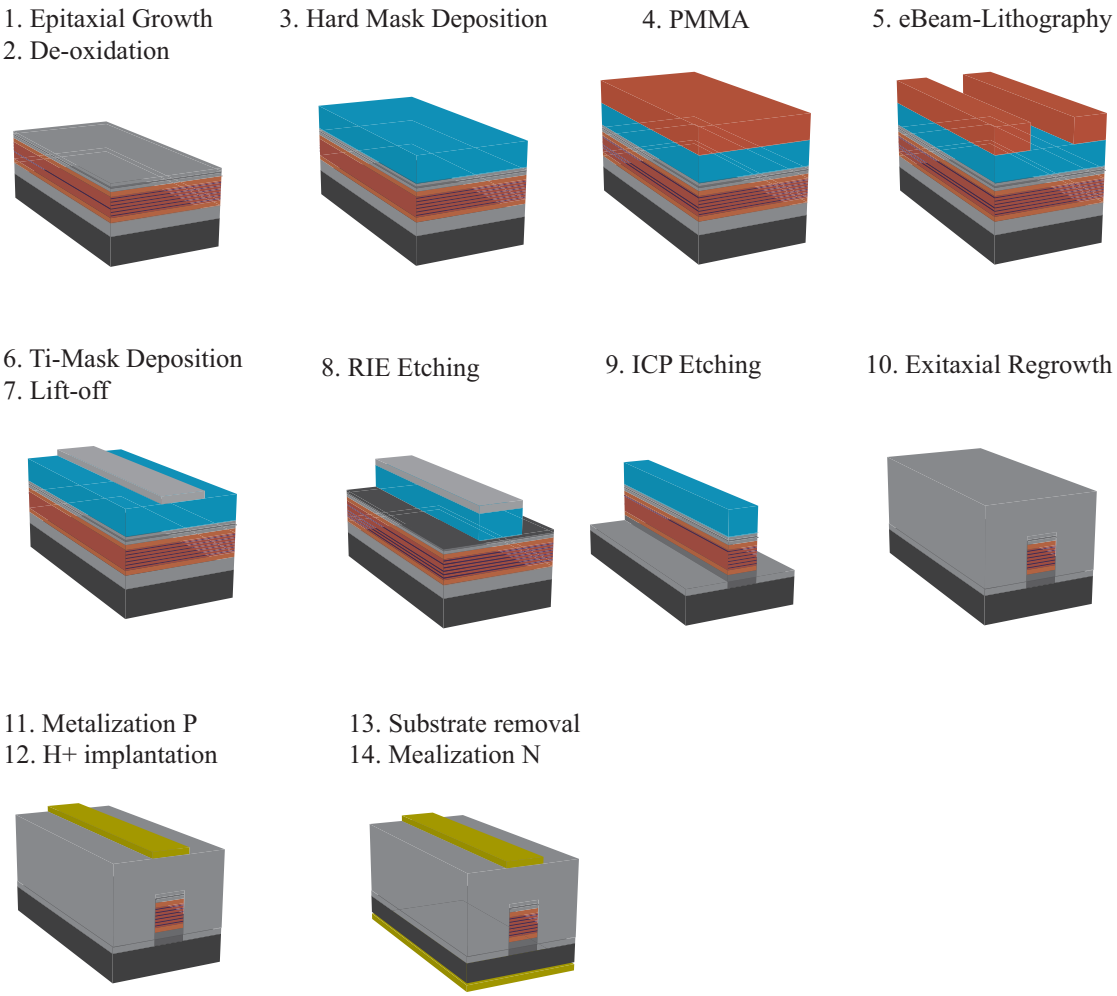

FIGURE 2.9: Illustration of technological steps followed for fabrication of a buried ridge structure laser using electron beam lithography

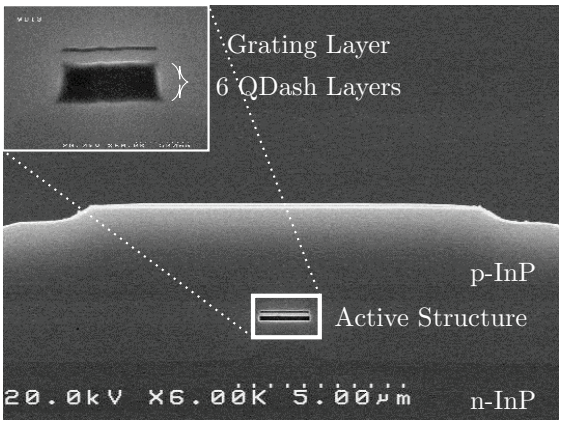

FIGURE 2.10: Scanning electron micrograph of the device fabricated using BRS technology

properties such as differential gain and linewidth enhancement. As compared to conventional quantum well material, QDash nano-structures show considerable improvement in both static and dynamic characteristics owing to the strong confinement of carriers in these nano-structures. However the properties of the nano-structures self assembled on InP have not reached the potential of truly 3D confined materials (QDots) due to their elongated shape which deviates from true 3D confinement. A further improvement in the shape of these nano-structure on InP is expected to result in performance as exhibited by the QDs on GaAs material system [77]. Nevertheless these nano-structures offer well established improvement over the conventional quantum well material. The properties of the Qdash structures have been further demonstrated to be improved using a p-doping of the active layers [13, 62, 75, 78–80]. Classically p-doping was used to fabricate QWell lasers with increased temperature sensitivity. In QDashes, p-doping not only increases the temperature sensitivity of the lasers but also shows enhancement in several other properties. This occurs as the p-doping eliminates the barrier and wetting layer levels and thus the QDash starts to mimic the behaviour of a QD. This results in thinning the density of states to the wire-like dashes towards delta-functions, thus improving the characteristics of a QDash material. The drawback however the increase in threshold due to the absorbing p-doping. The doping level thus needs to be optimized to achieve acceptable threshold currents and simultaneously mimic the QD DoS behaviour.

Chapter 3

Ultra low chirp quantum dash directly modulated lasers

Semiconductor lasers have been a key components for optical communication systems since their invention. Their potential for use in communication systems had been recognised in the infancy of optical communications [81]. Since then, much effort had been paid to develop semiconductor lasers. The invention of QWell (2D-materials) laser lead to better performances compared to the original double heterostructure laser [28]. This led towards the research on quantum confined materials for use in optoelectronic devices. Quantum dot lasers have been of much attention in recent years after the concept was proposed by Arakawa [34]. These low dimensional nano-structures are expected to display exceptional static and dynamic performances.

The recently discovered QDash material grown, on InP (100) substrates, have been demonstrated to operate at wavelengths of 1.5 μm i.e. in low loss fibre communication window [82]. Due to the 3-Dimensional carrier confinement, these lasers are expected to show interesting properties such as low threshold current, high material gain, high temperature performance, high differential gain and low line-width enhancement factor [2, 34, 40].

Directly modulated lasers are attractive to access networks owing to their small size and low power consumption. Combined with the properties of QDash material, these devices have the potential to play a pivotal role in the access network industry.

3.1 Background on semiconductor lasers

The characteristics of the QD/Qdash material like low (Jth), low LEF (α parameter), high material and modal gain, high differential gain, high tolerance to optical feedback makes QDash material a very attractive candidate for directly modulated lasers. It is necessary to understand the behaviour of a semiconductor laser under direct modulation. The following sections 3.1.1-3.1.4 would try to establish a understanding of basic laser properties.

3.1.1 Direct modulation of semiconductor lasers

A very attractive characteristics of a semiconductor laser is that the output power of the laser depends on the injected carriers. This property makes it possible for a semiconductor laser to convert an electrical data into an optical data signal, desirable for optical communication. The investigations on possibility of modulation of such lasers dates back to the first demonstration on SC lasers, an excellent review on early investigations on direct modulation of semiconductor laser can be found in [8]. It is essential to understand the static, spectral and dynamic characteristics of a diode laser. A unified approach to understand most of the laser properties is the study of laser rate equation [76, 83, 84].

3.1.1.1 Laser rate equation

The rate equations of a semiconductor laser diode is an efficient mathematical tool to model the optical and electrical properties of injection laser diodes. It consists of a set of coupled partial differential equations. These differential equations relate the density of photons in the laser cavity to the density of charge carriers in the semiconductor laser, to the injection current and material parameters such as carrier lifetime, photon lifetime, and the optical gain. The derivation of these rate equation is fairly simple and can be found in [76, 84].

If R_{sp} is the rate of spontaneous emission of an injection laser, τ_p is the photon lifetime, τ_c is the carrier lifetime, G is the net rate of stimulated emission, I is the current injected to the laser and e demotes elementary charge. Then, rate equations for

the photon number P and carrier number N of a diode laser can be written as

$$\frac{dP}{dt} = G.P - \frac{P}{\tau_p} - R_{sp} \tag{3.1}$$

$$\frac{dN}{dt} = \frac{I}{e} - \frac{N}{\tau_c} - G.P \tag{3.2}$$

The term R_{sp} takes into account the rate at which the spontaneously emitted photons are added to intra-cavity photon population. The net rate of of stimulated emission can be related to material gain g_m as

$$G = \Gamma v_g g_m \tag{3.3}$$

Due to the spreading of the optical mode outside the active layer, the power gain g_m needs to be corrected. If Γ is the mode confinement factor, the term Γg_m is known as modal gain of the laser. The dependence of the material gain can be empirically approximated to be proportional to the number of charge carriers and the gain cross section σ_g (differential gain) of the laser with active volume V as

$$g_m = \frac{\sigma_g}{V}(N - N_o) \tag{3.4}$$

The net rate of simulated emission can now be expressed in terms of the change in carriers in the active medium as

$$G = \Gamma v_g \frac{\sigma_g}{V}(N - N_o) \tag{3.5}$$

Also for lasing, the boundary condition is that the gain to a particular mode in the laser cavity of length L and facet reflectivity R_1 and R_2 should be at least equal to the net cavity losses, which imposes the condition

$$\Gamma g_m = \alpha_{int} + \frac{1}{2L} \ln\left(\frac{1}{R_1 R_2}\right) = \alpha_{int} + \alpha_{mirror} \tag{3.6}$$

Finally the photon cavity lifetime can be related to the cavity losses. The carrier lifetime accounts for the carrier recombination mechanisms that do not contribute to the stimulated emission.

$$\frac{1}{\tau_p} = v_g(\alpha_{int} + \alpha_{mirror}) \qquad and \qquad \frac{1}{\tau_c} = A_{nr} + BN + CN^2 \tag{3.7}$$

Here, A_{nr}N accounts for all the non-radiative recombination mechanism in the laser medium, $B_{sp}N^2$ accounts for the spontaneous emissions and CN^3 represents the recombination rate arising from the Auger process. If β is the fraction of spontaneous emission which falls into the lasing mode then the rate of spontaneous emission R_{sp} is given by

$$R_{sp} = \beta_{sp} B_{sp} N^2 \tag{3.8}$$

Eq 3.4 describes the material gain in any laser depending on the gain volume of the active medium. As the volume of the Qdots and Qdashes is low compared to the conventional Qwell or bulk materials, a high material gain is expected from the Qdashes.

3.1.1.2 Transient response and relaxation oscillations

When the laser is turned on by changing the injection current, a relatively long time elapses before a steady state is reached. In the transient regime the power distribution varies as the laser goes through relaxation oscillations. The understanding of transient regime and relaxation oscillation is very important for optical communications, as the laser is usually modulated at gigahertz frequencies and never actually attains a steady state condition for a pseudo random bit sequence. The rate equations (eq. 3.1 and 3.1) of a semiconductor laser can be solved using Runge-Kutta method in most cases, to obtain the relative levels of relaxation oscillations [85, 86].

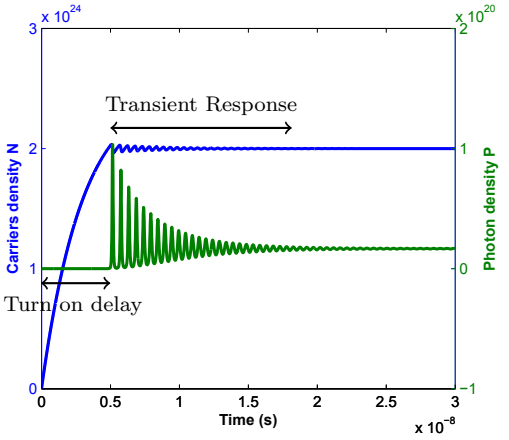

FIGURE 3.1: General solution of the rate equations of a semiconductor laser, showing the evolution of charge carrier and photons over time.

The relaxation oscillations upon turning on a semiconductor laser are presented in Fig. 3.1. The output of the laser exhibits damped periodic oscillations before settling down to a steady state value. The relaxation oscillations in any diode lasers are determined by carrier dynamics of the laser and are mainly a manifestation of the intrinsic resonances of the laser. If I_{th} is the threshold current of the laser, v_g is the group velocity, a is the gain coefficient, n_0 is the transparency carrier density, then the frequency

Ω_R of these relaxation oscillations can be expressed as

$$\Omega_R = \left[\frac{1+\Gamma v_g a n_0 \tau_p}{\tau_c \tau_p}\left(\frac{I}{I_{th}}-1\right)\right]^{\frac{1}{2}} \tag{3.9}$$

These relaxation oscillations due to the change in the carrier concentration would cause the laser to show an optical frequency chirping, this frequency chirping is also known as dynamic or transient frequency chirp. This amplitude of relaxation oscillation is however damped over the a period of time by a coefficient Γ_R, known as the damping factor Γ_R. The relaxation frequency Ω_R and the damping factor can be evaluated using the small signal analysis of the rate equations, and is presented in Section 3.1.2.

3.1.1.3 Turn on delay

It can also be noticed that, as the laser is turned on, there is a delay between the application of the injection current and the photon emission. This delay is known as 'turn on delay' as shown in Fig. 3.1. This delay time is determined by the carrier dynamics, thus faster the carrier dynamics of the active material shorter will be the turn on delay. The turn on delay t_d is approximately given by

$$t_d = \tau_c^{'}(n_{th})\left(\frac{I_{th}-I_0}{I-I_{th}}\right) \tag{3.10}$$

where, $\tau_c^{'} = (A_{nr} + 2BN + 3CN^2)^{-1}$ is the differential recombination time, I_o the initial current value. It can be noted that if $I_o = 0$, and $I >> I_{th}$ then the value of t_d approximately approaches

$$t_d = \tau_c(n_{th})\left(\frac{I_{th}}{I}\right) \tag{3.11}$$

It is thus possible to measure both carrier lifetimes $\tau_c(n_{th})$ and differential carrier lifetime $\tau_c^{'}(n_{th})$ from measurements on turn of delays of a laser. In optical communications, the laser needs to be biased above the threshold condition because the finite turn-on delay of the laser will always be a limitation on the laser modulation speeds.

3.1.2 Small signal analysis

Modulation characteristics of a semiconductor laser can be best understood by the small signal analysis of a laser. Under direct modulation of a semiconductor laser,

the laser is biased above the threshold current at I_b and deviates by $\Delta I(t) << I_b - I_{th}$. This variation in the bias current of the laser produces a change in both the number of carriers N_b and number of photons P_b by $\Delta N(t)$ and $\Delta P(t)$ respectively. The current, number of carriers and photons can be expressed as

$$I(t) = I_b + \Delta I(t) \tag{3.12}$$

$$N(t) = N_b + \Delta N(t) \tag{3.13}$$

$$P(t) = P_b + \Delta P(t) \tag{3.14}$$

Taking into account the gain saturation effect, the gain G of the laser can be related to number of carriers N and photons P as below

$$G(N,P) = \frac{\Gamma v_g \sigma_g}{V}(N - N_o)(1 - \epsilon_{NL}P) \tag{3.15}$$

where, ϵ_{NL}, the gain suppression factor, accounts for the suppression in gain observed at high values of P. The dependence of the gain G on power may occur due to several mechanisms such as carrier heating and two photon absorption. Expanding the gain $G(N,P)$ in Taylor series

$$G(N,P) \approx G_b + \left(\frac{\partial G}{\partial N}\right)_{P_b} \delta N + \left(\frac{\partial G}{\partial P}\right)_{N_b} \delta P \tag{3.16}$$

The gain derivatives G_P and G_N can be derived from eq 3.16 as below

$$\left(\frac{\partial G}{\partial N}\right)_{P_b} = \frac{\Gamma v_g \sigma_g}{V}(1 - \epsilon_{NL}P_b) = \frac{\Gamma v_g \sigma_g}{V} = G_N \tag{3.17}$$

$$\left(\frac{\partial G}{\partial P}\right)_{N_b} = -\epsilon_{NL}\frac{\Gamma v_g \sigma_g}{V}(N - N_o) = -\epsilon_{NL}G_b \tag{3.18}$$

It can also be seen from Eqs 3.7 and 3.8, that the carrier lifetimes τ_c and rate of spontaneous emission R_{sp} also depend on the carrier number. These can also be expressed in first order Taylor expansions as

$$R_{sp} = R_{sp}(N_b) + \frac{\partial R_{sp}}{\partial N}\delta N_b \tag{3.19}$$

$$\tau_c = \tau_c(N_b) + \frac{\partial R_{sp}}{\partial N}\delta N_b \tag{3.20}$$

substituting Equations 3.12, 3.16 and 3.19 into the rate equations 3.1 and 3.2

$$\frac{d\Delta P(t)}{dt} = \left[G_b - \frac{1}{\tau_p} - \epsilon_{NL} G_b\right] \Delta P + \left[G_N + \frac{\partial R_{sp}}{\partial N}\right] \Delta N \tag{3.21}$$

$$\frac{d\Delta N(t)}{dt} = -\left[G_b - \epsilon_{NL} G_b\right] \Delta P - \left[G_N + \frac{1}{\tau_c} + N_b \frac{\partial \frac{1}{\tau_c}}{\partial N}\right] \Delta N + \frac{\Delta I}{e} \tag{3.22}$$

Assuming that the current varies in a sinusoidal fashion with an angular frequency ω_m, with an amplitude I_m around the bias current I_b,

$$I(t) = I_b + I_m \sin(\omega_m t) \tag{3.23}$$

A criterion used for the validity of small signal modulation can generally be expressed using the depth of modulation defined as

$$m = \frac{(\delta P)_{max}}{P} = \frac{[I_m(t)]_{max}}{I_b - I_{th}} \tag{3.24}$$

Under the small signal approximation $m << 1$, the number of photons P and the carriers N are also expected to vary sinusoidally, thus $\Delta I(t)$, $\Delta P(t)$ and $\Delta N(t)$ can be expressed as

$$\Delta I(t) = \mathcal{R}(I_m \exp(j\omega_m t)) \tag{3.25}$$

$$\Delta P(t) = \mathcal{R}(P_m \exp(j\omega_m t)) \tag{3.26}$$

$$\Delta N(t) = \mathcal{R}(N_m \exp(j\omega_m t)) \tag{3.27}$$

introducing equations 3.25-3.27 and simplifying equations 3.21 and 3.22 results in

$$(j\omega_m + (\frac{R_{sp}}{P_b} + \epsilon_{NL} G_b P_b) P_m - G_N P_b N_m = 0 \tag{3.28}$$

$$G_b P_m + (j\omega_m + G_N P_b + \frac{1}{\tau_c}) N_m = \frac{I_m}{e} \tag{3.29}$$

These equations can be easily solved for $P_m(\omega_m)$, which is the quantity of interest

$$\begin{aligned} P_m(\omega_m) &= \frac{G_N P_b \frac{I_m}{e}}{(j\omega_m + \frac{R_{sp}}{P_b} + \epsilon_{NL} G_b P_b)(j\omega_m + G_N P_b + \frac{1}{\tau_c}) - G_b G_N P_b} \\ &= \frac{G_N P_b \frac{I_m}{e}}{(\Omega_R + \omega_m - j\Gamma_R)(\Omega_R - \omega_m + j\Gamma_R)} \end{aligned} \tag{3.30}$$

where Ω_R is the frequency of relaxation oscillations and Γ_R is the damping rate given by

$$\Omega_R = \sqrt{G_N G_b P_b} \tag{3.31}$$

$$\Gamma_R = \frac{1}{2}\left(\frac{R_{sp}}{P_b} + \epsilon_{NL} G_b P_b + G_N P_b + \frac{1}{\tau_c}\right) \tag{3.32}$$

The modulation transfer function is defined as the power of the signal at the modulation frequency relative to its dc counterpart

$$H(\omega_m) = \frac{P(\omega_m)}{P(0)} = \frac{\Omega_R^2 + \Gamma_R^2}{(\Omega_R + \omega_m - j\Gamma_R)(\Omega_R - \omega_m + j\Gamma_R)} \tag{3.33}$$

The modulation transfer function can be further simplified by normalising it with respect to $\omega_o = \Omega_R^2 + \Gamma_R^2$, in this case $H(\omega_m)$ takes the form

$$H(\omega_m) = \frac{1}{1 - \left(\frac{\omega_m}{\omega_o}\right)^2 + 2j\left(\frac{\Gamma_R}{\omega_o}\right)\left(\frac{\omega_m}{\omega_o}\right)} \tag{3.34}$$

The modulation depth of a semiconductor laser thus strictly depends on the frequency of relaxation oscillation and the damping factor as can be seen in Eq. 3.33. The bandwidth of the laser will be large if the relaxation frequency is large or if the damping is small. The relation frequency at a given bias current, in turn, as can be seen from Eq. 3.9 and 3.31 depends on material factors such as the active volume and carrier dynamics. The Qdash nano-structures owing to their fast carrier dynamics are expected to show higher relaxation oscillation frequency. The bandwidth of the lasers may be limited due well predicted damping characteristics of these oscillation in quantum dash structures [41]. This damping of the relation oscillations will be of advantage to lower the transient chirp of the fabricated laser structures.

3.1.3 Line-width enhancement factor(Small signal chirp)

Any change in the carrier density inside the laser gain medium is accompanied by a change in the refractive index of the medium (carrier induced change in refractive index) [87]. If n_b is the refractive index of an un-pumped material and Δn_p is the amount by which it changes in presence of charge carriers, then the refractive index n can be

approximated as

$$\mu = \mu_b + \Delta\mu_p \tag{3.35}$$

The amount by which the refractive index changes $\Delta\mu_p = \mathcal{R}(\chi_p)/2n_b$, is directly proportional to the real part if the complex susceptibility of the material, and thus is material dependent. Even if the amount of change in refractive index is very small, it plays a significant role in static and dynamic characteristics of SLDs. The complex susceptibility χ_p of any gain material can be related to the carrier density according to

$$\chi_p = \mu_b n \left((2b - \frac{ja}{k_o}) \right) \tag{3.36}$$

where, a is gain coefficient and b is the relative the change in refractive index with respect to the change in number of carriers. A quantity which is found extremely useful in analysis of laser chirp is the inverse of the argument of the complex susceptibility

$$\alpha_H = \frac{1}{\left(\frac{\mathcal{I}(\chi_p)}{\mathcal{R}(\chi_p)}\right)}^{-1} = -2k_o \left(\frac{\partial\mu/\partial n}{\partial g/\partial n} \right) \tag{3.37}$$

This parameter is often called line-width enhancement factor or anti-guiding factor. Change in number of electrical carriers by external pumping would produce a change in gain and index of the laser, resulting in an amplitude-phase coupling. The amplitude phase coupling also results in enhancement of the laser linewidth by a factor of $(1+\alpha_H^2)$ [88], where α is called Line-width enhancement factor (also known as α_H-parameter or Henry factor). LEF is considered one of the most important parameter for optical communications as the amplitude-phase coupling results in laser chirp.

Small signal chirp

The change in refractive index modifies the lasing frequency according to the laser resonance conditions (for DFB laser, the resonance condition is given by the grating period $\Lambda = \frac{m\lambda}{2n}$). The modulation of laser current not only leads to modulation in output intensity of the laser but also optical phase of the laser mode, resulting in a frequency shift of the laser under modulation. The small signal chirp can be expressed in terms of

the modulation frequency as

$$\delta\nu_o = \frac{\alpha_H I_P G_N}{4\pi e}\left(\frac{{\omega^2}_m + \frac{R_{sp}}{P} - \epsilon_{NL} G_b P}{({\omega^2}_m - {\Omega^2}_R - {\Gamma^2}_m) + 2{\omega^2}_m {\Gamma^2}_m}\right) \tag{3.38}$$

Thus, when a laser is driven with a time varying signal, a change in emission frequency is observed. This variation in frequency of the laser under direct modulation is known as frequency chirping. It can be noticed from Eq. 3.38, that the frequency chirp is directly related to the α_H parameter. Thus, the chirping in optical frequency of the laser is a direct consequence of amplitude phase coupling. The small signal chirp can also be related to the modulation depth m, giving a simple expression as

$$\delta\nu_o = \frac{\alpha_H}{2}\nu_m m \tag{3.39}$$

A measure of the small signal laser chirp is thus often expressed by α_H. It should be noted that the laser frequency chirping is a device dependent parameter, where as the α_H-parameter is material dependent by its definition.

3.1.4 Large signal frequancy chirping

The small signal analysis is useful for predicting the parameter dependence but is not usually applicable under practical conditions. In communication systems the lasers is often modulated with a large current variation, and does not satisfy the small signal condition for modulation depth $m << 1$. Thus the expression given in Eq. 3.39 cannot be applied in practical conditions. An expression for the chirp under large signal can be derived using the optical phase dependence under modulation, as performed in [76].

If $P(t)$ is the time varying output power of the laser, the frequency chirping $\Delta\nu$ of a laser under large signal modulation can be represented as

$$\Delta\nu = \nu - \nu_{th} = \frac{\alpha_H}{4\pi}\left(\underbrace{\frac{1}{P}\frac{dP}{dt}}_{TransientChirp} \underbrace{- \frac{R_{sp}}{P} + \frac{\epsilon_{NL} P}{\tau_P}}_{AdiabaticChirp}\right) \tag{3.40}$$

where, α_H is the line-width enhancement factor, R_{sp} is the spontaneous emission rate, ϵ_{NL} is the gain compression factor and τ_P is the photon cavity lifetime.

Transient chirp

The first term in equation 3.40, represent instantaneous change in frequency as the power of the laser changes over time. This is called dynamic or transient chirp. It should be noted that the transient chirp exists only when the power emitted by the laser changes over time, for example during the change in the applied current and induced relaxation oscillations.

$$\Delta\nu_{_T} = \frac{\alpha_H}{4\pi}\left(\frac{1}{P}\frac{dP}{dt}\right) \tag{3.41}$$

$\nu_{_T}$ represents the maximum transient frequency shift for a large signal modulation. The transient chirp is strongly related to the transient response of the laser. Thus it is dependent on the frequency of modulation, resonance frequency of the laser and the damping factor. Larger frequencies of modulation will lead to large transient chirps. The transient chirp will become more important if the laser is modulated at the relaxation oscillation frequency and if the damping factor is very small. The reduction of transient chirp is vital for the optical transmission experiments, as large transient chirps would lead to degraded optical transmission.

Adiabatic chirp

The second term in equation 3.40, represents the change in laser frequency between the maximum and minimum power levels. This is known as adiabatic chirp and can be represented as

$$\Delta\nu_{_A} = -\frac{R_{sp}}{P} + \frac{\epsilon_{NL}P}{\tau_P} = \kappa P \tag{3.42}$$

Here, κ is known as the adiabatic chirp co-efficient and is given by $\kappa = 2\epsilon_{NL}/\eta_d h\nu$ [76]. The adiabatic chirp can hence be related to the spontaneous emission and gain compression in the laser. Adiabatic chirp is thus the frequency difference between the transmitted 1-bits and 0-bits as these bits are at different optical power levels. This can however be compensated using several dispersion compensation techniques.

Thermal chirp

The laser frequency also shifts when the temperature of the laser is increased (red-shift) or decreased (blue-shift). It is well known that when a long stream of 1-bits

is fed to the laser, the temperature of the laser will increase slightly. The thermal chirp is associated with, a long stream of 1-bits. The value of this chirp will depend on the length of the stream of 1-bits, and would be hard to determine. Under semi-cooled or temperature controlled operation of the laser, the contribution of thermal chirp can be neglected.

3.2 Buried ridge lasers

For optical transmission using a DML as single transverse mode lasers with single wavelength is required. Due to this reason, as a starting point simulations were carried out using ALCOR, a proprietary software developed by France Telecom/CNET, to identify the ridge width suitable for single mode operation of the laser. This software operates using the beam propagation method [89] to evaluate the possible optical transverse modes depending on the thickness of the individual layers. These simulations were performed for the vertical structure as shown in Fig. 2.4 for a BRS structure. It is found out the structure shown a single mode operation for a ridge-width of up-to 1.7 μm. It should be noted here that unlike RGW structures, the beam propagation and hence the modal parameters within the BRS structure are affected negligibly by the etch-depth. It is also worthwhile to note that the active structure can also be designed on the contrary to increase or decrease the ridge width. The near-field transverse mode profile of the BRS laser is presented in Fig. 3.2. It can also be seen from the simulation that BRS structures result in a near-Gaussian mode profile as opposed to a pear-shaped mode observed in RGW structures.

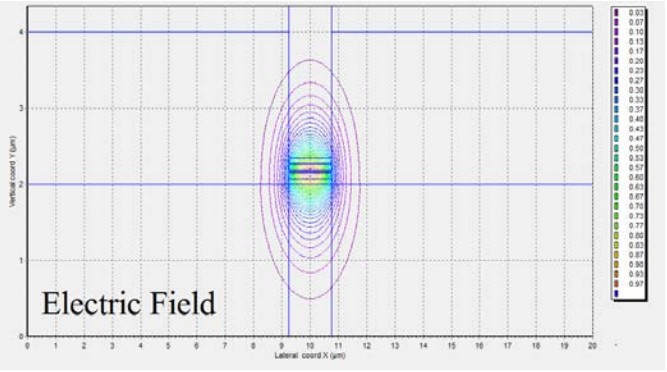

FIGURE 3.2: Near field calculation of electric field and intensity at the output of the BRS structure.

Buried Ridge lasers were subsequently fabricated using the technology described in Sec. 2.5.2. For the present study an electron beam lithography was used for the lithographic definition of the wave-guides.

3.3 Static characteristics

The static characteristics of the BRS lasers such as the light-current-voltage (LIV) characteristics, optical spectra and far-field profiles were studied for fabricated distributed feedback (DFB) and Fabry-Perot lasers in order to estimate the static quality of these lasers.

3.3.1 Light current characteristics

Light-current characteristics of the fabricated QDash FP are measured to evaluate the fabrication quality of these lasers. The L(I)-Characteristics of several un-doped 400 μm long Fabry–P'erot are presented in Fig. 3.3. The L(I)-curves of various lasers from the same active structure are almost identical revealing the excellent fabrication process and also the uniformity in the wafer growth.

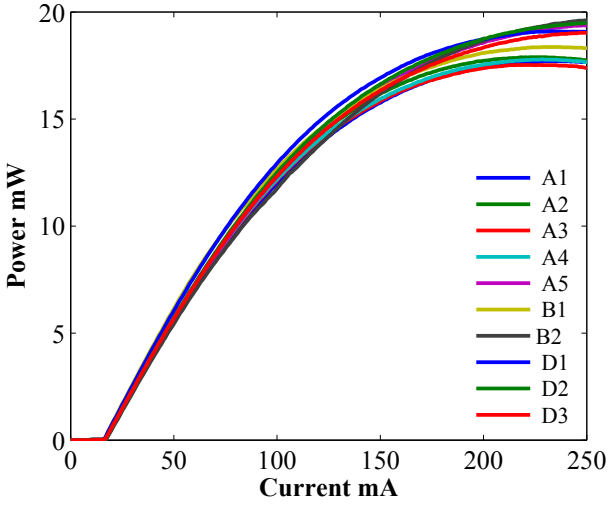

FIGURE 3.3: Light current characteristics of several un-doped cleaved mirror 400 μm long Fabry–P'erot laser showing uniformity in the fabrication process.

Light-current and voltage-current characteristics of a 1000 μm long Fabry–P'erot laser at various temperatures are also extracted and are presented in Fig. 3.4, showing

an output power of about 40 mW at 25°C and about 20 mW at 85°C. The series resistance extracted from the V(I) curve is found to be in range of 2 to 3 Ω even at elevated temperature. This shows that QDashes have a potential to operate at elevated temperatures. In a similar fashion the QDash DFB lasers are also capable of operating at

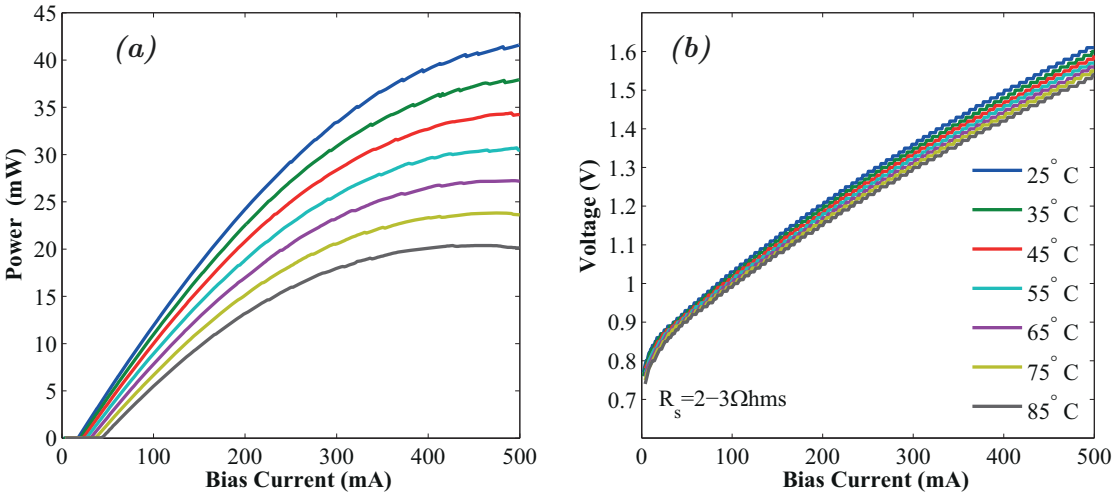

FIGURE 3.4: Light current and voltage-current characteristics of a 1000 μm long Fabry–P'erot at various temperatures.

high temperatures. Due to the phase shift introduced to the DFB laser a power of around 3 dB is lost in comparison to the FP counterpart. Nevertheless the DFBs fabricated using the buried ridge technology are very robust and display excellent performance in terms of L(I)-characteristics. A comparison of L(I) characteristics of a DFB laser with an FP counterpart is presented in Fig. 3.5

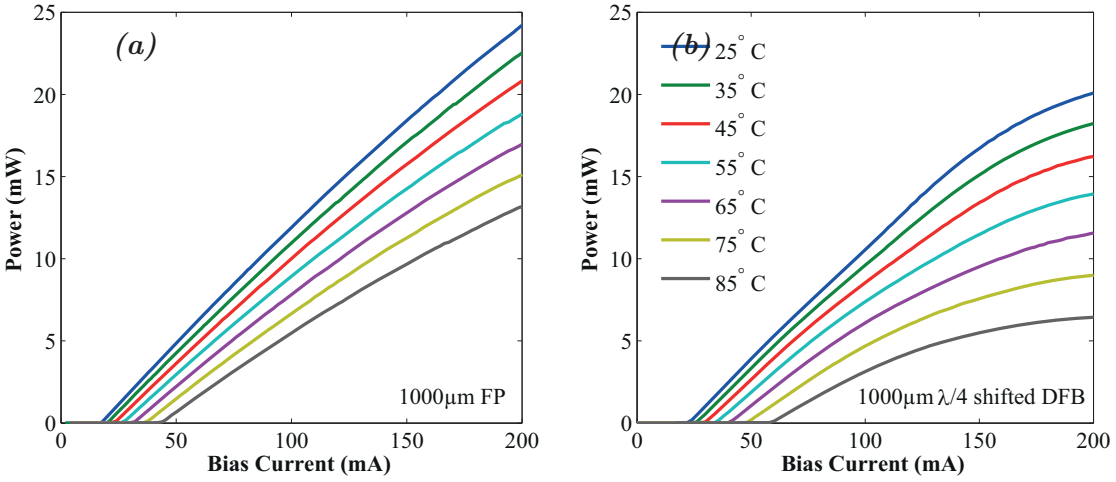

FIGURE 3.5: Comparison of the light current characteristics of a $\lambda/4$ phase shifted DFB laser with a FP laser of similar lengths (legends are the same for figure (a) and (b))

3.3.1.1 Characteristic temperature T_o

An important parameter which can be extracted from the threshold current of the laser is the characteristics temperature T_o. The temperature dependence of the device characteristics is very important from the application point of view. When the temperature of the laser is increased, the optical output power of laser diodes decreases under a constant injection current. This degradation is related to the fact that with an increase in device temperature the external quantum efficiency of the device decreases [90]. The T_o of semiconductor laser can be experimentally measured by measuring the L(I)-characteristics at various temperatures and then using Eg. 3.43 [91]

$$T_o = \frac{T_h - T_l}{\ln\left(\frac{I_{th}(T_h)}{I_{th}((T_l))}\right)} \tag{3.43}$$

where $I_{th}(T_h)$ is the threshold current of the laser at higher temperature T_h and $I_{th}((T_l))$ is the threshold current of the laser at lower temperature T_l. QDot and QDash based devices are theoretically predicted to exhibit very high T_o [34] and this has been experimentally demonstrated [37, 68]. An extraction of experimentally measured T_o for QDash lasers with p-doped, n-doped and un-doped structures is presented in Fig. 3.6. It can

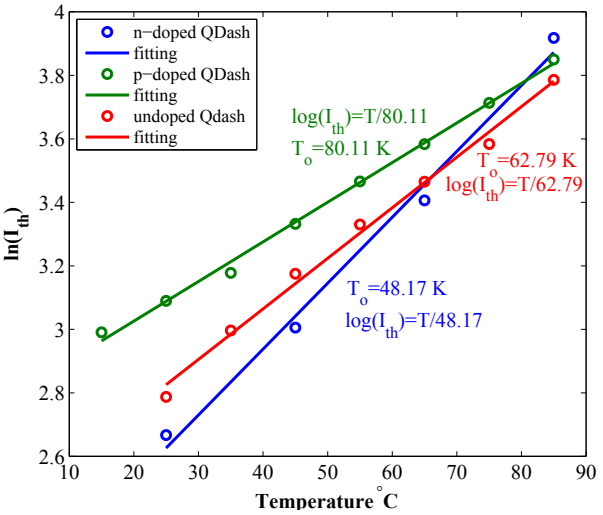

FIGURE 3.6: Comparison of T_o for a QDash laser with p-doped, n-doped and undoped active region.

be noticed here that the QDashes do not show an infinite T_o as had been theoretically predicted. These values are still large as compared to those reported in literature for QD structures. This again can be attributed to the density of states of the QDashes

which show a wire-like behaviour. It is very visible that the p-doped QDash laser shows a much higher characteristics temperature as compared to their un-doped counterparts. This effect of p-doping indicate a DoS narrowing effect by eliminating the carriers from the barriers and wetting layer energy levels. It can be asserted that the behaviour of a p-doped QDashes electronic level structure approaches that of QDs. The P-doped QDash lasers are therefore very interesting candidates for DMLs, as p-doping opens a way towards semi-cooled and un-cooled operation. The impact of p-doping on the static and dynamic properties of Qdash lasers is thus of interest and will be studied throughout this chapter.

3.3.2 Optical spectrum

The broadband gain spectrum of QDash lasers allows a very broad optical spectrum of Fabry-perot lasers as well as opens a way to fabricate DFB lasers with higher detuning from the gain peak of the spectrum. The optical spectra of Qdash FP and DFB lasers are acquired using a high resolution optical spectrum analyser with a resolution of 5 MHz. It is preferred for a DML to operate on a single wavelength, and therefore, the optical characteristics of a DFB laser are important. The optical characteristics of the FP lasers will be discussed in details in Chapter 5.

3.3.2.1 DFB optical spectrum

As stated earlier, a DML is preferred to operate with a single optical wavelength thus a DFB laser would be the most suitable for a DML. The optical spectrum of a quarter-wave-shifted 1230 μm p-doped QDash DFB laser is presented in Fig. 3.7.

The optical spectrum of the quarter-wave-shifted 1230 μm DFB shows a single longitudinal mode (single wavelength), with a side mode suppression ratio (SMSR) of about 45 dB. A high SMSR is always desirable for a DFB laser to ensure a good quality transmission for long range transmission distances. Another desirable feature of the DFB laser is a low optical linewidth. The optical linewidth of the DFB lasers is usually in the range of 1-5 MHz, depending on the active material used.

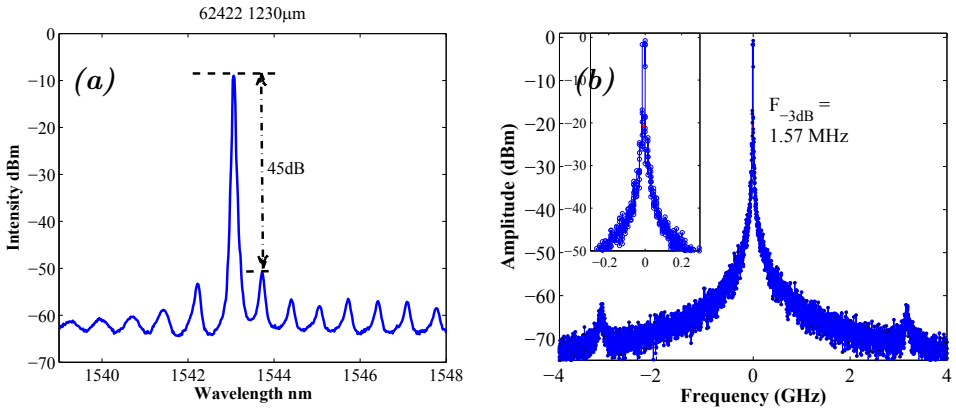

FIGURE 3.7: (a)Optical spectrum of a DFB lasers with a ridge-width of 1.5 μm showing a single longitudinal mode. (b) High resolution optical spectrum showing optical linewidth of the DFB laser.

3.3.3 Far field profiles

For telecommunications, it is essential for a laser (both DFB and Fabry-Perot) to operate with a single transverse mode. To ensure that the fabricated devices exhibited only a single transverse mode, far-field profiles of these lasers were measured and are presented in Fig. 3.8. The far-field profiles of these lasers display a single mode behaviour,

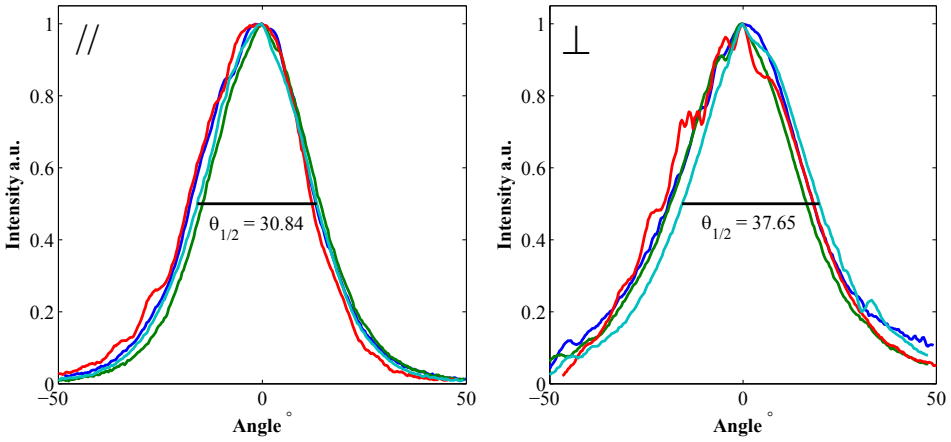

FIGURE 3.8: Far field profile of the DFB lasers with a ridge-width of 1.5 μm showing a single transverse mode.

as expected from the simulations. The divergence angle is very high (about 32° along ∥-axis and about 32° along ⊥-axis). This large divergence would result in a large amount of loss when the power is coupled to the optical fibre. It is thus useful to fabricate also mode shape converters in order to reduce the modal divergence. These mode shape converters reduce the modal divergence by expanding the mode profile. The far-field

profile of lasers with mode shape converters are measured and are presented in Fig. 3.9. The divergence angle is reduced to about 22° along ∥-axis and about 15° along ⊥-axis

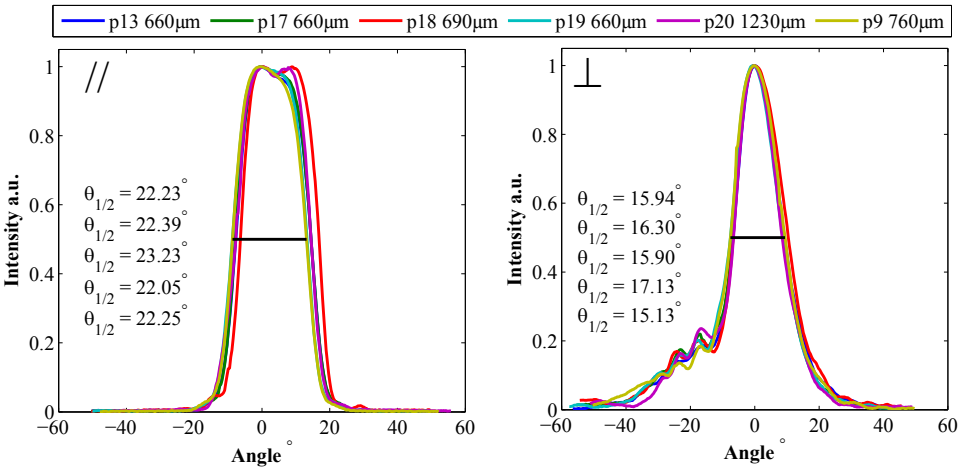

FIGURE 3.9: Far field profile of DFB lasers (ridge-width of 1.5 μm) with mode shape converters to reduce the divergence of the output beam.

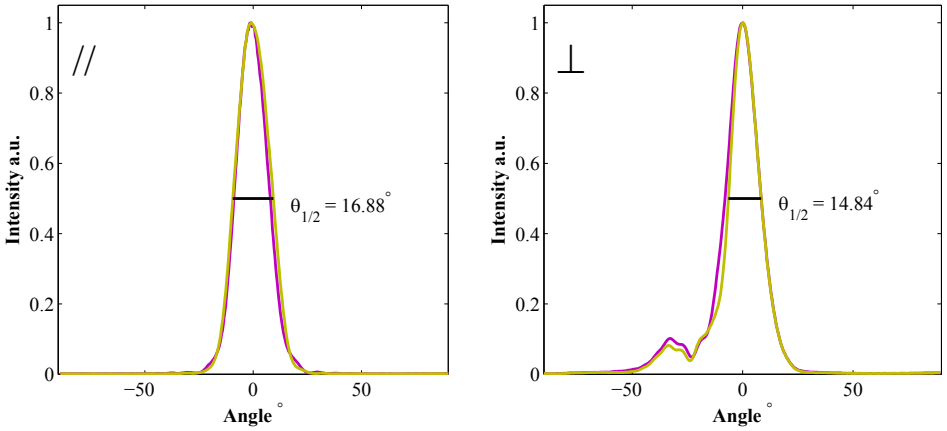

FIGURE 3.10: Far field profile of Fabry-Perot lasers (ridge-width of 1.5 μm) with mode shape converters to reduce the divergence of the output beam and reshape the beam to display a circular beam profile.

upon the used of a mode shape converter. This reduction in the mode divergence is vital to provide efficient power coupling to the optical fibres. Furthermore, these mode shape converters can be used to yield a perfectly circular mode profile as shown in Fig. 3.10. The laser power collected by the fibre with mode field diameter of 4.5 μm is presented in Fig. 3.12. Up-to 7 dBm power can be easily coupled from a DFB laser to the fibre. Powers in the orders of 3 dBm are sufficient for optical fibre communication as higher powers may excite non-linear behaviour in the optical fibre. Thus tapers are a valuable

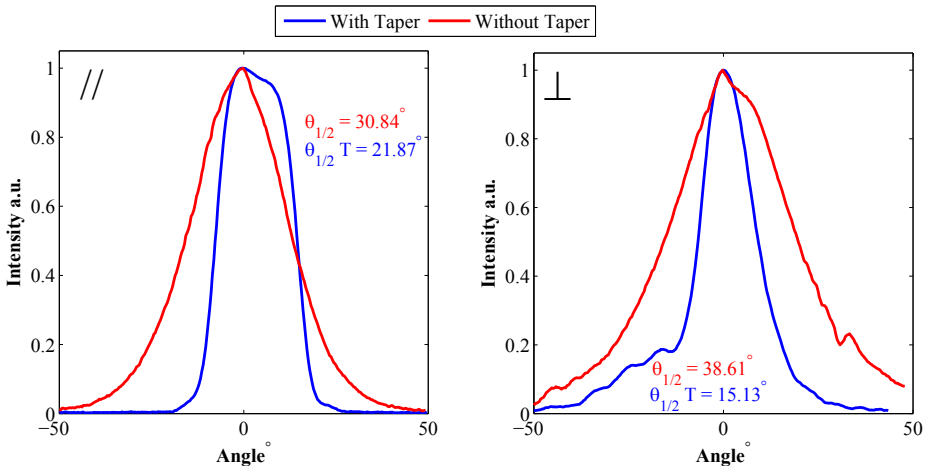

FIGURE 3.11: A comparison of far field profiles with and without mode shape converters.

component of the optical transmitters as the power lost in the coupling is reduced in excess of 5-6 dB.

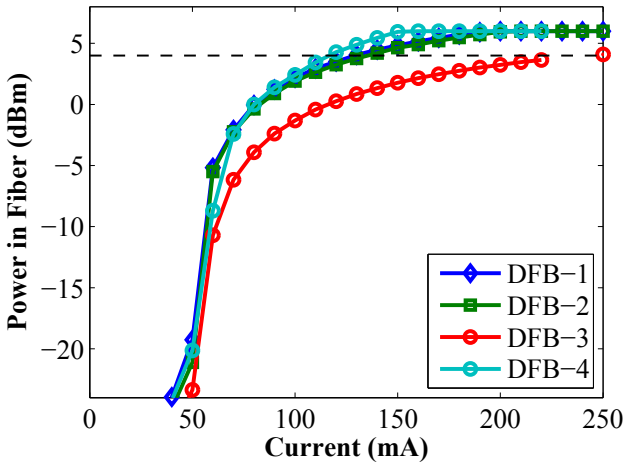

FIGURE 3.12: Power coupled in the fibre using a DFB with tapers.

3.4 Dynamic characteristics

For high bit-rates of modulations, it is of paramount importance to study the dynamic properties of the laser. The properties such as relaxation oscillations frequency Ω_R and damping factor Γ_D as well as α_H-parameter, large signal chirps and differential gain become of increased importance when a laser is modulated at high bit rates. It is specially important to study QDash lasers as they have a complicated dynamic response. The design parameters of QDash active layers, such as the width of the barrier, SCH

layers (and also the QWell for DWELL type structures) can have a profound effect on resonance frequency and damping behaviour. The laser geometry is expected to show an impact on the dynamic properties of lasers. In order to characterize these effect, BRS lasers presented in Table. 3.1 were fabricated and tested for various dynamic properties.

Wafer #	Design	Stack #	doping	Concentration
63505	DBAR	6	none	-
63504	DBAR	9	none	-
63602	DBAR	12	none	-
63605	DBAR	15	none	
62405	DWELL	6	Si	1e+18
63403	DWELL	6	Be	1e+18
62422	DWELL	6	Be	2e+18
62400	DWELL	4	none	-
62407	DWELL	6	none	-
62644	DWELL	9	none	-
62646	DWELL	12	none	-

TABLE 3.1: List of structures investigated for dynamic properties.

3.4.1 Small signal modulation

The small signal modulation response of a semiconductor laser has been described in Section 3.1.2. The modulation transfer function under small signal approximation gives us information about the relaxation frequency and its damping factor, parameters which are of prime importance for directly modulated lasers. Eq 3.34 gives the intrinsic small signal modulation response of a laser. The quantity which is of practical interest is the modulation bandwidth $f_{3\ dB}$, which indicates the frequency range over which the laser responds to current modulation. It is defined as the frequency for which the modulation response is dropped by 3 dB relative to the dc value [92]. Under ideal conditions the resonance oscillation frequency Ω_R provides a reasonable estimate of modulation bandwidth, which can be approximated as

$$f_{3\ dB} = \frac{\sqrt{3}\Omega_R}{2} \tag{3.44}$$

In practice $f_{3\ dB}$ is significantly lower than the value described in Eq. 3.44 if the electrical parasitics associated with the device structure leads to the premature roll-off of the modulation response. In presence of a parasitic response the modulation transfer

function can be rewritten as

$$H(\omega_m) = \underbrace{\frac{1}{1-\left(\frac{\omega_m}{\omega_o}\right)^2 + 2j\left(\frac{\Gamma_R}{\omega_o}\right)\left(\frac{\omega_m}{\omega_o}\right)}}_{intrinsic\ modulation\ response} \underbrace{\frac{1}{1+j\left(\frac{\omega_m}{\omega_c}\right)}}_{parasitic\ response} \tag{3.45}$$

This decrease in response occurs if an increasing fraction of the modulation current passes outside the active region of the laser. It is for this reason, the buried ridge structures suffer from a parasitic response in their modulation transfer functions. The parasitics can be modelled using an effective electrical circuit of the laser as described in [93]. The time constant inducing the parasitic roll-off is a product of series resistance R_s of the laser and the effective shunt capacitance C_p.

Small signal modulation response was extracted for the fabricated BRS devices using the small signal direct modulation of the laser for active structures presented in Table 3.1. For this the scattering parameters of the device was measured using a Lightwave Component Analyser (LCA), used in the configuration shown in Fig. 3.13. The measurement of modulation bandwidth consists of stimulating a laser or modulator with an electrical signal and measuring its response (modulated light) with a lightwave receiver. The frequency of the electrical signal injected into the laser is swept to allow characterization of the laser over a wide range of modulation frequencies.

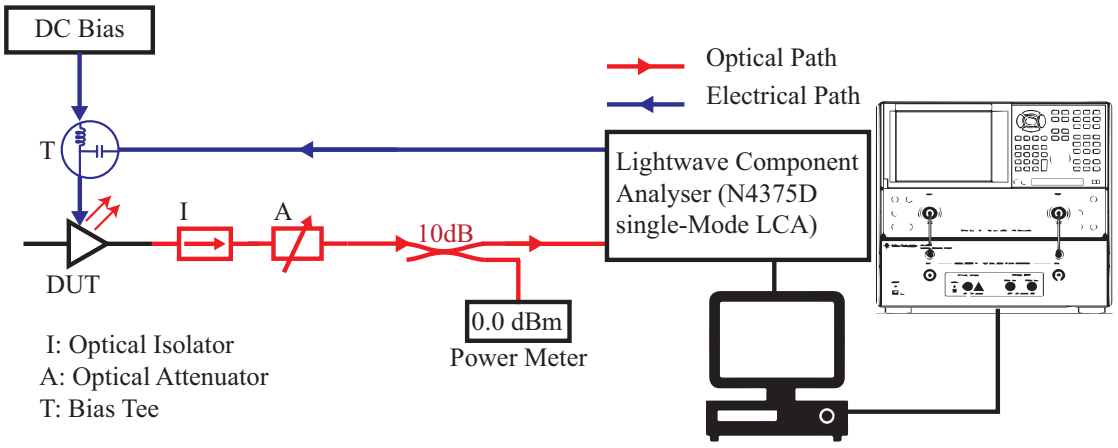

FIGURE 3.13: Schematics of test bench for measurement of small signal modulation response.

The frequency response of a laser is also dependent on biasing conditions. As the dc bias of the laser is increased, the bandwidth will generally increase. This is typically due to the relaxation oscillation characteristics that vary with laser bias (see Eq. 3.9). The relaxation oscillation phenomenon creates a resonance in the frequency response, noise,

and distortion of the laser. The bandwidths of various lasers were measured at different values of bias currents, starting from the threshold for each laser chip on carrier. Almost identical devices (in terms of ridge width and lengths) are selected for this comparison. The small signal response of various epitaxial structure designs at 100 mA is presented in Fig. 3.14. A current value of 100 mA provides a good comparison between the damping characteristics of modulation response for various designs. p-doping of the active layer

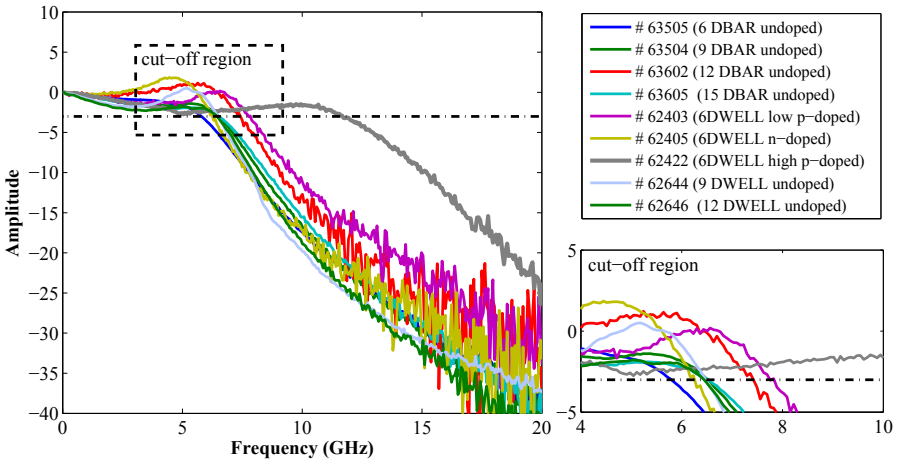

FIGURE 3.14: Small signal modulation response of a QDash lasers width various epitaxial structures for maximum possible 3 dB cut-off.

barriers significantly improves the modulation bandwidth of the devices. This behaviour of bandwidth p-doping in good agreement with [13, 62, 94, 95]. It is important to study the small signal characteristics of different designs, which are dealt in the following section on case by case basis.

Case of DBAR lasers

The bandwidths were measured for various DBAR structures as a function of number of stack layers at a fixed bias current. To study the impact of stacking layers, 4 devices having the same length (1000 μm) and the same ridge width (1.5 μm) are studied. A significant change in modulation response is not observed when the number of dash layers is increased from 6 to 15, the undoped-DBAR structures are nevertheless capable of modulation at frequencies in excess of 8 GHz as shown in Fig. 3.15. The damping of resonance frequency in these structures can be attributed to the device parasitics and the intrinsic response of the laser can be extracted using the band-width subtraction method described in [96]. One such extraction is presented in Fig. 3.16.

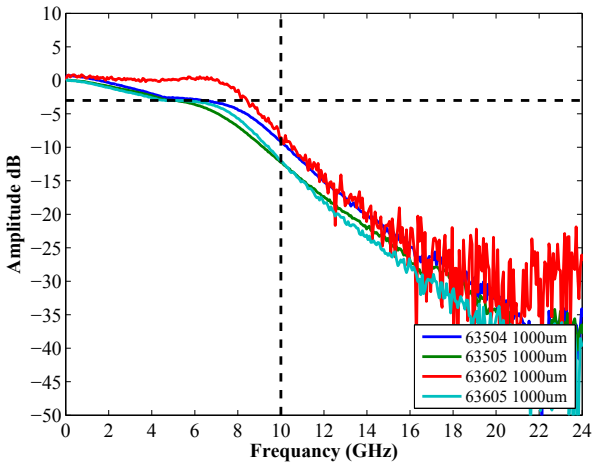

FIGURE 3.15: Small signal modulation of a dash in a barrier QDash lasers with different number of stack layers at around 100 mA bias current.

Even if the measured response of the laser leads to a degraded device performance, the intrinsic bandwidth is well beyond 10 GHz, which enforces the usefulness of QDash material system. The parasitic response is often related to the time constant given by $R_s C_p$, where C_p is the shunt capacitance arising from various technology related factors like metal-insulator-semiconductor (MIS) layer capacitance or due to the material itself like the reverse bias capacitance [93]. The series resistance R_s arises from the resistance due to the InP above and below the active layer. In the present case, both the series resistance and shunt capacitance were measured to be within acceptable limits for a BRS device. This behaviour of the laser modulation bandwidth can be attributed to the transport effects inherent to the QDash material.

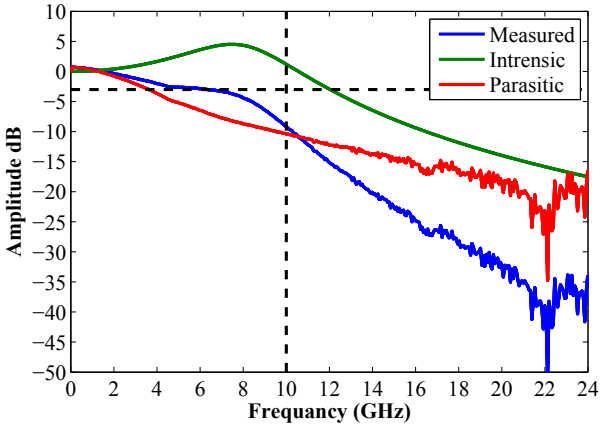

FIGURE 3.16: Extraction of intrinsic response of a DBAR lasers with 6 stack layers using the frequency response subtraction method.

Figure 3.16 shows that the relaxation oscillation frequency in case of DBAR suffers a large amount of damping. There are a number of mechanisms responsible for damping in resonance frequency such as spontaneous emission coupled to lasing mode [10], non-linearities due to spectral hole burning [97], spatial hole burning and related carrier diffusion[98]. These effects are generally accounted by the gain compression factor ϵ_{NL} [99]. The damping rate of the resonance frequency is given in Eq. 3.32. The damping rate depends on the rate of spontaneous emission R_{sp}, the carrier lifetime τ_c, and most importantly on the non-linear gain suppression factor ϵ_{NL}. It can be rearranged in terms of relaxation oscillation frequency Ω_R as follows

$$\Gamma_R = \Gamma_0 + K\Omega_R^2 \tag{3.46}$$

The damping offset $\Gamma_0 = 1/\tau_c$ is given by the damping rate at low frequencies (or in dc state) can be extracted by plotting the square of resonance frequency for each current values as shown in Fig. 3.17. The factor K is the phenomenological damping factor and is described as

$$K = \frac{4\pi^2}{v_g}\left(\frac{\epsilon_{NL}}{dg/dn} + \tau_p\right) \tag{3.47}$$

The K-facror is usually used to determine the maximum possible modulation bandwidth $f_{3\ dB}(max) = 2\pi\sqrt{2}/K$. A small K-factor would thus mean a large modulation bandwidth. The K-factor is only an indicative metric of the modulation bandwidth [100].

Wafer #	Stack #	$\Gamma_0 = 1/\tau_c$ (GHz)	K (ns)
63505	6	5.64	0.52
63504	9	5.92	0.42
63602	12	6.41	0.34
63605	15	6.73	0.33

TABLE 3.2: K-factors and damping offset for DBAR structures

The damping factor K is seen to systematically decrease with the number of dash layers, suggesting a high differential gain for higher number of dash layers. The K-factor however depends both on differential gain dg/dn and on non-linear gain compression and at the same time on the photon-cavity lifetime τ_p. The photon cavity lifetime is expected to decrease with increasing number of dash layers, as the cavity losses are expected to increase due to re-absorptions. In the present case, this phenomenon of re-absorption could be a reason behind the decrease of the K-factor. It should also be

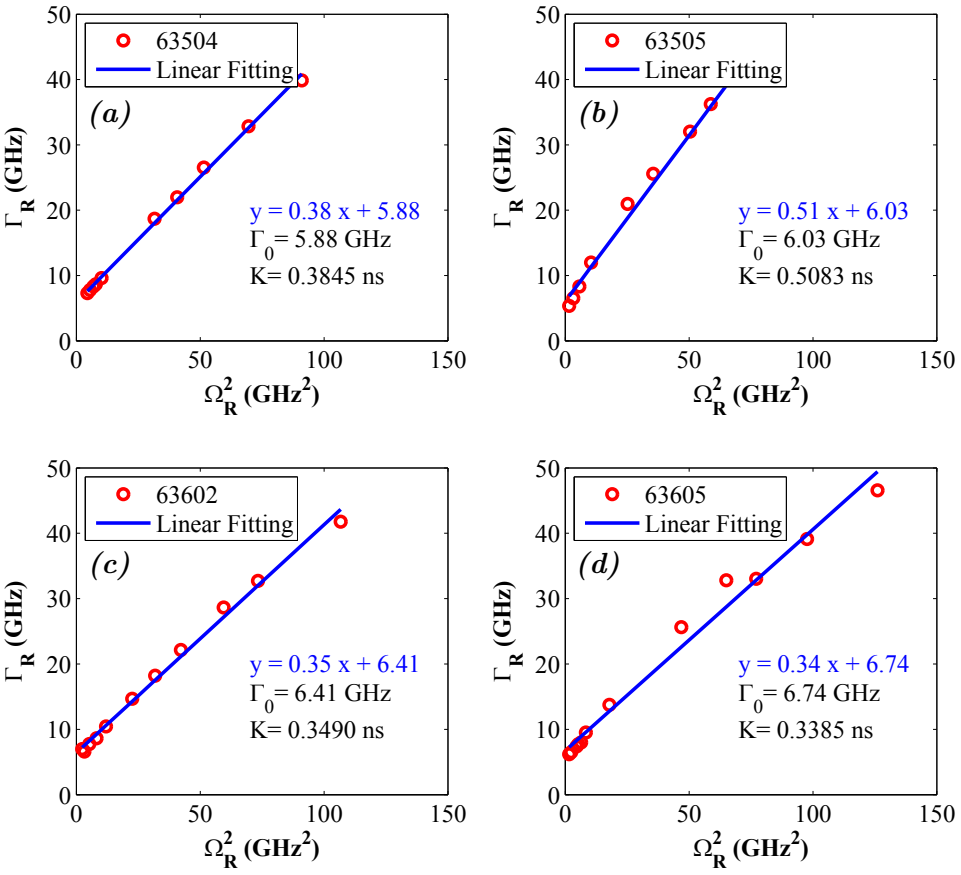

FIGURE 3.17: Damping rate Γ_R as a function of square of relaxation oscillation frequency Ω_R with extracted value of damping offset Γ_0 and damping factor K for 63505(6-BAR), 63504(9-DBAR), 63602(12-DBAR), 63605(15-DBAR)

noted that Eq 3.47 is valid only in the absence of carrier transport effects [100, 101]. The K-factor thus cannot be taken as a true metric of the dynamic response of the laser. The suppression in the amplitude of resonance peak (see Fig. 3.16) also indicates a high non-linear gain suppression, this is in agreement with measurements on other material systems [102]. Nevertheless, the relaxation oscillation frequency for DBAR structure is large and suggest fast carrier dynamics.

Case of DWELL lasers

The measured bandwidth is plotted for the case of DWELL lasers, also for varying number of dash layers from 4 to 12 dash layers and the damping offset and K-factor are extracted (see Table 3.3). The DWELL designs, irrespective of the number of dash

layers, show an almost constant damping factor K. At the same time the damping offset is also very small. The low K-factor indicates that these lasers would have higher relaxation oscillation frequency for large current values. Thus, DWELL lasers are expected to perform better than DBAR lasers in terms of modulation capability.

Wafer #	Stack #	Γ_0 (GHZ)	K (ns)
62400	4	3.48	0.40
62407	6	3.98	0.27
62644	9	4.78	0.27
62646	12	4.20	0.28

TABLE 3.3: K-factors and damping offset for DWELL structures

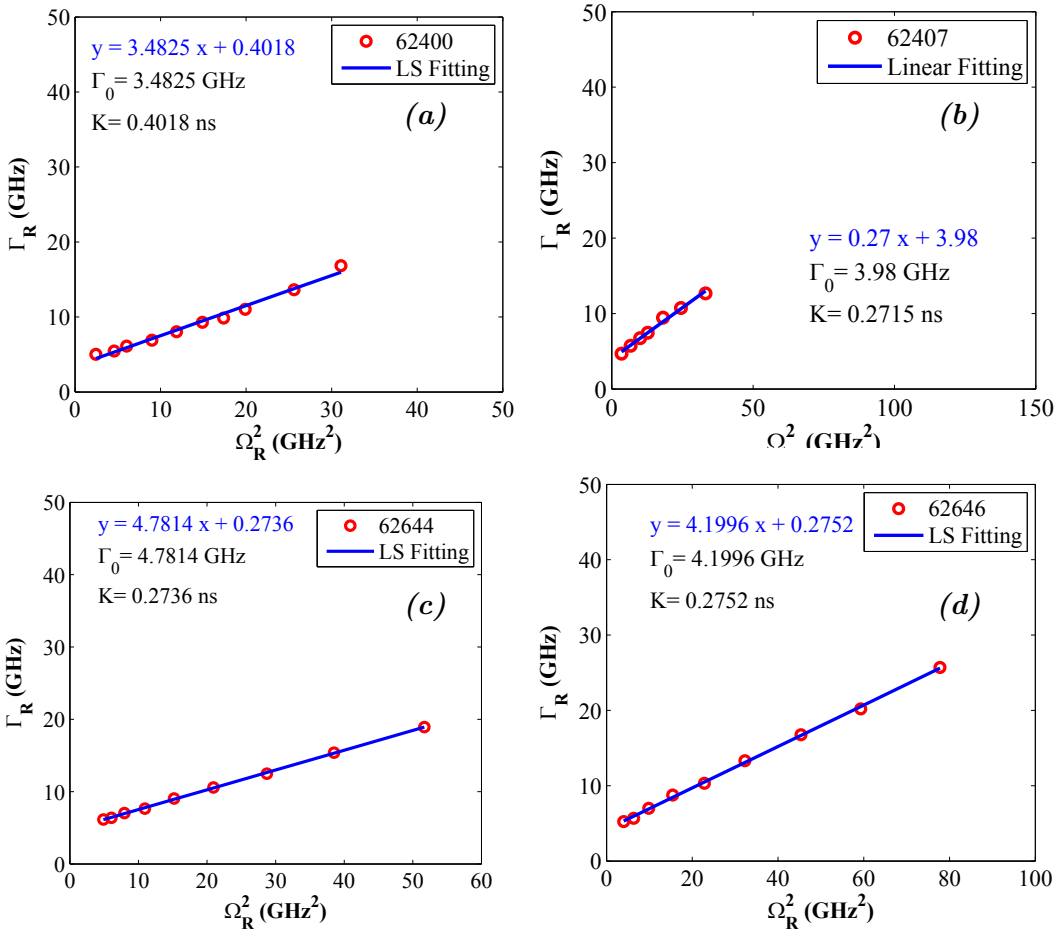

FIGURE 3.18: Damping rate Γ_R vs square of relaxation oscillation frequency Ω_R with extracted value of Damping offset Γ_0 and Damping factor K for 62400(4-DWELL), 62407(6-DWELL), 62644(9-DWELL), 62646(12-DWELL)

Case of doping variation

A p-doping in the barriers of the QDashes is known to improve the dynamic properties of these nano-structures [13, 62, 94, 95]. It is thus necessary to study the effect of p-doping on the K-factor. For this, various doping concentration in the barriers of DWELL structures with 6 dash layers in the active region are studied. The extracted K-factors are presented in Fig 3.19 and in Table 3.4.

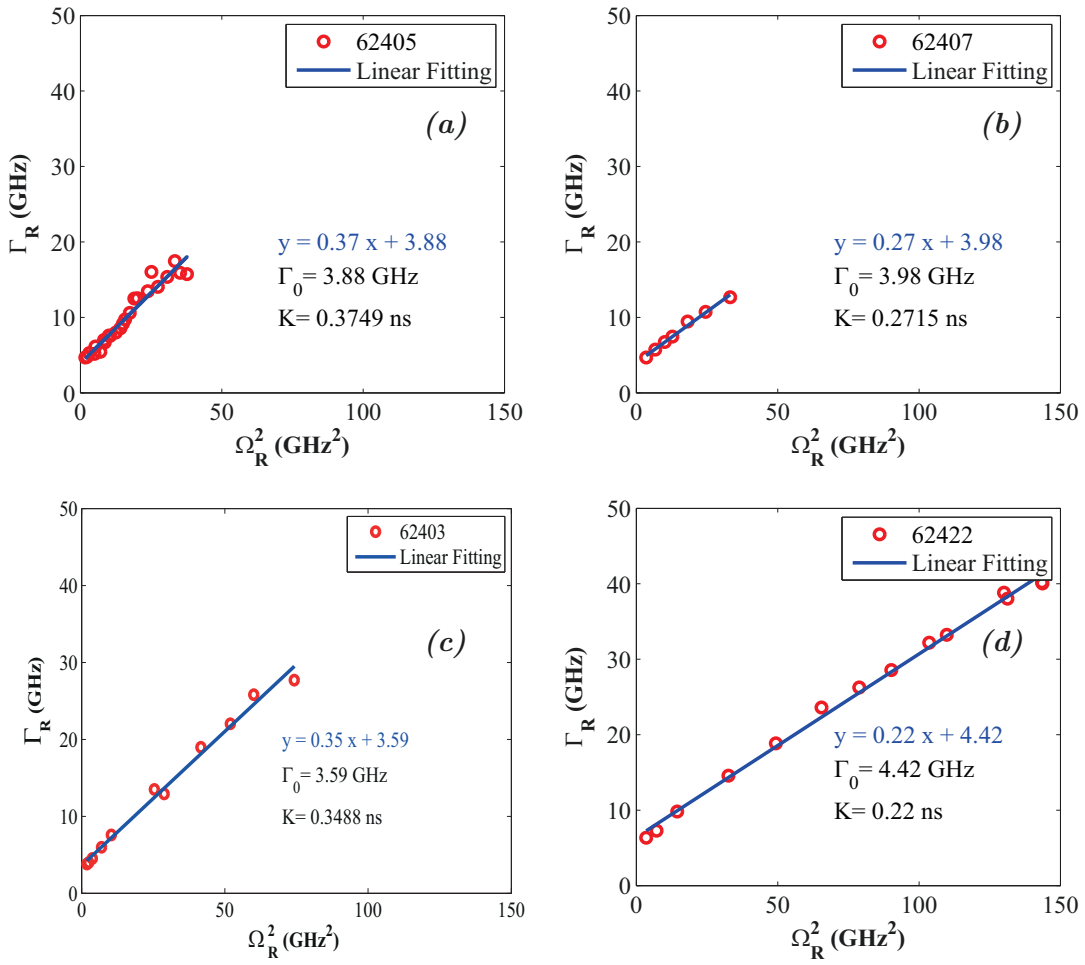

FIGURE 3.19: Damping rate Γ_R as a function of square of resonance frequency Ω_R with extracted value of damping offset Γ_0 and K-factor for DWELL structures with various doping levels.

The K-factor decreases for higher p-doping concentrations. This results is important to identify the best possible doping level for optimum performance of the laser device. The doping level is indeed decided based on a trade-off between optical losses and dynamic characteristics. A very high level of p-doping would also increase the laser threshold, which is not desirable for direct modulation of laser, as keeping the threshold

low is one of the objectives for directly modulated lasers. Another problem posed by very high doping is related to the diffusion of the dopants, (in this case Be). The diffusion of Be as p-dopant is not excellent due to its low mobility on the wafer surface during the growth. This would induce non-uniformity of dopants on the wafer surface, which is also not desirable. This can be solved using other dopant species such as carbon.

Nevertheless low K-factor values are promising for the measured structures. The best K-factor value of 0.22 ns is observed for the p-doped structure with a dopant concentration of 2×10^{-18} cm^{-2}. Thus this structure is expected to give high modulation bandwidths for high biasing currents.

Wafer #	Doping Type	Γ_0 (GHZ)	K (ns)
62405	Si-Doped	3.15	0.37
62407	un-Doped	3.98	0.27
62127	Be 2.5e+17	4.01	0.27
62406	Be 3e+17	4.41	0.26
62426	Be 6e+17	4.41	0.26
62403	Be 1e+18	4.61	0.29
62422	Be 2e+18	5.69	0.22

TABLE 3.4: K-factors and damping offset for various doping concentrations in DWELL structures with 6 dash layers

Case of p-doped DWELL

The modulation response of the specific structure with doping concentration of 2×10^{-18} cm^{-2} as a function of bias current is presented in Fig. 3.20. This particular structure shows a modulation bandwidth as high as 12 GHz, which is valuable for the device to operate in the 10 Gbps bit rate range. p-doped structures are in general expected to show a very large differential gain due to their improved dynamic characteristic.

3.4.2 Differential gain

The K-factor is a useful tool to make a rough estimate about the dynamic characteristics of the material but it is vastly considered an indicative parameters [100, 102]. As stated earlier Eq 3.47 is valid only in the absence of carrier transport effects [101]. The K-factor thus cannot be taken as a true metric of the dynamic response of the laser. The

Function	Material	No of Layers	Thickness	Total Thickness
Buffer	InP	1	1000	1000
SCH	InGaAsP 1.17	1	70	70
Barrier	InGaAsP 1.17	1	20	20
QWell	InGaAsP 1.45	6	3.5	21
QDash	InAs	6	1	6
QWell	InGaAsP 1.45	6	3.5	21
Barrier	InGaAsP 1.17	6	20	120
SCH	InGaAsP 1.17	1	20	20
Top	InP	1	100	100
Grating	InGaAsP 1.17	1	35	35
Top	InP	1	30	30

TABLE 3.5: Vertical structure of the active layer for the p-doped DWELL design.

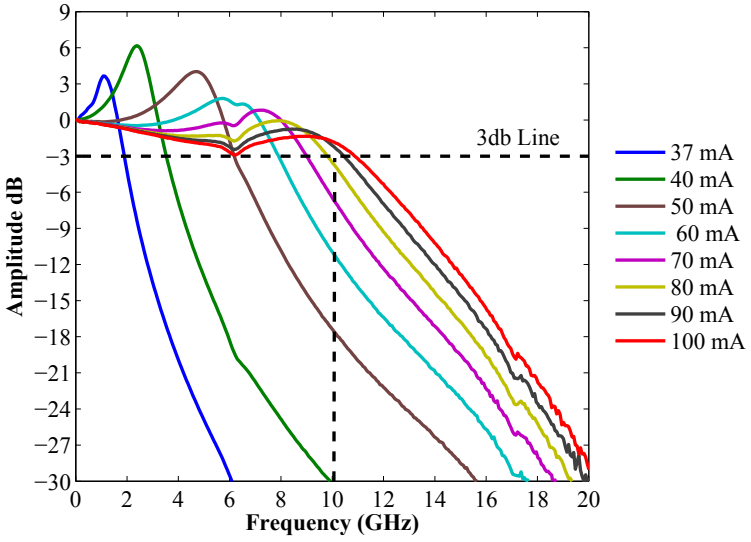

FIGURE 3.20: Small signal modulation of a QDash laser showing a -3 dB bandwidth of around 10 GHz at around 80 mA bias current.

differential gain or the gain cross section of the laser can be useful to measure the true potential of the laser in terms of modulation performance. Differential gain $dg(n,E)/dn$ at a photon energy E is defined as the derivative of bulk gain with respect to the carrier concentration. The differential gain can be extracted from the small signal modulation response of the lasers as it figures in the modulation response through the following expression

$$\Omega_R^2 = \frac{\Gamma \eta_i v_g}{4\pi^2 eV} \frac{dg}{dn}(I - I_{th}) \tag{3.48}$$

where Γ is the optical confinement factor, η_i is the internal quantum efficiency, v_g is the group velocity e is the electronic charge, V is the active volume of the laser and $I - I_{th}$

is the bias offset with respect to the threshold current I_{th}. The differential gain is given by the slope of the linear fit between Ω_R^2 vs $I - I_{th}$. Differential gains were extracted for DWELL structures with various doping levels and are presented in Fig. 3.21.

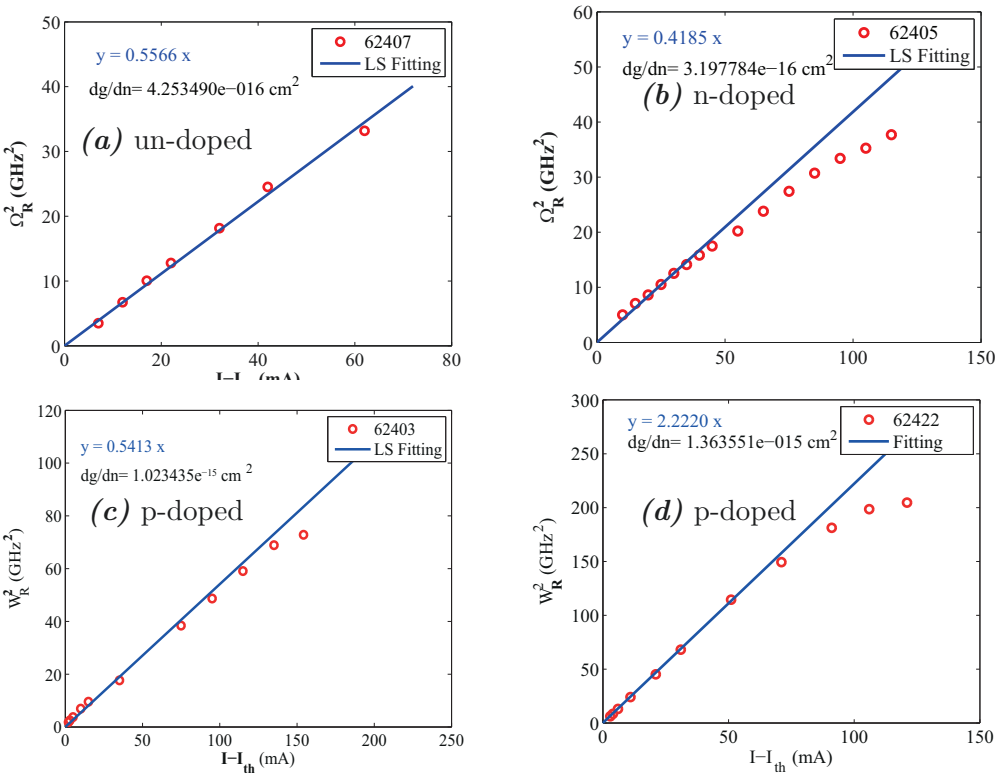

FIGURE 3.21: Square of resonance frequency Ω_R vs bias $I - I_{th}$ with extracted value of differential gain for various structures

A quantitative comparison between the differential gain of these structures can be made by comparing the slopes of the linear fitting between Ω_R^2 vs $(I - I_{th})$, where higher slopes mean a higher differential gain for the same active volume and similar confinement factor of the device. The differential gain of lasers increase as a function of doping concentration, being the least for n-doped and being the highest for p-doped structures as can be seen in Fig. 3.22. These extractions of differential gain produce a conclusive statement on the quality of modulation capacity of various QDash structures. It can be concluded from these measurements that the p-doped structure would prove to be the best solution for high speed modulation of QDash lasers. Henceforth this thesis will focus on this p-doped DWELL structures as long as directly modulated lasers are concerned.

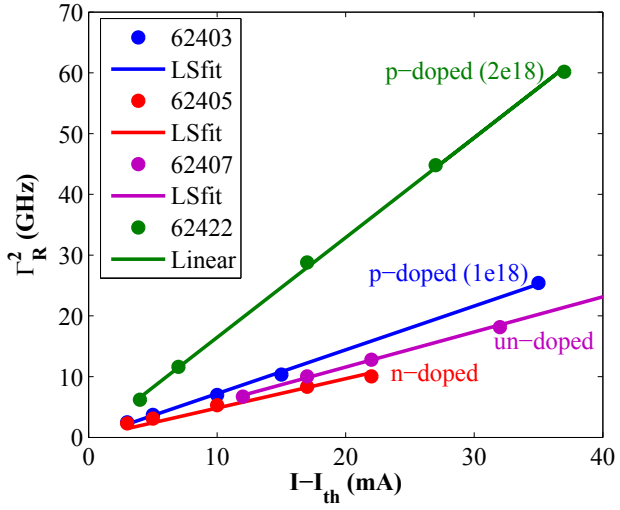

FIGURE 3.22: Square of resonance frequency Ω_R vs $I - I_{th}$ for different doping in barriers.

3.4.3 Small signal chirp (α_H-parameter)

The analysis of small signal modulation response, provides hints on the modulation bandwidth of the laser. The modulation bandwidth of the laser is a parameter which decides if the laser could be modulated at high bit rates. Transmission of the modulated signal through an optical channel is more complicated due to the frequency chirping in the laser. This frequency chirping limits the transmission due to the chromatic dispersion of the fibre. A decisive parameter for the laser transmission is α_H-parameter, also known as Henry factor or Linewidth Enhancement Factor (as discussed in Sec 3.1.3). The α_H-parameter is important as it acts as a factor enhancing the laser chirp (see Eq. 3.40). Thus it is fundamental to a study on directly modulated lasers, to evaluate the α_H-parameter and, to assess the transmission quality of the laser. A high α_H-parameter would lead to a higher chirp and consequently a dispersion limited transmission for a directly modulated laser. Several methods have been proposed to measure the α_H-parameter. These include

— ***Hakki-Paoli method*** [103]: The Hakki Pauli method relies on direct measurement of the refractive index change (measured by the frequency shift of longitudinal Fabry–Perot mode) and the gain as the carrier density is varied by slightly changing the current of a laser below–threshold. This technique only gives the value of α_H-parameter below the laser threshold. The quantity of interest is the α_H-parameter above threshold which varies greatly below and above threshold current of the laser.

— ***Fiber Transfer Function method***: This method exploits the interaction between the chirp of a high–frequency modulated laser and the chromatic dispersion of an optical fiber, which produces a series of minima in the amplitude transfer function vs. modulation frequency. By fitting the measured transfer function, the α_H-parameter can be retrieved [104].

— ***Using High Resolution OSA***[105]: Measurement using a high-resolution optical spectrum analyzer (OSA) have also be used recently to make a direct measurement of the optical line-width of a laser under modulation. These measurements are often limited by the resolution of the OSA.

— ***Optical self-locking method*** [106] is based on the relation between the upper and lower bounds of the locked and unlocked regimes when the detuning between a pump and slave lasers is plotted as a function of the injection power.

— ***Optical feedback self-mixing effect*** [107]: The mixing of the returned and the lasing fields generates a modulation of the optical output power in the form of an interferometric waveform, with a shape that depends on the optical feedback strength and the α_H-parameter, according to the Lang-Kobayashi theory. It had been shown by Yanguang et al [107] that the value of α_H-parameter can be retrieved from a simple measurement of two characteristic time intervals of the interferometric waveform.

— ***Fourier series expansion method*** [108] Fourier series expansion (FSE) method can be used to calculate alpha by first finding the round trip gain. By performing a Fourier series expansion on each longitudinal mode in the cavity and finding the ratio of two successive Fourier coefficients.

— ***The FM/AM method*** [109] relies on high–frequency modulation of laser which generates both amplitude (AM) and optical frequency (FM) modulation. The ratio of the FM over AM gives a direct measurement of the α_H-parameter.

Other techniques including injection-locking technique [110] and modified direct frequency-modulation method [111] etc. . . have been frequently used in literature. In the present study two techniques were used. Firstly, the α_H-parameter above threshold is measured using the FM-AM method as α_H above threshold is important for practical applications. Secondly, the alpha parameter is measured using Hakki-Pauli method to observe behaviour of α_H below threshold. For QDashes α_H below threshold have been shown to have near-zero values [112–115] and thus is it interesting to compare the alpha below

threshold with the results in the literature.

The α_H parameter was measured for various devices with different lengths for p-doped structures using the AM/FM method described in [109]. In this method the characteristics of the frequency modulation induced by the modulation of electrical carrier in the laser cavity is evaluated. The experimental arrangement for this measurement is presented in Fig. 3.23. The signal at the output of the laser is analysed through a tunable MZ interferometer. The free-spectral range (FSR), of the MZ can be tuned by changing the delay between the two arms, the FSR being the inverse of the differential delay between the two arms. A polarization controller makes sure that the two signals at the input of the second coupler have parallel polarisation states. The optical path difference between the two arms is accurately controlled using a piezoelectric transducer. The transducer located onto one of the MZ's arms is directly controlled by an external locking circuit. For instance, points A and B (see inset Fig. 3.23) being in opposition, they correspond to two signals interfering in quadrature with each other. The interferometer characteristics are around these two points, linear and the photo-current coming out from the photo-detector is proportional to the phase (or frequency) variations of the optical signal to be analysed.

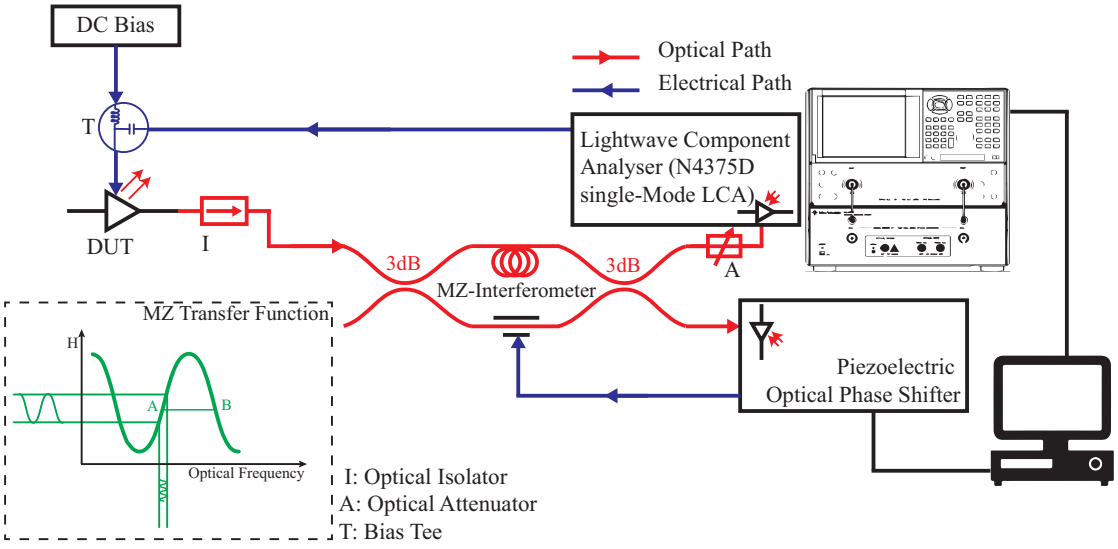

FIGURE 3.23: Schematics of test bench for measurement of α_H-parameter using a MZ-modulator.

If M_+ is the output at the network analyser at point A and M_- is the output at point B, then

$$\frac{2\beta}{m} = \frac{1}{\tan\left(\frac{\pi f_m}{FSR}\right)} \left| \frac{M_+ - M_-}{M_+ + M_-} \right| \tag{3.49}$$

where f_m is the frequency of the electrical signal provided by the network analyser, FSR is the free spectral range of the MZ interferometer, β is the modulation rate in frequency. The α_H-parameter can then be determined using the relationship of the form [116]

$$\alpha_H = \frac{2\beta}{m}\sqrt{1 + \left(\frac{f_c}{f_m}\right)^2} \tag{3.50}$$

where f_c is the corner frequency. It can be seen from Eq. 3.50 that when $f_m >> f_c$, α_H is directly given by

$$\alpha_H = \frac{2\beta}{m} = \frac{1}{\tan\left(\frac{\pi f_m}{FSR}\right)} \left| \frac{M_+ - M_-}{M_+ + M_-} \right| \tag{3.51}$$

α_H can thus be extracted from the ratio of AM and FM components as shown in Fig. 3.24.

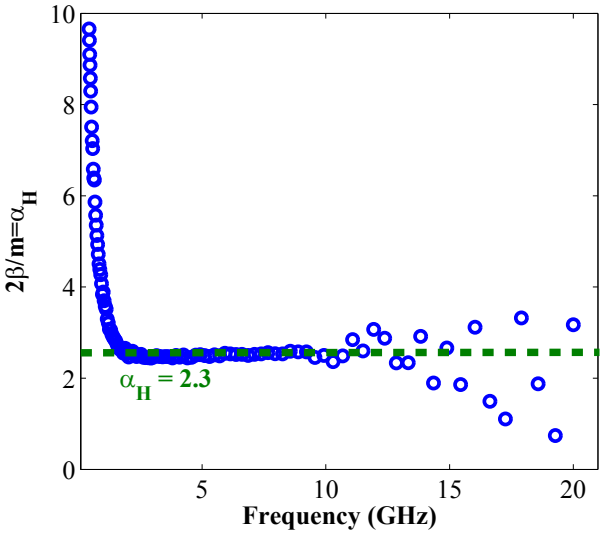

FIGURE 3.24: The extracted value of $\frac{2\beta}{m}$ as a function of the modulated frequency. The value of α_H-parameter is shown by the green dashed line.

Various DFB designs were fabricated to assess the effect of coupling co-efficient on the α_H-parameter for the p-doped structure. These designs are presented in Fig. 3.25. The decrease in the coupling coefficient results in increasing α_H. The exact mechanism and relations which affect the α_H-parameter with variation in coupling co-efficient need to be studied in details. This could be attributed to the fact the DFB with higher coupling

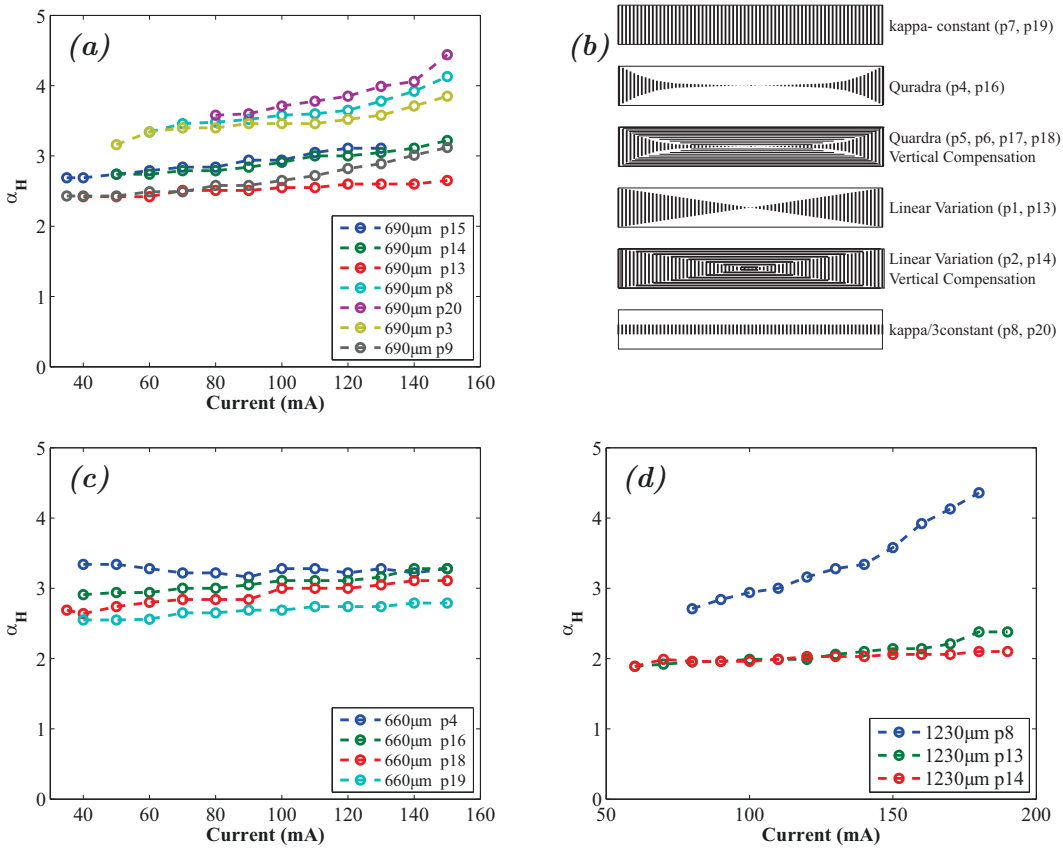

FIGURE 3.25: α_H-parameter measured for various DFB designs (a) for a length of 690μm (c) for 690μm (d) for 1230μm. (b) shows the different DFB structures evaluated.

co-efficients would generate higher gain for the same number of injected carriers and thus result in lower α_H, in agreement with Eq. 3.37.

The α_H-parameter for QDash structures is nevertheless seen to be considerably lower than for the conventional material. These low values of α_H-parameters are very promising and valuable for optical transmission. α_H-parameters was also measured for these chips at high temperatures up to 65°C as presented in Fig 3.26. The stability of α_H-parameters with bias current and with temperature is noticeable. α_H remains nearly constant with the bias currents for p-doped samples at low temperatures, suggesting an unsaturated behaviour of QDashes when the barriers are p-doped [117] and also suggest an ultra-fast carrier transport as expected by the QDashes.

α_H-parameter using Hakki Pauli Method α_H-parameters is also measured using the Hakki-Pauli to estimate the α_H-parameter below threshold of a 1000 μm long laser. An extraction for a negative detuning is presented in Fig. 3.27. It can be noted

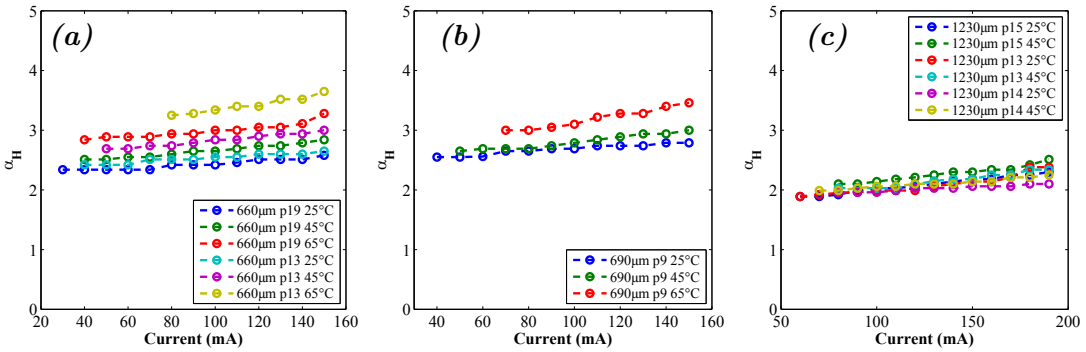

FIGURE 3.26: α_H-parameter measured at higher temperatures for lasers of similar lengths

from Fig. 3.27(a), that the extraction of α_H-parameter below threshold depends on accurate measurements of wavelength shift and gain due to change in carrier density. The measurement of gain is not affected by the injection current and can be easily measured accurately. The wavelength shift measured should be only due to carrier induced refractive index change. This carrier induced index change results in a blue shift of the wavelength. The wavelength also changes as the injection current is increased due to the heating of the device, causing a red-shift. These two effects contributing to the change in wavelength have to be decorrelated before anything can be concluded on the α_H-parameter. There are two ways to compensate for the heating effects in the laser. A first method is to use a pulsed injection with a very low duty cycle to allow enough cooling time for the device between the injected pulses. The second method is to compensate the heating effect by calculating the wavelength shift above threshold. The wavelength shift above threshold is expected to be mainly due to heating effects as the carrier density is clamped above the threshold.

Measurement were also performed with continuous injection current and compensation for device heating and were found to be consistent with the results obtained using the pulsed current method. These extractions were performed for various wavelength detunings in the optical spectrum, and the results are presented in Fig. 3.28.

The value obtained from measurements above and below the threshold current are found to be consistent. This is intrinsic to the nature of Qdash material, which show similar values of α_H-parameters above and below threshold, and had been theoretically studied in [117]. This is a valuable result as it indicates that p-doped QDashes show an unsaturated behaviour. This is understood by the fact that the p-doping results in DoS

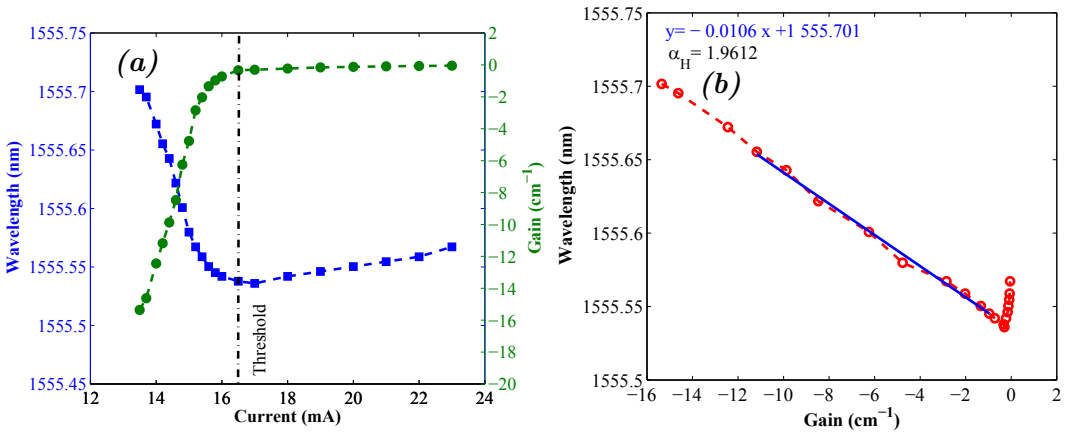

FIGURE 3.27: (a) The gain and wavelength as a function of the bias current of the laser for a 1000 μm long cavity for a negative detuning of 10 nm from the gain peak using 10% duty cycle pulsed current injection. (b) Gain vs wavelength and extracted α_H-parameter.

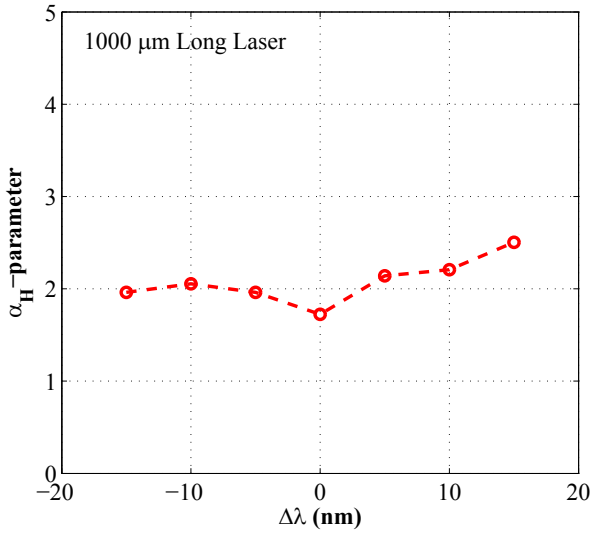

FIGURE 3.28: α_H-parameters measured using Hakki Pauli method for a 1000 μm long cavity for various detunings from the gain peak.

narrowing effect, meaning that the carrier population in the barrier and wetting layer levels is eliminated considerably. The p-doping of QDashes thus makes them behave like QDs. The increase in concentration of the dopant species will still result in improved carrier dynamic behaviour, however it will degrade the static characteristics like material gain. Thus, there is a trade-off between the static and dynamic laser characteristics related to the dopant concentration.

3.4.4 Large signal chirp

The chirp under small signal modulation is valuable for predicting the chirp behaviour of the laser but it is not necessarily valid under practical conditions due to the small signal approximation. This is because of the dependence of laser chirp on modulation index m (see Eq. 3.50). In practical conditions for transmission the modulation index is large ($m > 1$). Thus it is important to measure the value of the laser frequency chirp under large signal conditions.

The large signal chirp measurement is also based on the AM/FM separation method originally developed by Saunders et al [118, 119]. The experimental setup is presented in Fig. 3.29 is similar to that used for α_H-parameter with the difference that the electrical source is replaced with a large signal pulse pattern generator and the output is analysed using a digital oscilloscope. The frequency deviations due to chirp are

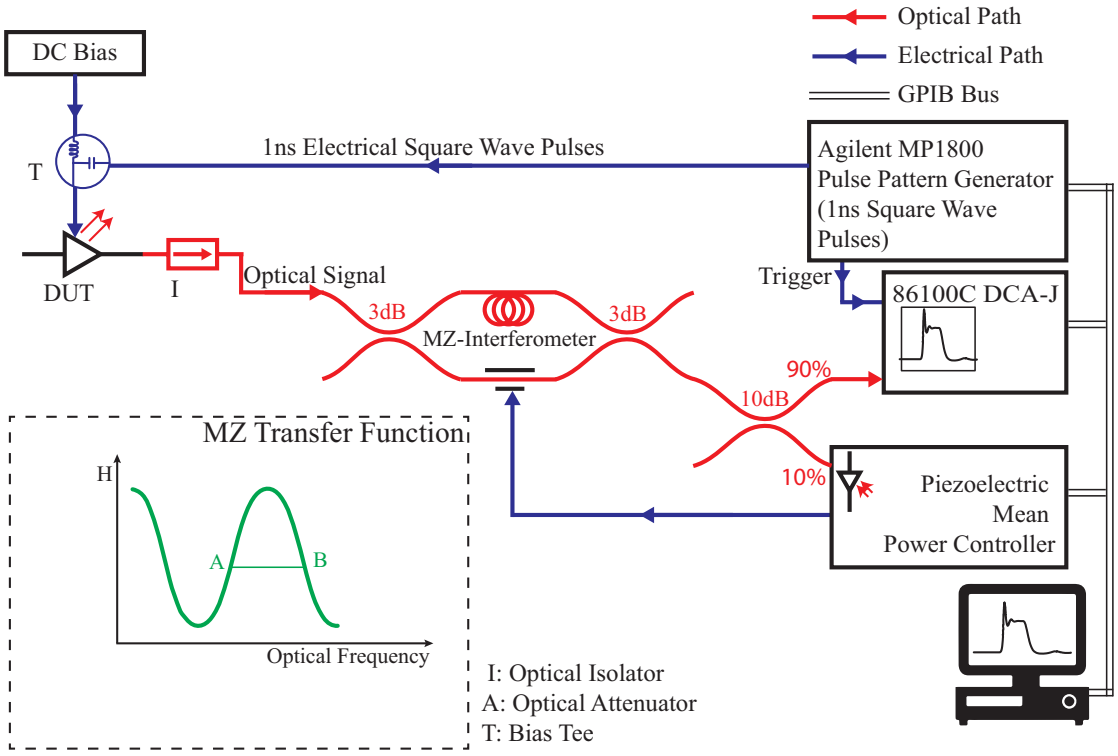

FIGURE 3.29: Schematics of test bench for measurement of α_H-parameter using a MZ-modulator.

measured using a MZ-Interferometer as an optical discriminator. The mean power at the output of the MZ is maintained using a piezoelectric controller by controlling the relative phase between the two arms of the MZ. The laser wavelength is then tuned to A on the MZ (see inset Fig. 3.29), which is on the positive slope of the MZ transfer

function. At this point any frequency deviations would result in a change in intensity and the time resolved data at this point would result in AM component (V_{AM}) plus the FM component (V_{FM}). Similarly, when the laser is placed on the negative slope, the time resolve data results in in an AM component (V_{AM}) minus the FM component (V_{FM}).

$$V_A = V_{AM} + V_{FM} \tag{3.52}$$

$$V_B = V_{AM} - V_{FM} \tag{3.53}$$

If the free spectral range of the MZ is larger than the modulated spectrum of the source, then the large signal chirp is given by

$$\Delta\nu = \frac{1}{2\pi}(FSR)\sin^{-1}\left(\frac{V_{FM}}{V_{AM}}\right) = \frac{1}{2\pi}(FSR)\sin^{-1}\left(\frac{V_A - V_B}{V_A + V_B}\right) \tag{3.54}$$

The large signal chirp induced by the modulation of injected current by 1 ns long square pulses was characterized using the method described above. The output at the MZ gives the time-resolved amplitude and frequency response. The frequency chirp is presented in Fig. 3.30. The value of transient chirp (ν_T) can be extracted by measuring the first ripple in the time domain response of optical frequency, shown in Fig. 3.30 in red. Similarly the Adiabatic chirp (ν_A), which is difference in frequency between the '0-bit' level and the '1-bit' level can be extracted by measuring the difference in frequency between these levels marked with green dotted line in Fig. 3.30. This is not a universal metric for the measurement of laser chirp, however this methods gives a rough chirp estimate of the particular laser under test. It should be noted here that the time resolved measurements also give information on positions of the 0-bit and 1-bit. The 0-bit is slightly red shifted as compared to 1-bit suggesting a positive chirp parameter.

As stated previously, it is essential to extract the chirp for various values of modulation depths as it gives a useful measure of the modulation response of the semiconductor laser. The values of adiabatic and transient chirps were thus extracted for various devices at a constant bias current of 100 mA with varying modulation depths. These are presented in Fig. 3.31. Both the transient chirp and adiabatic chirp increase with modulation depth. The lasers with low transient chirps are expected to show better transmission performances, this can be achieved only at low modulation depths, which also decreases the dynamic extinction ratio.

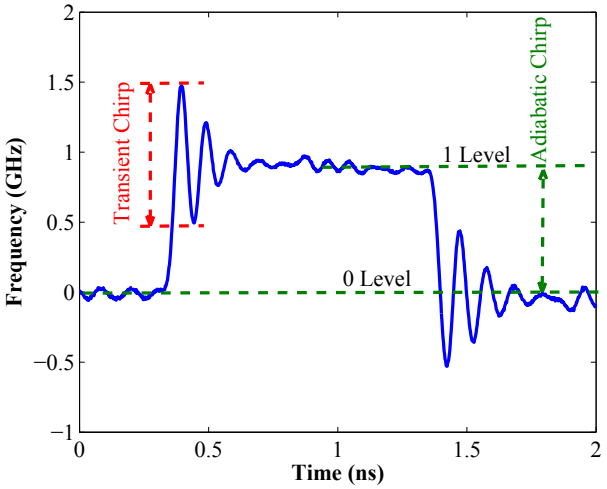

FIGURE 3.30: Time-resolved chirp measurements showing the transient chirp (in red) and adiabatic chirp (in green) for a p-doped QDash laser at 80 mA

The transient and adiabatic chirps are also measured for a constant extinction ratio of 3 dB at various biasing points. The value of 3 dB extinction ratio is chosen as a nominal value for a good transmission quality in the present study. This measurement actually helps to determine the correct operating points for transmission experiments.

The two extractions, as stated above give complete chirp information of the devices under consideration. The value of transient chips is of special importance, as it plays a vital role in transmission and cannot be controlled using any spectral filtering devices. It can be noticed that the adiabatic chirp ν_A increases with both biasing current and modulating voltage. The increase in ν_A is generally much stronger with the bias current and compared to its increase with modulating voltage. The transient chirp ν_T on the other hand only increases with modulating voltage and remains constant or decreases with increasing bias current. This is very logical as the transient behaviour of the laser occurs in a region where the power changes rapidly with the current. Thus, it would be convenient to choose a biasing point which is higher in current to avoid the effect of transient chirp. At higher biasing currents the adiabatic chirp would limit the transmission distance due to the fibre dispersion. Using these two measurements, its is possible to categorise the DFB devices into three different categories on the basis of measured transient chirp. These are

1. ***Lasers with very high chirp***: Notably the lasers with high length-coupling(κL) coefficient product show a very high transient chirp. This can be understood from Eq 3.41. The high coupling coefficient helps to produce a large change in

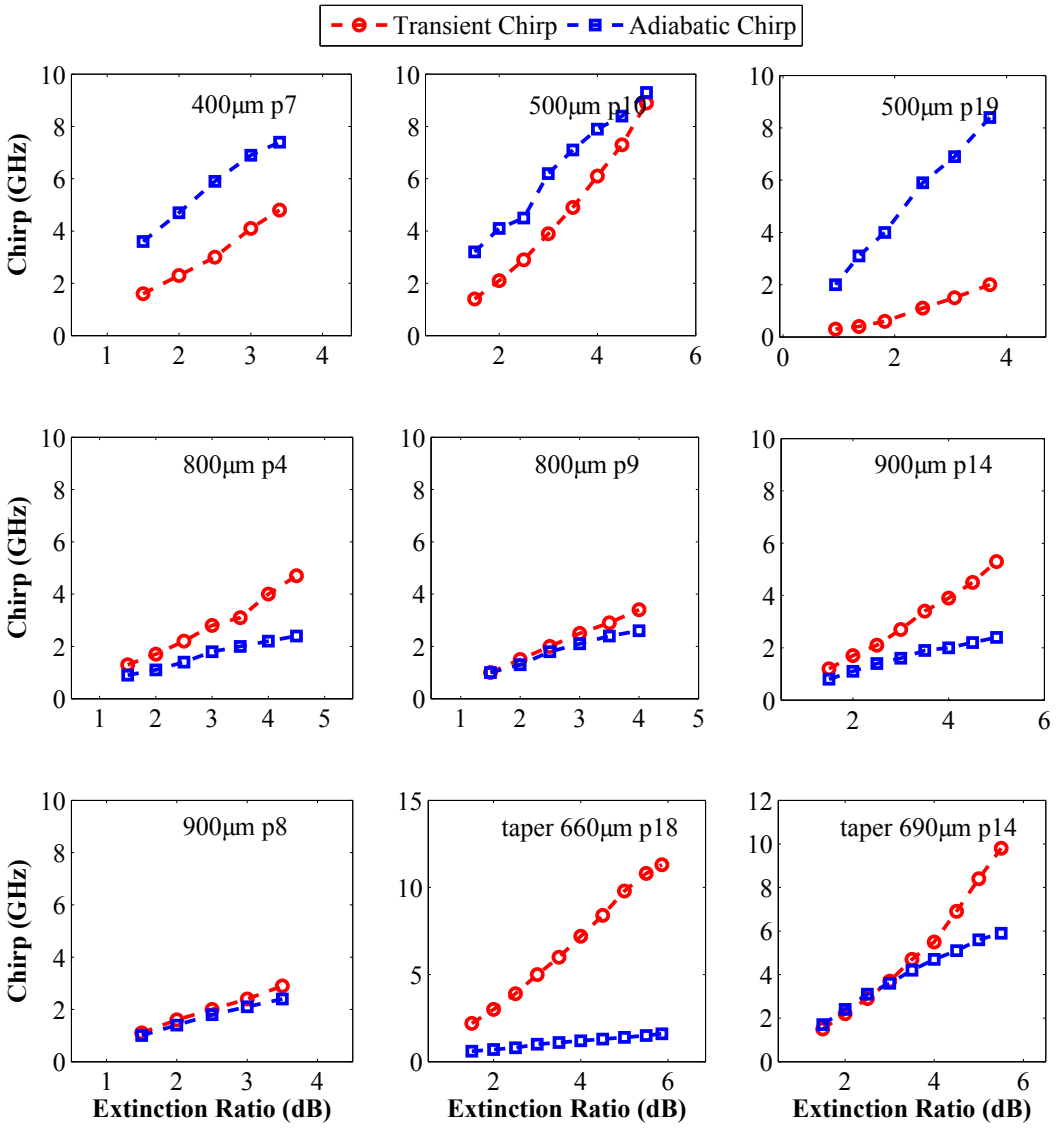

FIGURE 3.31: Extracted chirp values vs dynamic extinction ratios for various DFB lasers. The DER is increased here by increasing the modulation depth and the bias is kept constant at 100mA.

power in a short time, inducing a large transient chirp. These lasers are not expected to show transmissions to very short distances ($0 - 15\ km$).

Lasers with intermediate chirp: The lasers with the intermediate value of κL will consequently produce a low transient chirp and the chirp limits the transmission distances between $0 - 25\ km$.

Lasers with very low chirp: Some chips can be observed to show a very low chirp (in the range of 1-2 GHz). These lasers are expected to show transmission in distance ranges of 0-65 km.

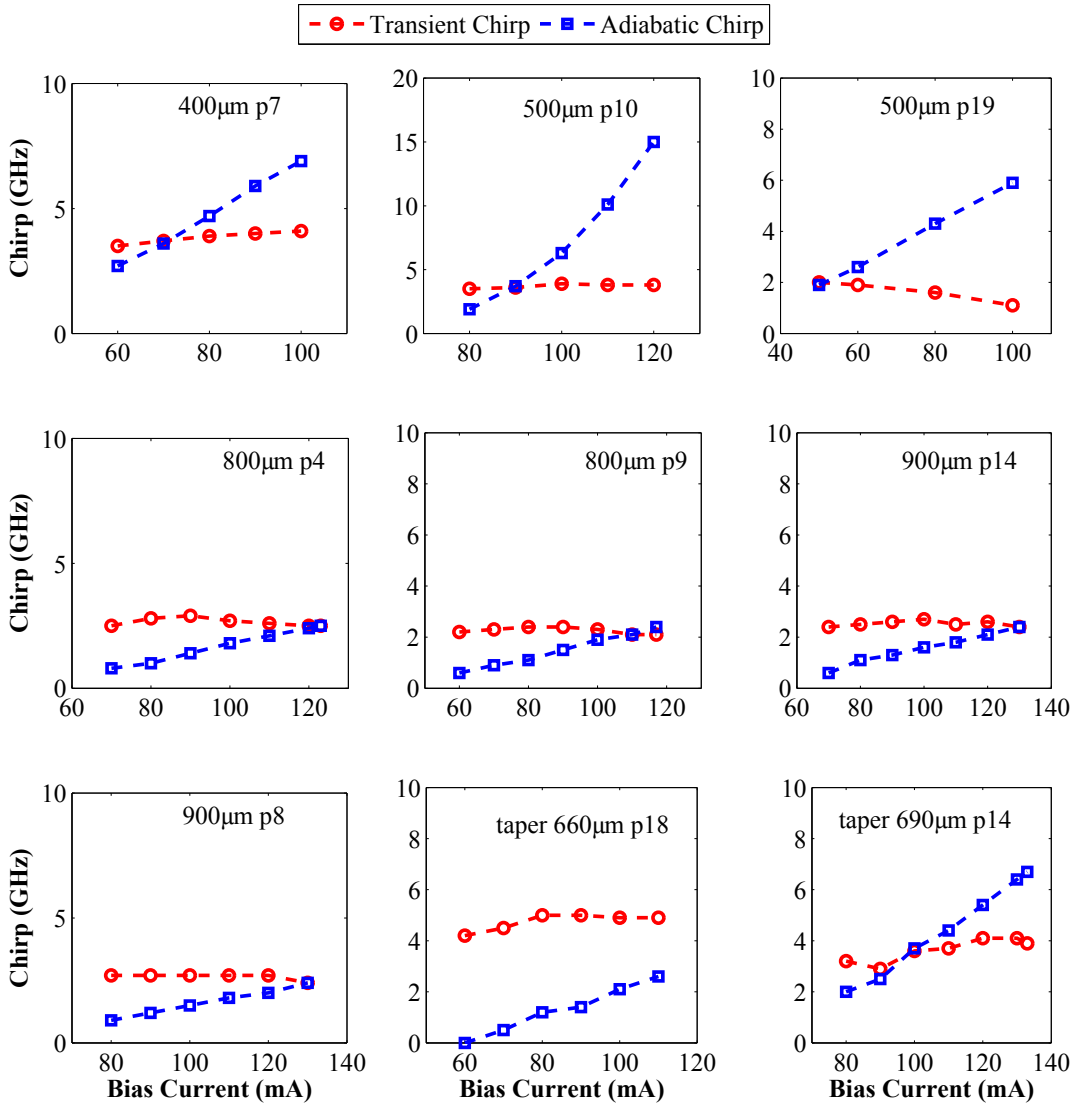

FIGURE 3.32: Extracted chirp values vs biasing current for various DFB lasers. The DER is kept constant at 3 dB.

It is worthwhile to note here that the measurement of α_H-parameter for these lasers yield similar values (in the range of 2-3 GHz). The chirps were extremely different for various DFB designs, and specially for the lasers with mode shape converters. This is because the laser chirp also depends on the laser geometry in addition to other factors. The large signal chirp behaviour of the semiconductor lasers is a device dependent parameter as opposed to the α_H-parameter which depends more on the active material.

Case of laser with active mode shape converters

As stated previously while evaluating the static characteristics of these lasers, the lasers with mode shape converters show a very narrow divergence and thus help in coupling a large amount of power into the fibre. It is noted from the measurements on frequency chirp, that the lasers with a mode-shape-converters show an enormously large chirp, specially the transient chirp irrespective of the DFB design. This behaviour can be attributed to two phenomena

— The active Region in the Mode Shape Converter is not properly injected with carriers.

— The tapers induce a very high power in a small region of the laser inducing a high transient chirp due to power variation.

Thus, it is necessary to make these mode shape converters passive in order to achieve high power in the optical fibre, and simultaneously maintain low chirp.

3.5 Transmission performance of quantum dash directly modulated lasers

The high-modulation bandwidth, low α_H-parameter and low chirp of the QDash lasers make these lasers excellent candidates for optical transmission devices. To assess the transmission quality of these devices, they were subjected to transmission test bench presented in Fig. 3.33. For this measurement the device under test (DUT) is biased with a bias point selected from the large signal chirp measurements. The electrical data, from a pulse patten generator is transferred to the laser, using a bias tee. The optical data from laser is then transmitted to an optical switch which can then be used to divert the optical signal to a Digital Communication analyser (Agilent DCA-81600C) to record the optical eyes or to an attenuator, which then transfer the attenuated signal for error detection.

A standard 10 Gbps nonreturn-to-zero (NRZ) laser modulation is realized with a pseudorandom binary sequence (PRBS) generator emitting $2^{31}-1$ long words. The power launched into the fibre is maintained to +3 dBm in order to minimize the non-linear effects. The transmitted NRZ signal is sent to an APD receiver before error detection.

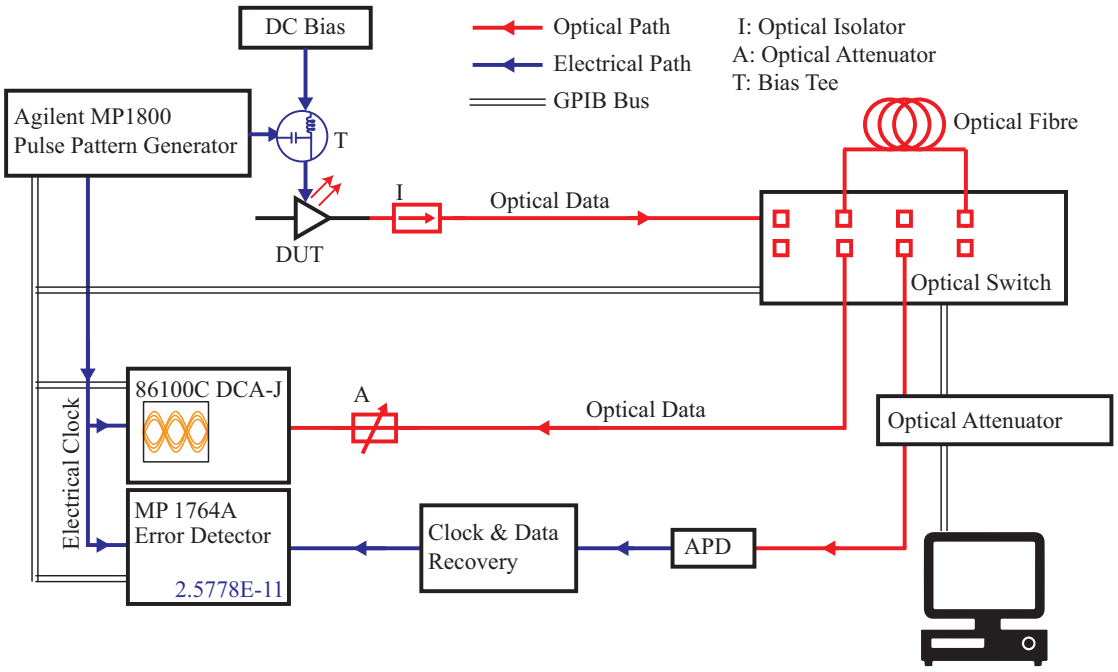

FIGURE 3.33: Schematics of test bench for measurement of bit error rates and analysis of eye diagrams.

Biasing current and peak-to-peak modulation current are chosen to optimize the transmission to a maximum possible distance in a standard single mode fibre (SSMF) and these conditions are kept constant for other transmission distances. Keeping the biasing condition constant makes sure that the chirp parameters are the same for the all distances. It is thus suitable to choose the chirp parameters for the longest possible distance.

3.5.1 Case of lasers with active tapers

It had been seen that the lasers with active tapers show a very large transient chirp (see Fig. 3.31 and 3.32). Bit error ratios are measured for the DFB laser devices under direct modulation are presented in Fig. 3.34.

As had been states earlier, that the large transient chirp of these lasers would limit the transmission using these lasers to very small distances. It is very evident from the BER tests on these lasers that they indeed cannot perform for distances greater than 15 km, even after careful adjustment of the biasing conditions. Also the eye patterns show they impact of transient chirp.

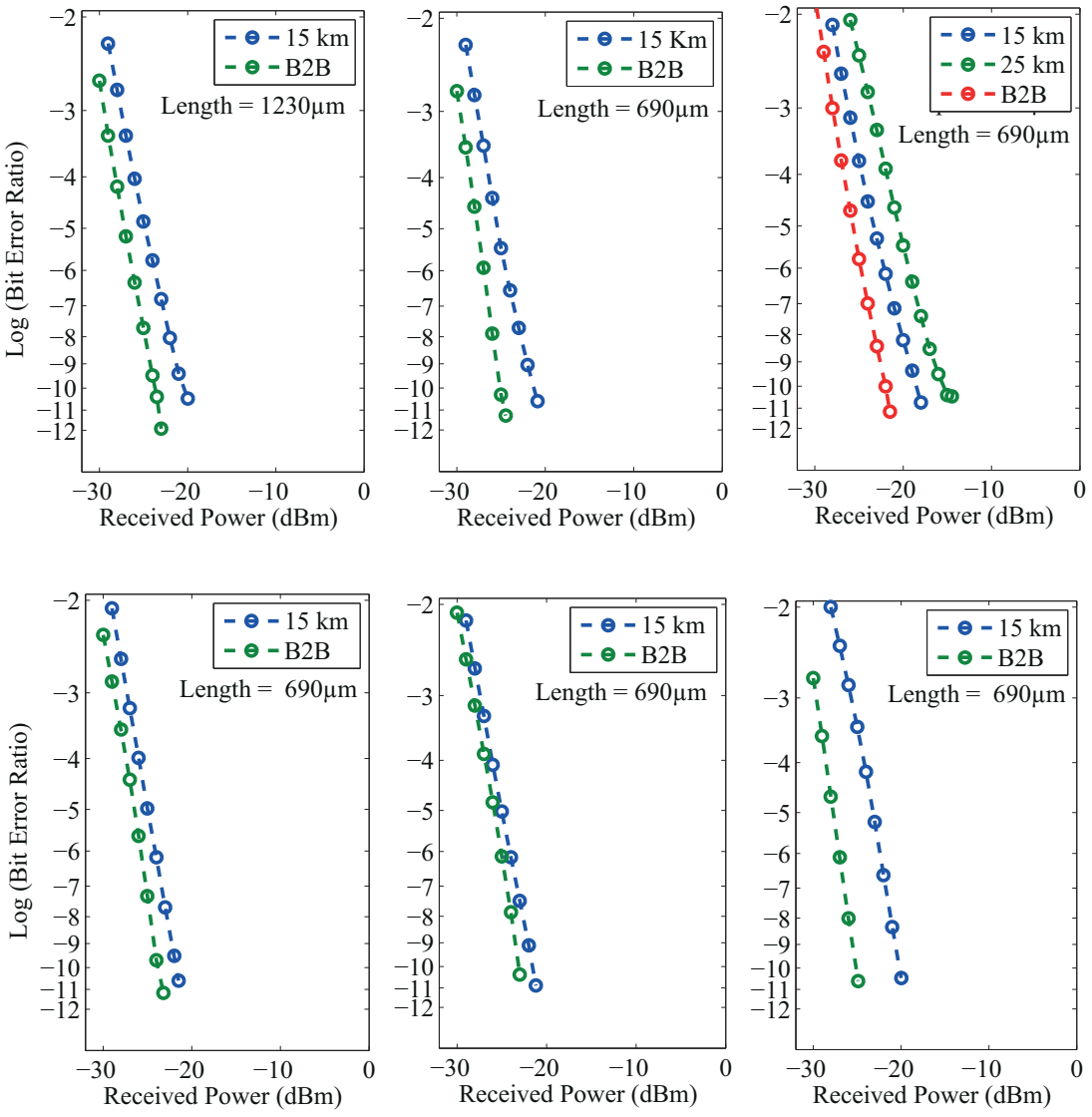

FIGURE 3.34: A standard 10 Gbps transmission using a $\lambda/4$-phase shifted DFB having active mode shape converters

3.5.2 Case of lasers without tapers

The lasers without tapers were also tested on BER test bench. These laser can effectively be categorised in three transmission ranges as was done with chirp. The lasers with large chirp which do not show transmissions above 15 km, secondly the lasers showing transmission in range of 0-25 km, and finally the lasers with very small chirp which show transmission ranges beyond 50 km. If the two chirp components (adiabatic and transient) of the lasers are compared with these measurements, the impact of transient

chirp clearly seen to be a determining factor for the optical transmission. The transmission is seen to be limited even if the adiabatic chirp is small as shown in Fig. 3.39.

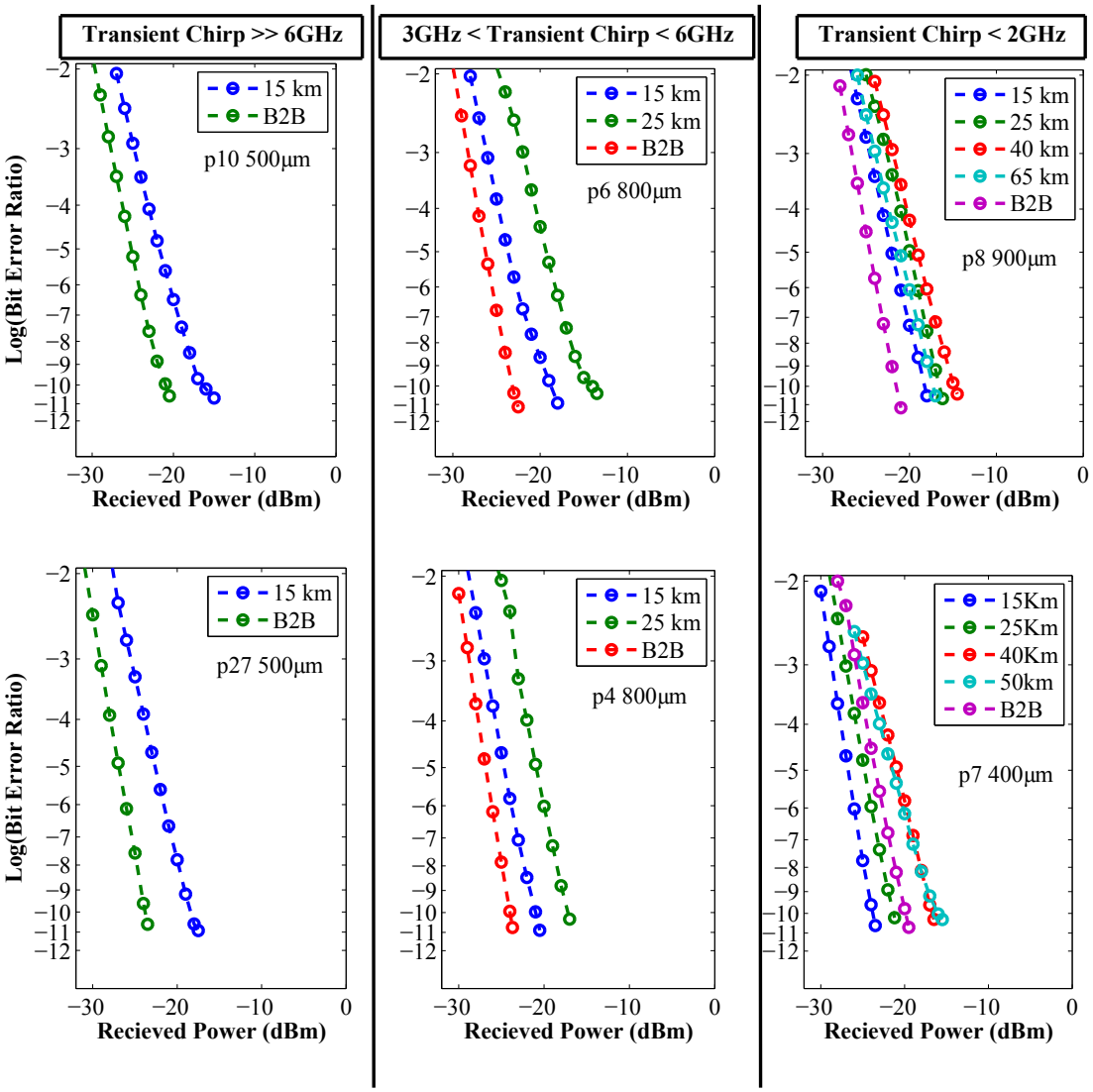

FIGURE 3.35: A standard 10Gbps transmission using a $\lambda/4$-phase shifted DFB for lasers with different transient chirps.

3.5.3 Case of lasers with ultra-low chirp

The bit error ratio and the eye diagrams for a low chirp laser for transmission through a SSMF is presented in Fig. 3.36 for fibre lengths from 0 to 100 km. The low chirp of the laser allows the transmissions in ranges from 0 to 100 km, at constant biasing condition with low penalty. The Dynamic Extinction Ratio (DER) remains considerably low($<<$ 3 dB). The distortion in eye diagram can specifically be noticed for

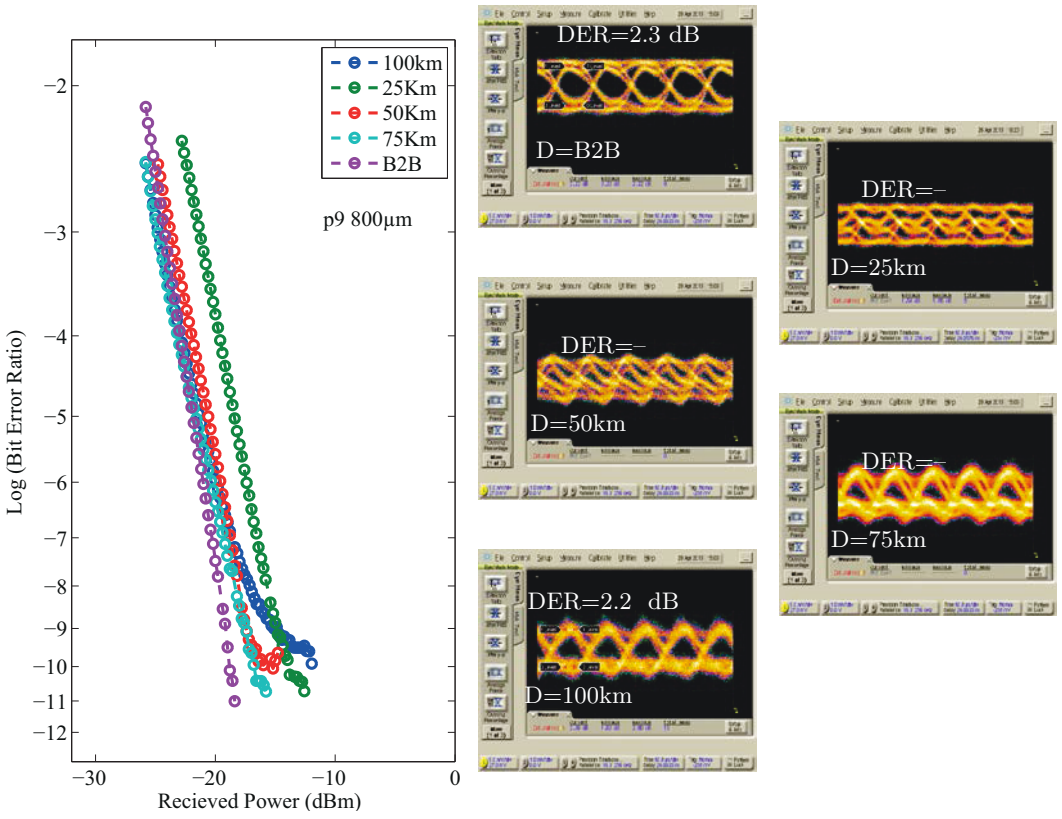

FIGURE 3.36: A standard 10Gbps transmission using a $\lambda/4$-phase shifted DFB with p-doped QDash as active material showing transmission up to 100 km

the distances after 25 km, where the eye diagram appears to be completely closed. This can be related to the interaction of the laser chirp with the dispersion of the SSMF ($\approx$ 17 ps/nm/km) as discussed in [11, 120]. The distances beyond 100 km show an open eye, as the transmission regime here is dispersion supported [11].

Nevertheless, Figure. 3.36 demonstrates that the ultra low frequency chirp and low α_H-parameter of QDashes it possible for the QDash DML to show tranmission distances in the range of 0-100 km without any change in the biasing conditions. The dynamic extension ratio can be increased using a passive optical filter.

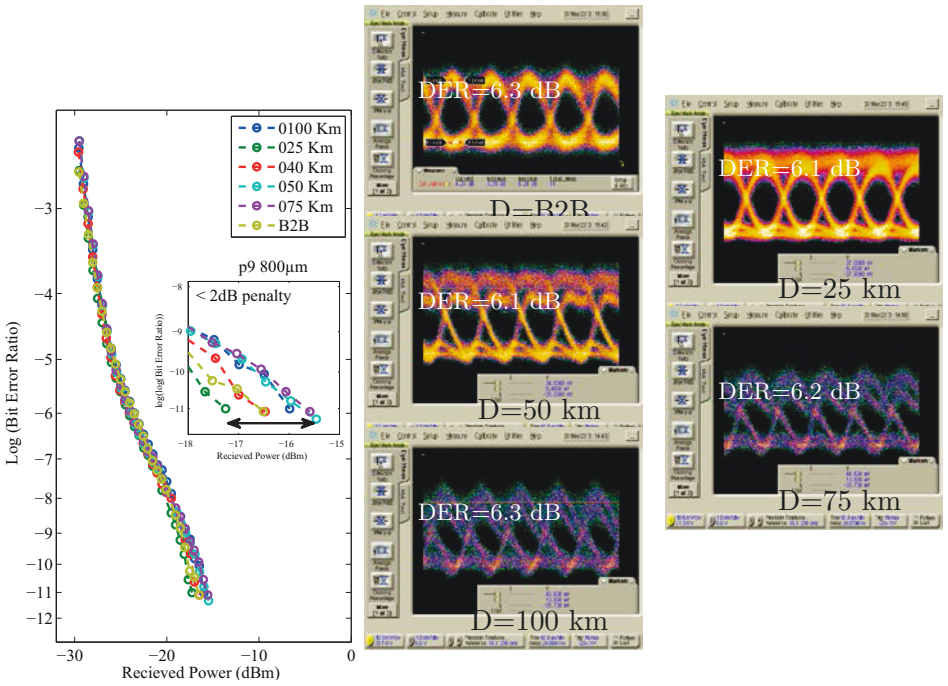

FIGURE 3.38: A standard 10Gbps transmission using a $\lambda/4$-phase shifted DFB with p-doped QDash as active material showing transmission up to 100 km with 6 dB extinction ratio.

3.5.4 Effect of passive etalon filter

As the 0-bit is red shifted in wavelengths due to the adiabatic chirp (see Sec. 3.4.4), the amplitude related to its wavelength can be selectively filtered using an interferometric device such as a passive etalon filter. This would help to increase the DER by suppressing the amplitude of 0-level in the optical eye. The simulated amplitude transfer function of such an etalon filter is presented in Fig. 3.37, the placement of the laser emission wavelength on the negative slope of this filter would help in reducing the amplitude of 0-bit with respect to the 1-bit.

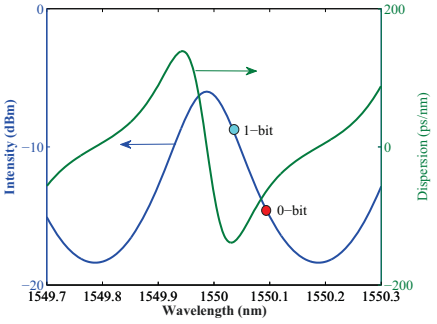

FIGURE 3.37: Amplitude transfer function of the passive optical filter.

The BER is measurements are repeated again with a passive etalon filter. The etalon filter is places between the isolator and the optical switch (see Fig. 3.33). The BER and optical eyes for the lasers showing low chirp to open the optical eyes as presented in Fig. 3.38 and 3.39.

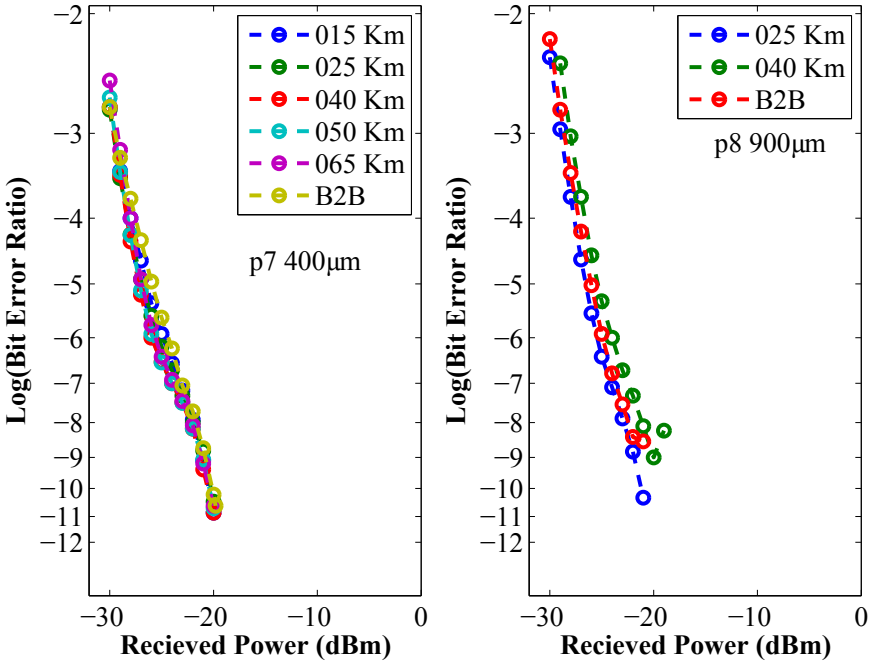

FIGURE 3.39: A standard 10Gbps transmission using a $\lambda/4$-phase shifted DFB with p-doped QDash as active material showing transmission up to 65 km

The eye diagrams as expected show an increase in dynamic extinction ratio and are increased to a value >6 dB for all the distances as opposed to 2 dB without using the filter. In addition to the increase in DER, there are two noticeable effects which come with the filter. Firstly the penalty in the bit-error-ratio is reduced to < 2 dB (see inset Fig.3.38) which means that the extinction ratio would be constant for all the distances. Secondly the filter improves both the BER and the DER irrespective of the adiabatic chirp of the laser. A third added effect is the reshaping of the optical eyes at low distances (compare Fig. 3.38 and Fig. 3.36). This occurs due to the phase action of the filter (discussed in Sec.3.6.2).

At this point it should be noticed that lasing wavelength has to be placed at the right position on the negative slope of the filter in order to benefit the maximum from the filter. If the position of the filter relative to the laser wavelength is detuned, the transmission performance will change depending on the amount of detuning. In the present case this detuning is achieved by increasing the temperature of the laser assuming that the changes in range of $\pm 1°$C will not have a large impact on the laser chirp. BERs at filter detuning from the maximum (at 25°C) are presented in Fig 3.40(a). Indeed by varying the detuning the BER shows optimum performance for values of detuning

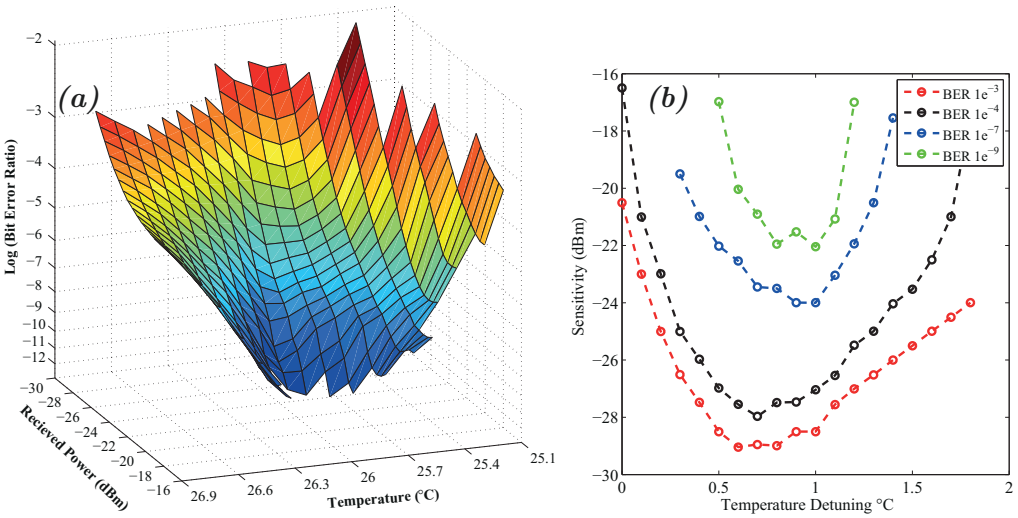

FIGURE 3.40: (a) Bit error ratio vs received power vs temperature showing the tolerance of etalon. (b)Sensitivity at specific bit error ratios vs temperature of the laser

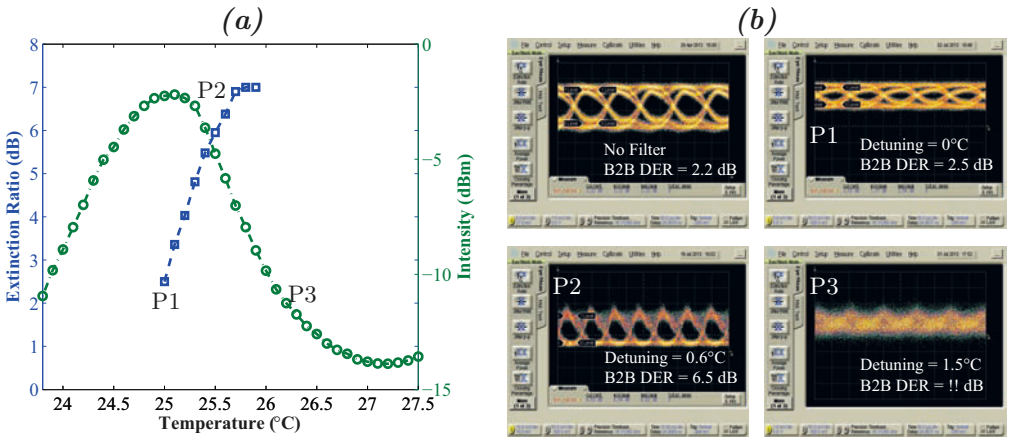

FIGURE 3.41: (a) Measured intensity transfer function of the filter as a function of temperature and the DER at respective points. (b) Eye diagrams at point P1, P2 and P3 on the filter with detuning of 0°C, 0.6°C and 1.5°C respectively

in the range of 0.4-0.7°C from the maximum of the filter. This relatively high range of temperatures for which the filter can actually maintain similar bit error ratios as compared to other approaches (eg. CML, where the filter tolerance is very small). This is true only for the negative slope of the filter, on the positive slope of the filter, the BER deteriorates and the optical eye is observed to be completely closed and distorted. This effect can also be observed from the BER curves presented in Fig. 3.40. At large detuning of the laser from the filter maximum, the bit error rate starts to deteriorate again as the relative intensity suppression between the bits decreases. The eye diagrams are recorded for various detuning with respect to filter maximum and are presented in Fig. 3.41. For

detuning up to 1°C, the filter opens the optical eyes and increases the extinction ratio. After a certain detuning (1.5°C) the extinction ratio cannot be measured as the power is too low. Large detuning values are not interesting as the loss in optical powers is very large. At the same time, if the laser chirp is large the filter starts to enhance the power of 0-bit wavelength.

3.6 Discussion on passive optical filter

As stated earlier one of the objectives of this thesis is to study the use of an optical filter to improve the transmission behaviour. The passive filter improves the dynamic extinction ratio by suppressing the intensity related to 0-bit and thus opening the eye. At the same time, it is well known that there is a component of dispersion involved in any interferometric filter. Thus, it is also important to study the effect of filter related to the optical phase. Some filters can be used to compensate the dispersion introduced by the fibre to an optical data signal [92, 121, 122]. A classic example of such a dispersion equalizing filter is a Gires-Tournois interferometer, where if losses are constant over the signal bandwidth, only spectral phase is modified by the filter. In a Fabry-Perot type filter, both the phase and amplitude are changed. Thus there are two effects that can be expected from a Fabry-Perot filter, a filtering effect arising from change in amplitude and dispersion equalizing effect arising due to the phase profile of the filter.

3.6.1 Amplitude action of filter

In addition to abrupt temporal phase shifts, a more important effect of the etalon-filter is the suppression of zero bit. Due to the frequency chirping in a directly modulated laser modulated at high-bit rates, the '0-bit' is slightly red shifted as compared to the '1-bit.' Because the amplitude transfer function of the filter is frequency dependent as shown in Fig. 3.42 and Fig. 3.37, the etalon filter makes use of this shift in the wavelengths of the bits to damp the amplitude of the '0-bit.' Thus the filter would increase the difference in power levels between the 1-bit and the 0-bit, changing their levels in and optical eye diagrams. The amplitude action of filter becomes more important at larger distances ($>$ 50 km), as the signal has suffered a large amount of loss due to propagation

in the fibre. The propagation in fibre at large distances becomes similar to dispersion supported transmission [1].

3.6.2 Spectral phase action of filter

As the transfer function of any optical interferometer is dependent on the phase of input optical field, a dispersion is expected to be introduced by the interferometric filter. In this section, a simple expression for dispersion due to a FP filter is derived. If R is the facet reflectivity of the FP filter, then the complex transfer function for a FP interferometer can be expressed as

$$\mathcal{F} = \frac{1-R}{1-R\exp i\theta} \tag{3.55}$$

Mathematically it is possible to calculate the phase ϕ of the complex transfer function as

$$\tan\phi_f = \frac{\mathcal{I}(\mathcal{F})}{\mathcal{R}(\mathcal{F})} \tag{3.56}$$

where,

$$\mathcal{R}(\mathcal{F}) = \frac{(1-R)(1-R\cos\theta)}{1+R^2-2R\cos\theta} \quad and \quad \mathcal{I}(\mathcal{F}) = \frac{(1-R)(iR\sin\theta)}{1+R^2-2R\cos\theta} \tag{3.57}$$

The phase of the input optical field can be expressed in terms of free spectral range (FSR) of the filter and the wavelength of the input optical field as

$$\theta = \frac{2\pi c}{FSR * \lambda} \tag{3.58}$$

The phase profile ϕ of the filter for different values of R is presented in Fig 3.42. The phase profile of the filter becomes sharper as the mirror reflectivity increases. At very high mirror reflectivity, the abrupt phase change occurs around the points of maximum intensity.

This phase shift around points of the maximum intensity will produce a group delay between the wavelengths generated in a directly modulated laser due to the laser

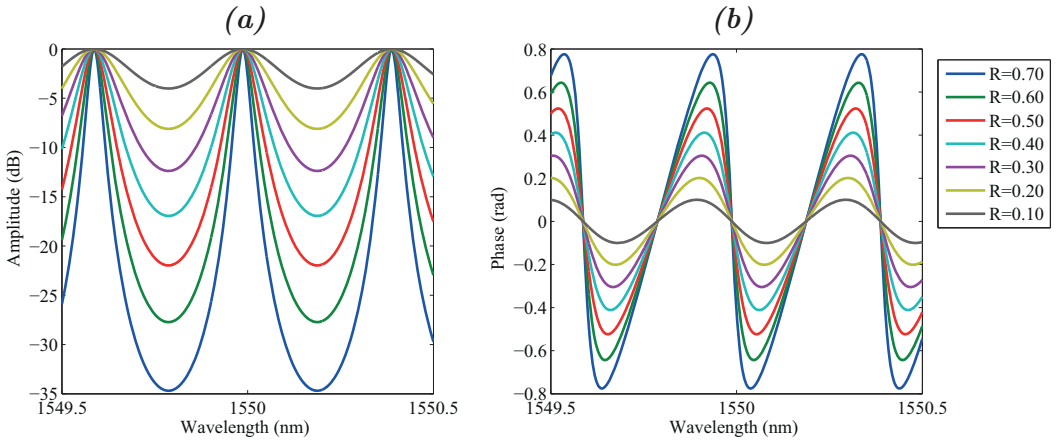

FIGURE 3.42: The intensity and phase profile of Fabry Perot filter at different values of facet reflectivity R

chirp. This delay equal to the slope of the filter phase profile with respect to the frequency. This gives the following relation

$$\tau_f = \frac{d\phi_f}{d\omega} \tag{3.59}$$

In terms of wavelength Eq. 3.59 can be rearranged as

$$\tau_f = -\frac{\lambda^2}{2\pi c}\frac{d\phi_f}{d\lambda} \tag{3.60}$$

The dispersion $\mathcal{D}_f$, introduced by the filter can be expressed as the slope of the delay with respect to the wavelength.

$$\mathcal{D}_f = \frac{d\tau_f}{d\lambda} = -\frac{\lambda}{\pi c}\frac{d\phi_f}{d\lambda} - \frac{\lambda^2}{2\pi c}\frac{d^2\phi_f}{d\lambda^2} \tag{3.61}$$

The delay and dispersion introduced by the filter are presented in Fig. 3.43. Thus due to the introduced dispersion, the optical filter is expected to chirp the bit-pulses emitted by a directly modulated laser, the filter should be able to manage a small amount of transient chirps, introduced by the laser modulation. This pulse chirping is similar to the pulse chirping observed in a Gires-Tournois interferometer, but in the case of FP filters it is weaker in magnitude.

It can also be seen that the filter will offer a normal or an anomalous chromatic

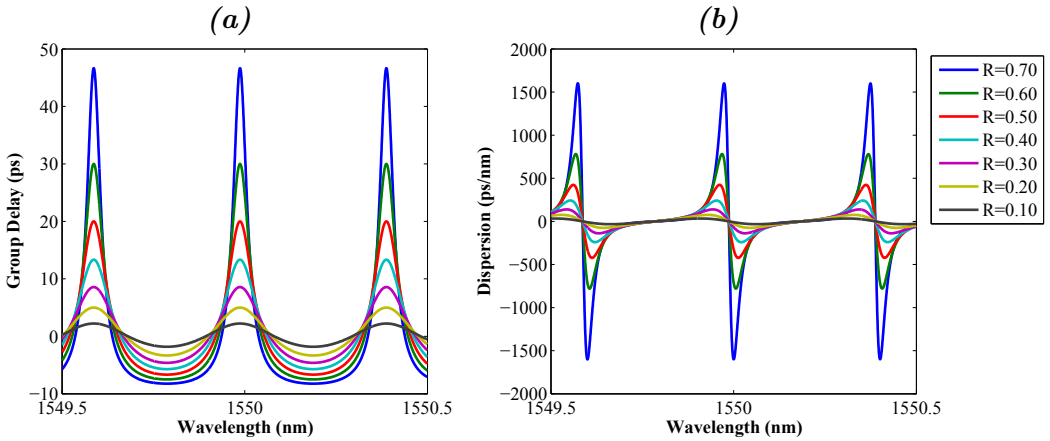

FIGURE 3.43: The delay (a) and dispersion (b) of the etalon filter at different values of facet reflectivity R

dispersion to the laser field depending on the relative position of the laser wavelength and the filter. The filter used in the transmission experiments for this work is a commercial Fabry–P'erot filter with a reflectivity $R \approx 30\%$, with a free spectral range of 50 GHz. The insertion losses to the filter are close to 6 dB, it offers an on-off ratio of about 12 dB. The modelled profile of filter is presented in Fig. 3.37. The filter is also expected to offer a negative anomalous dispersion for positive detuning of the filter with respect to the filter maxima.

3.6.3 Experimental results on filter measurements

To understand the impact of filter on the transmission performance, small signal modulation response of a low chirp QDash laser is measured using a network analyser with and without filter for a detuning of 0.6°C with respect to the maximum of the filter for distances between 0-50 km and are presented in Fig. 3.44. The small signal response of the laser before and after the introduction of the filter in the transmission channel change significantly. The filter results in enhancing the small signal modulation response of the laser from 10 GHz to a value close to 15 GHz for B2B condition (see Fig. 3.44(a)). This 50% increase in modulation bandwidth is valuable for the transmission. Similar results are observed for the transmission distances of 25 km and 50 km where the perturbation in the transmission channel due to the fibre is recovered using the filter (see Fig. 3.44(b-c)).

The anomalous chromatic dispersion is known to manifest itself as a peaking in the small signal modulation. The enhancement of small signal modulation amplitude

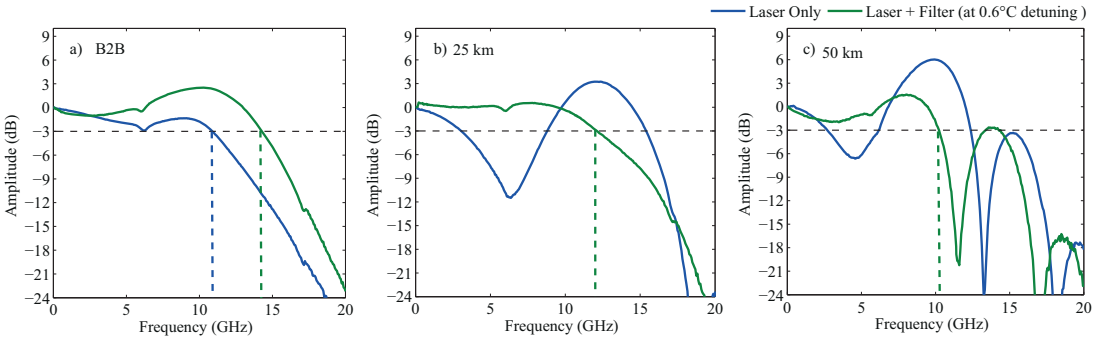

FIGURE 3.44: Measured small signal response of the laser at filter detuning between -1°C and 1°C with respect to the filter. (a) In B2B condition, (b) after 50 km fiber transmission.

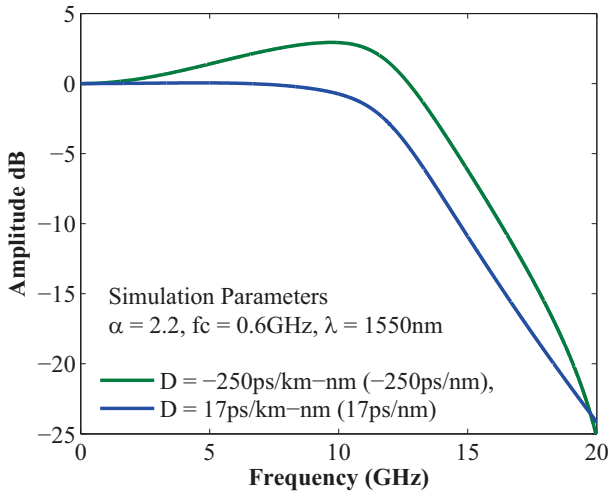

FIGURE 3.45: Simulated small signal response of the laser with and without negative dispersion

depends on the amount of dispersion introduced in the optical channel [123]. The anomalous dispersion in the present case is believed to be responsible for such a gain in bandwidth. The small signal modulation of the laser is simulated with and without negative dispersion for B2B condition (see Fig. 3.45). It is clearly observed in simulations that the dispersion plays an important role in the transmission with the filter. The results from the simulation are very close to that of the measured values for modulation bandwidths.

Bandwidths were then measured at filter detuning between -1°C and 1°C with respect to the filter maximum in B2B condition and with an optical fibre of 50 km in the optical channel. These measurements are presented in Fig. 3.46. For the fibre length

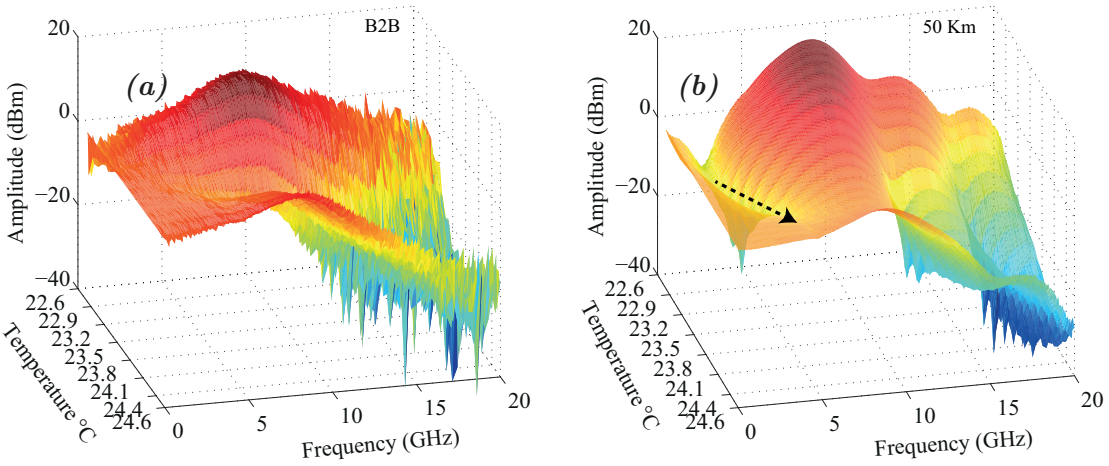

FIGURE 3.46: Map of small signal response as a function of temperature shift of the laser with respect to the filter (a) In B2B condition, (b) after 50 km fiber transmission.

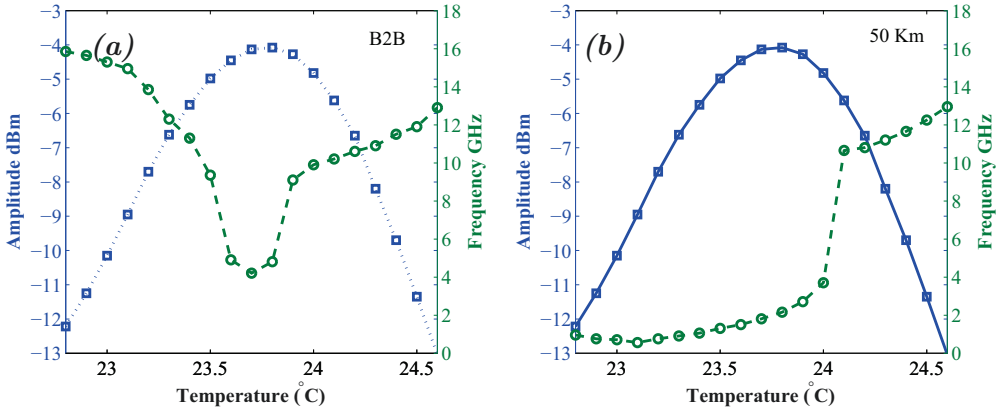

FIGURE 3.47: Measured 3 dB bandwidths of the laser at filter detuning between -1 °C and 1°C with respect to the filter maxima. (a) In B2B condition, (b) after 50 km fiber transmission.

of 50 km the recovery of the distortion in the passband is clearly observed as indicated with the arrow in Fig. 3.46(b). The behaviour of the filter in B2B condition is not well understood and needs further attention as the filter shows enhanced bandwidths for both positive and negative detuning of the filter. This behaviour may occur if the reflectivity for the two facets of the filter are not identical. This would require a precise extraction of phase information from the filter. The phase information of the filter can be extracted using optical frequency-domain reflectometry [124], this is beyond the scope of the present work.

The measured bandwidth in B2B and after a fibre span of 50 km as a function of filter detuning are presented in Fig. 3.47, an enhancement of the measured bandwidth is

observed for positive filter detuning in the range of 10-14 GHz for a fibre span of 50 km.

3.7 Electrical pre-emphasis on QDash DML

Pre-shaping of the injected electrical current pulse is usually helpful in cancelling the signal distortion in orthogonal frequency division multiplexed (OFDM) DML systems [125]. However as stated earlier pre-emphasis shows very limited improvement for intensity modulated and direct detection. Nevertheless pre-emphasis can be used to improve the power budget for the QDash DMLs.

For applying a pre-emphasis to the electrical data signal a pre-emphasis module is added after the pulse pattern generator. The pre-emphasis modules pre-distorts the electrical signal at certain points as shown in Fig. 3.48(c). The eye amplitude can be controlled by the peak to peak voltage from the emphasis module. The voltage levels C1, C2 and C3 (see Fig 3.48(c)) are adjusted to pre-distort the electrical signal. To compensate for the transient chirp of the laser, the level C1 is minimized and the level C2 and C3 are maximized in accordance with the chirp of the laser as shown in Fig. 3.30. Notably, a precise knowledge of laser chirp is necessary in order to set the pre-emphasis parameters correctly.

The operations of increasing or decreasing the voltage within the pulse shape at certain points result in the electrical eye as shown in Fig. 3.49. The different levels in the electrical eyes correspond to the levels C1-C3 and the offset. The values of the pre-emphasis parameters had to be changed with each distance in order to compensate for the distortion arising from the chromatic dispersion of the fibre.

The optical eyes after transmission are re-shaped in accordance with the electrical eyes set by the pre-emphasis parameters. Optical eyes after 50 km of fibre transmission are presented in Fig. 3.50. It can be clearly seen that the eyes improve after the application of pre-emphasis, the extinction ratio still remains small.

The passive optical filter, remains superior to the electrical pre-emphasis as it both re-shapes the optical eye and increases the extinction ratio, at the same time the filter is not a power consuming device, where as the electrical pre-emphasis would consume electrical power.

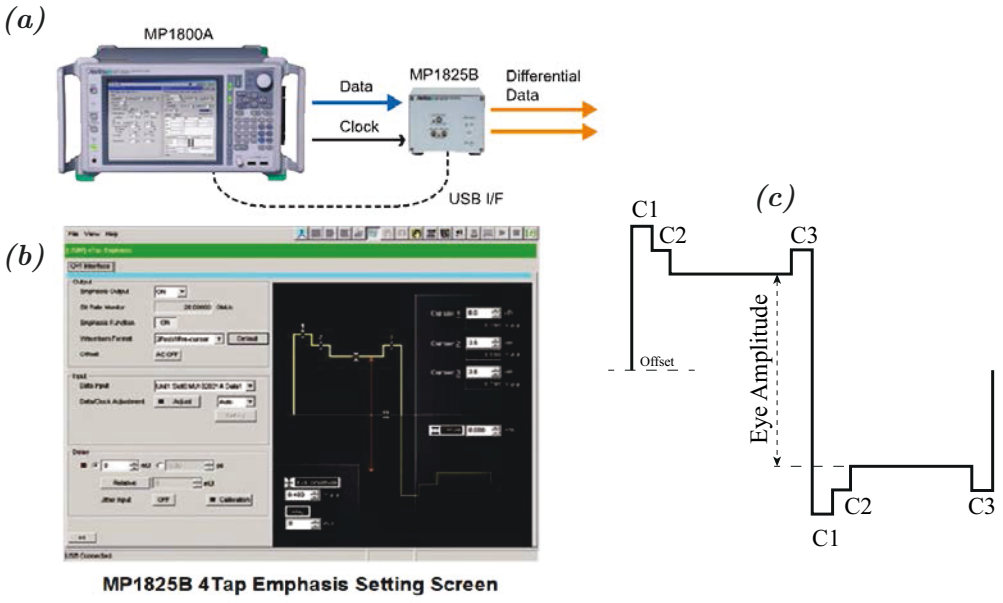

FIGURE 3.48: (a) Pre-emphasis module added after the pulse pattern generator. (b) The software interface of the module which allows to adjust the levels C1, C2 and C3 in a given pulse shown in (c)

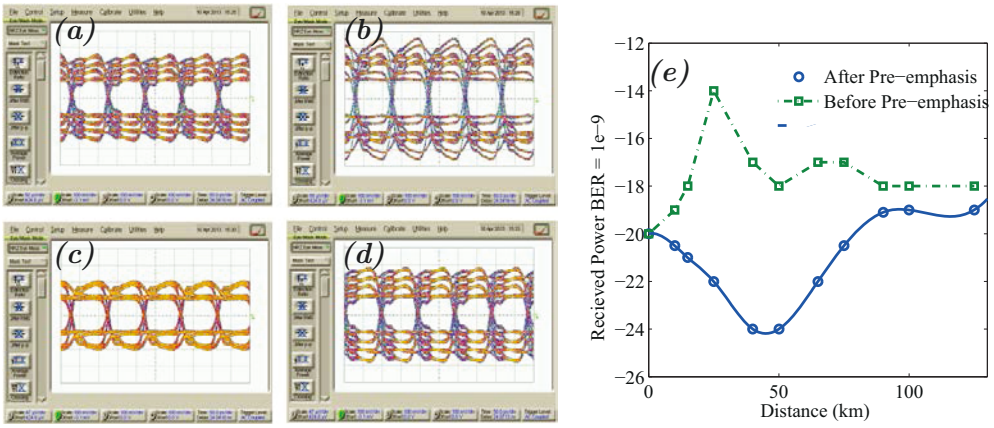

FIGURE 3.49: The electrical eyes after application of pre-emphasis by adjusting the levels C1, C2 and C3 at (a)in B2B (b) for 25 km (c) for 50 km and (d) for 100 km fibre transmission

3.8 Summary

This chapter discussed about the static and dynamic properties of Qdash based DFB lasers. The dynamic characterstics of QDash lasers were studied and the impact of epitaxial design was presented. A specifically grown p-doped QDash in a DWELL design were studied in details and were identified as the ideal candidates for transmission after a careful analysis of their dynamic performance.

(a) Electrical Eyes ***(b)*** Before Pre-emphasis ***(c)*** After Pre-emphasis

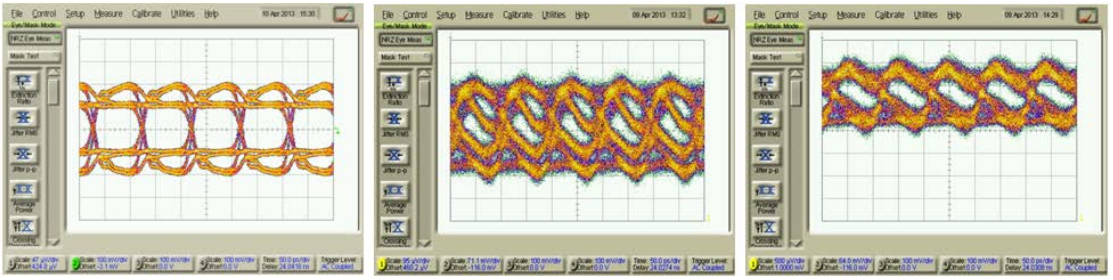

FIGURE 3.50: (a) The electrical eyes after application of pre-emphasis. (b) Optical eyes before pre-emphasis and (c) after pre-emphasis

On the side of static characteristics, the p-doped DFBs are shown to have a high temperature tolerance. They offer an output power in range of 15-20mW, which is sufficient for optical transmission. The optical spectrum of a $\lambda/4$ shifted DFD was observed to show and optical side-mode-suppression ratio in range of 45-50 dB. On the other hand the Qdash DFB also displayed excellent dynamic performance. K-factor as low as 0.22ns were observed on several devices. High Differential gain of up to $12e^{-16}$ cm^{-1} was also observed with the p-doped Qdash material. α_H-parameters were extracted for DFB devices above and below threshold and were found to be identical. Ultra low transient and adiabatic chirp were measured for QDash DFB lasers as compared to the conventional material and impact of DFB designs on the chirp and α_H parameter were discussed.

Transmissions experiment were set up for a 10 Gbps data rate and a record transmission distance range of 0-100 km was obtained. The impact of passive optical Filter on the optical transmission was studied in details and compared against the use of a electrical pre-emphasis.

Chapter 4

Monolithic integration of DML and ring resonator on InP PIC platform

Sec. 3.5.4 of the previous chapter explains the use of a passive optical filter with QDash MLL and improvement in transmission performance owing to the optical properties of the passive filter. A passive optical filter therefore, proves to be a vital component for the fabrication of dispersion immune optical transmitters. Passive filter used in the previous study was an external discrete component. For a compact optical transmission device, it is necessary to design an optical filter which can be integrated to the DFB lasers on InP platform. One simple solution is to use an optical ring resonator as a passive optical filter. Ring resonators are attractive candidates, due to the fact that several important filter parameters can be controlled by changing the design of the ring resonator.

This chapter provides a background on the design and fabrication of ring resonators for integration on InP-platform. The integration of a ring resonator as a passive optical filter can be done using the Butt-Joint technology. The Butt Joint integration technology of the DFB lasers is discussed in details. Finally this chapter discusses the results on transmission using a ring resonator device.

4.1 A review on passive optical filters

As stated earlier, passive optical filters are a vital component for the design of a dispersion immune optical transmitter. There are several methods to realize passive optical filters on PICs such as thin-films, planar arrayed waveguides, Bragg gratings and MZ-interferometers. The properties of particular interest for the filter are the slope of the filter ($dI/d\lambda$) often expressed in dB/GHz, on-off ratio, insertion losses, compactness in terms of the device foot-print. On-off ratio is usually measured as the ratio between the on-level and the off-level of the filter and is given in dBs. The insertion loss of the filter is the measured as the power difference between the on-level with the 0 dB power level as presented in Fig. 4.1. It is possible to use various types of optical filters for the present application. A comparison of these properties for various filters are presented in Table. 4.1.

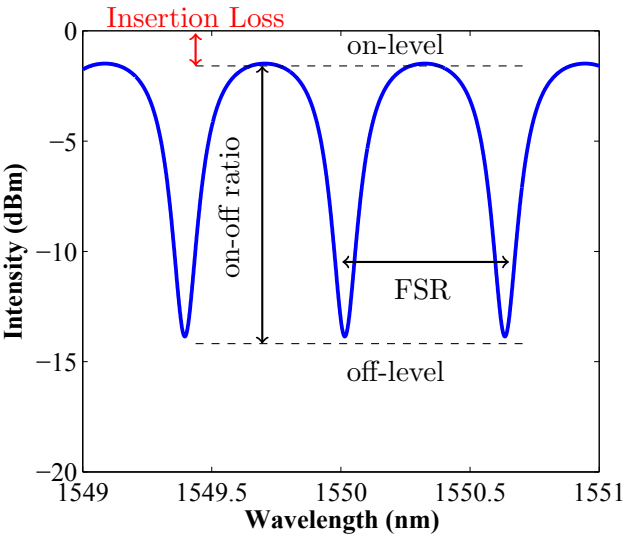

FIGURE 4.1: Intensity transfer function of a passive optical filter showing on-off ratio, insertion losses and filter slope.

It would be desirable to fabricate a filter with a high on-off ratio in order to suppress the wavelength related to '0-bit' as much as possible (see Fig.3.37) as well as strict control on the slope $dP/d\lambda$ of the optical filter such that it can be used with a laser having an arbitrary value of adiabatic chirp. This can be achieved using a Bragg grating based filter. These filters would have a feedback and thus would make the used of an isolator imperative, compromising the integrability of such a filter. Another way is to use arrayed waveguide grating (AWG) which offer decent wavelength selectivity, AWG filter are usually avoided due to the complicated fabrication technology. One viable solution is MZ based interferometer. MZ offers a very high wavelength selectivity and is easy to fabricate. In addition there is no problem related to feedback in this kind of filter. It would require a precise knowledge on the phase shift to be introduced, which makes design of such filter difficult on InP substrates. Also the phase shift between the two arms of a MZ interferometer would have to be too large to produce $FSR << 50\ GHz$.

Another solution is the use of passive optical ring resonator. Ring resonators are versatile optical filtering elements which offer a great control on on-off ratio and filter slope. In addition, it is easy to tune the FSR of the filter by tuning the radius of the ring. They are also easy to fabricate and offer a very small device footprint.

Filter Type	On-off ratio	Feedback	Filter Slope $dI/d\lambda$	Complexity	Compactness	Comments
Thin Film	Low (uncontrolled)	Yes	Low	Low	High	Feedback to Laser is not desired
Arrayed	Medium	No	High	High	Medium	Fabrication Complexity
Bragg Grating FP	Medium	Yes	Tunable	Medium	High	Difficult to produce a broadband filter
MZ Interferometer	High and Tunable	No	Tunable	Low	High	Phase shift is required to generate fringes
Ring resonator	High and Tunable	No	High and Tunable	Low	High	High Control on parameters

TABLE 4.1: A short comparison of passive optical filters for PICs

Ring resonators can thus be easily identified as a excellent optical filter which can be readily integrated on the InP-PIC platforms. In addition, high control on filter parameters using a ring resonator makes them the best candidate for passive filters. It is thus necessary to study this passive device in order to successfully integrate a ring resonator with a DFB laser. The filter used in Chapter 3 to demonstrate record transmission was an FP filter with a FSR of 50 GHz, an on-off ratio of 10 dB and had a slope of 1 dB/GHz. Thus, for the present application it is desirable to have similar filter characteristics in addition to integration compatibility of the filter. For the ring resonators parameters like on-off ratio, filter slope and FSR can be specifically engineered.

4.2 Ring resonators

Use of ring resonators as an optical filter had been proposed as early as 1969 [126]. The layout of a general ring resonator is presented in Fig. 4.2, showing an optical ring with two optical buses coupled to the ring. If light at wavelengths ($\lambda_1, \lambda_2, \lambda_3$ and λ_4) is fed through the input port and the resonance of the ring corresponds to wavelength λ_2, the wavelength λ_2 will be suppressed from the throughput port and would be dropped at the drop port. The key is the resonance frequency of the ring resonator, which depends on

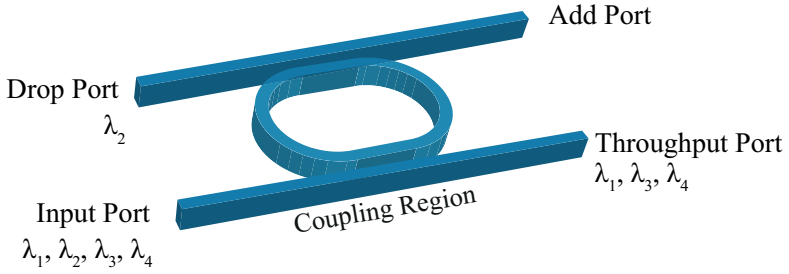

FIGURE 4.2: Illustration of a dual bus single ring resonator showing Add, Drop and Throughput ports

the coupling of the light to and from the ring. This resonance occurs due to interference of the light propagating in the ring resonator with the light coming from the input port. Generally, a ring resonator is used as an add-drop filter, which filters a particular wavelength (λ_2) from the input port and drop this wavelength at the drop port. This wavelength, thus does not appear at the through port. For simple wavelength filtering, it is not necessary to implement a drop port and a single bus ring resonator is sufficient for the present application (see Fig. 4.3(a)). To implement a single bus ring resonator as a passive filter, it is important to precisely define the coupling relations into the ring resonator.

4.2.1 Coupling in single bus ring resonators

A schematic of a single bus ring resonator is presented in Fig. 4.3(a) showing the input and throughput ports. In this case if the input port is injected with light at wavelengths ($\lambda_1, \lambda_2, \lambda_3$ and λ_4) and if the λ_2 is the resonant wavelength for the ring, then this wavelength is filtered at the throughput port by the ring resonator. To understand the operation, consider a ring resonator with single optical bus as shown in Fig. 4.3 (b). Assuming that the amplitudes of the optical fields at the input port is a_1 at an arbitrary

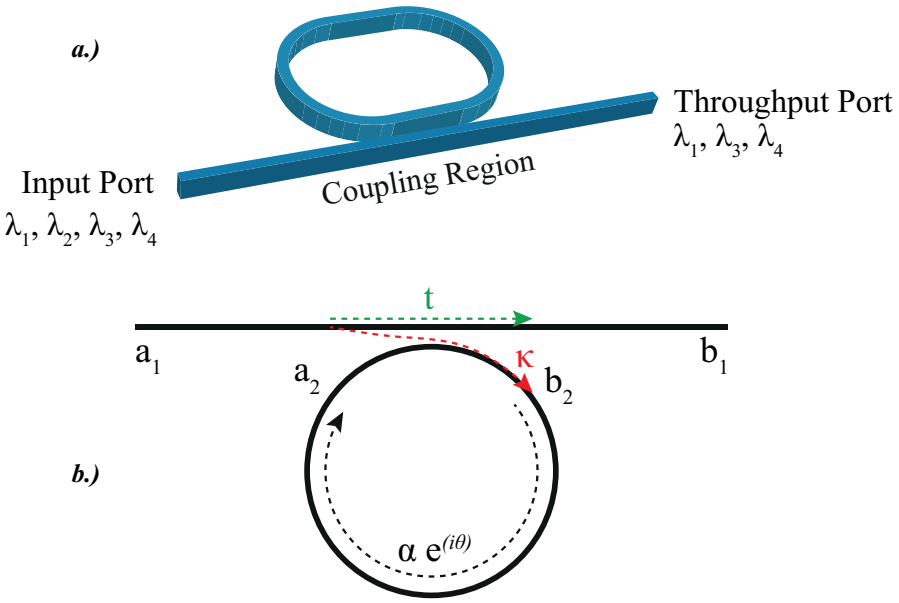

FIGURE 4.3: a.)Illustration of a single bus single ring resonator showing input and throughput ports. b.) Schematics of coupling in a single bus ring resonator for the case of lossless coupling.

wavelength λ. The amplitude at the through port b_1 can be written in terms of the sum of field from the input waveguide a_1 and the field after propagation inside the ring a_2 in relation with coupling factor κ and t as

$$b_1 = a_1 t + a_2 \kappa \tag{4.1}$$

On reaching the coupling region this light is coupled to the ring with a coupling efficiency of κ, resulting in an amplitude b_2 inside the ring. A small part of b_2 is also contributed by the light resonating inside the ring. The amplitude b_2 can thus be expressed as

$$b_2 = \kappa^* a_1 - t^* a_2 \tag{4.2}$$

Also from the law of conservation of energy (in case of lossless coupling)

$$\left|\kappa^2\right| + \left|t^2\right| = 1 \tag{4.3}$$

The light propagates through the ring suffering loss by a loss-coefficient α. At this time the light also suffers a phase shift by an amount θ, thus the amplitude a_2 of the light before exiting the ring can be related to the light entering the ring by the propagation factor $\alpha e^{i\theta}$ as

$$a_2 = b_2 \alpha e^{(i\theta)} \tag{4.4}$$

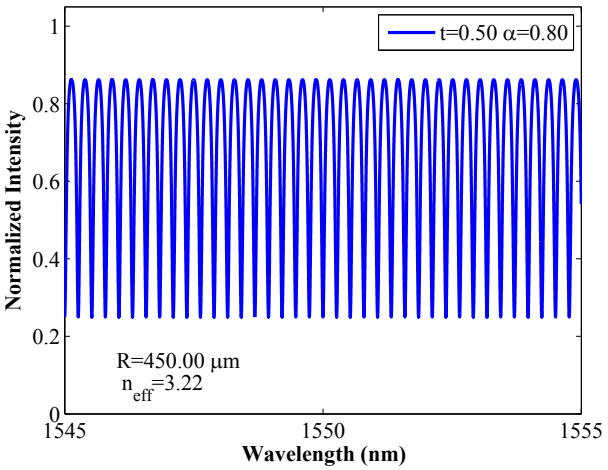

FIGURE 4.4: Simulated output at the throughput port of a single bus ring resonator with a radius of 450 μm at $\alpha = 0.8$ and $t = 0.5$.

where $\theta = 4\pi^2 n_{eff} R/\lambda$ is the phase term dependent on the ring parameters such as radius of the ring and the effective index of the waveguide. The free spectral range of the ring resonator is defined as $FSR = \lambda^2/n_{eff}(2\pi R)$. Thus the FSR of the ring resonator can be tuned by adjusting the ring radius. From Eq. 4.1 4.2, and 4.4, the output at the throughput port b_1 can be arranged as

$$b_1 = a_1 \left(\frac{t - \alpha e^{i\theta}}{1 - \alpha t e^{i\theta}} \right) \tag{4.5}$$

The intensity at the output can thus be written as

$$I_{out} = |b_1|^2 = \frac{|t|^2 + \alpha^2 e^{2i\theta} - 2\alpha |t| e^{i\theta}}{1 + \alpha^2 |t|^2 e^{2i\theta} - 2\alpha |t| e^{i\theta}} |a_1|^2 \tag{4.6}$$

It can be noticed from Eq. 4.6 that at $\theta = 2m\pi$, output at the throughput port is minimum. This is known as the resonance condition for the ring resonator. As the term θ is wavelength dependent, the output spectrum would result into optical fringes as a function of wavelength. At the resonance the output at the throughput port can be expressed as[127, 128]

$$I_{out} = \frac{(|t| - \alpha)^2}{(1 - \alpha |t|)^2} \tag{4.7}$$

The output at the throughput port for a optical ring resonator with radius of 450 μm is presented in Fig. 4.4, showing typical fringes obtained from a single-bus ring resonator. It is also seen from Eq. 4.6 that when $|t| = \alpha$, the output vanishes completely. This is known as the critical coupling condition [128]. Figure. 4.5(a) shows the transfer function

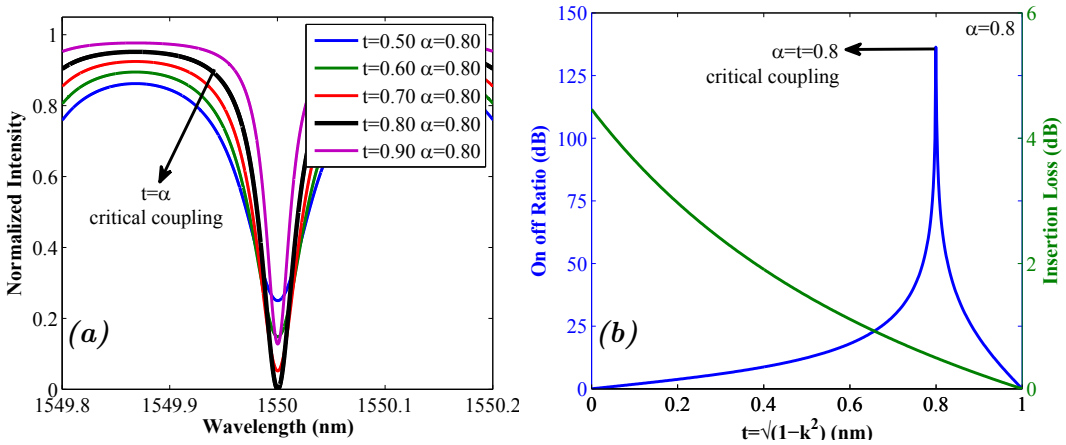

FIGURE 4.5: (a) Simulated output at the throughput port of a single bus ring resonator with a radius of 450 μm at $\alpha = 0.8$ and various values of $|t|$ including the critical coupling condition. (b) on-off ratio and insertion losses as a function of κ.

of the ring resonators at constant α for different values of $t = \sqrt{1-\kappa^2}$, as t approaches α the on-off ratio increases and is maximum when $t = \alpha$ as represented in Fig. 4.5(b). The critical coupling condition is highly desirable to benefit from a very large on-off ratio for the filter. It would however need some tuning mechanism to tune either the losses in the resonator or the coupling factor. The coupling factor is usually fixed once the resonator is fabricated, however the losses in the ring can always be tuned using a semiconductor optical amplifier inside the ring resonator.

The losses in the ring might arise from two main phenomena, these include the propagation loss and the radiation losses. Both these loss mechanism have different origins. The propagation loss arises from the loss caused by the absorption of the guided wave by the material or due to scattering etc. The radiation losses, similar to the bent loss in optical fibres, arise from the fact the light propagation length at the inner radius of the ring is less as compared to the outer radius. For very short radius of the ring these losses will be very high. The bent radiation loss can be controlled and minimised by increasing the radius of the ring resonator. The propagation losses can be controlled by certain technological steps which will be discussed in Sec. 4.3.1.

The relations given in Eq. 4.6 and 4.7 are derived for a specific condition of lossless coupling from the optical bus to the ring resonator. In practical cases, the coupling is not always lossless. An analysis of the ring with coupling loss is presented in [129]. The transfer functions of the ring resonators with coupling losses are presented in Fig. 4.6.

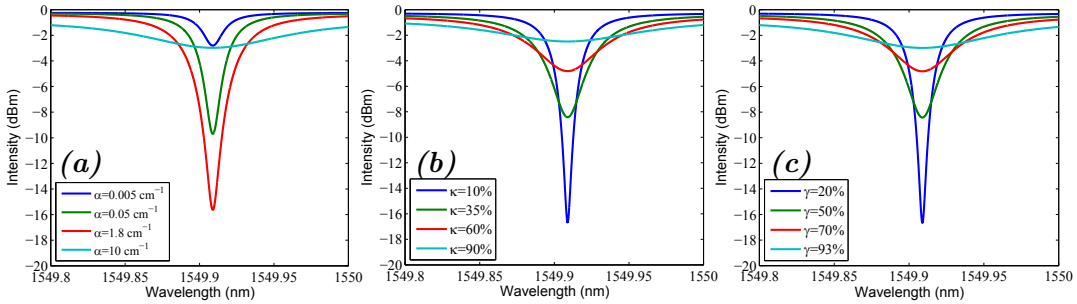

FIGURE 4.6: Simulated output at the throughput port of a single bus ring resonator with a radius of 450 μm as a function of (a) ring losses α (at fixed κ and γ), (b) coupling factor κ (at fixed α and γ) and (c) coupler loss γ (at fixed α and κ).

Figure. 4.6(b) and (c), show the strong correlation between coupling factor and the coupling losses. Thus, the contribution of coupling losses γ can actually be included in the losses in the ring α, which accounts for various losses.

4.2.2 Coupling of light to the ring resonator

As stated earlier the operation of the ring resonator depends on the coupling of the light into the ring. The operation of the ring resonator and most of its optical characteristics, such as the on-off ratio, slope of the filter and, insertion losses are dependent on coupling constant $\kappa = \sqrt{1-t^2}$. It is also desirable to operate under the critical coupling condition (see Fig. 4.5) to obtain a large on-off ratio. The first concern towards the design of an efficient optical filter, is the mechanism of coupling of the optical field into the ring resonator. The optical coupling to the ring resonator can be performed using various methods such as direct contact of the ring and the bus, a coupling using a multi-mode interference (MMI) coupler and finally coupling by evanescent field as illustrated in Fig. 4.7. It should be noted that the coupling mechanism should offer a feature to desirably tune the coupling factor in accordance with the ring losses. This feature is required as almost all of the filter properties would depend on the relative value κ with respect to α. It is known that on InP PIC-platform the waveguides are expected to offer finite amount of losses, thus a control on κ is highly desired.

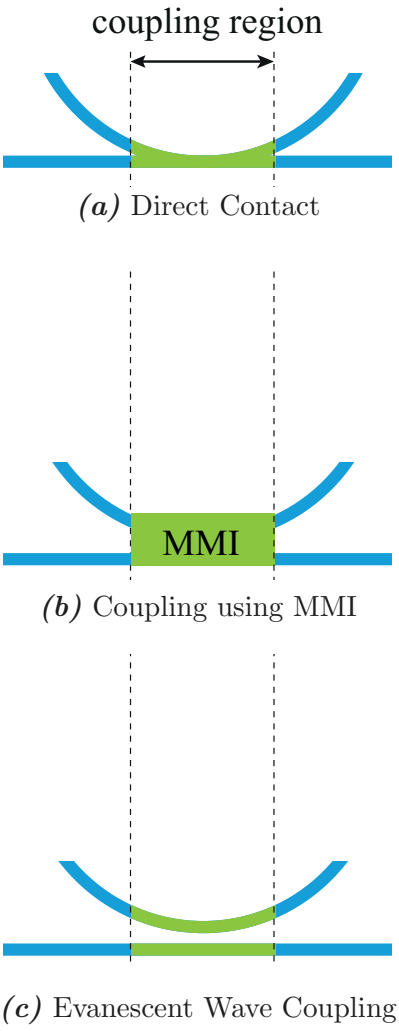

(a) Direct Contact

(b) Coupling using MMI

(c) Evanescent Wave Coupling

FIGURE 4.7: Various possible coupling mechanisms between the optical bus and ring resonator

— ***Direct Contact*** of optical bus with the ring: In this approach the coupling ratio between the ring and the optical bus waveguide is very low and at the same time cannot be controlled relative to the losses in the ring. Thus this coupling mechanism is not very suitable for the present application.

— ***MMI coupling***: A MMI device is an interferometric coupler that can be used as a power divider. In a MMI, without any adjustment, the coupling ratio is fixed to 50%. This would be too low if the losses in the ring are high. To change the coupling ratio one can insert a slab of different material inside the MMI

region. This will complicate the fabrication process. A further complication of the fabrication technology is also not desirable.

— ***Evanescent coupling***: Evanescent coupling of the optical field between waveguides is well known in fibre optics. This scheme is usually used to fabricate power dividers in optical fibre communication. Evanescent coupling of optical power between two waveguides allows the adjustment the coupling ratio depending on coupler parameters (coupling length and coupling distance). In addition, evanescent coupling can be made lossless or to have very low coupling losses as compared to the other schemes. Evanescent coupling thus is one of the most suitable coupling schemes for fabricating an optical filter.

4.2.2.1 Evanescent wave coupler

Evanescent wave coupling of the ring to the optical bus waveguide was simulated using FIMMWAVE to observe the coupling efficiency of the ring with the bus. It is found that the coupling of the ring to the bus is inefficient even for small coupling distance of 100 nm. At larger coupling distances the power coupled to the ring almost vanishes as shown in Fig. 4.8. The coupling in an evanescent wave coupler can be increased by either

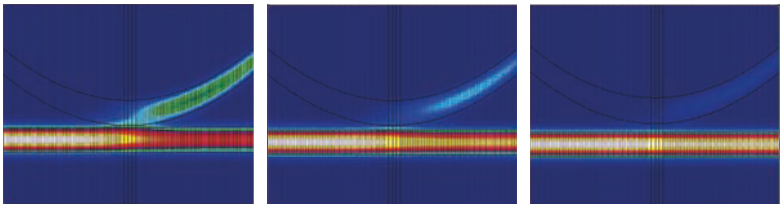

FIGURE 4.8: Simulations of coupling in optical ring resonator, showing coupling without a race-track at coupling distances of 100 nm, 250 nm and 500 nm respectively.

decreasing the coupling distance or by increasing the coupling length. Decreasing the coupling distance is not a viable option as, the etching of small coupling distance is may pose technological difficulties, which will be discussed later. Thus to make an efficient coupling scheme it is necessary to increase the coupling length. The coupling length can be easily increased by adding a so called racetrack coupling region (see Fig. 4.9(a)). Various evanescent wave couplers were analysed to find the optimum coupling distance and the coupler length using the simulations scheme shown in Fig. 4.9(c). The splitting ratio various gaps between the waveguides were analysed against different coupler lengths. Clearly, the slopes of the splitting ratio vs the coupler lengths of the couplers

with small coupling distance are higher than those with larger coupling distance between the guides. It is thus easier to tune the splitting ratio easily for short coupling distances. For short coupling distances between the waveguides the power splitting, defined by the

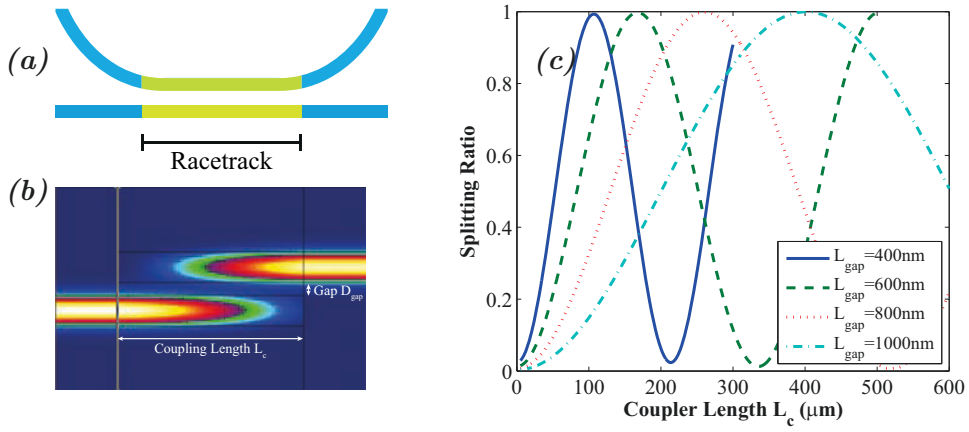

FIGURE 4.9: (a) Illustration of a ring resonator with a racetrack coupler. (b) Simulation of directional coupler to calculate the ideal coupling distance and length of the coupler. (c) The splitting ratio between the two waveguides as a function of coupler length L_C for various values of gap between the waveguides.

splitting ratio, changes rapidly with respect to the coupler length as compared to longer coupling distances as shown in Fig. 4.9(c). From these simulations it can be asserted that a very large coupling distance will also not be suitable as larger coupling distances would require a large coupler length for full tuning in the splitting ratio. Within this work, the coupling distance was thus limited from 400 nm to a maximum of 800 nm. The choice of lower limit is due to the limitation in fabrication and the higher limit is to limit the size of the directional coupler while still being able to achieve the entire range of splitting ratios.

4.3 Fabrication of ring resonators on InP Substrate

Fabrication of passive devices with buried ridge stripe technology is rather simple as compared to fabrication of active components, which require several cumbersome steps. Care needs to be taken on several aspects of design of the passive structures due to the limitations in technology. These limitations and the solutions to successful fabrication of ring resonators are discussed within the following sections.

The first step is to select a passive waveguide which could offer an effective index very close to that of the active region of the laser. This is done in order to minimize the losses at the active passive interface when the ring resonator is integrated to the laser (discussed in Sec. 4.6). The 215 nm thick passive waveguide of InGaAsP(λ_g = 1.3 μm) quaternary material is selected after simulations as best compromise between the absorptions at 1.55 μm by the waveguide material and reflections due to index mismatch. The width of the waveguide in these simulations is 1.5 μm, which matches the width of the active part and also yields a single transverse mode operation.

The fabrication of any passive structure on InP involves the following steps

1. De-oxidation and SiO_2 deposition: The wafer is first de-oxidized to ensure that the oxidation on the wafer surface is eliminated. A 200 nm thick layer of SiO_2 is then deposited, which serves as a hard mask for the electron beam lithography.
2. Lithography: The ridges are then defined by electron beam lithography. The electron beam pattern is transferred to the deposited oxide hard mask using RIE.
3. Mesa Etching: The ridge structures defined on the hard-mask are etched using ICP to define waveguides. The etching is restored using a small chemical etch, which smoothens the surface of the waveguide and helps in reducing the scattering losses.
4. Regrowth: InP is regrown using a standard BRS re-growth process on the wafer after ridge definition. This covers the waveguide and results in a BRS structure for the waveguide.
5. Hydrogenation and Ternary Removal: The finished structures are hydrogenated in order to minimize losses and the ternary grown during the regrowth process is also removed.

Theoretical estimations and simulations reveal several important aspects related to the design of ring resonators and their operation as passive filters. Basic requirements for the fabrication of ring resonators as passive optical filters can be summarized as below.

4.3.1 Low loss passive waveguides

The coupling to the ring resonator occurs via a passive optical waveguide, it is thus very important to fabricate low loss (or lossless) waveguides. As stated earlier, the ring resonator is also expected to show losses due to radiation of optical field from the ring resonator. It is necessary to find the right radius of the ring resonator so as to have minimum radiation losses and at the same time lowest possible footprint.

Propagation Losses in the waveguides should be minimum. Thus for fabricating the passive devices, it is necessary to achieve a straight waveguide with low propagation losses. High losses in the passive structure are undesirable as combined with the radiation losses in the ring resonator as described earlier would make these ring-resonators of limited use. Straight waveguides were thus fabricated and propagation losses were measured from these straight-guides using optical low-coherence reflectometry (OLCR)[130]. The results on measurements are presented in Fig. 4.10. The waveguides without hydrogenation show losses as large as 28 dB/cm, hydrogenation is thus necessary for the passive structures. Thus, throughout this work, the level of hydrogenation was calibrated for passive structures to maintain least possible propagation losses for straight waveguides. The propagation losses with calibrated hydrogenation were reduced to as low as 1.6 dB/cm as shown in Fig. 4.10.

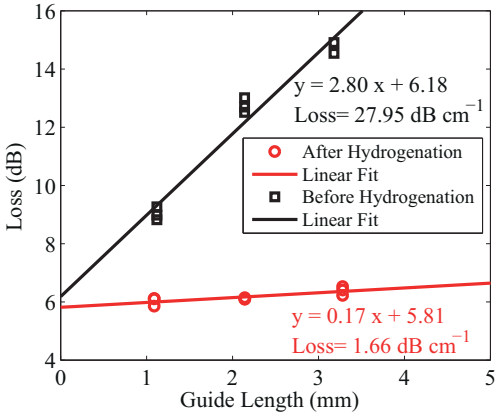

FIGURE 4.10: Evaluation of propagation losses in straight passive waveguides using OLCR. The black line shows the un-hydrogenated waveguides where as the red line (circle data points) represent hydrogenated waveguide.

Radiation Losses need to be estimated and minimized to find the lowest possible ring radius. The OLCR measurements were also performed on semi-circular waveguide structure (as shown in Fig. 4.11(a)) to evaluate the radiation losses that are expected

to occur in the ring-resonators. To evaluate the radiation losses the total loss due to structures at various radii were measured and then the propagation losses evaluated in straight waveguides were subtracted for each length of the semi-circular waveguide. The radiation losses extracted from these structures are presented in Fig. 4.11(b). The radiation losses are seen to decrease exponentially settle down to a constant value after a ring radius of 300 μm. This is an important result which defines the radius of curvature and hence the minimum footprint of the final device. Due to the exponential scaling of the radiation losses with the radius of the ring, it would be useful for the ring resonators to take a radius more than 300 μm. The radiation losses are expected to vanish for large ring radius (above 800μm), however finite losses are still observed which may be due to fabrication related issues.

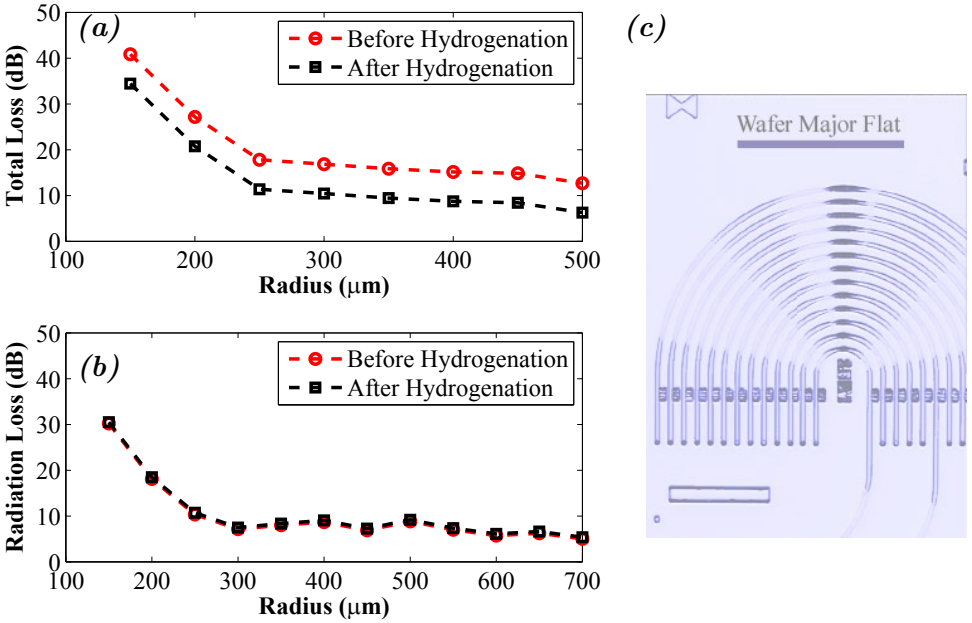

FIGURE 4.11: (a) Total loss as a function of radius of the semi-circular waveguide. (b) Extracted radiation losses from the waveguides. (c) Fabricated semi-circular structures for evaluation of radiation losses in the ring resonator.

This in an important result as it imposes a minimum radius that a ring resonator can achieve in order to have low losses. Severe radiation losses are undesirable and will limit the use of resonator as a filter, thus a radii of 400 μm is chosen for next generation of ring resonators.

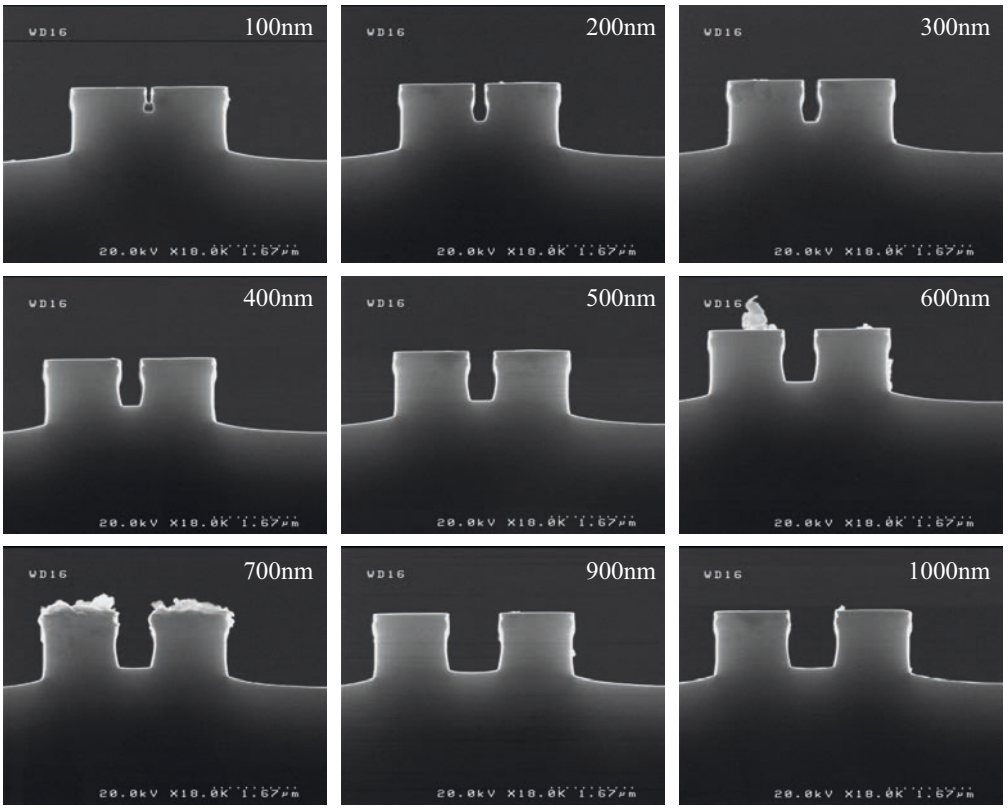

FIGURE 4.12: SEM images of coupler region with various gaps between the rings and the optical bus measured before the regrowth step.

4.3.2 Evanescent coupler with racetrack

A second feature of the desired passive device is a directional coupler. Simulation on the splitting ratio using the racetrack reveal that it is possible to tune the splitting easily with a short range of coupler lengths if the coupling distance is small (see Fig. 4.9). One of the technological problems, as discussed earlier, is the etching of gap between the waveguides. The etching should be deep enough to etch the guiding later completely between the ring and the bus to allow low-loss evanescent coupling. It is known from the fabrication of grating layers on the DFB devices that etch depth in short gaps is much smaller than the expected etching depth. Devices were fabricated to measure the etching depth between the waveguides at different gaps. The etching depths for various gaps were measured using the SEM micrograph (see Fig. 4.12). A total etching of 1.5 μm was performed in a single step. The etch depth in the gap between the waveguide is smaller for small waveguide gaps. Thus, for smaller coupling distances, it would not be possible to obtain a low loss evanescent wave coupler. The designed gap is plotted for various measured values of etch depth in the gap and is presented in Fig. 4.13, where

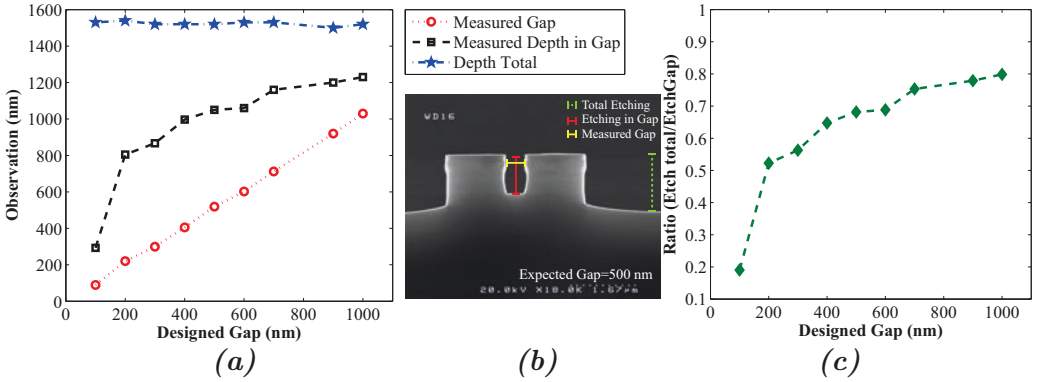

FIGURE 4.13: (a) Observed gap vs expected gap showing a linear relation (shown in red), the etch-depth in the gap as a function of expected gap (in black). (b) SEM image of an etched mesa after restoration illustrating measurements of gap and etch-depth in gap. (c) The ratio of the measured depth in the gap with the total etching as a function of expected gap.

the measurement extraction procedure is shown in Fig. 4.13(b). Fig. 4.13(a) proves that the etch depth for the small gaps is much lower than the etch-depth for the higher gap for the same net-etching on the wafer. A low gap between the guides is possible by performing a very deep etching of the mesa structures on the wafer. In addition the ratio (see Fig. 4.13(c)) between the etching far from the mesa structures and the gap is seen to produce an increase in logarithmic fashion, saturating for very wide gaps as the depth of mesa.

From the analysis of Fig. 4.13(a-c) it is clear that, gaps below 400 nm would be of high-risk and may pose problem in technological feasibility. It is possible to increase the etching depth in gap by increasing the total etching of the mesa but very deep mesa etching is also undesirable as it would pose problems at the regrowth step. The ratio between total etch and the etching depth in the gap presented in Fig. 4.13(c) can be used to calculate the minimum required total etching, for a given gap between the guides, which would allow the etching of the guide layers completely from the gap region. As an example, for a 400 nm gap between the guides a ratio of at least 0.5 would be required. This means that to etch 600 nm between the waveguides a total etching depth of 1200 nm would be required. This is another important result which gives twofold information. Firstly, it sets the minimum gap that would be possible for a given mesa etch depth. Secondly it gives an information on the depth of mesa etch to be performed. For practical purposes a nominal mesa etching of 1200 nm is selected which corresponds to a gap etch depth of 600 nm for a gap of 400 nm. This etching depth between the gap is sufficient

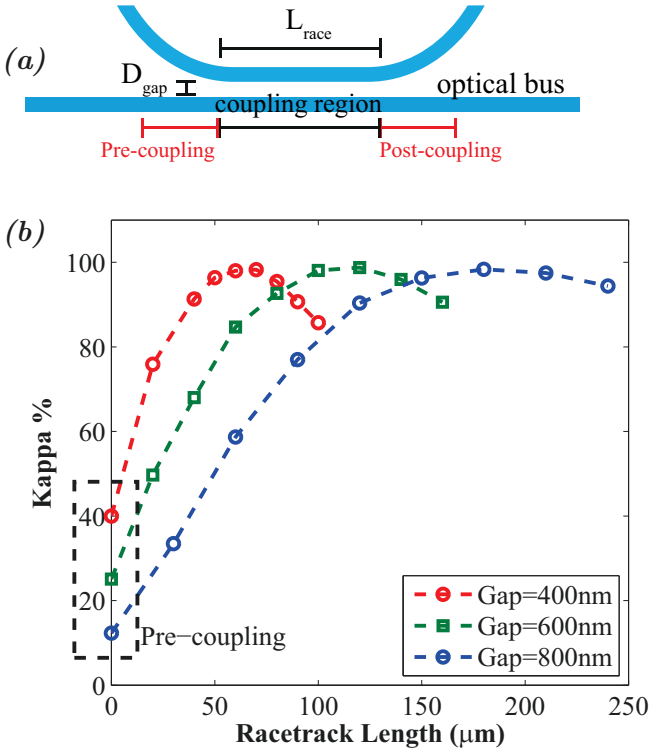

FIGURE 4.14: (a) Layout of the optical coupler tested experimentally. (b) Coupling efficiency from the racetracks to the ring resonators as a function of racetrack lengths for different gaps between the waveguide and the ring.

to etch the guiding layer between the waveguides. Thus, waveguide gaps of 400, 600 and 800 nm are selected for future devices.

Passive directional couplers are fabricated to test the coupling efficiency and splitting ratio. The coupling efficiency of the couplers following the coupling scheme as shown is Fig. 4.14(a), were extracted and are presented in the Fig. 4.14(b). It is seen that as compared to the simulations (see Fig. 4.9) the coupling efficiency is similar to the simulated values of given coupling gap and coupler length. There is a coupling offset in the measured couplers. This offset is attributed to the pre-coupling that occurs in the pre-coupling region indicated (in red in Fig. 4.14(a)). Similarly there is a post coupling which occurs on the other side of the coupler. This can be adjusted by assuming an effective length of the coupler. Nevertheless, the fabricated couplers show expected behaviour.

4.3.3 Ring resonators

From the above tests on the radiation losses, the information on the critical ring radius for low radiation losses is obtained and the gap between the waveguides for the

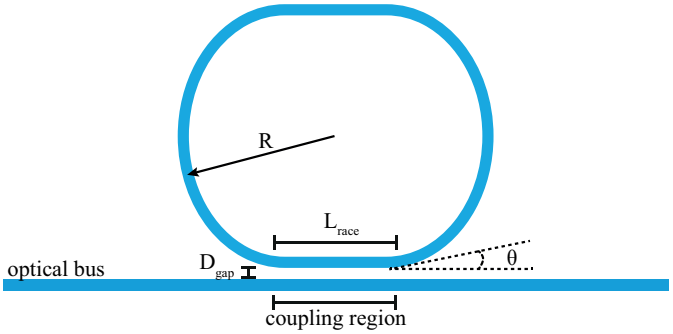

FIGURE 4.15: Schematic of a ring-resonator of radius R with race-track length L_{race} coupled to an optical waveguide with a gap D_{gap}.

directional coupler are obtained. These result form a fundamental basis for fabricating an efficient ring resonator filter on InP PIC platform. Using this information ring resonators were fabricated with the technology described in Sec. 4.3. The structure of the device is shown in Fig. 4.15, where R=400 μm, $D_{gap} =$ 400nm, 600nm, *and* 800nm. L_{race} is selected based on the simulation (see Fig. 4.9) for the specific D_{gap}. Ring resonators

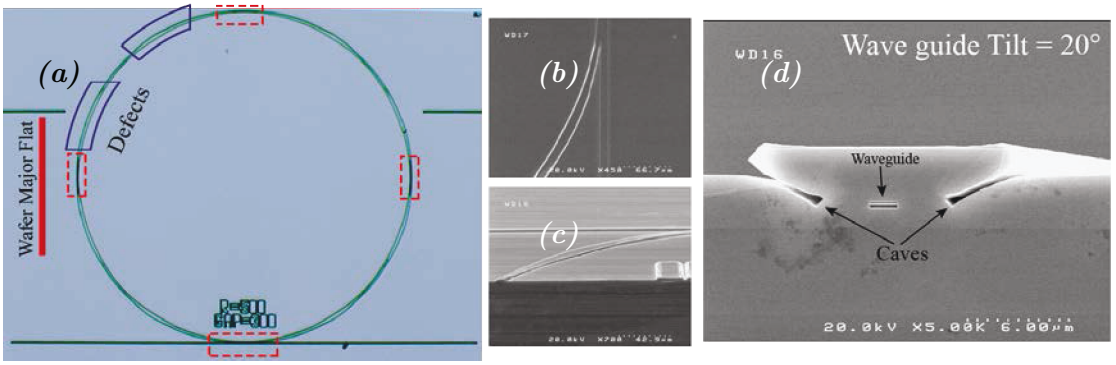

FIGURE 4.16: (a) Optical micro-graphs of fabricated ring resonator showing defects in the waveguide widths at specific angles. (b,c) SEM micrograph in plane view of these specific regions. (d) SEM of device cross section showing the waveguides and "caves" near the waveguide at an angle of 20° from the major flat of the wafer.

are fabricated using the passive device technology, optical micrograph of one such ring resonator is presented in Fig. 4.16(a). Observations under an optical microscope of these ring resonator reveals certain anomalies on the surface of the regrown structures. Firstly, the surface defects parallel to major flat and at angle of 90° from the major wafer flat are observed (red dashed boxes, Fig. 4.16(a)). Secondly, the width of the waveguide is not uniform and varies as a function of angle with respect to the main wafer flat (blue boxes, Fig. 4.16(a)). SEM observations are performed on these ring resonator to investigate the origin of these anomalies and are presented in Fig. 4.16(b,c). The surface defects parallel to (and at 90°) do not appear in the SEM observations. A closer evaluation of variation in

waveguide width using the SEM reveals that these defect are actually improper regrowths manifested as "*caves*" around the waveguide as shown in Fig. 4.16(d). These defects in the rings may account for the excess loss observed in semi-circular structures 4.11.

This behaviour may arise due to certain technological steps, for example due to improper restoration after the dry etching process. They may also occur due to the condition of regrowth of InP while forming a buried structure. Thus detailed tests on restoration process and regrowth were thus performed to eliminate these waveguide deformations, which may contribute to excess losses in the ring resonators. As these defects occur between a range of specific angles with respect to the main flat, it is necessary to test the restoration and regrowths at these particular angles. The test structures fabricated for this study, presented in Fig. 4.17, consist of tilted waveguides at angles from 0° to 90° with respect to the main wafer flat.

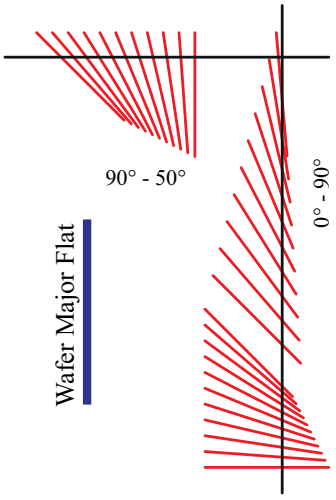

FIGURE 4.17: Test structures fabricated to study the excess losses arising in the ring resonators due to orientation of the guides. The black lines indicate the cleaving marks to observe the tilted waveguides.

4.3.3.1 Restoration tests

Waveguides were fabricated using the mask layout shown is Fig. 4.17. Test were performed on the restoration of the tilted and etched mesa structures with various mesa restoration methods at a standard regrowth temperature of 610°C and growth rate of 20 nm/min. The distance of the cave structures were measured from the etched mesas for each restoration procedure. The measurements of distances (in μ) between etched mesa and the caves from these test are presented in Table. 4.2, and a single measurement at 20° is shown in Fig. 4.18. The restoration of the etched mesa does improve for bromine but does not contribute significantly to the caves. The caves are found to be present near the mesa structures irrespective of the restoration procedure used.

The measurements on waveguides titled at various angles indicate an improvement with Bromine as the zone of presence of the caves is reduced. A Bromine restoration is usually very fast and may results in etching the mesa. To sum up, it can be concluded

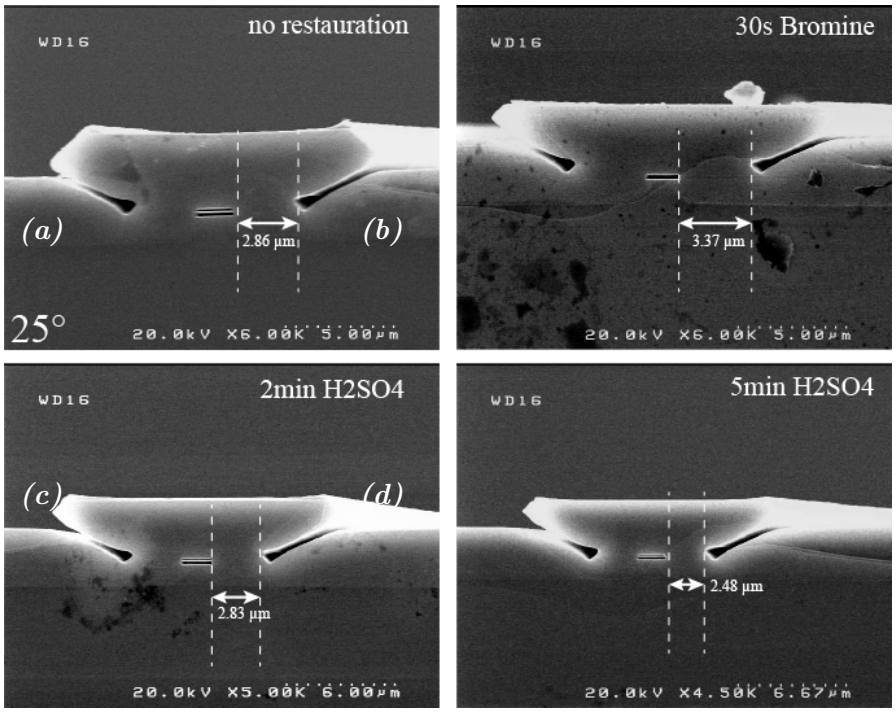

FIGURE 4.18: Test for restoration using bromine and sulphuric acids for a waveguide tilt of 20°, showing the distance between the waveguide and *the cave*

from this study that the restoration has no or little impact on the presence of cave structures.

4.3.3.2 Re-growth tests

The caves are present at only certain angles with respect to the major flat of the wafer and restoration has no or little effect on the caves. Tilted waveguides were fabricated and regrowths were performed at various regrowth conditions in temperatures and speed of regrowth to see its effect on the formation of caves.

Both the temperature and growth speed play an important role on regrowth of the titled structures and the caves can be removed by either lowering the temperature of regrowth or by reducing the speed of re-growth on the wafer. The analysis of the origin of these caves was done by growing markers layers at given thickness of regrowth. Figure 4.19, show a comparison of growth of InP between straight waveguide with a waveguide tilted at 25° at a temperature of 610° and growth speeds of 20 nm/min. The scaling of markers is found to be different for two different tilts. At a tilt of 25° the growth is favoured for (311)B axial direction of the crystal, thus propagating a growth

Distance of the *"Cave"* from waveguide (in μm)

Angle	No Restoration	H_2SO_4 2-min	H_2SO_4 5-min	Bromine 30-sec
10°				
15°	4.35	3.21	2.38	
20°	2.82	2.76	2.31	3.36
25°	2.86	2.83	2.48	3.37
30°	2.95	2.93	2.61	3.52
35°	3.80	3.76	3.14	4.42
40°	6.00	6.01	5.18	
45°-60°				
65°	5.11	4.91		
70°	3.23	2.99	3.24	4.07
75°	2.59	2.53	2.60	3.60
80°	2.68	2.57	2.73	3.28
85°	3.63	3.91	2.92	
90°				

TABLE 4.2: Test of restorations for presence of caves at various angles with respect to the mesa normal to the main flat.

Regrowth Conditions

Type	Temperature	Speed	Caves
BRS	610°C	20 nm/min	Present
BRS	610°C	7 nm/min	Absent
BRS	595°C	20 nm/min	Absent
BRS	625°C	20 nm/min	Present
SiBH	610°C	20 nm/min	Present within small angle ranges

TABLE 4.3: Test of regrowths for presence of caves at various regrowth conditions.

defect and creating a cave. Reducing the speed or the temperature of the regrowth relaxes the growth, which then scales normally like a straight guides even at high tilt angles as shown in Fig 4.19(b).

The propagation and radiation losses were measured again for different regrowth conditions. The mesa etch restoration was retained to 2-min H_2SO_4. The propagation and radiation losses measured from the hydrogenated straight waveguides are presented in the Fig. 4.20. The propagation losses are not perturbed due to the change in regrowth temperatures. A change of about 2 dB in radiation losses is observed, which accounts for the loss caused by scattering due to the improper regrowth at the cave regions. This change is not very significant for the actual losses in the ring resonator which change by a small amount.

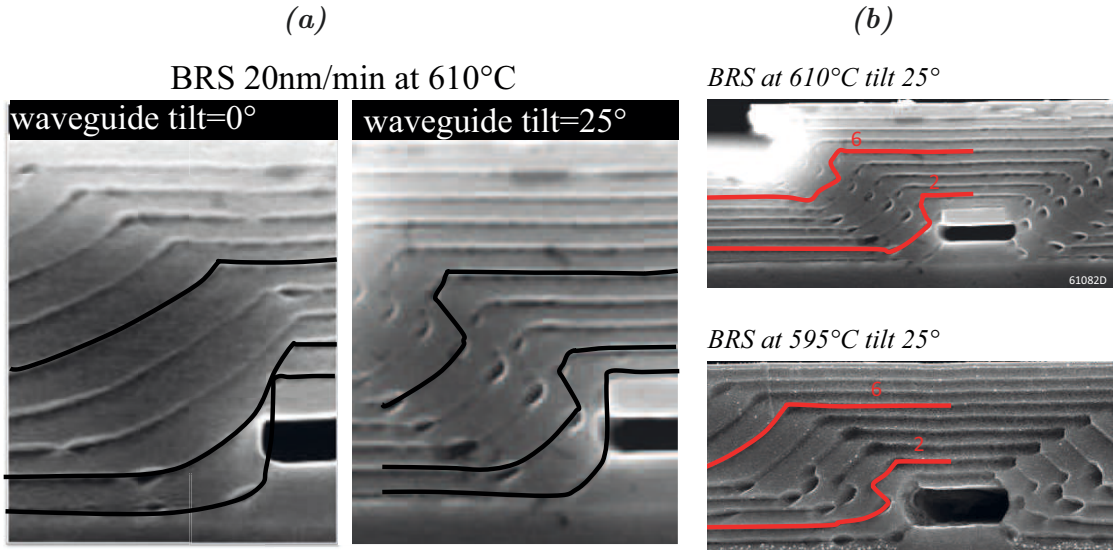

FIGURE 4.19: (a) Test of regrowth direction using markers reveals the points from where the defect in the growth starts to nucleate. (b) Regrowth at low temperature (595°C) compared to standard (610°C) regrowth.

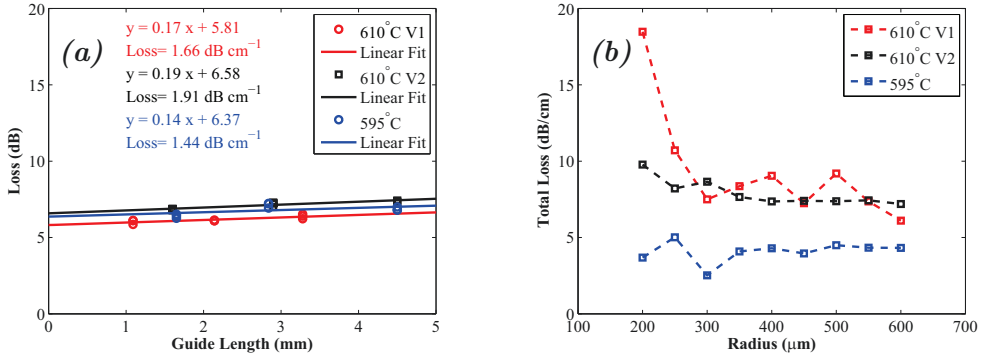

FIGURE 4.20: (a) Propagation losses for various regrowth temperatures. (b) Radiation losses at temperatures of (595°C) compared to standard (610°C) regrowth.

4.3.4 Conclusion on ring resonator fabrication

Two different tests were performed to understand the excess losses in the ring resonators. Firstly, the restoration of the mesa etching was tested and again the regrowth conditions were varied. The restoration of the mesa structure is not seen to play a significant role in inducing excess losses. A change in losses by a factor of 2 dB to 3 dB is indeed observed as a function of regrowth conditions. The regrowth condition which reduce the excess losses are discarded as a significant improvement in losses is not observed. A deviation from the standard regrowth temperature conditions is not desired as the calibration of the MOVPE reactors is a long and cumbersome process, which

should be avoided. The slow regrowth is an alternative option but the regrowth time is increased by 3 times, which is not good for production. The ring resonators can thus be fabricated using the standard passive technology using the standard restoration of 2 mins H_2SO_4 and a regrowth temperature of 610°C at a growth speed of 20 nm/min.

4.4 Characterization of passive devices: ring resonators

Ring resonators were fabricated with a radius of 400 μm, for various lengths of racetracks(directional couplers) for selected coupling distance of 400 nm, 600 nm and 800 nm. The racetrack length for each of these coupling distance was selected based on the analysis performed for directional couplers (see Fig. 4.14), such that the combination of particular coupler gap and coupler distance allows a tuning of the coupling coefficient from 0 to 100%. With this tuning range of κ, it would be possible to achieve a large range of filter characteristics. At the same time it should be possible to achieve filters with high on-off ratios and high filter slopes.

4.4.1 Hakki-Pauli spectra

Optical Intensity transfer functions of the ring resonators can be measured by passing TE-polarised white light or a wavelength sweep from a tunable laser through the input port and measuring the optical spectrum at the output using a high resolution OSA. The schematics of this measurement in shown in Fig. 4.21. The measurement of these spectra can be used to extract several important information about the ring resonator performance such as the coupling coefficient and the ring-losses by fitting the theoretical values curves. A typical measured intensity transfer function of the ring is presented in Fig. 4.22(a), showing the dips corresponding to the resonance condition of the ring resonator.

The on-off ratio provided by the ring resonator when used as a filter can be directly extracted from the HP-spectra by measuring the difference between the maximum and minimum intensity in the observed spectrum as shown in Fig. 4.22(b). The on-off ratio, as stated earlier is an important quantity as it would determine the amount by which the 1-bit will be suppressed with respect to the 0-bit. on-off ratios of ring resonators with different racetrack length and coupling distances were measured from the HP spectra

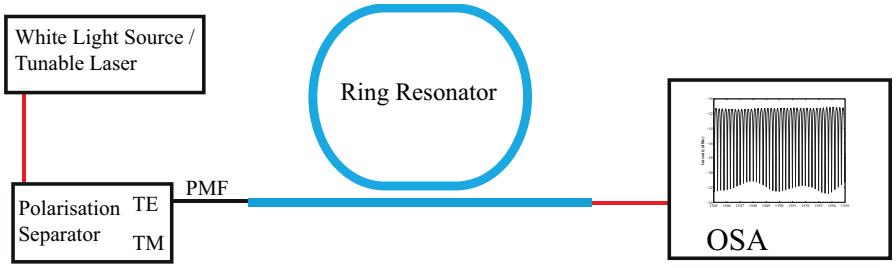

FIGURE 4.21: Schematics of the Hakki Pauli Spectrum measurement.

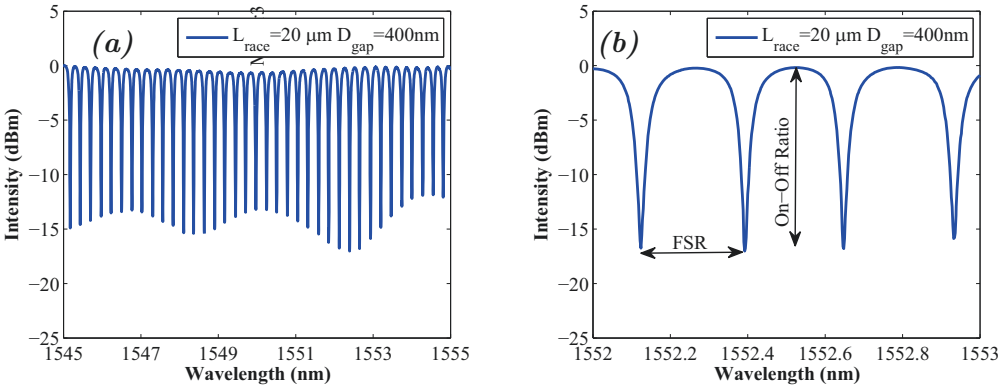

FIGURE 4.22: (a) Optical intensity transfer function of a ring of radius 450 μm with a coupling distance of 400 nm and a racetrack length of 20 μm. (b) Zoom of the same measurement indicating the FSR and on-Off ratio

and is presented in Fig. 4.23. This ratio follows the same trend as the coupling ratio presented in Fig. 4.14. Firstly an on-off ratio of more than 15 dB can be observed for each of the coupling distances, which would prove to be vital to replace the commercial filter. And secondly, the on-off ratio can be tuned by tuning the coupler length, which means using a certain tuning mechanism the on-off ratio can be increased. It is noticeable that these ring resonators were not at the critical-coupling condition. To obtain the critical-coupling condition the losses in the ring should be equal to the coupling factor. This can be only achieved by adding a gain section to the ring resonator to compensate and adjust for undesired losses in the ring resonator (tune the loss in ring resonator).

Another very important quantity is the slope of the filter. The slope of the filter would determine how much chirp of the laser can actually be accommodated by the filter to suppress the 0-bits during the transmission. A laser with low chirp would thus be most suitable with a filter having a very sharp slope and a laser with larger chirp can be used with a filter with smaller chirp. The slope of the filter is strongly related to its on-off ratio for a given radius of the ring and a low slope will always be accompanied

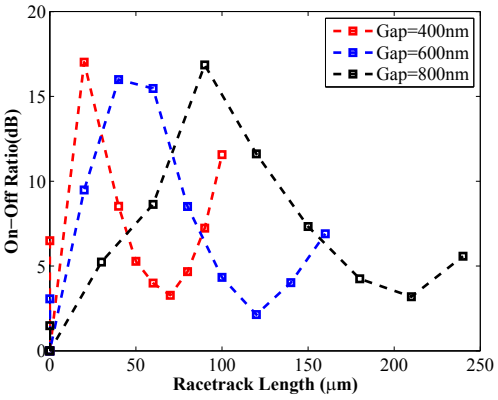

FIGURE 4.23: On-off ratio for ring resonator as a function of racetrack length

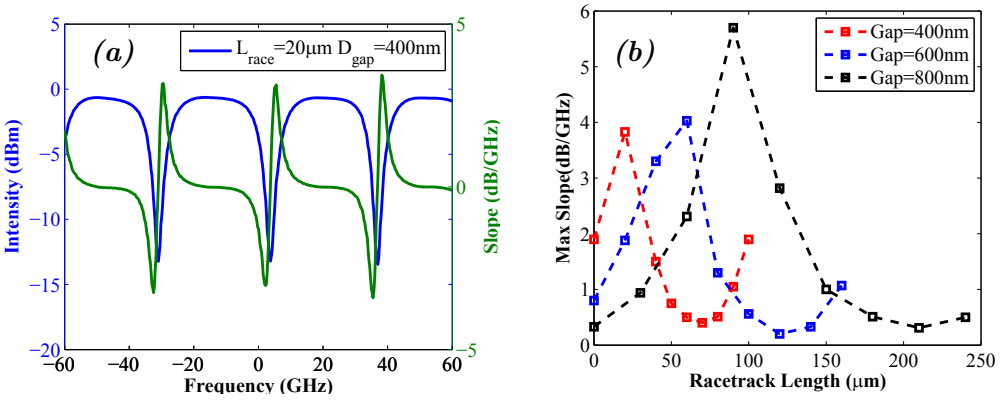

FIGURE 4.24: (a) Slope of filter with racetrack length 20 μm and a coupling gap of 400 nm. (b) Racetrack lengths vs slopes for different coupling gaps.

by a low on-off ratio. This might limit the use of filters with lasers having very high chirp as the relative suppression of the bits will not be very efficient. The slope of the filter can be evaluated by taking the first derivative of the intensity with respect to the frequency in the acquired optical spectrum. The slope extracted for each wavelength for a filter with a racetrack length 20 μm and a coupling gap of 400 nm is shown in Fig. 4.24(a). These slopes are extracted for various racetrack lengths for ring resonators with different coupling gaps and are presented in Fig. 4.24(b). Figure. 4.24(b) shows that it is possible to reach any value of slope by for a given coupling distance by adjusting the corresponding coupler length. It enables to design a filter which can be adapted to specific laser chirp value.

4.5 Combination of low chirp laser and ring resonator

The transmission experiments discussed in Sec. 3.5.4 shows the impact of a free-space passive etalon filter on the eye patters and transmission behaviour. Having fabricated a ring-resonator which shows excellent optical properties it is necessary to evaluate the transmission quality with the ring resonator.

4.5.1 Tolerance in filtering

An important concern is the tolerance of the bit error rate and dynamic extinction ratio with respect to the tuning of ring resonator as has been discussed in Sec. 3.5.4. It has been demonstrated earlier, for the etalon filter with a slope of 1 dB/GHz, that the temperature can be tuned in range of $\Delta T = \pm 0.4°C$ (see Fig. 3.40). This tuning range will depend on the slope of the filter and is expected to be inversely proportional to the filter slope. The tuning range and extinction ratios with the ring resonator are measured for slopes between 1 dB/GHz and 6 dB/GHz and are presented in Fig. 4.25. In B2B condition the DER is seen to scale with the slope of the filter slope. The maximum DER is obtained for filter slopes of 4 and 6 dB/GHz as shown in Fig. 4.25(a). Similar behaviour is found after a fibre transmission of 65 km. These rings are selected using the information provided by the measurements on ring resonator slopes (see Fig. 4.24). The ring resonator at low filter slope of 1 dB/GHz does not offer a large on-off ratio and consequently the extinction ratio of the eye pattern (at 10 Gbps) is not seen to improve with this filter. A maximum extinction ratio of 5.5 dB is observed using this particular ring resonator. On the other hand the resonators with filter slope of 4 dB/GHz and 4 dB/GHz provides an on-off ratio in range of 10 to 12 dB and also shows considerable improvement of the extinction ratio, and a maximum DER of 10 dB is observed with these ring resonators. The tuning range for higher slope of filter is seen to decreased to about 0.3°C, at the same time the extinction ratio increases rapidly and can reach values higher than the etalon filter owing to its steeper slope as shown in Fig. 4.25(c) and (d). Thus, for transmission experiments filters with higher slopes are expected to show a better performance as compared to filters with low slopes.

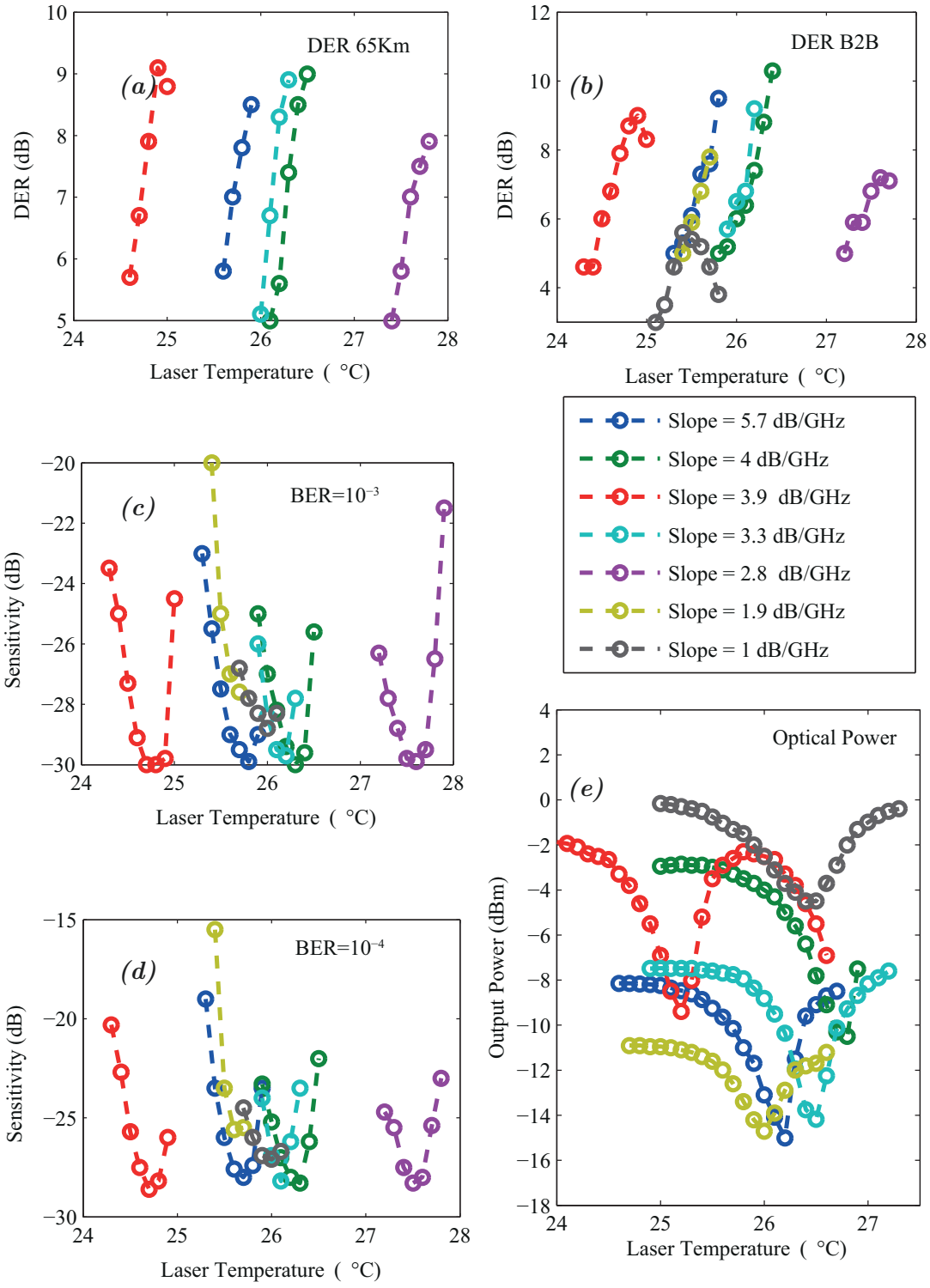

FIGURE 4.25: (a) DER for various ring resonator slopes after 65 km fibre transmission (b) in back to back condition. (c) Sensitivity measurement for ring resonator slopes at a BER of 10^{-3} in B2B condition (d) at a BER of 10^{-4} in B2B condition (c) Intensity transfer functions for ring resonator slopes at B2B condition

4.5.2 Transmission performance

As stated earlier, a selection of the correct ring resonator for the transmission study is crucial, as a high on-off ratio is strictly desired. Ring resonators with high on-off ratios were selected (from Fig. 4.23). At the same time, it is know that a high slope is necessary for the present laser in question, which shows a net chirp of 4 GHz at 100 mA. For a coupling gap D_{gap} of 600 nm at a racetrack length of L_{race}=60 μm, a filter slope of 4 dB/GHz can be achieved. Figure. 4.26 (a), shows the that the ring resonator at 4 dB/GHz slope shows an on-off of about 10 dB and the DER of the eye pattern can be as large as 8.5 dB at a detuning of 0.6°C from the filter maximum.

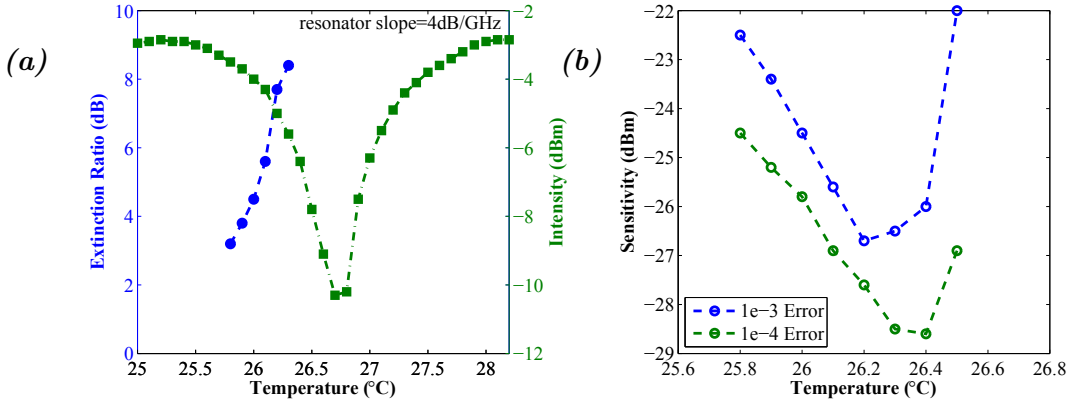

FIGURE 4.26: (a) Tolerance of the ring with respect to the detuning of the laser wavelength (expressed in temperature) for 4 dB/GHz filter slope (b) Sensitivity at given BER

A 10 Gbps NRZ OOK transmission experiment was realised again and the passive optical filter was replaced by the ring resonator. A PRBS sequence of $2^{31}-1$ bit long words was selected. The TE polarisation of light entering the ring was carefully maintained using polarisation maintaining fibres. The ring resonator with a slope of 4 dB/GHz (D_{gap}=600nm,L_{race}=60 μm) displays a maximum with respect to the laser wavelength corresponding to a laser temperature of 25.8°C. This temperature is varied in steps of 0.1°C to introduce a detuning between the laser and ring resonator. The BER and eye diagrams are captured for each detuning in B2B condition and are presented in Fig. 4.27.

The eye pattern for a ring filter is seen to expand as a function of the detuning. The dynamic extinction ratio after a filter detuning of 0.6°C is measured to be as high as 8.5 dB. This large augmentation in DER is due to the combination of low laser chirp

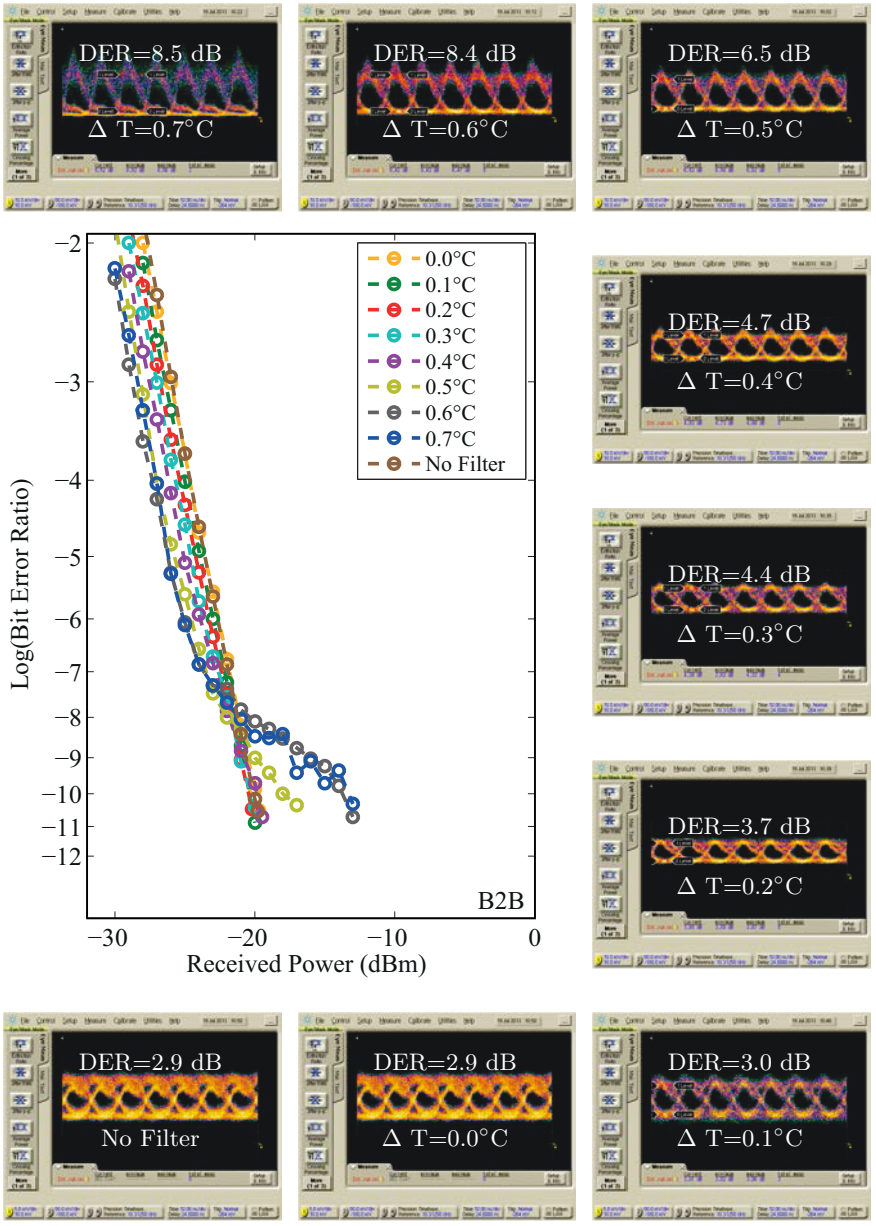

FIGURE 4.27: Optical transmission using a ring-resonator as a passive optical filter with radius 400 μm, gap between guides (D_{gap})=600nm and a racetrack length (L_{race})=60 μm corresponding to a slope of 4 dB/GHz at various detuning in B2B condition

and high slope of the filter. The measurements were repeated with a 65 km fibre span in the transmission channel and DER as high as 8.35 dB were again recovered as shown in Fig. 4.28. It is notable that the DER with and without the fibre remain equivalent for each of the detuning. This means that the given the low chirp of the laser and correct slope of the filter the optical transmitter can be made completely immune to the fibre dispersion.

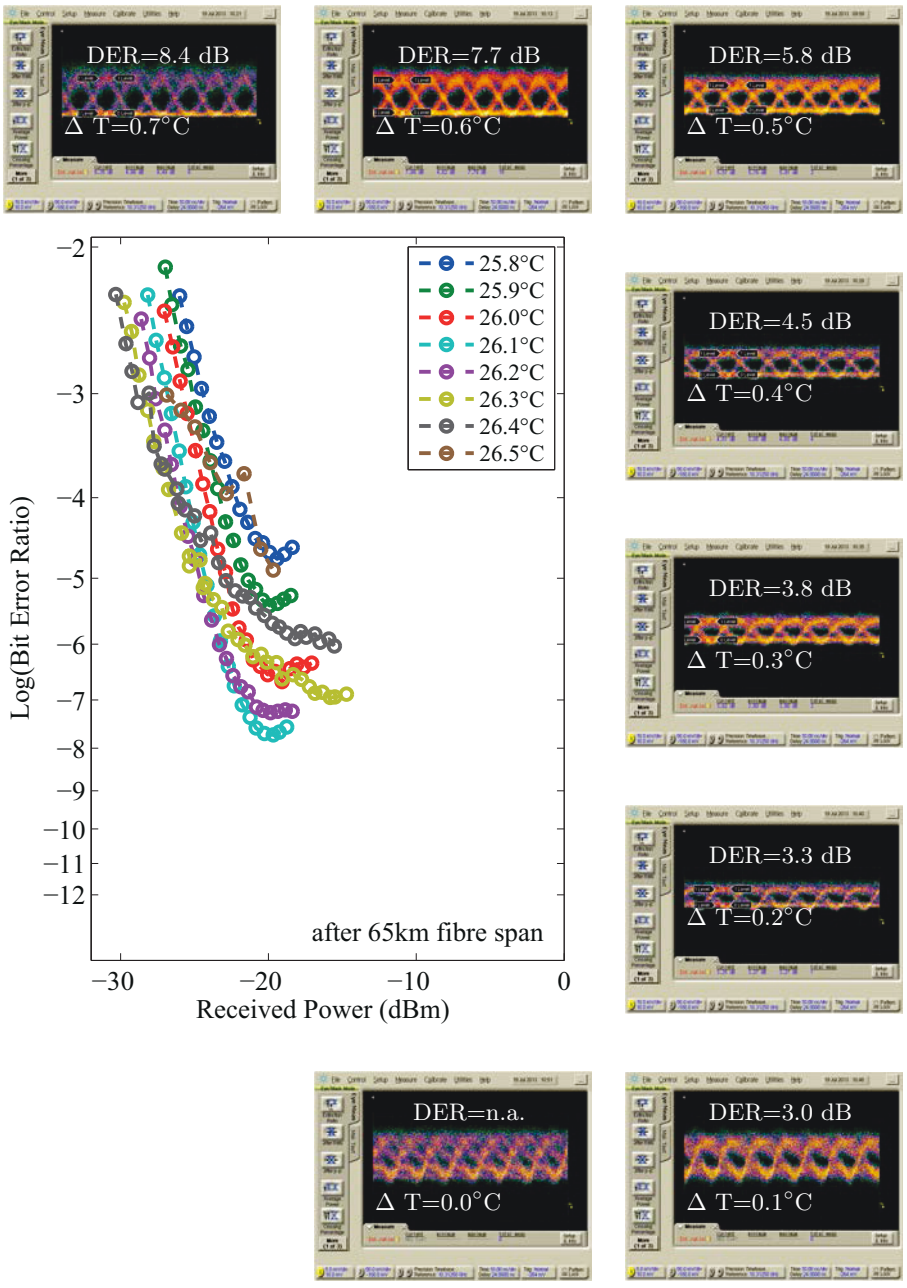

FIGURE 4.28: Optical transmission using a ring-resonator as a passive optical filter with radius 400 μm, gap between guides (D_{gap})=600 nm and a racetrack length (L_{race})=60 μm at at various detuning after a fibre span of 65 km

Measurements were performed for various distances at a fixed detuning of 0.6°C (see Fig. 4.29). As expected, the DER recovered for each of the distances remains above 8 dB and no significant change in the eye diagram is observed. The high DER are observed as a result of a low chirp of the laser (2 GHz) and the filter slope of 4 dB/GHz which is expected to result in relative suppression of about 8 dB for the 0-bit wavelength.

Using a ring resonator with a low slope with the same laser (adiabatic chirp of

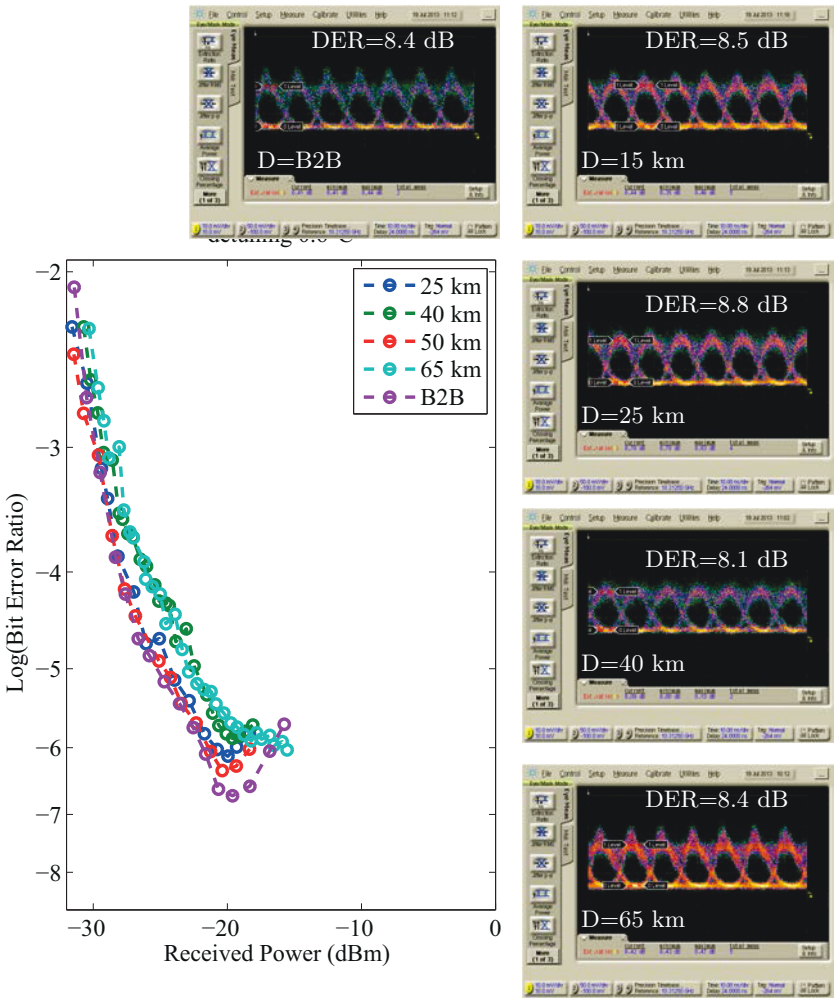

FIGURE 4.29: Optical transmission using a ring-resonator as a passive optical filter with radius 400 μm, gap between guides (D_{gap})=600 nm and a racetrack length (L_{race})=60 μm at at a fixed detuning of 0.6°C after a fibre spans from 0-65 km

2 GHz) results in lower dynamic extinction ratio, as the relative suppression of the 0-bit with respect to the 1-bit is around 4 dB leading to a maximum dynamic extinction ratio in range of 4-5 dB.

4.6 Integration of QDash DFB with ring resonator

In previous sections bit-error-ratios tests were realized using discrete components, i.e. a ring resonator and a low chirp QDash DML were used as two separate components. The discrete components give a very promising performance, which can be improved further if the coupling losses between the ring resonator and the DFB laser can be reduced. This can be realized using a Butt-Joint integration technology, where an active

devices can be integrated to a passive device on the same InP substrate wafer. The discrete components can thus be butt-coupled, resulting in reduction of losses.

4.6.1 Requirements for integrated device

To design an efficient integrated device, we will first list out the requirements for the light source and that of the ring resonator. Firstly for the laser, as in Chapter 3, it was shown that the p-doped QDashes give high output power and are capable of modulation above 10 GHz. In addition the α_H parameter was shown to be as low as 2. The chirp of the laser can be tuned by an efficient DFB design, yielding lasers with chirp as low as 2 GHz. An important point is the type of grating to be used, it was discussed in Chapter 3 that the gratings with low coupling coefficient would result in augmentation of the α_H-parameter, at the same time if the coupling coefficient is too high it would result either in a multi-wavelength laser or the laser chirp will be very large. Thus choosing the coupling coefficient is of prime importance. For the first test, a standard DFB laser design is selected as it was shown to yield low chirp and α_H-parameter. A $\lambda/4$ phase shift is selected for the present design.

For ring resonator filter several properties such as the on-off ratio, filter slope were discussed in Chapter 4. The design of ring resonator is thus based on the detailed analysis performed earlier.

1. Radius : For a compact device it is necessary to fabricate a ring resonator with a small radii. As discussed earlier the radiation losses for the rings below a radius of 300 μm increase exponentially. These losses start to saturate for the ring resonators above 300 μm. Thus it could be safely said that a radii of 400 μm (margin of 100 μm) would yield the least device footprint possible.
2. Coupler gap and racetrack lengths: again the gap between the ring resonator and the bus should be restricted to the values of 400 nm, 600 nm and 800 nm. At the same time race-track lengths should be adjusted in accordance with the gap between the ring and bus as had been discussed in Section 4.3.2.
3. Heating Resistances: It is rather preferable to tune the ring by increasing the temperature of the ring then to heat the laser in order to tune the wavelength. It is thus necessary to fabricated heating electrodes around the ring resonator.

4. In-ring Amplifier: An additional amplifier inside the ring is needed to tune the ring losses and to achieve critical coupling condition, if necessary.

5. Amplifier: SOA at the end of the ring resonator to compensate for losses and to amplify the signal obtained at the end of the device.

These characteristics would lead to the two class of devices as presented in Fig. 4.30. In both the designs a photo-diode at the rear of the DFB laser is added to avoid the anti reflection coating and the SOA at the end of the throughput port of the ring resonator would help to recover the optical losses suffered in the ring resonator. A passive taper is also introduced at the end of the SOA as active tapers have been seen to enhance the chirp behaviour of the device. The passive taper would be very useful to change the mode-shape and hence allow reduction of the power lost at the fibre coupling interface.

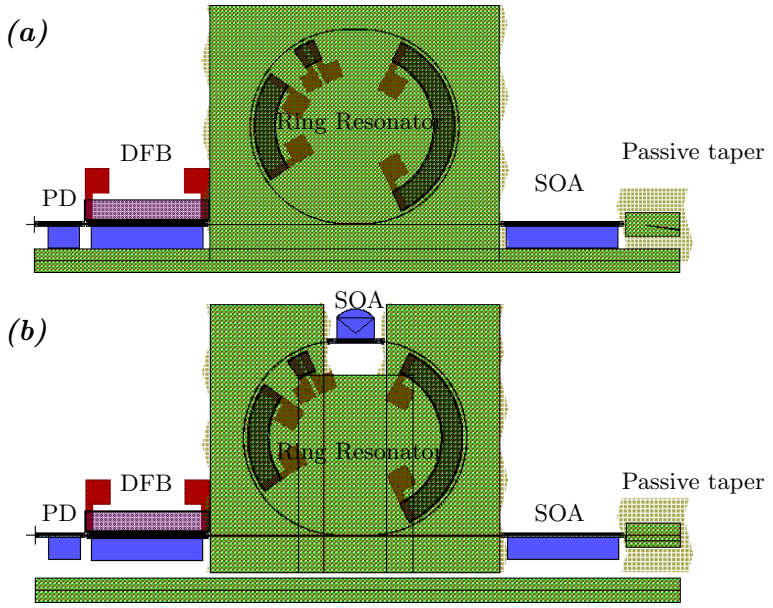

FIGURE 4.30: (a) DFB-Ring resonator integrated device layout with integrated photo-diode and passive taper. (b) DFB-Ring resonator integrated device layout with integrated photo-diode and passive taper and an in-ring amplifier to tune the losses in ring resonator

The ring resonator in the device presented in Fig. 4.30(b), is also supported with an in-ring amplifier. This amplifier would be used to tune the ring losses in order to achieve the critical coupling condition. The tuning of the wavelength in both the designs is achieved by heating electrodes present both near the DFB laser and the ring resonator.

4.6.2 Butt joint fabrication technology

The devices described in Fig. 4.30 contain the following components

— Active Components

QDash DFB Laser

QDash Photo-diode

QDash SOA

— Passive Components

Ring Resonator

Mode Shape Converters

An integrated device having both the active and passive components on the same substrate can be realized using a Butt Joint Buried Ridge Stripe (BJ-BRS) fabrication technology. The BJ-BRS technology is customized to fabricate these specific devices and involve following steps

1. ***E-beam squares*** The epitaxial wafer is firstly cleaned using concentrated sulphuric acid to clean the wafer. As this technology uses two or more electron beam (E-beam) lithographies, the first step is to etch the alignment marks for electron beam lithography. For this, 4 squared marks are patterned on the surface of the wafer using the photo-lithography, such that the intersection of these marks is at the centre of the wafer. These marks are then etched as 4 μm deep square holes in the wafer.
2. ***Grating Definition***: A 100 nm thick layer of SiO_2 is deposited on the wafer. The grating pattern is then defined using an E-beam lithography using the alignments defined in the E-Beam square step. The defined grating is then transferred to the SiO_2 using RIE and is carefully etched to the wafer surface using ICP till the depth of the grating layer (40 nm) is reached. The grating layer is then regrown with 300 nm thick InP using GSMBE.

FIGURE 4.31: Optical image of the epi-wafer after the definition of gratings

3. ***Butt-joint definition***: A thick layer of Si_3N_4 is deposited on the wafer and a second photo-lithography step is performed to define the areas in which the passive devices are located. In these regions the active region is etched completely and the etch depth is precisely recorded. The recorded etch depth is used to calculated the vertical structure of the passive sections to be grown in these zones. Also the vertical layer structure to be grown is precisely calculated on such a way that the passive waveguide is perfectly gingered with the active counterpart.

4. ***BJ regrowth - GSMBE*** : A GSMBE regrowth is performed to grow the passive part of the wafer with the calculated structure in Butt-Joint step. The residual Si_3N_4 on the active part of the wafer restricts the growth only to the parts which are etched for growing the passive structure. Over the Si_3N_4 the growth of poly-crystals occur which can be easily removed.

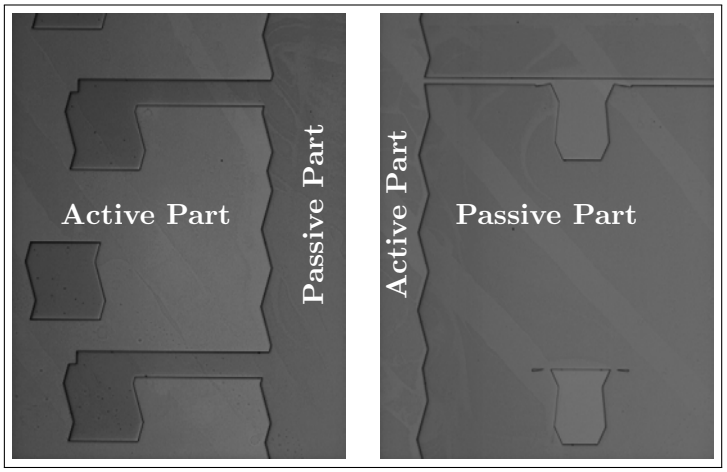

FIGURE 4.32: Butt joint definition showing the active and passive parts on the wafer. The darker regions are passive.

5. ***Lift off poly crystals*** The poly-crystals formed on the oxide layer during the GSMBE growth of the passive structures are removed by lifting-off the oxide layer. A cleaning with ultra-sonic cleaner is done in both HF and DI water to make sure that the poly-crystal impurities are completely removed from the surface of the wafer. The process following this step is the same as a buried ridge stripe technology.

6. ***Waveguide definition***: The waveguide are defined using e-beam lithography. For this a 200 nm thick oxide layer is deposited on the wafer surface. The e-beam mask is transferred to this oxide hard mask, and the mesa structures are

finally etched using ICP. An important point at this step is that the etching has to be accurately to a given depth calculated for the gap between the passive waveguide and the ring resonator (see Fig. 4.12). The etch-depth should also not too large to affect the active ridges.

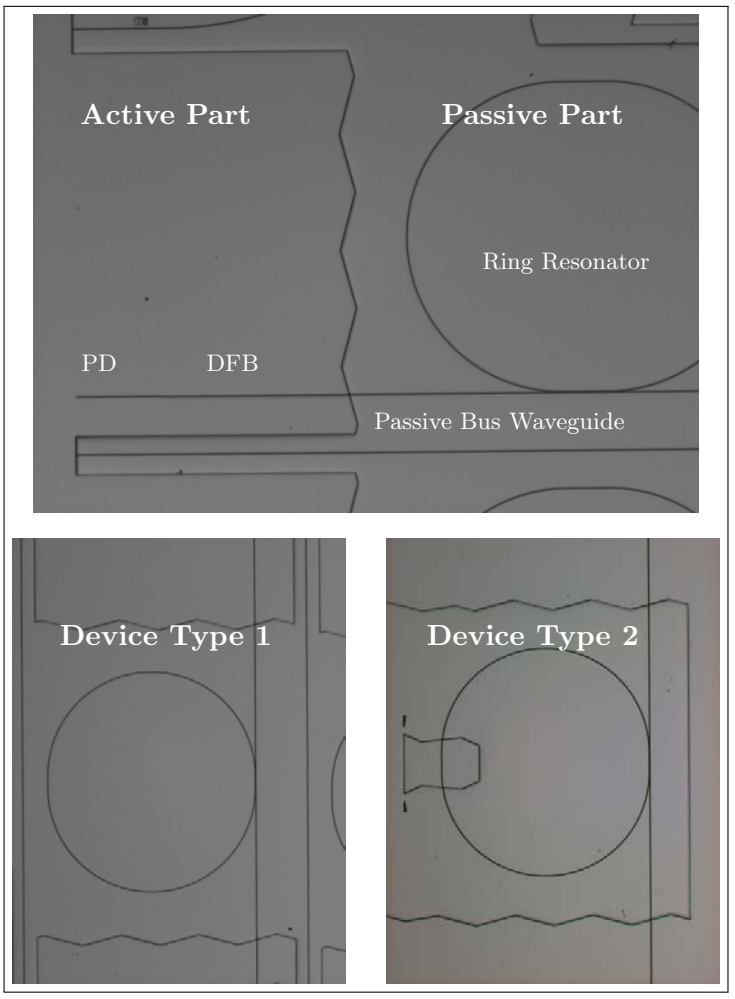

FIGURE 4.33: Optical images of the active and passive parts of the devices after the ridge definition

7. ***BRS regrowth***: A MOVPE regrowth of InP is then performed to deposit the p-InP over the ridges and bury the ridges under 2.5 μm thick InP. A 300 nm ternary layer of InGaAs is also deposited to facilitate the p-contact. The waveguides defined in the previous step are now buried.

8. ***Metallisation p-contact*** : Another lithographic step is performed to localize the areas in the active region where the metal contact is to be deposited. Metal deposition is performed on the active regions of the wafer. The wafer surface is

deposited with Ti/Pt/Au. Thus the lasers, SOA and photo-diode are provided with a p-contact in this step.

9. ***Implantation H^+***: The active parts of the wafer are also subjected to ion-implantation. Fo this the implantation areas are localized using a photo-lithography. In this case the passive area are protected with a thick layer of photo-resist.
10. ***Hydrogenation***: As had been discussed earlier, passive waveguides suffer large amount of propagation losses and the hydrogenation of these waveguides is necessary to reduce the losses in the passive waveguides. A lithographic step is performed to localize the passive section which are then passivated by hydrogenation.
11. ***Ternary etching***: The ternary layer grown in the MOVPE regrowth step is etched from certain areas of the passive section and some zones of the active section using another photo-lithographic step.
12. ***Heating Resistance and Contact***: A 200 nm oxide layer is deposited in order to insulate the heating metal from the wafer surface. The metallisation zones are localized using a photo-lithography and 300 nm thick Ni-Cr is finally deposited on the oxide. The oxide is then etched using an RIE step.
13. ***Substrate Removal - Contact N*** Finally the substrate of the InP wafer is removed using a chemical mechanical polishing and is provided with a Pt/Au n-contact.

The process thus requires three electron beam lithography steps, 8-photo-lithography mask steps and 3-regrowth steps. It can be noticed that the technology described here, deviates from the standard butt-joint technology. In the standard BJ technology the first step is the definition of the Butt-joint, to grow the active and passive structure on the same substrate. However this would pose a problem with the regrowth on the grating layer. The grating layer regrowth is usually doped with Be-ions to produce a p-type doping in the grating layer. If the BJ step is performed before the grating regrowth there is a risk of p-doped growth over the passive structure, which is not desired. To avoid this the gratings are defined before the BJ step.

4.7 Summary

This chapter develops a basis for active passive integration on InP substrate. The passive optical filters are studied with reference to the commercial filter used in Chapter 3. It analyses different passive filters and isolates the ring resonators as a viable approach for integrated filters. The ring resonators are then studied theoretically in details. This chapter then systematically develops step by step fabrication of the passive filter by isolating and solving the related technological issues. Firstly the waveguide losses in the passive section are reduced with calibrated hydrogenation from 28 dB/cm to 2 dB/cm. The radiation losses in the curved waveguide are studied to evaluate the minimum possible radius of the ring, which is found to be 400μm. The attention is then paid to the coupling schemes between the bus waveguide and the ring resonator. It is found from simulations that a directional coupler would be an ideal solution for such a coupling. Directional coupler with several coupling distances have been studied. The coupling distances of 400 nm, 600 nm and 800 nm are then selected based on experimental results. Ring resonators with a range of filter slopes are fabricated and tested for optical transmission. Filter slopes as high as 6 dB/GHz are observed with fabricated resonators resulting in on-off ratios as large as 20 dB. The filters with higher slope result in better transmission characteristics owing to their high on-off ratio. Further a butt-joint integration technology is developed within this chapter for an integrated laser-ring resonator assembly. The problems related to the realisation of butt joint technology are discussed.

Chapter 5

Quantum Dash Mode Locked Lasers for Photonics Integrated Circuits

InAs QDash based lasers grown on commercially favoured InP(100) substrate have been of significant interest in recent years. This material system has been used to perform several demonstrations for directly modulated lasers [13, 131] as well as for mode locked lasers (MLLs). MLLs based on QDashes have been studied extensively both as frequency comb generators [132] and as sub-pico-second pulsed laser sources.

It is therefore of great interest to monolithically integrate these frequency comb generators in PICs to fully exploit the unique performance of these lasers[133]. As QDash lasers exhibit a wide spectral envelope, in the form of a frequency comb, the prime interest is to enable the integration with other devices on the indium phosphide platform and a possibility to set the channel spacing with lithographic precision. SOAs integrated to quantum well based MLL have been previously demonstrated by Akbar et al. [134] and by Sato et al [135], but the radio-frequency (RF) linewidth of the Quantum Well based MLs remains in the mega-Hertz range, making them maladapted for many applications. On the other hand single-section QDash Fabry-Perot (FP) lasers exhibit RF linewidths as low as 10 kHz, making them interesting for low timing jitter applications.

A detailed study of an effective Bragg grating (BG) design that can be efficiently used to close the cavity without compromising the mode locking performance of the QDash laser is presented in the following sections. The approach of Bragg mirror used within this work, maintains a kilo-hertz order RF-line-width intrinsic to QDash Material system. As a demonstration of integration, a QDash-SOA is integrated and the amplification of optical power is demonstrated. The integration of QDash based devices on InP and a demonstration of the on-chip generation and amplification of optical frequency combs for telecommunication applications generated by single-section QDash based ML laser is discussed.

5.1 Quantum dash mode locked lasers

One of the very interesting features of QDs is a very broad emission spectrum, owing to a large gain-bandwidth. This broad gain spectrum, results in a large laser envelope in a FP cavity. Additionally, the QDash FP lasers show strong phase locking of the optical modes resulting in the self-pulsation of the optical intensity from the device. The QDash MLL have been investigated in both the two-section [136, 137] and single section [61, 138] configurations. Of particular interest are single section devices, which exhibit self-mode locking and self-pulsation. In QDash lasers the phase relations between the optical modes allows achieving typical MLL pulsations after propagation of the emitted light through a properly chosen length of standard single mode fibre.

5.1.1 Quantum dash single section MLL BRS

Single section QDash MMLs were fabricated using the BRS technology during the course of this work to study the impact of the number of dash layers on the phase noise and optical line-width of the laser. As stated earlier the QDash FP lasers exhibit a large optical envelop, the FWHM of this optical spectra typically ranges between 10-14 nm. The broad optical spectrum of QDashes FP is uniquely interesting as it acts as an optical frequency comb source for various telecommunication applications such as ultra-dense wavelength division multiplexing, or radio-over fibre applications. The acquired optical spectrum for a 400 μm long QDash FP laser is presented in Fig. 5.1(a). This length of the FP laser corresponds to a FSR of 100 GHz, thus providing frequency

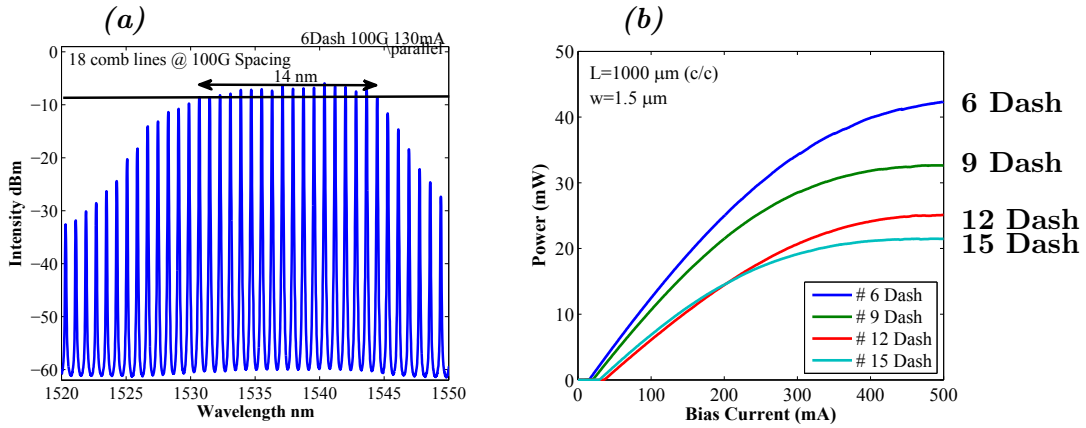

FIGURE 5.1: (a) Optical spectrum of a 400 μm long QDash FP MLLD showing 18 comb lines. (b)Light current characteristics of a 1000 μm long as cleaved FP QDash laser with a ridge withd of 1.5 μm for various dash layers in a DBAR structure

comb with a channel spacing of 100 GHz. The number of comb lines N within this spectrum can be calculated as $N = 2\pi f_{(Hz)}/\omega_r$, where $f_{(Hz)}$ is the full width at half maximum of the spectrum envelop in Hz and ω_r(in Hz) is the free spectral range. A typical QDash FP results in a FWHM of 12 nm or 1.48 THz, resulting in 16 comb lines at 100 GHz channel spacing, 25 comb lines at 60 GHz channel spacing, 38 comb lines at 40 GHz channel spacing and about 60 comb lines at 25 GHz channel spacing. The accurate control over the material quality and the know-how in the growth of the InAs/InP QDashes has allowed numerous demonstrations for MLL based on this material system. QD MLLs are grown with varying number of stack layers (from 6-15) and are systematically studied for the static and dynamic properties. The laser active region is thus composed of x-InAs QDash layers embedded in InGaAsP barriers in dash-in-a-barrier (DBAR) design [62]. The light current characteristics of 1000 μm long FP lasers with a ridge width of 1.5 μm are presented in Fig. 5.1(b) as a function of stack layers. The threshold current increases as the stacking is increased, at the same time the slope efficient decreases. This degradation in performance is in agreement with the measurement of modal gain and efficient on BA laser (see Table 2.1).

The optical spectra measured, as shown in Fig.5.2, at same current densities in similar length of BRS-lasers do not show much difference apart from the power coupled per mode which remains to be relatively higher for 6 and 9 dash stacks. At the same time FP lasers from such material also leads to a narrow RF line-widths of the order of tens of kilohertz irrespective of the stack layers (see Fig.5.3). The RF-linewidth is the

measure of phase noise between the various modes in the laser spectrum and thus can be taken as an effective measure of efficiency of mode locking. At this point it should be noted that the shape of optical spectrum observed on the OSA is highly co-related to the measured phase noise. For a low phase noise source a box shaped spectrum is usually observed.

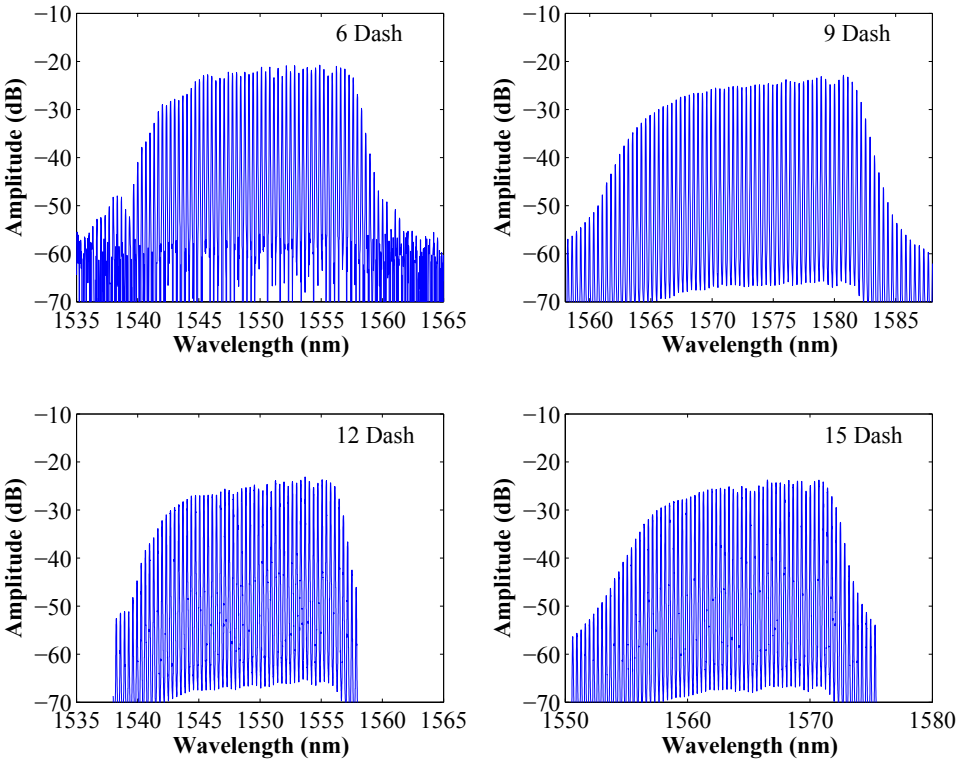

FIGURE 5.2: Optical spectra of a 1000 μm long as cleaved FP QDash laser with a ridge withd of 1.5 μm for various dash layers in a DBAR structure

Optical line-widths

One of the important optical properties which have been rarely studied for QDash MLLDs is the optical linewidth of these lasers. QDash MLLDs are expected to show an optical line-width in the orders of a few MHz as opposed to the optical line-width of conventional material which is in the range of hundreds of MHz. This improvement in optical line-width can be attributed to the strong locking of the optical modes. A systematic study of optical line-widths is performed and optical line shape is extracted using a high resolution optical spectrum analyser for various stack layers in DBAR structures. These linewidths are extracted at the centre frequency of the optical spectrum

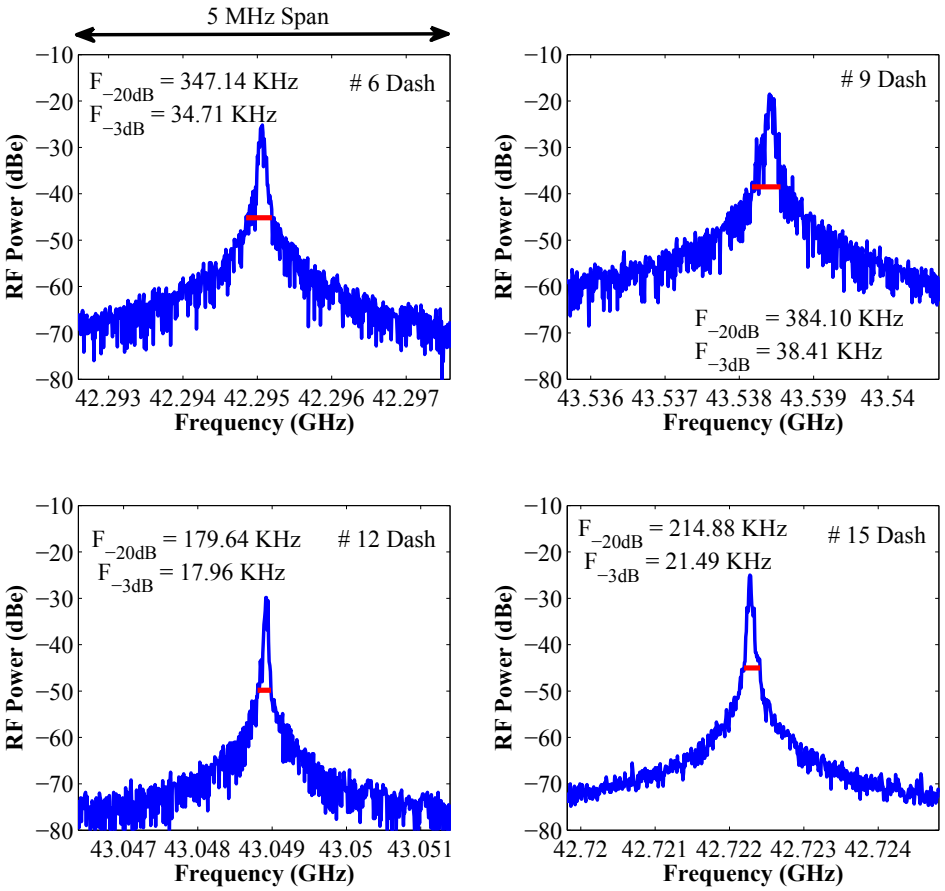

FIGURE 5.3: Radio-frequency linewidths of a 1000 μm long as cleaved FP QDash laser with a ridge withd of 1.5 μm for various dash layers in a DBAR structure

as they are expected to be the lowest at centre of the spectrum and are presented in Figure 5.4.

Despite the fact that the different stacking layers do not show a strong change in RF line-widths, the optical line-widths are observed to be larger for high stack numbers. The reason behind this effect has be to studied in details to be understood. However it could be said that the range of mode-locking with respect to be bias current of the lasers are larger with the lower stack layers. In addition it is observed that the optical line-shapes for higher stack layers are not purely Lorentzian in nature. There appears to be a shoulder to each optical mode. It is always possible to find certain small current ranges where the optical line-shape would be a Lorentzian.

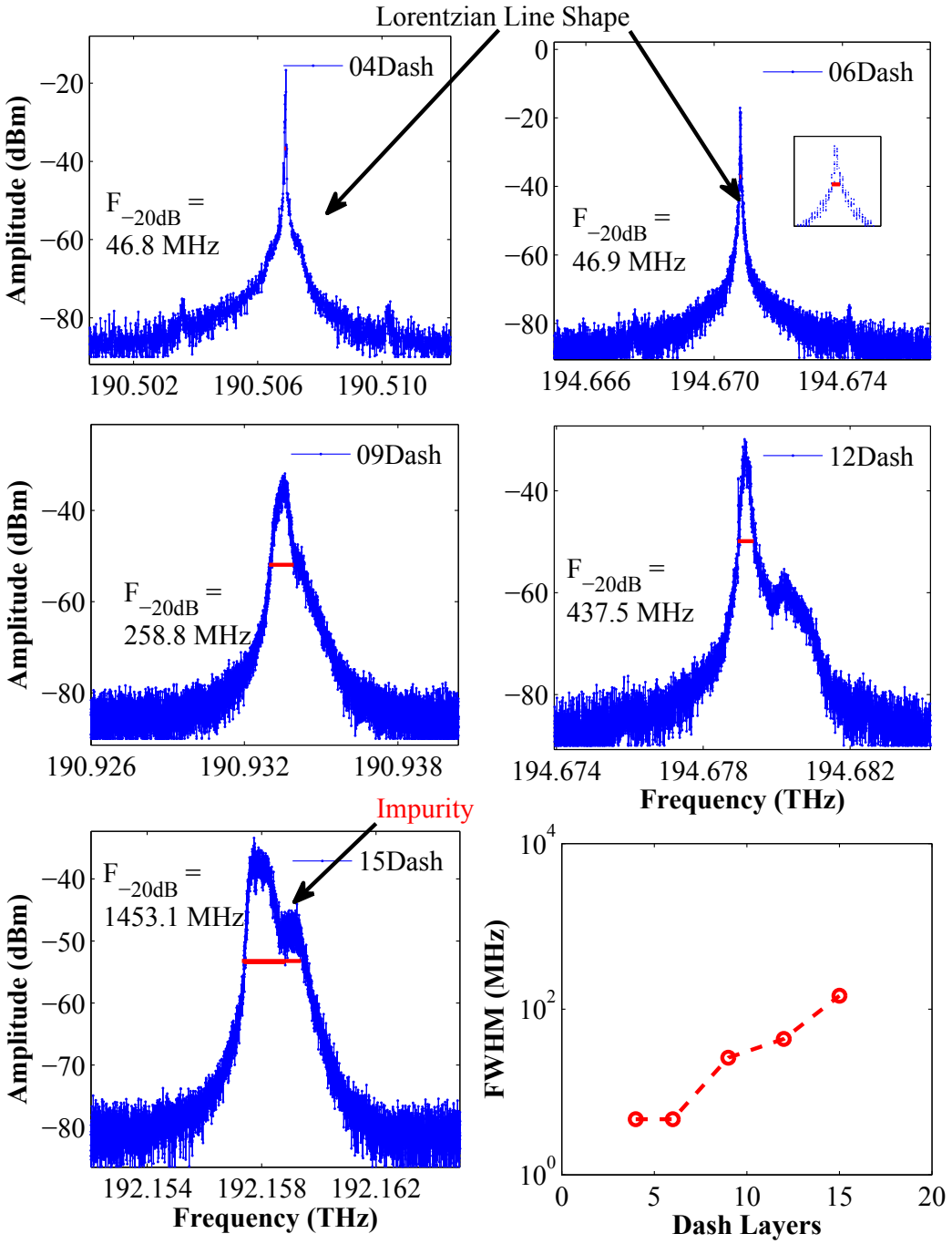

FIGURE 5.4: Optical line-widths of a 1000 μm long as cleaved FP QDash laser with a ridge withd of 1.5 μm for various dash layers in a DBAR structure

5.2 Quantum dash based mode locked lasers for PICs

For a FP laser with 6 stack layers, the threshold current as low as 20 mA and optical power output as large as 40mW can be achieved at 25°C as shown in Fig 5.5. A fast photo-detection of the signal emitted by the device demonstrates effective mode locking for operating temperatures up to 90°C, highlighting the potential of QDash lasers for uncooled operation. RF line-widths down to 35 kHz and emission spectrum FWHM up to 12 nm (∼1.5 THz) were measured for a large range of temperatures on FP lasers of length 1000 μm and ridge width 1.5 μm, as shown in Fig 5.6. These results demonstrate the robustness of frequency combs generated by QDash material.

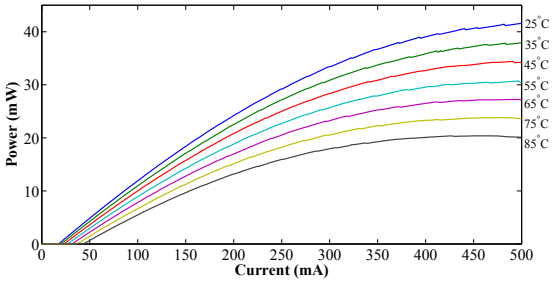

FIGURE 5.5: Light current characteristics of a 1000 μm long as cleaved FP QDash laser with a ridge withd of 1.5 μm at temperatures between 25°C, and 85°C, showing optical powers of up to 40 mW at 25°C

There are two direct ways of integrating these lasers on PICs. The first way is to close the FP cavity on a PIC using a very broadband and highly efficient Bragg-grating. In this case the effective length of the cavity is decided by the penetration depth in the Bragg grating. The challenge in this type of integration is to find an efficient Bragg grating design which would leave the optical spectrum and the phase noise properties of the laser unperturbed.

The second approach is again to use ring laser where the radius of ring resonator would define the FSR and thus the channel spacing of the laser. There are several problems related to the ring resonator approach. The first very evident problem with the ring resonator approach is the control of the clockwise and counter-clockwise propagating modes. This can be managed using a asymmetric reflectivity on either side of the bus wave-guide. The second problem is as seen from the passive devices on InP is that the radiation losses are very large below a certain ring radius (see Fig. 4.11). Thus large

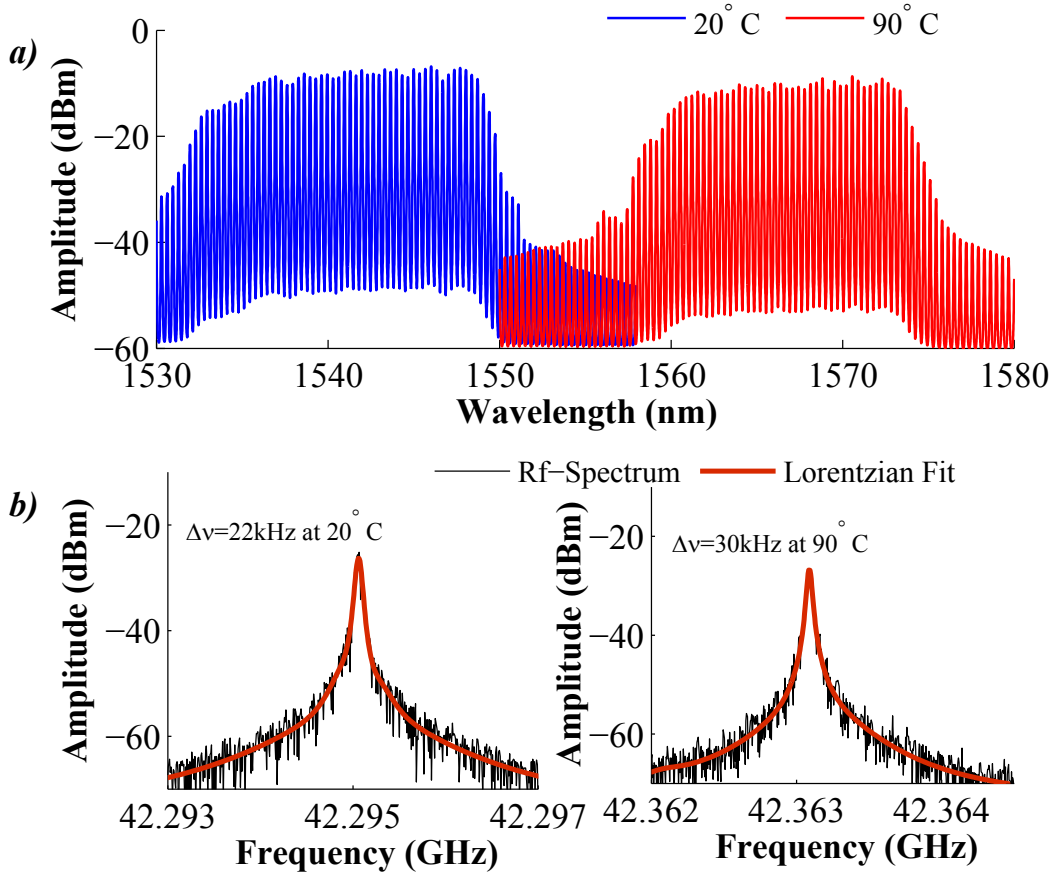

FIGURE 5.6: (a) Optical spectrum of the FP laser of 1000 μm length and 1.5 μm ridge width at 20°C, and 90°C and (b) corresponding RF line-widths

free spectral range would not be possible for this approach. However the ring resonator approach would prove to be very interesting for small repetition rates.

5.2.1 Distributed Bragg reflector design and theory

It is necessary to identify a Bragg reflector design and also the parameters of a Bragg reflector suitable to close the cavity of a FP laser, maintaining the envelope in the orders of 10nm to 12nm. The specific requirement for such a Bragg reflector is a large passband to allow the entire FP spectrum to fit in, as opposed to conventional for the DBR lasers, where it is preferable to have a very narrow passband allowing emission of a single wavelength.

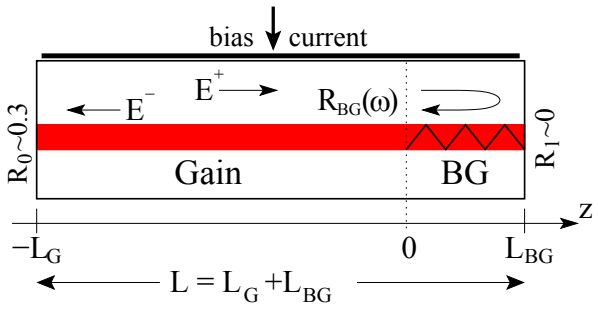

FIGURE 5.7: Schematic representation of the ML laser with the Bragg grating induced frequency dependent field reflection $R_{BG}(\omega)$.

The temporal-spatial evolution of the slowly varying complex amplitudes of the counter-propagating optical fields $E^+(z,t)$ and $E^-(z,t)$ within the uniform Bragg grating can be modelled by the travelling wave (TW) equations [139]:

$$\frac{n_g}{c_0}\partial_t E^{\pm} = \left[\mp\partial_z - i\beta(z,t) - \mathcal{D}\right] E^{\pm} - i\kappa E^{\mp} + F_{sp}^{\pm}. \tag{5.1}$$

The parameters c_0, n_g, and κ are the speed of light in vacuum, the group velocity index in semiconductor, and the field coupling coefficient due to the Bragg grating, respectively. To get basic field reflection and transmission properties in the passive Bragg grating, the Langevin noise term $F_{sp}^{\pm}$ is neglected in the present study, the complex propagation factor $\beta(z,t)$ which should be defined by the dynamics of the carriers, and the linear operator $\mathcal{D}$ used to describe the gain dispersion. In the frequency domain such a simplified system reads as

$$\partial_z \hat{E}^+(z,\omega) = -\frac{i\omega n_g}{c_0}\hat{E}^+(z,\omega) - i\kappa\hat{E}^-(z,\omega) \tag{5.2}$$

and

$$\partial_z \hat{E}^-(z,\omega) = i\kappa\hat{E}^+(z,\omega) + \frac{i\omega n_g}{c_0}\hat{E}^-(z,\omega), \tag{5.3}$$

where ω is an optical frequency of the optical field relative to the reference frequency $\frac{2\pi c_0}{\lambda_0}$ ($\lambda_0 \approx 1.55\,\mu$m: central wavelength). The solution of this system can be written as

$$\hat{E}(z,\omega) = \begin{pmatrix} \cosh\eta z - \frac{i\omega n_g}{c_0\eta}\sinh\eta z & -\frac{i\kappa}{\eta}\sinh\eta z \\ \frac{i\kappa}{\eta}\sinh\eta z & \cosh\eta z + \frac{i\omega n_g}{c_0\eta}\sinh\eta z \end{pmatrix} \hat{E}(0,\omega), \tag{5.4}$$

where $E = \begin{pmatrix} E^+ \\ E^- \end{pmatrix}$, $\hat{E}$ denotes a frequency domain representation, $\eta = \sqrt{\kappa^2 - \left(\frac{\omega n_g}{c_0}\right)^2}$, and z is a longitudinal position within the Bragg grating such that $z = 0$ and $z = L_{BG}$ are

the left and the right edges of the grating: see Fig 5.7(a). Let us assume a non vanishing field incoming into the grating through its left side ($\hat{E}^{+}(0,\omega) \neq 0$), as well as a vanishing field reflection ($R_1 = 0$) and, therefore, a vanishing backward propagating field at the right edge of the grating ($\hat{E}^{-}(L_{BG},\omega) = 0$). Then the Bragg grating induced wavelength (or frequency) dependent field *amplitude* and *intensity* reflections $r_{BG}(\omega) = \frac{\hat{E}^{-}(0,\omega)}{\hat{E}^{+}(0,\omega)}$ and $R_{BG}(\omega) = |r_{BG}(\omega)|^2$ are determined by

$$r_{BG}(\omega) = \frac{-i \sinh \eta L_{BG}}{\frac{\eta}{\kappa} \cosh \eta L_{BG} + \frac{i\omega n_g}{\kappa c_0} \sinh \eta L_{BG}}, \tag{5.5}$$

$$R_{BG}(\omega) = \frac{\sinh^2 \eta L_{BG}}{\cosh^2 \eta L_{BG} - \left(\frac{\omega n_g}{\kappa c_0}\right)^2}. \tag{5.6}$$

Equivalent expressions can be derived using the coupled mode formalism of Erdogan et al [140].

Using the above definition for the Bragg mirror, different gratings are modelled modelled while maintaining the same peak reflectivity for each of the grating. Figure 5.8 shows the modeled reflectivity spectra of the designed Bragg gratings. Note that the passband is calculated at the 0.2 dB from maximum, assuming that the reflectivity below this level will not contribute to lasing.

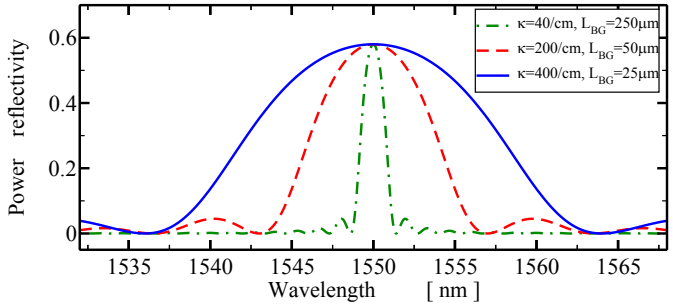

FIGURE 5.8: Designed Bragg gratings with $\kappa = 40\,\mathrm{cm}^{-1}$, $L_{BG} = 250\,\mu$m; $\kappa = 200\,\mathrm{cm}^{-1}$, $L_{BG} = 50\,\mu$m; $\kappa = 400\,\mathrm{cm}^{-1}$, $L_{BG} = 25\,\mu$m showing corresponding 0.2 dB bandwidths of 1.1nm, 5.3nm and 10.6 nm respectively at the same maximum reflectivity of about 60%

With increase in coupling coefficient for the same length of the grating, both the reflectivity and the pass band increases, while increasing the length of the grating produces a minor increase in bandwidth while largely increasing the reflectivity. Thus, in order to emulate an as-cleaved facet, allowing the full mode-locked spectrum to pass

through the Bragg grating, a grating with large coupling coefficient κ and a small length L_{BG} is the most appropriate.

5.2.2 Device fabrication and influence on mode locking characteristics

Devices were fabricated in buried ridge strip (BRS) geometry to qualify the Bragg grating, and also the influence of internal filtering on mode locking characteristics due to the Bragg mirrors. Three different types of grating-mirror lasers were fabricated with the pass bands as shown in Fig 5.8. The desired coupling coefficient of each Bragg grating was achieved by controlling the etch depth of the grating. These gratings are etched on the ridge such that the effective gain section length is 1000 μm, giving an expected free spectral range of around 40 GHz. The fabricated structure had a gain section of 500 μm, and a Bragg section of 500 μm. The gain and Bragg sections have separate metallizations, which are connected together via a wire bonding. Thus both the gain and Bragg sections are injected with electrical current.

The gratings with low coupling coefficient ($\kappa = 40\,\mathrm{cm}^{-1}$) were fabricated with smaller etch depth than those with high coupling coefficient ($\kappa = 400\,\mathrm{cm}^{-1}$), for which a deep etch process was used. It is observed that increasing the passband of the Bragg grating produces a narrowing of the minimum RF linewidth achievable for the device. Figure 5.9 presents a comparison of the different Bragg gratings with the corresponding RF line-widths. Line-width values down to 40 kHz can be achieved for the laser with a passband of 10 nm which are comparable to those of as-cleaved FP lasers.

It can be noted that the deep etch used for high coupling coefficient modifies the index contrast and hence for the same pitch of the grating the laser spectrum shifts towards longer wavelengths. It appears that for self-mode locked single section devices, in order to obtain a narrow RF-line-width and consequently low timing jitter pulse generation [141], it is necessary to have a certain number of longitudinal modes propagating inside the cavity. Previously it had been shown that this can be attributed to the influence of the intrinsic phase modifications due to Bragg gratings.

For the laser with the largest pass band, the dependence of repetition frequency and RF line-width is studied as a function of injection current. Figure 5.10(a) shows a

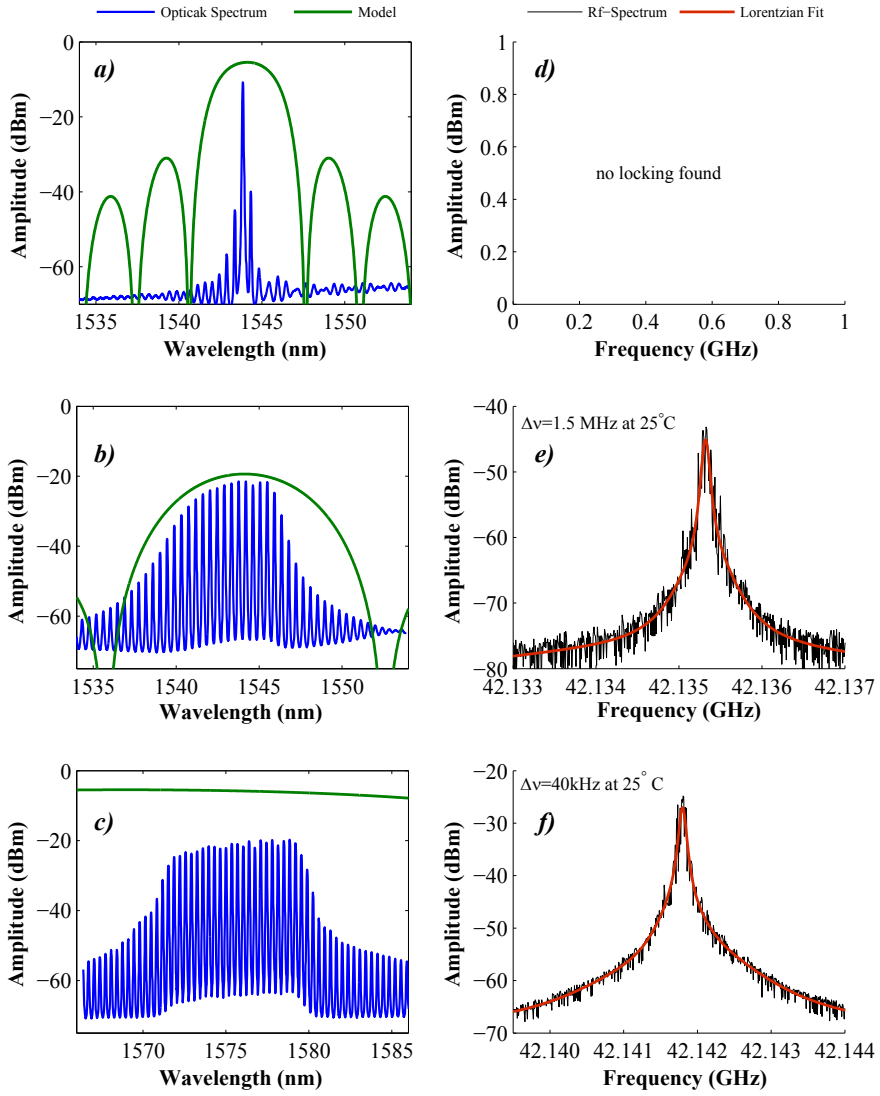

FIGURE 5.9: Optical spectra and RF line-widths of Bragg Lasers with (a,d) $\kappa = 40\,\mathrm{cm}^{-1}$, $L_{BG} = 250\,\mu$m; (b,e) $\kappa = 200\,\mathrm{cm}^{-1}$, $L_{BG} = 50\,\mu$m; (c,f) $\kappa = 400\,\mathrm{cm}^{-1}$, $L_{BG} = 25\,\mu$m

mapping of the RF spectrum with the laser bias current and the RF line-width for a current value of 300 mA.

The RF line-width is observed to assume lower values for high injection currents, with discrete regions of instability determined by the laser dynamics. Regions of effective mode locking are highlighted in the mapping in Fig 5.10(a). Effective mode-locking with RF line-widths on the order of 100 kHz and below is observed for broad current ranges of 20 to 50 mA around the current values of 300 and 450 mA. The fluctuation in the RF linewidth around these regions are related to dynamics of the MLLs, which had been

studied in details by Kefelian et al [142]. A comparison of a FP laser of 1000 μm length is presented in figure 6(c).

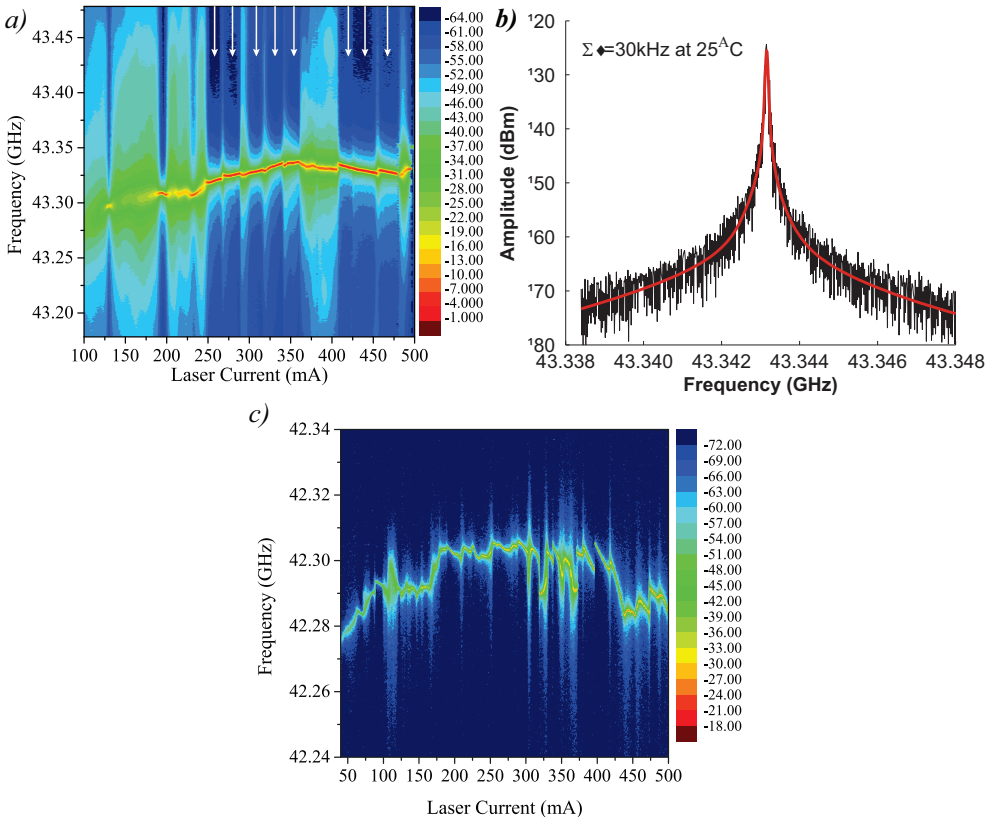

FIGURE 5.10: (a) RF-spectrum mapping for grating with $\kappa = 400$ cm^{-1}, $L_{BG} = 25\,\mu$m, which shows regions with very narrow line-width (marked with arrows) with some fluctuations. (b) Corresponding RF line-width of 30 kHz obtained at a bias current of 310 mA. (c) RF-spectrum mapping for FP laser with similar fluctuations in RF line-width.

5.2.3 Influence of Bragg grating design on intrinsic phase of optical modes

It is observed from the results on the various designs of the Bragg gratings that the gratings with the low passband would result in a laser with very broad radio-frequency linewidth resulting in no auto-pulsations or very broad pulses. This can be attributed to the modification of the optical modes due to the Bragg grating. To evaluate an impact of the Bragg gratings on optical modes a mathematical study of the TW equations is performed (5.1) governing dynamics of the optical fields in a whole ML Bragg laser represented schematically in Fig. 5.7. The TW equations (5.1) are supplemented by the

reflecting boundary conditions at the facets $z = -L_G$ and $z = L_{BG}$ of the laser:

$$E^+(-L_G, t) = r_0\, E^-(-L_G, t), \qquad E^-(L_{BG}, t) = r_1\, E^+(L_{BG}, t), \tag{5.7}$$

where $r_0 = \sqrt{R_0}\, e^{i\phi_0}$ and $r_1 = \sqrt{R_1}\, e^{i\phi_1}$ denote the complex field reflectivity coefficients at the laser facets. For ease in simulations the group velocity index $n_g = 3.6$, the total length of laser $L = L_G + L_{BG} = 1$ mm, the amplifying section facet reflectivity coefficient $R_0 = 0.3$ with the phase $\phi_0 = 0$, and the BG facet reflectivity $R_1 = 0$ with $\phi_1 = 0$ are assumed. It is noted also that the field coupling coefficient κ is non-vanishing only within the BG part of the laser, $\kappa(z) = \kappa_{BG} \neq 0$ for $z \in [0, L_{BG}]$. A few different Bragg gratings are considered for the simulations, such that $\kappa_{BG} L_{BG} = 1$ within the BG section and is compared to a single section FP laser of length L and the right facet reflectivity determined by $R_1 = 0.6$and $\phi_1 = 0$, which corresponds to the peak reflectivity of the considered BG sections.

Like in discussions of Section 5.2.1, the spontaneous emission $F_{sp}^{\pm}$ and gain dispersion $\mathcal{D}$ is ignored in (5.1), assuming that the gain spectra within the wavelength range of interest is flat, whereas the main contribution to the gain dispersion comes from the BG part of the laser.

Let us rewrite the TW equations (5.1) in the operator form

$$-i\partial_t E = H(\beta)E, \qquad H(\beta) \overset{def}{=} \frac{c_0}{n_g} \begin{pmatrix} i\partial_z - \beta & -\kappa \\ -\kappa & -i\partial_z - \beta \end{pmatrix}, \tag{5.8}$$

which for each fixed distribution β in conjunction with the boundary conditions (5.7) gives rise to the spectral problem

$$\Omega(\beta)\, \Theta(\beta, z) = H(\beta)\Theta(\beta, z), \quad \Theta(\beta, 0) \sim \binom{r_0}{1}, \quad \Theta(\beta, L) \sim \binom{1}{r_L}. \tag{5.9}$$

For each fixed complex Ω this is a linear system of ODEs with some given boundary relations. It has a solution $\Theta(\beta, z) = \binom{\Theta^+}{\Theta^-}$ only for some infinite set of properly selected values of Ω, which are the eigenvalues of the spectral problem (5.9). Complex vector-eigenfunctions $\Theta(\beta, z)$ define spatial distribution of the optical modes, whereas real and imaginary parts of the complex eigenvalues Ω represent the main contribution to the optical frequency and the damping of the optical mode, respectively [143]. That is, the

amplitude $f_k(t)$ of the k-th mode evolves according to

$$\frac{d}{dt}f_k = i\Omega_k f_k + \sum_l K_{kl} f_l, \tag{5.10}$$

where carrier dependent functions K_{kl} define coupling between the modes, are proportional to the (small) ratio between the photon and carrier relaxation times, are inverse proportional to the separation between the complex mode frequencies, and vanish at all for single-section lasers with stationary and uniformly distributed β [144].

In general, the complex propagation factor $\beta(z,t)$ in the QDot or QDash lasers operating at the ground state (GS) depends on the GS occupation probability [145]. For ML lasers with a nearly constant emission intensity this parameter should be nearly constant in time, and, therefore, should have a rather uniform distribution within each of the gain and the Bragg grating parts of the device. For simplicity in the following analysis it is assumed that within all laser device β remains independent on carriers, i.e., $\beta \equiv -i\alpha/2$, where α is the scattering losses of the field within the laser. This assumption does not allow to simulate the laser dynamics, but admits a proper description of the relations between the complex mode frequencies $\Omega(\beta)$. In the case of the FP laser ($\kappa \equiv 0$, $L_{BG} = 0$, $R_1 = 0.6$) one can easily solve Eq. (5.9) and find an infinite number of complex frequencies Ω, all of which have the same damping

$$\gamma_k = \Im m(\Omega_k) = \gamma, \qquad \gamma \stackrel{def}{=} -\frac{c_0}{n_g}\left(\Im m(\beta) + \frac{\ln(R_0 R_1)}{L}\right), \tag{5.11}$$

and the same frequency separation

$$\Delta_k = \Re e(\Omega_k - \Omega_{k-1}) = \Delta, \qquad \Delta \stackrel{def}{=} \frac{\pi c_0}{n_g L}, \tag{5.12}$$

between the adjacent modes: see black bullets in Fig. 5.11(a) and (b). Such configuration of the mode frequencies is one of the decisive factors for the ML pulsations, since the complex mode amplitudes f_k mainly evolve according to

$$f_k(t) \sim e^{i\Omega_k t} = e^{(\gamma + i\varphi_k + ik\Delta)t}. \tag{5.13}$$

Once the time independent contributions φ_k to the phases of $f_k(t)$ become equal, the intensity of the superposition of several consequent modes shows ML pulses, separated by the period $\frac{2\pi}{\Delta}$.

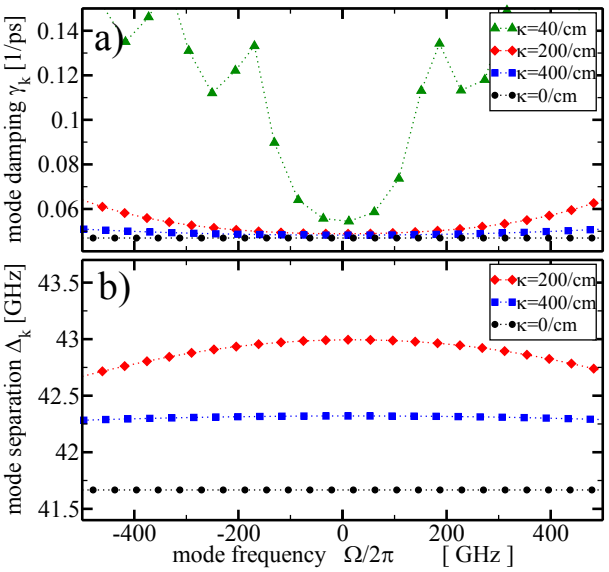

FIGURE 5.11: Calculated mode damping $\Im m(\Omega_k)$ (top) and frequency separation $\Re e(\Omega_k - \Omega_{k-1})$ of the adjacent modes (bottom) vs mode frequency $\Im m(\Omega_k)$ for the FP laser with $R_1 = 0.6$ and the lasers with different BG satisfying $\kappa_{BG} L_{BG} = 1$ and $R_1 = 0$.

The introduction of the BG changes the relative positions of the complex mode frequencies Ω. For $\kappa_{BG} = 40$ cm^{-1} and $L_{BG} = 250\,\mu$m only a few modes located within the $\sim 300GHz$ wide stop-band have similar thresholds, whereas all other modes are strongly damped (green triangles in Fig. 5.11(a)). A typical performance of such distributed Bragg reflector (DBR) laser is cw operation at the maximal gain mode, or the mode-beating type pulsations involving a couple of modes [146]. No good quality ML pulsations can be expected (see also Fig. 5.9 (a),(d)).

In the cases of $\kappa_{BG} = 200$ cm^{-1}, $L_{BG} = 50\,\mu$m (diamonds) and $\kappa_{BG} = 400$ cm^{-1}, $L_{BG} = 25\,\mu$m (squares) the damping of 20 or even more modes within the stop band is not very different. Actually, a similar modal gain dispersion can be implied by the dispersion operator $\mathcal{D}$ (omitted in this case), which, nevertheless, does not destroy ML in the lasers with saturable absorber [145]. A more crucial for ML effect of the BG is represented in Fig. 5.11(b). The implementation of the BG violates the equidistance of the mode frequencies. In the case of the laser with $\kappa_{BG} = 400$ cm^{-1} (squares) the frequency separations of ~ 20 adjacent modes shown in Fig. 5.11 vary between 42.28 and 42.32 GHz. On the other hand, these mode frequency separations in the laser with $\kappa_{BG} = 200$ cm^{-1} (diamonds) vary in almost by an order larger frequency range between 42.7 and 43 GHZ.

This strong variation of the mode separations is the main effect which drastically increases the RF-line-width as observed in experiments: compare panels (e) and (f) of Fig. 5.9.

5.2.4 Integration of Bragg reflector laser with a semiconductor optical amplifier

To exploit the Bragg mirror approach for integration were fabricated. The devices were then integrated monolithically to a QDash based semiconductor optical amplifier (SOA). Figure 5.12 shows a micrograph picture of the device in which the first two sections on the left act as gain section, followed by an SOA with tilted taper. The length of the gain section is 1000 μm and that of the tapered SOA section of 1000 μm. The tapered facet of the SOA is anti-reflection coated.

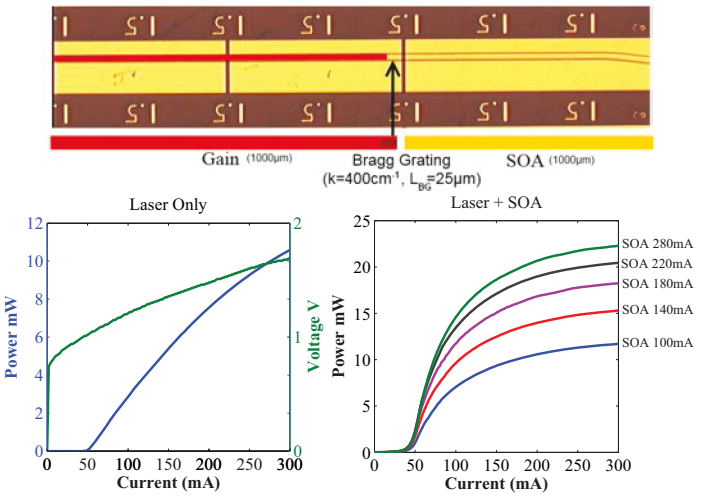

FIGURE 5.12: Optical micrograph of the device (top). Light current characteristics of the device shown above with 1000 μm gain section followed by a 1000 μm SOA having a ridge width of 1.5μm at 25°C. Figure also shows the LI characteristics of such a laser when SOA is pumped with different currents.

The Light Current characteristics of the Bragg Mirrored Laser can also be seen in Fig5.12, where figure on the left show pure characteristics of the Laser, while the figure on the right indicated the amplification produced due to the SOA.

The radio frequency mapping was repeated after the amplification of the comb by the SOA, and it is observed that the SOA does not induce significant changes to the locking performance of the laser. This has also been observed by Akbar et al. [134] on

conventional quantum well material. A similar RF line width is obtained after amplification from the SOA. The narrowest RF line width after amplification of comb is found to be ∼33 kHz. The RF mapping for constant current of 300 mA in the gain sections and varying current in the SOA and the RF linewidth for an SOA current of 200 mA is shown in Fig 5.13.

The narrowest RF line-width with and without bias current for the SOA section are found to be comparable. However, current injection in the SOA section produces a change in the regions of effective mode-locking, with respect to laser operation in absence of bias on the SOA. This effect is attributed to the interaction of the laser emission with the amplified spontaneous emission coming from the SOA, in addition to the device heating due to current injection in the SOA. Effective mode-locking regions for current ranges in excess of 50 mA can still be found. The narrow RF line-widths is accompanied by self pulsation with pulse duration down to 1.4 ps, measured by intensity autocorrelation, after chirp compensation with 120 m of SMF. Thanks to the mode shape converter of the SOA, an effective gain of about +10 dB can be obtained in the optical power coupled in the fiber. This opens the way for integration of QDash lasers with e.g. a modulator section for Radio-over-Fibre applications.

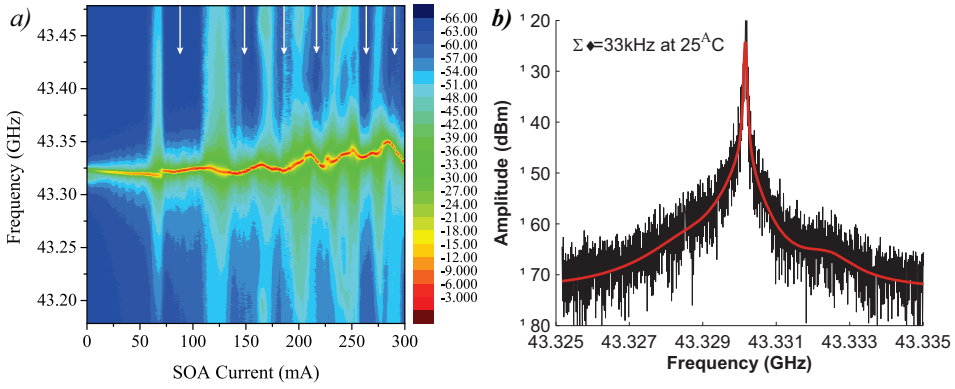

FIGURE 5.13: (a) RF-spectrum mapping for grating with κ =400cm^{-1}, $L_{BG} = 25\,\mu$m, which shows regions with very narrow line-width with some fluctuations at discrete SOA current regions. In this mapping the current electrical injection on the gain section is kept constant to around 300 mA and the electrical current on the SOA section is varied between 0 and 300 mA. (b) Corresponding RF line-width of 33 kHz obtained at 300 mA current to bias and 150 mA on SOA.

5.2.5 Frequency comb modulation

It is desirable to modulate the mode locked lasers for certain applications, like Radio over Fibre (RoF). In RoF the mode beating frequency is used as a carrier wave

thus eliminating the need of an external RF source. However it is still necessary to modulate the light signal with the data, which is performed using an external Mach Zehnder modulator or by directly modulating the laser. The direct modulation scheme is favourable due to its compactness but it had been demonstrated that the direct modulation of the gain section produces a perturbation of the RF-line-width [147]. The monolithic integration of a modulator section with the Bragg laser would solve the issue. The device as shown in Fig 5.12 can be configured to modulate the SOA to obtain a modulated frequency comb. Up to 5 Gbps on-off keying modulation was demonstrated on the present device, as shown in Fig 5.14.

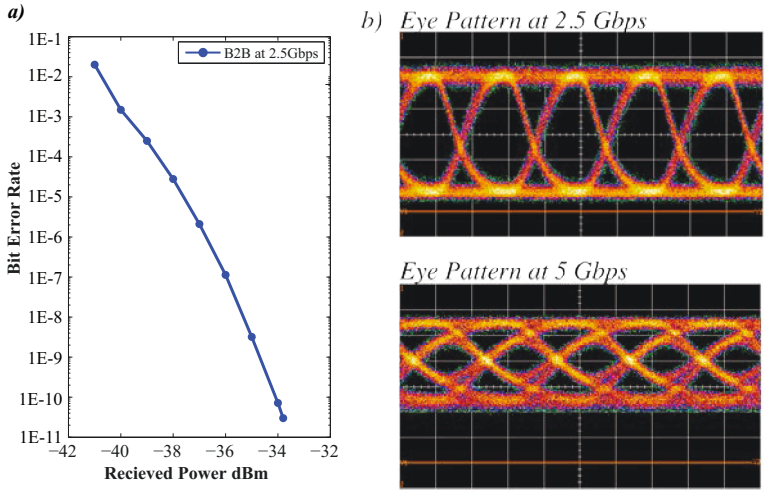

FIGURE 5.14: (a) Bit error ratio, using the SOA section as a modulator (b)Eye pattern at 2.5 Gbps with an 8dB extinction ratio and at 5Gbps with 3dB extinction ratio

Such BRS based SOA is however not an ideal candidate for the modulation operation but it demonstrates the potential of the Bragg section for the PICs. Thus, if used with a short modulator section, this approach could provide efficient modulation without producing any significant changes in the mode-locking characteristics of the laser.

5.3 Summary

This first demonstration of a Bragg based QDash-MLL opens the way for integration of QDash based frequency combs generators on InP photonic integrated circuits. A specific Bragg mirror design is presented allows to close the cavity without compromising the ML performance. Based on a detailed travelling-wave model it is found that the difference of mode-separation due to dispersion of the grating can be minimized for

gratings with high coupling coefficient. This allows modes to phase lock just as they do in a single section FP device. The approach of Bragg mirrors for closing the cavity is of particular interest as it allows integration of such lasers on photonic integrated circuits and in addition provide with a possibility to set the channel spacing and repetition frequency with lithographic precisions. The Bragg-ML laser is then integrated with a semiconductor optical amplifier as a demonstration of the potential of this approach for integration. The Bragg mirror can also be used to compensate the laser intra-cavity dispersion as presented by Sato et al. [135] and Strain et al. [148], but this would need detailed study on the material dispersion property of QDash material and also consequent change in the design of the Bragg mirror according to the gain spectrum of QDashes.

Chapter 6

Conclusions and Future Outlook

6.1 Conclusions

This PhD dissertation successfully demonstrated photonic integrated circuits on InP substrates based on specifically grown quantum dash structures. It explored in details the properties of quantum dash nano-structures. The increased know-how and improvement in growth quality of QDash material over the past few years has resulted in excellent static and dynamic characteristics. Two specific applications of QDash material for optical telecommunications were identified as directly modulated optical transmitters and low phase noise optical sources. This research work reported various epitaxial designs of QDash structure and compared their properties to identify best candidates for respective application areas.

As a first part single wavelength lasers in the 1.55 μm telecommunication window were fabricated. These DFB lasers displayed record static and dynamic characteristics. A relatively low threshold, high modal and differential gain, owing to the low dimensionality of these nano-structures was observed. The so called line-width enhancement factor was specifically observed to be very low for p-doped structures and was studied in details. The p-doped QDash lasers were then used to fabricate state of the art quantum dash directly modulated lasers. The DML based on Qdash material displayed record performance in terms of laser chirp and transmission distances. Optical transmission between a fibre span of 0-100 km was hence demonstrated. The use of an optical filter in

combination with a QDash DML was also explored. It was demonstrated that an off-the-shelf passive optical filter improves the transmission quality and increases the dynamic extinction ratio of the optical eyes. A reshaping of optical eyes in access distances was also observed and explained using a simple theory of phase inversion due to optical filter. Further, integration of an optical filter to fabricate a compact optical transmitters for access/metro networks was aimed. The commercial optical filter with a slope of 1dB/GHz was used as a reference to fabricate an integrated optical filter. The integration of DML and passive filter was achieved by designing a filter in form of a ring resonator. A vast flexibly and a large control over the filter parameter such as the on-off ratio and filter slope was demonstrated using several ring resonators designs. These ring filters were further tested for optical transmission and an unprecedented improvement was observed in the transmission performance. The transmission was however still limited due to the use of discrete components. The next steps in this activity was to reduce the losses caused by the coupling between the discrete optical components. This was achieved using the butt joint fabrication technology. A comprehensive butt joint technology was developed for fabrication of such compact transmission devices. This has resulted in a state of the art improvement in static and dynamic characteristics of directly modulated Lasers for use in access networks. For the directly modulated lasers, the self assembled quantum dash material when studied carefully indeed exceeds the performance of conventional QWells for certain specific properties. However, this improvement is not very significant in comparison to the QWell lasers. For example the low threshold current densities and linewidth enhancement factors have been as well demonstrated with QWell Lasers. The properties of quantum dashes which approach that of conventional material can be attributed to the specific wire-like density of states of QDashes. QDots (on GaAs substrate) on the other hand show a significant improvement in both static and dynamic properties owing to a true 3D confinement of the carriers. Thus for application in low loss communication window (λ =1.55 μm), the shape of the island growth needs to be further controlled in order to achieve true 3D carrier confinement. The improvement in growth of these self-assembled structures on InP substrates may have a strong impact on electronic and optical properties. Recently, the progress towards the growth of p-doped barrier in quantum dashes mimic a dot-like behaviour by limiting the free-carriers that can be transported to the quantum dashes. This results in improved dynamic characteristics for the quantum dash material. The drawback however is the increase in threshold current due to the losses induced by the p-doping. Nevertheless, as optical

telecommunication networks evolve, there is expected to be an increase in use of the coherent communication systems. The low-dimensional heterostructure would definitely outperform the conventional counterparts owing to their high spectral purity and narrow optical line-widths.

Another unique feature of QDashes is the magic-mode locking or self locking observed from the FP cavities based on QDashes. This unique feature of these nanostructure which results in ultra-low phase noise sources had been exploited for several applications. However there is a strong need for efforts towards the explanation of the phenomenon which gives rise to mode locking in FP lasers from these structures. This would help the growers to enhance the mode-locking properties of the material. MLLs based on QDashes have been studied extensively both as frequency comb generators and as sub-pico-second pulsed laser sources. However, there had been no-effort to integrate these lasers in order to increase the functionality of these optical sources. Integration of these frequency comb generators in PICs to fully exploit the unique performance of these lasers was hence studied. A detailed study of an effective Bragg grating (BG) design that can be efficiently used to close the cavity without compromising the mode locking performance of the QDash laser was performed. The approach of Bragg mirror used within this work, maintained a kilo-hertz order RF-line-width intrinsic to QDash Material system. As a demonstration of integration, a QDash-SOA was integrated and the amplification of optical power was demonstrated. The integration of QDash based devices on InP and a demonstration of the on-chip generation and amplification of optical frequency combs for telecommunication applications generated by single-section QDash based ML laser was discussed. The second method of integration of such comb sources using a ring lasers configuration is nevertheless worth investing.

InAs Qdashes on InP substrate are capable of emissions between a wavelength range of 1.3μm and 2.3μm (see appendix: A). To be able to perform growth on such a wide range of wavelength, on a single substrate, is another area of interest for quantum dash material system. Efforts need to be expanded for the growth optimisation in order to reach the performance displayed by the dashes in 1.55μm window.

Appendix A

Quantum Dash Lasers beyond 1.55 μm

A.1 QDash long wavelength lasers

Quantum Dot/Dash structure have a remarkable property of tunability in their wavelength. The tuning in the emission wavelength comes from the fact that the band-gap of QD/Qdash depends on the size of the QD/QDash. It can be observed in Eq. 2.11, that the band-gap of a QD is inversely proportional to their size. Thus, when $L_x, L_y or L_z$ is increased the band-gap is reduced. This reduction in electronic band-gap produces a change in emission wavelength.

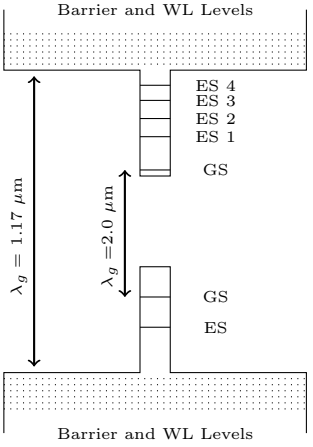

FIGURE A.1: DBAR band strudture configuration used for epitaxial growth of long wavelength QDash, notice the high number of excited states.

Within the course of this work, attempts were made to achieve photo-luminescence from the QDash at wavelength up-to 2 μm. The size of the InAs quantum dashes was increased by increasing the deposition time of the InAs Qdashes by up-to 60 %?, which increases the size of the quantum dashes from 1 nm to about 1.6 nm. Photo-luminescence spectres from a series of growths with varying (average) size of Qdashes are presented in Fig A.2. Here, the PL from different samples are plotted normalized to the PL obtained at 1.5 μm. It can be observed that the relative PL intensity decreases considerably after the wavelength of 1.7 μm. This fall in PL intensity is attributed to the detector sensitivity, as sensitivity sharply falls after wavelength of 1.8 μm.

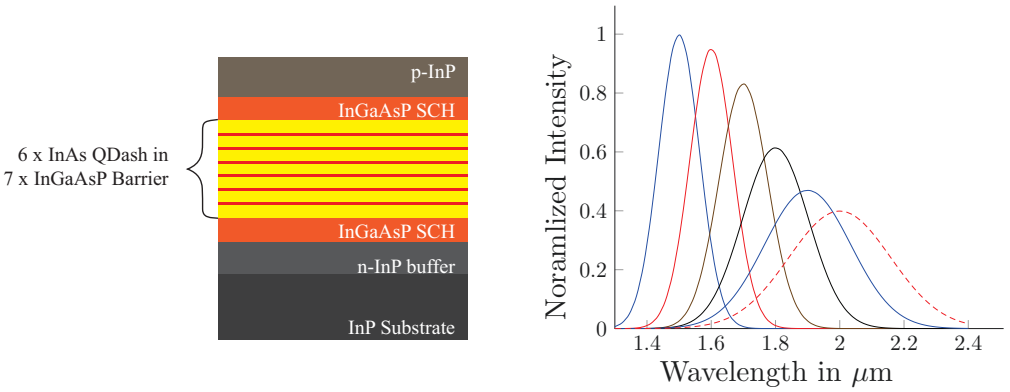

FIGURE A.2: The epitaxial structure used for the first campaign of growth of long wavelength QDashes. Photoluminescence spectra from QDash lasers, achieved by increasing the size of QDash.

Broad area and Ridge wave-guide Fabry Perot Lasers were fabricated at the clean-room facility of *LPN-CNRS* and lasing was achieved to about 1,78 μm. However, this scheme of increase in wavelength of the Qdash did not show any lasing beyond this wavelength. This is because the increase in the size of QDash also attracted large number of excited states inside the dashes (see Fig. A.1), thereby increasing the non-radiative recombinations and consequently high amount of internal losses in the laser cavity.

To reduce the non-radiative recombinations, it is desirable to have not more than 1 excited state in the band structure of QDash. The number of excited states can however be reduced by careful selection of the barrier material. As it can be seen in Fig. A.1, the difference in bandgap between the QDash material (λ_g=2.0 μm) and the InGaAsP barrier material (λ_g=1.17 μm) is relatively large, which allows large number of excited states inside the QDash band structure. If we select a material with λ_g=1.45 or μm λ_g=1.65 μm, we will lower this energy difference. This will push most of the excited states in the barrier.

A second growth campaign was run to grow Qdashes in which InGaAsP quaternary barrier material (λ_g=1.17 μm) is replaced with InGaAs ternary barrier material (λ_g=1.17 μm). The PL spectres from the second growth campaign are presented in Fig. A.3. The PL spectres are plotted normalized to λ =1.55 μm, the PL intensity decreases again in agreement with the detector sensitivity. Lasing was achieved however up-to a wavelength of 2.0 μm.

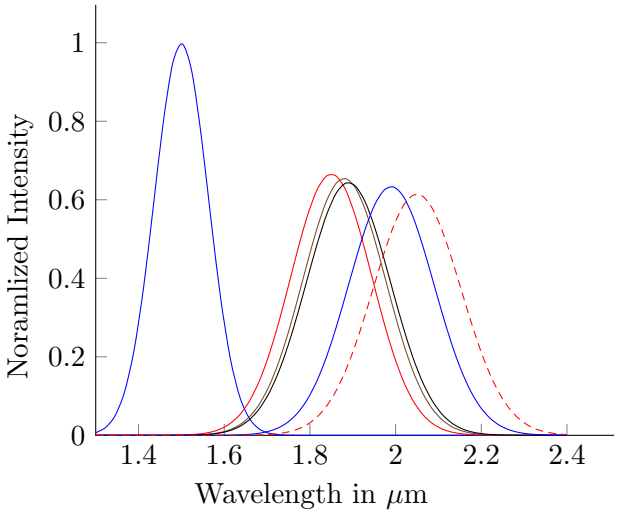

FIGURE A.3: Photoluminescence spectre from QDash epitaxial structure with InGaAs ternary barrier material (λ_g=1.17 μm), achieved by increasing the size of QDash.

A.2 QDash laser at 1.3 μm wavelength

The wavelength of the emission from QDash can similarly be reduced by reducing their size. The only problem in this case is that if InGaAsP barrier material (λ_g=1.17 μm) is used, the QDash ground state is at a risk to be pushed into the barrier. The problem can be solved by increasing the barrier height. Two wafers were grown with reduced size of the quantum dashes and increased barrier heights of λ_g=1.10 μm and λ_g=1.13 μm as shown in Fig. A.4.

Broad area lasers were fabricated to access the quality of the material and to extract the static parameters. Both the epitaxial designs were seen to lase near 1.3μm wavelength range. The wafer with the increased barrier height (λ_g=1.10 μm) however showed better static characteristics as compared to the one with lower barrier height.

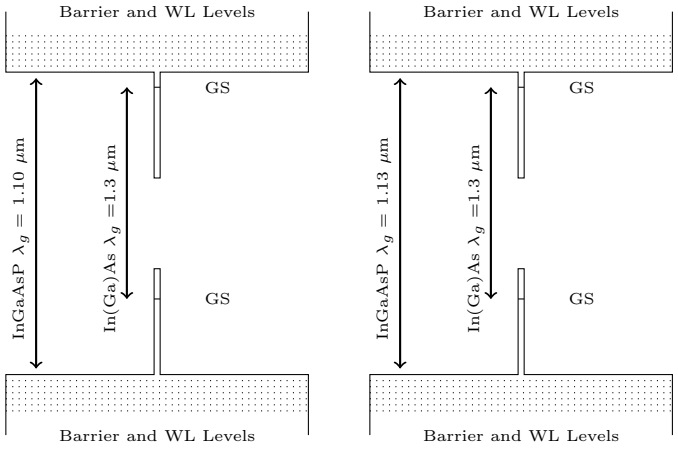

FIGURE A.4: DBAR band strudture configuration used for epitaxial growth of QDash for 1.3μm, showing InGaAsP barriers and In(Ga)As Qdashes

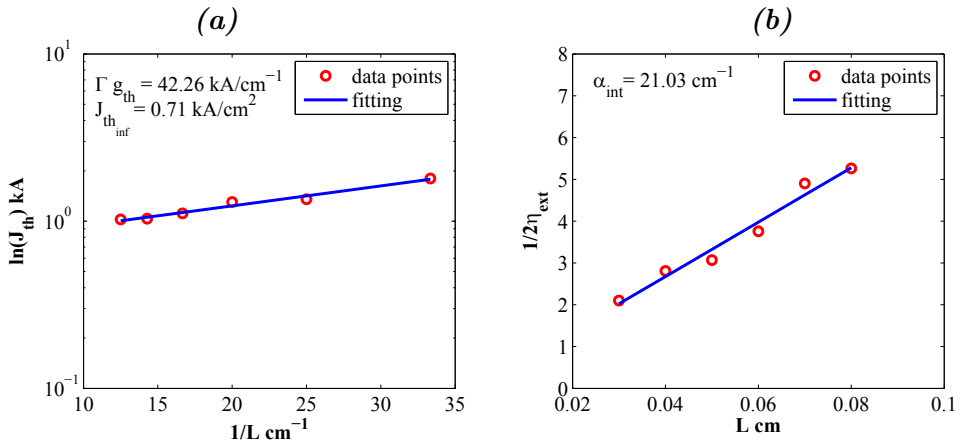

FIGURE A.5: BA lasers characteristics for barrier height of λ_g=1.10 μm showing (a) Threshold current density J_{th} as a function of inverse cavity length, the intercept on y-axis gives the value of $J_{th_{inf}}$ (b) Inverse of external quantum efficiency as a function of length of the broad area laser

It is expected that this material should also show phase noise characteristics comparable to the material at 1.55μm wavelength. Ridge waveguide lasers were thus fabricated to access the mode locking performance of this material. The light current curve and optical spectrum of a 900μm long fabricated RWG laser is presented in Fig. A.7. The material however failed to show efficient phase locking possibly due to the unoptimized barrier. This nevertheless is a promising result as it proves that the QDash material system on InP can be used to fabricate lasers at wavelengths around 1.3μm.

The capability to fabricate lasers at wavelengths ranging between 1.3μm and 2μm makes InAS/InP material system very versatile. State of the art results of moce locking characteristics the 1.55μm wavelength range have been achieved. It would be interesting

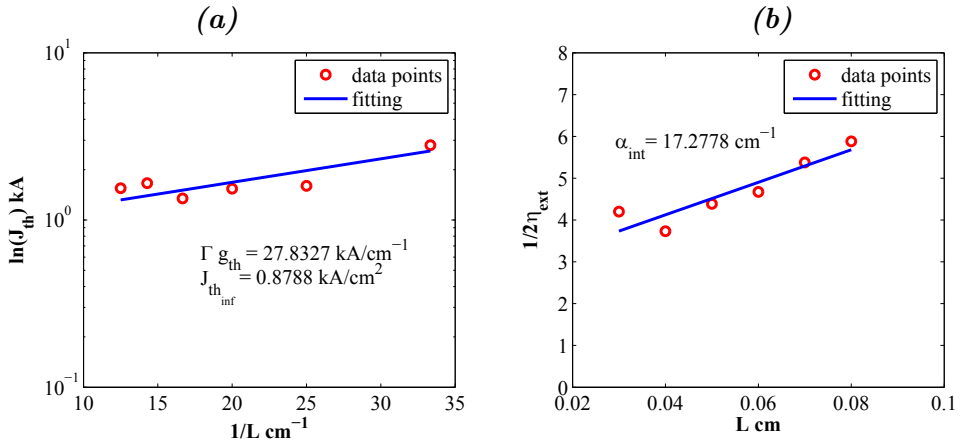

FIGURE A.6: BA lasers characteristics for barrier height of λ_g=1.13 μm showing (a) Threshold current density J_{th} as a function of inverse cavity length, the intercept on y-axis gives the value of $J_{th_{inf}}$ (b) Inverse of external quantum efficiency as a function of length of the broad area laser

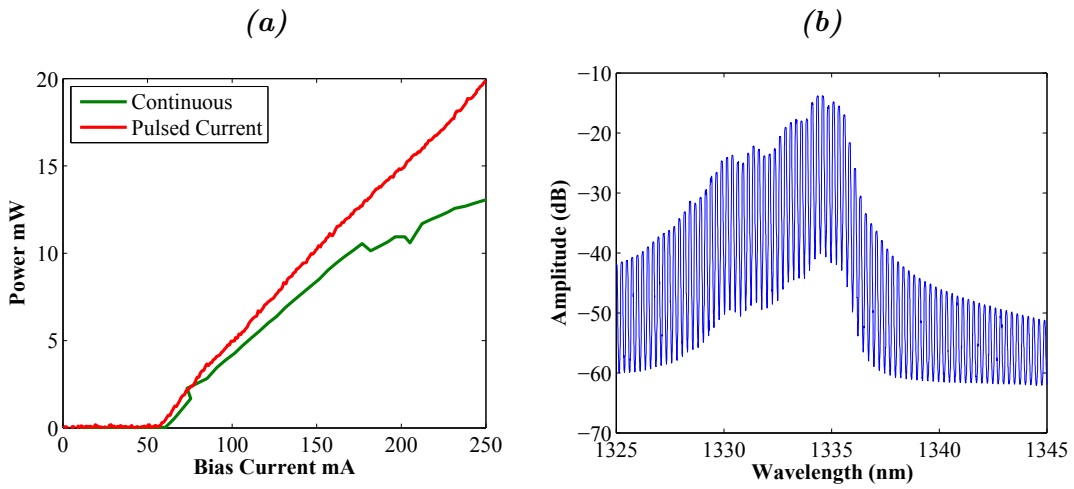

FIGURE A.7: (a) Light current characterstics of a 900μm long FP laser cavity (b) Optical Spectrum

to optimize this material for the dispersion free communication window of 1.3μm and free space communication window of 2.0μm.

Bibliography

[1] B. Wedding. Analysis of fibre transfer function and determination of receiver frequency response for dispersion supported transmission. *Electronics Letters*, 30(1):58–59, Jan 1994.

[2] N.N. Ledentsov, M. Grundmann, F. Heinrichsdorff, D. Bimberg, V.M. Ustinov, A.E. Zhukov, M.V. Maximov, Zh.I. Alferov, and J.A. Lott. Quantum-dot heterostructure lasers. *Selected Topics in Quantum Electronics, IEEE Journal of*, 6(3):439–451, May 2000.

[3] G. Kramer and G. Pesavento. Ethernet passive optical network (epon): building a next-generation optical access network. *Communications Magazine, IEEE*, 40(2):66–73, Feb 2002.

[4] P. Chanclou, Stephane Gosselin, J.F. Palacios, V.L. Alvarez, and E. Zouganeli. Overview of the optical broadband access evolution: a joint article by operators in the ist network of excellence e-photon/one. *Communications Magazine, IEEE*, 44(8):29–35, Aug 2006.

[5] V. Moeyaert and G. Maier. Network technologies for broadband access. In *Transparent Optical Networks (ICTON), 2011 13th International Conference on*, pages 1–5, June 2011.

[6] M. Hajduczenia and H.J.A da Silva. Next generation pon systems - current status. In *Transparent Optical Networks, 2009. ICTON '09. 11th International Conference on*, pages 1–8, June 2009.

[7] E. Skaljo, M. Hodzic, and I Bektas. Migration from g(e)pon to ngpon. In *Ultra Modern Telecommunications Workshops, 2009. ICUMT '09. International Conference on*, pages 1–4, Oct 2009.

[8] Thomas L Paoli and J Ripper. Direct modulation of semiconductor lasers. *Proceedings of the IEEE*, 58(10):1457–1465, 1970.

[9] Steward E Miller, Enrique AJ Marcatili, and Tingye Li. Research toward optical-fiber transmission systems. *Proceedings of the IEEE*, 61(12):1703–1704, 1973.

[10] PM Boers, MT Vlaardingerbroek, and M Danielsen. Dynamic behaviour of semiconductor lasers. *Electronics Letters*, 11(10):206–208, 1975.

[11] B. Wedding. New method for optical transmission beyond dispersion limit. *Electronics Letters*, 28(14):1298–1300, 1992.

[12] D. Mahgerefteh, C. Liao, X. Zheng, Y. Matsui, B. Johnson, D. Walker, Z.F. Fan, K. McCallion, and P. Tayebati. Error-free 250 km transmission in standard fibre using compact 10 gbit/s chirp-managed directly modulated lasers (cml) at 1550 nm. *Electronics Letters*, 41(9):543–544, April 2005.

[13] B. Dagens, D. Make, F. Lelarge, B. Rousseau, M. Calligaro, M. Carbonnelle, F. Pommereau, A. Accard, F. Poingt, L. Le Gouezigou, C. Dernazaretian, O. Le Gouezigou, J. G Provost, F. Van Dijk, P. Resneau, M. Krakowski, and G-H Duan. High bandwidth operation of directly modulated laser based on quantum-dash InAs -InP material at 1.55 μ m. *Photonics Technology Letters, IEEE*, 20(11):903–905, June 2008.

[14] M Sugawara, N Hatori, M Ishida, H Ebe, Y Arakawa, T Akiyama, K Otsubo, T Yamamoto, and Y Nakata. Recent progress in self-assembled quantum dot optical devices for optical telecommunication: temperature insensitive 10 Gbps directly modulated lasers and 40 Gbps signal-regenerative amplifiers. *Journal of Physics D: Applied Physics*, 38(13):2126, 2005.

[15] Y. Matsui, D. Mahgerefteh, Xueyan Zheng, C. Liao, Z.F. Fan, K. McCallion, and Parviz Tayebati. Chirp-managed directly modulated laser (CML). *Photonics Technology Letters, IEEE*, 18(2):385–387, Jan 2006.

[16] Y. Yokoyama, T. Hatanaka, N. Oku, H. Tanaka, I. Kobayashi, H. Yamazaki, and A. Suzuki. 10.709-gb/s-300-km transmission of plc-based chirp-managed laser packaged in pluggable transceiver without any optical or electrical dispersion compensation. In *Optical Communication, 2008. ECOC 2008. 34th European Conference on*, pages 1–2, Sept 2008.

[17] I. P. Kaminow and W. D. Johnston. Quantitative determination of sources of the electro-optic effect in lithum niobate. *Phys. Rev.*, 160:519–522, Aug 1967.

[18] S. K. Kurtz and F. N. H. Robinson. A physical model of the electro-optic effect. *Applied Physics Letters*, 10(2):62–65, 1967.

[19] J.L. Jackel. Mach-zehnder integrated optical modulator, Dec 1 1987. US Patent 4,709,978.

[20] C. Rolland, R.S. Moore, F. Shepherd, and G. Hillier. 10 gbit/s, 1.56 μm multi-quantum well inp/ingaasp mach-zehnder optical modulator. *Electronics Letters*, 29:471–472(1), March 1993.

[21] Ling Liao, Dean Samara-Rubio, Michael Morse, Ansheng Liu, Dexter Hodge, Doron Rubin, Ulrich Keil, and Thorkild Franck. High speed silicon mach-zehnder modulator. *Opt. Express*, 13(8):3129–3135, Apr 2005.

[22] T. Ido, H. Sano, D.J. Moss, S. Tanaka, and A. Takai. Strained ingaas/inalas mqw electroabsorption modulators with large bandwidth and low driving voltage. *Photonics Technology Letters, IEEE*, 6(10):1207–1209, Oct 1994.

[23] K. Morito, R. Sahara, K. Sato, and Y. Kotaki. Penalty-free 10 gb/s nrz transmission over 100 km of standard fiber at 1.55μm with a blue-chirp modulator integrated dfb laser. *Photonics Technology Letters, IEEE*, 8(3):431–433, March 1996.

[24] O. Mitomi, S. Nojima, I. Kotaka, K. Wakita, K. Kawano, and M. Naganuma. Chirping characteristic and frequency response of mqw optical intensity modulator. *Lightwave Technology, Journal of*, 10(1):71–77, Jan 1992.

[25] Brendon JC Schmidt, Arthur James Lowery, and Jean Armstrong. Experimental demonstrations of electronic dispersion compensation for long-haul transmission using direct-detection optical ofdm. *Journal of Lightwave Technology*, 26(1):196–203, 2008.

[26] R. N. Hall, G. E. Fenner, J. D. Kingsley, T. J. Soltys, and R. O. Carlson. Coherent Light Emission From GaAs Junctions. *Physical Review Letters*, 9:366–368, November 1962.

[27] M. I. Nathan, W. P. Dumke, G. Burns, F. H. Dill, Jr., and G. Lasher. Stimulated Emission of Radiation from GaAs p-n Junctions. *Applied Physics Letters*, 1:62–64, November 1962.

[28] H. Kroemer. A proposed class of hetero-junction injection lasers. *Proceedings of the IEEE*, 51(12):1782–1783, Dec 1963.

[29] Zh I Alferov, VM Andreev, EL Portnoi, and MK Trukan. Alas-gaas heterojunction injection lasers with a low room-temperature threshold. *Sov Phys Semiconductors*, 3(9):1107–1110, 1970.

[30] I Hayashi, M Panish, and P Foy. A low-threshold room-temperature injection laser. *Quantum Electronics, IEEE Journal of*, 5(4):211–212, 1969.

[31] Zh I Alferov. The history and future of semiconductor heterostructures. *Semiconductors*, 32(1):1–14, 1998.

[32] R. Dingle, W. Wiegmann, and C. H. Henry. Quantum states of confined carriers in very thin alxga1-xas-gaas-alxga1-xas heterostructures. *Phys. Rev. Lett.*, 33:827–830, Sep 1974.

[33] Raymond Dingle and Charles Howard Henry. Quantum effects in heterostructure lasers, Sep 1976. US Patent 3,982,207.

[34] Y. Arakawa and H. Sakaki. Multidimensional quantum well laser and temperature dependence of its threshold current. *Applied Physics Letters*, 40(11):939–941, 1982.

[35] S. V. Zaitsev, N. Yu Gordeev, V.M. Ustinov, A.E. Zhukov, A. Yu Egorov, I. V. Kochnev, N.N. Ledentsov, M.V. Maximov, P.S. Kop'ev, Zh.I. Alferov, and D. Bimberg. Room temperature quantum dot lasers: From basic experiments to first device oriented structures. In *Lasers and Electro-Optics Society Annual Meeting, 1996. LEOS 96., IEEE*, volume 1, pages 320–321 vol.1, Nov 1996.

[36] R. Mirin, A. Gossard, and J. Bowers. Room temperature lasing from ingaas quantum dots. *Electronics Letters*, 32(18):1732–, Aug 1996.

[37] Misturu Sugawara, N Hatori, M Ishida, Hi Ebe, Y Arakawa, T Akiyama, K Otsubo, T Yamamoto, and Y Nakata. Recent progress in self-assembled quantum-dot optical devices for optical telecommunication: temperature-insensitive 10 gb s- 1 directly modulated lasers and 40 gb s- 1 signal-regenerative amplifiers. *Journal of Physics D: Applied Physics*, 38(13):2126, 2005.

[38] Johann Peter Reithmaier and Alfred Forchel. Recent advances in semiconductor quantum-dot lasers. *Comptes Rendus Physique*, 4(6):611–619, 2003.

[39] W.W. Chow, M. Lorke, and F. Jahnke. Will quantum dots replace quantum wells as the active medium of choice in future semiconductor lasers? *Selected Topics in Quantum Electronics, IEEE Journal of*, 17(5):1349–1355, Sept 2011.

[40] M. Asada, Y. Miyamoto, and Y. Suematsu. Gain and the threshold of three-dimensional quantum-box lasers. *Quantum Electronics, IEEE Journal of*, 22(9):1915–1921, Sep 1986.

[41] H. Dery, E. Benisty, A. Epstein, R. Alizon, V. Mikhelashvili, G. Eisenstein, R. Schwertberger, D. Gold, J. P. Reithmaier, and A. Forchel. On the nature of quantum dash structures. *Journal of Applied Physics*, 95(11):6103–6111, 2004.

[42] D. Bimberg, N. Kirstaedter, N.N. Ledentsov, Zh.I. Alferov, P. S. Kop'ev, and V.M. Ustinov. Ingaas-gaas quantum-dot lasers. *Selected Topics in Quantum Electronics, IEEE Journal of*, 3(2):196–205, Apr 1997.

[43] J. H. Wei and K. S. Chan. A theoretical analysis of quantum dash structures. *Journal of Applied Physics*, 97(12), 2005.

[44] F Heinrichsdorff, M-H Mao, N Kirstaedter, A Krost, D Bimberg, AO Kosogov, and P Werner. Room-temperature continuous-wave lasing from stacked inas/gaas quantum dots grown by metalorganic chemical vapor deposition. *Applied physics letters*, 71(1):22–24, 1997.

[45] N Kirstaedter, OG Schmidt, NN Ledentsov, D Bimberg, VM Ustinov, A Yu Egorov, AE Zhukov, MV Maximov, PS Kop'ev, and Zh I Alferov. Gain and differential gain of single layer inas/gaas quantum dot injection lasers. *Applied physics letters*, 69(9):1226–1228, 1996.

[46] Dieter Bimberg. Quantum dots for lasers, amplifiers and computing. *Journal of Physics D: Applied Physics*, 38(13):2055, 2005.

[47] Anthony Krier. *Mid-infrared semiconductor optoelectronics*. Springer, 2006.

[48] Qi Lu, Qiandong Zhuang, Andrew Marshall, Manoj Kesaria, Richard Beanland, and Anthony Krier. Insb quantum dots for the mid-infrared spectral range grown on gaas substrates using metamorphic inas buffer layers. *Semiconductor Science and Technology*, 29(7), 2014.

[49] N. Chimot, F. Lelarge, R. Brenot, A. Accard, J.-G. Provost, and H. Debregeas. 1550nm directly modulated lasers for 10gb/s smf transmission up to 65km at 45 degree c with chirp optimized inas/inp quantum dashes. In *Optical Communication (ECOC), 2010 36th European Conference and Exhibition on*, pages 1–3, 2010.

[50] A. Ghatak and S. Lokanathan. *Quantum Mechanics: Theory and Applications*. Fundamental Theories of Physics. Springer Netherlands, 2004.

[51] D. Bimberg, M. Grundmann, and N.N. Ledentsov. *Quantum Dot Heterostructures*. Wiley, 1999.

[52] Alfred Forchel, Helmut Leier, Bernd E Maile, and Roland Germann. Fabrication and optical spectroscopy of ultra small iii–v compound semiconductor structures. In *Festkörperprobleme 28*, pages 99–119. Springer, 1988.

[53] S Birudavolu, N Nuntawong, G Balakrishnan, YC Xin, S Huang, SC Lee, SRJ Brueck, CP Hains, and DL Huffaker. Selective area growth of inas quantum dots formed on a patterned gaas substrate. *Applied physics letters*, 85(12):2337–2339, 2004.

[54] Steven P Beaumont. Nanofabrication and optical assessment of quantum wires and dots. In *Granular Nanoelectronics*, pages 67–78. Springer US, 1991.

[55] Keiko Ogai, Yoshihide Kimura, Ryuichi Shimizu, Junichi Fujita, and Shinji Matsui. Nanofabrication of grating and dot patterns by electron holographic lithography. *Applied physics letters*, 66(12):1560–1562, 1995.

[56] Masanori Komuro, Hiroshi Hiroshima, Hisao Tanoue, and Toshihiko Kanayama. Maskless etching of a nanometer structure by focused ion beams. *Journal of Vacuum Science & Technology B*, 1(4):985–989, 1983.

[57] Stephen Y Chou, Peter R Krauss, and Preston J Renstrom. Nanoimprint lithography. *Journal of Vacuum Science & Technology B*, 14(6):4129–4133, 1996.

[58] KC Rajkumar, K Kaviani, J Chen, P Chen, A Madhukar, and DH Rich. In-situ growth of three-dimensionally confined structures on patterned gaas (111) b substrates. In *MRS Proceedings*, volume 263, page 163. Cambridge Univ Press, 1992.

[59] J Cibert, PM Petroff, DJ Werder, SJ Pearton, AC Gossard, and JH English. Kinetics of implantation enhanced interdiffusion of ga and al at gaas-gaxal1- xas interfaces. *Applied physics letters*, 49(4):223–225, 1986.

[60] K Brunner, G Abstreiter, M Walther, G Böhm, and G Trankle. Optical characterization of gaas/algaas nanostructures fabricated by focussed laser beam induced thermal interdiffusion. *Surface science*, 267(1):218–222, 1992.

[61] Ricardo Rosales, S. G. Murdoch, R.T. Watts, K. Merghem, Anthony Martinez, Francois Lelarge, Alain Accard, L. P. Barry, and Abderrahim Ramdane. High performance mode locking characteristics of single section quantum dash lasers. *Opt. Express*, 20(8):8649–8657, Apr 2012.

[62] F. Lelarge, B. Dagens, J. Renaudier, R. Brenot, A. Accard, F. van Dijk, D. Make, O. Le Gouezigou, J. Provost, F. Poingt, J. Landreau, O. Drisse, E. Derouin, B. Rousseau, F. Pommereau, and Guang-Hua Duan. Recent advances on InAs/InP quantum dash based semiconductor lasers and optical amplifiers operating at 1.55 μm. *Journal of Selected Topics in Quantum Electronics, IEEE*, 13(1):111–124, Jan 2007.

[63] A.J. Zilkie, J. Meier, M. Mojahedi, P.J. Poole, P. Barrios, D. Poitras, Thomas J. Rotter, Chi Yang, A. Stintz, K.J. Malloy, P. W E Smith, and J. Stewart Aitchison. Carrier dynamics of quantum-dot, quantum-dash, and quantum-well semiconductor optical amplifiers operating at 1.55 μm. *Quantum Electronics, IEEE Journal of*, 43(11):982–991, Nov 2007.

[64] LV Asryan and RA Suris. Theory of threshold characteristics of semiconductor quantum dot lasers. *Semiconductors*, 38(1):1–22, 2004.

[65] G. T. Liu, A. Stintz, H. Li, K.J. Malloy, and L.F. Lester. Extremely low room-temperature threshold current density diode lasers using inas dots in in0.15ga0.85as quantum well. *Electronics Letters*, 35(14):1163–1165, Jul 1999.

[66] A Stintz, GT Liu, H Li, LF Lester, and KJ Malloy. Low-threshold current density 1.3-μm inas quantum-dot lasers with the dots-in-a-well (dwell) structure. *Photonics Technology Letters, IEEE*, 12(6):591–593, 2000.

[67] Hitoshi Shimizu, Shanmugam Saravanan, Junji Yoshida, Sayoko Ibe, and Noriyuki Yokouchi. Inas quantum dot lasers with extremely low threshold current density (7 a/cm 2 /layer). *Japanese Journal of Applied Physics*, 44(8L):L1103, 2005.

[68] CY Liu, SF Yoon, QQ Cao, CZ Tong, and HF Li. Low transparency current density and high temperature operation from ten-layer p-doped 1.3 μm inas/ingaas/gaas quantum dot lasers. *Applied physics letters*, 90(4):041103–041103, 2007.

[69] Y Suematsu, M Yamada, and K Hayashi. Integrated twin-guide algaas laser with multiheterostructure. *Quantum Electronics, IEEE Journal of*, 11(7):457–460, 1975.

[70] Naresh Chand, EE Becker, JP Van der Ziel, SN Gu Chu, and NK Dutta. Excellent uniformity and very low (¡ 50 a/cm2) threshold current density strained ingaas quantum well diode lasers on gaas substrate. *Applied physics letters*, 58(16):1704–1706, 1991.

[71] S. Joshi, N. Chimot, L.A. Neto, A. Accard, J.-G. Provost, F. Franchin, A. Ramdane, and F. Lelarge. Quantum dash based directly modulated lasers for long-reach access networks. *Electronics Letters*, 50(7):534–536, March 2014.

[72] K. Merghem, R. Rosales, A. Martinez, G. Patriarche, A. Ramdane, N. Chimot, F. Van Dijk, Y. Moustapha-Rabault, F. Poingt, and F. Lelarge. Improvement of modal gain of inas/inp quantum-dash lasers. In *Compound Semiconductor Week (CSW/IPRM), 2011 and 23rd International Conference on Indium Phosphide and Related Materials*, pages 1–4, May 2011.

[73] Z. Mi and Pallab Bhattacharya. Analysis of the linewidth-enhancement factor of long-wavelength tunnel-injection quantum-dot lasers. *Quantum Electronics, IEEE Journal of*, 43(5):363–369, May 2007.

[74] S. Azouigui, B. Dagens, F. Lelarge, J. Provost, D. Make, O. Le Gouezigou, A. Accard, A. Martinez, K. Merghem, F. Grillot, O. Dehaese, R. Piron, S. Loualiche, Qin Zou, and A. Ramdane. Optical feedback tolerance of quantum-dot- and quantum-dash-based semiconductor lasers operating at 1.55 μ m. *Selected Topics in Quantum Electronics, IEEE Journal of*, 15(3):764–773, May 2009.

[75] Q. Zou, K. Merghem, S. Azouigui, A. Martinez, A. Accard, N. Chimot, F. Lelarge, and A. Ramdane. Feedback-resistant p-type doped inas/inp quantum-dash distributed feedback lasers for isolator-free 10 Gbps transmission at 1.55 μm. *Applied Physics Letters*, 97(23):231115–231115–3, Dec 2010.

[76] Govind P Agrawal and Niloy K Dutta. *Semiconductor Lasers*. Kluwer Academic Publishers, 1993.

[77] C. Gilfert, V. Ivanov, N. Oehl, M. Yacob, and J. P Reithmaier. High gain 1.55 μm diode lasers based on inas quantum dot like active regions. *Applied Physics Letters*, 98(20):201102–201102–3, May 2011.

[78] Mariangela Gioannini. Investigation of p-type doping effect on the gain characteristics of quantum dash semiconductor lasers, 2004.

[79] A. Ramdane, A. Martinez, S. Azouigui, D.-Y. Cong, K. Merghem, A. Akrout, C. Gosset, G. Moreau, F. Lelarge, B. Dagens, J.-G. Provost, A. Accard, O. Le Gouezigou, I. Krestnikov, A. Kovsh, and M. Fischer. Recent advances in long wavelength quantum dot based lasers, 2008.

[80] S. Hein, V. von Hinten, S. Höfling, and A. Forchel. The impact of p-doping on the static and dynamic properties of 1.5μm quantum dash lasers on inp. *Applied Physics Letters*, 92(1):–, 2008.

[81] P.R. Selway. Special issue paper. semiconductor lasers for optical communication. *Electrical Engineers, Proceedings of the Institution of*, 123(6):609–618, 1976.

[82] R.H. Wang, A. Stintz, P.M. Varangis, T.C. Newell, H. Li, K.J. Malloy, and L.F. Lester. Room-temperature operation of inas quantum-dash lasers on inp [001]. *Photonics Technology Letters, IEEE*, 13(8):767–769, 2001.

[83] Simon M Sze and Kwok K Ng. *Physics of semiconductor devices*. John Wiley & Sons, 2006.

[84] Christophe Peucheret. Direct current modulation of semiconductor lasers.

[85] D. Marcuse and Tein-Pei Lee. On approximate analytical solutions of rate equations for studying transient spectra of injection lasers. *Quantum Electronics, IEEE Journal of*, 19(9):1397–1406, Sep 1983.

[86] D. Marcuse and Tein-Pei Lee. Rate equation model of a coupled-cavity laser. *Quantum Electronics, IEEE Journal of*, 20(2):166–176, Feb 1984.

[87] Brian R Bennett, Richard A Soref, and Jesus A Del Alamo. Carrier-induced change in refractive index of inp, gaas and ingaasp. *Quantum Electronics, IEEE Journal of*, 26(1):113–122, 1990.

[88] C.H. Henry. Theory of the linewidth of semiconductor lasers. *Quantum Electronics, IEEE Journal of*, 18(2):259–264, Feb 1982.

[89] MD Feit, JA Fleck Jr, and A Steiger. Solution of the schrödinger equation by a spectral method. *Journal of Computational Physics*, 47(3):412–433, 1982.

[90] M. Fukuda. *Optical Semiconductor Devices*. A Wiley Interscience publication. Wiley, 1999.

[91] Gordon Lasher and Frank Stern. Spontaneous and stimulated recombination radiation in semiconductors. *Phys. Rev.*, 133:A553–A563, Jan 1964.

[92] G.P. Agrawal. *Fiber-Optic Communication Systems*. Wiley Series in Microwave and Optical Engineering. Wiley, 2012.

[93] RodneyS Tucker. High-speed modulation of semiconductor lasers. *Electron Devices, IEEE Transactions on*, 32(12):2572–2584, 1985.

[94] G Moreau, S Azouigui, D-Y Cong, K Merghem, A Martinez, G Patriarche, A Ramdane, F Lelarge, B Rousseau, B Dagens, et al. Effect of layer stacking and p-type doping on the performance of inas/inp quantum-dash-in-a-well lasers emitting at 1.55 μm. *Applied physics letters*, 89(24):241123–241123, 2006.

[95] L Bach, W Kaiser, R Schwertberger, JP Reithmaier, and A Forchel. 1.54 μm singlemode inp-based q-dash lasers. *Electronics Letters*, 39(13):985–987, 2003.

[96] P.A. Morton, T. Tanbun-Ek, R.A. Logan, A.M. Sergent, P.F. Sciortino, and D.L. Coblentz. Frequency response subtraction for simple measurement of intrinsic laser dynamic properties. *Photonics Technology Letters, IEEE*, 4(2):133–136, Feb 1992.

[97] MJ Adams and M Osiński. Influence of spectral hole-burning on quaternary laser transients. *Electronics Letters*, 19(16):627–628, 1983.

[98] Kazuhito Furuya, Yasuharu Suematsu, and Tchanghee Hong. Reduction of resonancelike peak in direct modulation due to carrier diffusion in injection laser. *Applied optics*, 17(12):1949–1952, 1978.

[99] DJ Channin. Effect of gain saturation on injection laser switching. *Journal of Applied Physics*, 50:3858–3860, 1979.

[100] R Nagarajan, M Ishikawa, and JE Bowers. Effects of carrier transport on relative intensity noise and critique of k factor predictions of modulation response. *Electronics Letters*, 28(9):846–848, 1992.

[101] R. Nagarajan, Masayuki Ishikawa, Toru Fukushima, Randall S. Geels, and J.E. Bowers. High speed quantum-well lasers and carrier transport effects. *Quantum Electronics, IEEE Journal of*, 28(10):1990–2008, Oct 1992.

[102] RodneyS Tucker and I Kaminow. High-frequency characteristics of directly modulated ingaasp ridge waveguide and buried heterostructure lasers. *Lightwave Technology, Journal of*, 2(4):385–393, 1984.

[103] Basil W Hakki and Thomas L Paoli. Gain spectra in gaas double- heterostructure injection lasers. *Journal of Applied Physics*, 46(3):1299–1306, 1975.

[104] R.C. Srinivasan and J.C. Cartledge. On using fiber transfer functions to characterize laser chirp and fiber dispersion. *Photonics Technology Letters, IEEE*, 7(11):1327–1329, Nov 1995.

[105] Asier Villafranca, José A Lázaro, Inigo Salinas, and Ignacio Garcés. Measurement of the linewidth enhancement factor in dfb lasers using a high-resolution optical spectrum analyzer. *IEEE photonics technology letters*, 17(11):2268–2270, 2005.

[106] G.H. Shin, M. Teshima, and M. Ohtsu. Novel measurement method of linewidth enhancement factor in semiconductor lasers by optical self-locking. *Electronics Letters*, 25(1):27–28, Jan 1989.

[107] Yanguang Yu, G. Giuliani, and S. Donati. Measurement of the linewidth enhancement factor of semiconductor lasers based on the optical feedback self-mixing effect. *Photonics Technology Letters, IEEE*, 16(4):990–992, April 2004.

[108] D. Byrne, W-H Guo, R. Phelan, Q-Y Lu, J.F. Donegan, and B. Corbett. Measurement of linewidth enhancement factors for ingaalas laser diode by fourier series expansion method. *Electronics Letters*, 43(21):1145–1145, Oct 2007.

[109] J Provost and Frederic Grillot. Measuring the chirp and the linewidth enhancement factor of optoelectronic devices with a mach-zehnder interferometer. *Photonics Journal, IEEE*, 3(3):476–488, 2011.

[110] G. Liu, X. Jin, and S. L Chuang. Measurement of linewidth enhancement factor of semiconductor lasers using an injection-locking technique. *Photonics Technology Letters, IEEE*, 13(5):430–432, May 2001.

[111] K. Kikuchi and H. Iwasawa. Measurement of linewidth enhancement factor of semiconductor lasers by modified direct frequency-modulation method. *Electronics Letters*, 24(13):821–822, Jun 1988.

[112] Piotr Konrad Kondratko, Shun-Lien Chuang, Gabriel Walter, Theodore Chung, and Nick Holonyak. Observations of near-zero linewidth enhancement factor in a quantum-well coupled quantum-dot laser. *Applied Physics Letters*, 83(23):4818–4820, 2003.

[113] G. Moreau, K. Merghem, A Martinez, F. Lelarge, and A Ramdane. Low linewidth enhancement factor (α_h 0.5) of 9- layer inas/inp quantum dash lasers emitting at 1.55 μm. In *Indium Phosphide and Related Materials Conference Proceedings, 2006 International Conference on*, pages 116–118, 2006.

[114] AJ. Zilkie, J. Meier, P. W E Smith, M. Mojahedi, J.S. Aitchison, P.J. Poole, P. Barrios, D. Poitras, R.H. Wang, T.J. Rotter, C. Yang, A Stintz, and K.J. Malloy. Linewidth enhancement factors in 1.55 μm quantum dot, quantum dash, and quantum well amplifiers. In *Lasers and Electro-Optics, 2007. CLEO 2007. Conference on*, pages 1–2, May 2007.

[115] N.A Naderi, F. Grillot, V. Kovanis, and L.F. Lester. Simultaneous low linewidth enhancement factor and high bandwidth quantum-dash injection-locked laser. In *Photonics Conference (PHO), 2011 IEEE*, pages 115–116, Oct 2011.

[116] R. Schimpe, J.E. Bowers, and T.L. Koch. Characterisation of frequency response of 1.5 μm InGaAsP dfb laser diode and ingaas pin photodiode by heterodyne measurement technique. *Electronics Letters*, 22(9):453–454, April 1986.

[117] Sergey Melnik, Guillaume Huyet, and Alexander Uskov. The linewidth enhancement factor α of quantum dot semiconductor lasers. *Opt. Express*, 14(7):2950–2955, Apr 2006.

[118] R.A Saunders, J.P. King, and I Hardcastle. Wideband chirp measurement technique for high bit rate sources. *Electronics Letters*, 30(16):1336–1338, Aug 1994.

[119] C. Laverdiere, A Fekecs, and M. Tetu. A new method for measuring time-resolved frequency chirp of high bit rate sources. *Photonics Technology Letters, IEEE*, 15(3):446–448, March 2003.

[120] S. Mohrdiek, H. Burkhard, F. Steinhagen, H. Hillmer, R. Losch, W. Schlapp, and R. Gobel. 10-gb/s standard fiber transmission using directly modulated 1.55 μm quantum-well dfb lasers. *Photonics Technology Letters, IEEE*, 7(11):1357–1359, 1995.

[121] W. Loedhammacakra, W.P. Ng, and R.A. Cryan. An improved chromatic dispersion compensation technique employing an optical all pass filter equaliser in a 10 gb/s optical system. In *High Frequency Postgraduate Student Colloquium, 2005*, pages 105–108, Sept 2005.

[122] C.K. Madsen, G. Lenz, A.J. Bruce, M.A. Cappuzzo, L.T. Gomez, and R.E. Scotti. Integrated all-pass filters for tunable dispersion and dispersion slope compensation. *Photonics Technology Letters, IEEE*, 11(12):1623–1625, Dec 1999.

[123] J. Wang and K. Petermann. Small signal analysis for dispersive optical fiber communication systems. *Lightwave Technology, Journal of*, 10(1):96–100, Jan 1992.

[124] Bruno Robillart, Cosimo Calò, Abdoulaye Fall, François Lamare, Yaneck Gottesman, and Badr-Eddine Benkelfat. Spectral and temporal phase measurement by optical frequency-domain reflectometry. In *SPIE LASE*, pages 896134–896134. International Society for Optics and Photonics, 2014.

[125] Sangyeup Kim, Jun Terada, and Naoto Yoshimoto. Snr optimization through digital frequency-domain pre-emphasis for extending transmission distances in dml-based ofdm-pon systems. In *Optical Fiber Communication Conference/National*

Fiber Optic Engineers Conference 2013, page JTh2A.69. Optical Society of America, 2013.

[126] EAJ Marcatili. Bends in optical dielectric guides. *Bell System Technical Journal*, 48(7):2103–2132, 1969.

[127] Amnon Yariv. Universal relations for coupling of optical power between microresonators and dielectric waveguides. *Electronics Letters*, 36(4):321–322, 2000.

[128] Amnon Yariv. Critical coupling and its control in optical waveguide-ring resonator systems. *IEEE Photonics Technology Letters*, 14(4):483–485, 2002.

[129] Dominik G Rabus, Michael Hamacher, Ute Troppenz, and Helmut Heidrich. Optical filters based on ring resonators with integrated semiconductor optical amplifiers in gainasp-inp. *Selected Topics in Quantum Electronics, IEEE Journal of*, 8(6):1405–1411, 2002.

[130] Y. Gottesman, E.V.K. Rao, D. Piot, E. Vergnol, and B. Dagens. An in-depth analysis of reflections in mmi couplers using optical low-coherence reflectometry: design optimization and performance evaluation. *Applied Physics B*, 73(5-6):609–612, 2001.

[131] N. Chimot, S. Joshi, F. Lelarge, A. Accard, J.-G. Provost, F. Franchin, and H. Debregeas-Sillard. Qdash-based directly modulated lasers for next-generation access network. *Photonics Technology Letters, IEEE*, 25(17):1660–1663, Sept 2013.

[132] A. Akrout, A. Shen, R. Brenot, F. Van-Dijk, O. Legouezigou, F. Pommereau, F. Lelarge, A. Ramdane, and Guang-Hua Duan. Separate error-free transmission of eight channels at 10 gb/s using comb generation in a quantum-dash-based mode-locked laser. *Photonics Technology Letters, IEEE*, 21(23):1746–1748, Dec 2009.

[133] EU Rafailov, MA Cataluna, and Wilson Sibbett. Mode-locked quantum-dot lasers. *Nat. Photonics*, 1(7):395–401, 2007.

[134] Jehan Akbar, Lianping Hou, Mohsin Haji, Michael J. Strain, John H. Marsh, A. Catrina Bryce, and Anthony E. Kelly. High power (130mw) 40ghz 1.55μm mode-locked distributed bragg reflector lasers with integrated optical amplifiers. *Opt. Lett.*, 37(3):344–346, Feb 2012.

[135] K. Sato, A. Hirano, and H. Ishii. Chirp-compensated 40-ghz mode-locked lasers integrated with electroabsorption modulators and chirped gratings. *Journal of Selected Topics in Quantum Electronics, IEEE*, 5(3):590–595, May 1999.

[136] R. Rosales, K. Merghem, A. Martinez, A. Akrout, J. P Tourrenc, A. Accard, F. Lelarge, and A. Ramdane. InAs/InP quantum-dot passively mode-locked lasers for 1.55/mum applications. *Journal of Selected Topics in Quantum Electronics, IEEE*, 17(5):1292–1301, Sept 2011.

[137] Eamonn Martin, Regan Watts, Laurent Bramerie, Alexandre Shen, Harry Gariah, Fabrice Blache, Francois Lelarge, and Liam Barry. Terahertz-bandwidth coherence measurements of a quantum dash laser in passive and active mode-locking operation. *Opt. Lett.*, 37(23):4967–4969, Dec 2012.

[138] E. Sooudi, G. Huyet, John G. McInerney, F. Lelarge, K. Merghem, A. Martinez, A. Ramdane, and S.P. Hegarty. Observation of harmonic-mode-locking in a mode-locked InAs/InP-based quantum-dash laser with cw optical injection. *Photonics Technology Letters, IEEE*, 23(9):549–551, May 2011.

[139] U. Bendelow, Mindaugas Radziunas, J. Sieber, and M. Wolfrum. Impact of gain dispersion on the spatio-temporal dynamics of multisection lasers. *Journal of Quantum Electronics, IEEE*, 37(2):183–188, Feb 2001.

[140] Turan Erdogan. Fiber grating spectra. *Journal of Lightwave Technology*, 15(8):1277–1294, Aug 1997.

[141] F. Kefelian, S. O'Donoghue, M.T. Todaro, John G. McInerney, and G. Huyet. Rf linewidth in monolithic passively mode-locked semiconductor laser. *Photonics Technology Letters, IEEE*, 20(16):1405–1407, Aug 2008.

[142] Fabien Kéfélian, Shane O'Donoghue, Maria Teresa Todaro, John McInerney, and Guillaume Huyet. Experimental investigation of different regimes of mode-locking in a high repetition rate passively mode-locked semiconductor quantum-dot laser. *Opt. Express*, 17(8):6258–6267, Apr 2009.

[143] M. Radziunas and H.-J. Wunsche. *Multisection Lasers: Longitudinal Modes and their Dynamics*. Springer New York, 2005.

[144] M. Radziunas. Numerical bifurcation analysis of the traveling wave model of multisection semiconductor lasers. *Physica D: Nonlinear Phenomena*, 213(1):98 – 112, 2006.

[145] Mindaugas Radziunas, Andrei G. Vladimirov, Evgeny A. Viktorov, G. Fiol, H. Schmeckebier, and D. Bimberg. Pulse broadening in quantum-dot mode-locked semiconductor lasers: Simulation, analysis, and experiments. *Journal of Quantum Electronics, IEEE*, 47(7):935–943, July 2011.

[146] M Radziunas, KH Hasler, B Sumpf, Tran Quoc Tien, and H Wenzel. Mode transitions in distributed bragg reflector semiconductor lasers: experiments, simulations and analysis. *Journal of Physics B: Atomic, Molecular and Optical Physics*, 44(10):105401, 2011.

[147] F. Brendel, Jianjia Yi, J. Poette, B. Cabon, and T. Zwick. Properties of millimeter-wave signal generation and modulation using mode-locked q-dash lasers for gigabit rf-over-fiber links. In *The 7th German Microwave Conference (GeMiC), 2012*, pages 1–4, March 2012.

[148] M.J. Strain, P.M. Stolarz, and M. Sorel. Passively mode-locked lasers with integrated chirped bragg grating reflectors. *Journal of Quantum Electronics, IEEE*, 47(4):492–499, April 2011.